3D Real-Time Stockpile Mapping and Modelling with Accurate Quality Calculation using Voxels

Shi Zhao

School of Mechanical Engineering
University of Adelaide

This dissertation is submitted for the degree of
Doctor of Philosophy

Robotics Research Group February 2016

In loving memory of my grandparents …

Declaration

Originality

I certify that this work contains no material which has been accepted for the award of any other degree or diploma in my name in any university or other tertiary institution and, to the best of my knowledge and belief, contains no material previously published or written by another person, except where due reference has been made in the text. In addition, I certify that no part of this work will, in the future, be used in a submission in my name for any other degree or diploma in any university or other tertiary institution without the prior approval of the University of Adelaide and where applicable, any partner institution responsible for the joint award of this degree.

Permissions

I give consent to this copy of my thesis when deposited in the University Library, being made available for loan and photocopying, subject to the provisions of the Copyright Act 1968. The author acknowledges that copyright of published works contained within this thesis resides with the copyright holder(s) of those works.

I also give permission for the digital version of my thesis to be made available on the web, via the University's digital research repository, the Library Search and also through web search engines, unless permission has been granted by the University to restrict access for a period of time.

Shi Zhao
February 2016

Acknowledgements

I would like to take this opportunity to express my deepest and most sincere thanks and expressions of gratitude to my principal supervisor, Tien-Fu, Lu. Your broad knowledge and logical pattern of thought, combined with a generous and friendly manner, have always helped me improving. Your encouraging guidance and mentorship have motivated me throughout my candidature.

I would not have been able to continue without the financial and practical assistance offered by my supervisor Ben Koch of MatrixGroup through the ARC Linkage LP0989780 Grant. Thank you for providing me with the opportunity to do this unique research in an exciting field. Your insightful discussions and industry experience make my Ph.D. experience more productive and stimulating.

In the course of my research, I have been worked with many others in the Robotics Group at the School of Mechanical Engineering, University of Adelaide. Their supports and advices were invaluable. I thank all the current members of the team: Kuan Tan, Mohamed Awadalla, Maung Myo, Da Sun and Di Gao.

Lastly, I owe my greatest thanks to my family. They deserve special gratitude for the support and understanding of my research career. Without them I would not have been able to travel and study in Australia. To my wife, Soyeon Oh, thank you for your abundant love and support throughout the years.

Publications

Journal

1. Shi Zhao, Tien-Fu Lu, Ben Koch, Alan Hurdsman, "Automatic quality estimation in blending using a 3D stockpile management model," Advanced Engineering Informatics, Volume 29, Issue 3, August 2015, Pages 680-695, ISSN 1474-0346, http://dx.doi.org/10.1016/j.aei.2015.07.002.
2. Shi Zhao, Tien-Fu Lu, Ben Koch, Alan Hurdsman, "Stockpile modelling and quality calculation for continuous stockpile management," International Journal of Mineral Processing, Volume 140, 10 July 2015, Pages 32-42, ISSN 0301-7516, http://dx.doi.org/10.1016/j.minpro.2015.04.012.
3. Shi Zhao, Tien-Fu Lu, Ben Koch, Alan Hurdsman, "Dynamic modelling of 3D stockpile for life-cycle management through sparse range point clouds," International Journal of Mineral Processing, Volume 125, 10 December 2013, Pages 61-77, ISSN 0301-7516, http://dx.doi.org/10.1016/j.minpro.2013.09.009.

Conference

1. Shi Zhao, Tien-Fu Lu, Ben Koch, Alan Hurdsman, "3D stockpile modelling to improve the quality control in iron ore handling," Proceedings of the International Conference on Mining, Material and Metallurgical Engineering, Prague, Czech Republic, 11-12, Aug., 2014.
2. Shi Zhao, Tien-Fu Lu, Ben Koch, Alan Hurdsman, "Stockpile modelling using mobile laser scanner for quality grade control in stockpile management," 12th International

Conference on Control Automation Robotics & Vision (ICARCV), Guangzhou, China, 5-7 Dec., 2012.

3. Shi Zhao, Tien-Fu Lu, Ben Koch, Alan Hurdsman, "A simulation study of sensor data fusion using UKF for bucket wheel reclaimer localization," 2012 IEEE International Conference on Automation Science and Engineering (CASE 2012), Seoul, Korea (South), 20-24 Aug., 2012.
4. Tien-Fu Lu, Shi Zhao, Shihong Xu, Ben Koch, Alan Hurdsman, "A 3DOF system for 3 dimensional stockpile surface scanning using laser," 6th IEEE Conference on Industrial Electronics and Applications (ICIEA), Beijing, China, 21-23 June, 2011.

Poster

1. Shi Zhao, Tien-Fu Lu, Ben Koch, Alan Hurdsman, "3D real-time stockpile modelling and voxelization to estimate quality during blending operation, " 11th South Australian Exploration and Mining Conference (SAEMC), Adelaide, Australia, 5 Dec., 2014.

Abstract

Stockpile blending is widely accepted as an effective method to reduce the short-term quality variations and optimise the homogeneity of bulk materials, such as iron ore. Currently, both industry practice and academic research focus on planning, scheduling and optimisation algorithms to stack a stockpile that meets the predefined quality requirements. Namely, using 'selective stacking' algorithms to optimise the quality of a stockpile and improve the operational efficiency. However, it has been identified that stockpiled products are currently being reclaimed at approximately 50% of their potential engineering productive rates after applying such 'selective stacking' methods at most iron ore loading ports in Australia. There is an evident lack of solutions to this issue in the literature. This study focuses on stockpile modelling techniques to estimate the quality of a stockpile in both stacking and reclaiming operations for consistent and efficient product quality planning and control.

The main objective of this work is to build an up-to-date geometric model of a stockpile using laser scanning data and apply this model to quality calculations throughout the stacking and reclaiming operations. The significant elements of the proposed research are to: (1) upgrade a stockyard machine used to stack or reclaim the stockpile (i.e. a Bucket Wheel Reclaimer) into a mobile scanning device using Kalman filtering to measure the stockpile surface continuously; (2) build a 3D stockpile model from the measurement data in real time using polynomial and B-spline surface modelling techniques and use this model to calculate the quality of a stockpile with a great degree of accuracy when the quality composition is available; (3) associate the 3D model with the reclaiming machine model to achieve autonomous operation and predict the quality of the reclaimed material through voxelization techniques. In order to validate the developed techniques, several experimental tests were conducted using simulation and real scenarios. It was verified that the proposed 3D stockpile modelling algorithms are adequate to represent the real geometric shape with great accuracy. The percentage error in volume is better than 0.2%. Therefore, the combination of stock-

pile and BWR (Bucket Wheel Reclaimer) models enables the reclaiming to be conducted automatically.

To the best of author's knowledge, this is the first time that a stockpile is modelled automatically in real-time and the integration of the stockpile and BWR model generates a novel stockpile management model allows true reclaiming automation. Thus, the quality of material composition after every stacking/reclaiming operation is calculated from the geometric shape/volume, density and quality assay results.

Through accomplishing this project, the quality of a stockpile and its distribution inside the stockpile can be tracked continuously and the stacking/reclaiming trajectory of the machine can be controlled precisely. By making available such information, it is then possible to develop proactive stacking or reclaiming pattern strategies with more accurate product quality grade planning and control. Therefore, the workload of current selectively stacking and reactive reclaiming algorithms can be relieved, and the production rates can be improved with good output product quality control.

Table of contents

List of figures **xvii**

List of tables **xxi**

List of acronyms **xxiii**

1 Introduction **1**

1.1 Iron Ore Exportation 1

1.2 Mining Operation and Quality Control 2

1.3 Motivation 4

1.4 Objectives 6

1.5 Thesis Structure 7

2 Literature Review **9**

2.1 Stockpile Blending 9

2.2 Stockpile Modelling 13

2.2.1 Mathematical Model 13

2.2.2 Geometric Model 17

2.3 Machine Operation Control 19

2.4 Stockyard Management 21

2.5 Research Gap 22

2.5.1 Summary 23

2.5.2 Innovations 24

3 BWR Localization for Stockpile Scanning **25**

3.1 Mobile Laser Scanning 25

3.1.1 Kalman Filter 27

3.1.2 UKF 30
3.1.3 UKF Sensor Data Fusion for BWR Localization 32
3.2 Simulation Framework 37
3.2.1 Encoder Module 37
3.2.2 GPS Module 38
3.3 Simulation Results 39
3.4 Indoor Laser Scanning System 44
3.4.1 Mechanical and Electrical Aspects 44
3.4.2 Preliminary Experiment 46
3.5 Summary 51

4 Stockpile Modelling from Point Cloud Data 53
4.1 Problem Statement 53
4.2 Wireframe Modelling from Raw Scanning Data 54
4.3 Point Cloud Segmentation 58
4.4 Surface Modelling 60
4.4.1 Polynomial Approximation 60
4.4.2 B-Spline Interpretation 64
4.5 Experiments and Results 68
4.5.1 Data Preparation 68
4.5.2 Experiment Design 69
4.5.3 Blending Simulation 71
4.5.4 Modelling Result 73
4.6 Summary 97

5 Quality Estimation and BWR Automation 101
5.1 3D Stockpile Management Model 101
5.1.1 BWR Automation 102
5.1.2 Landing Point Estimation 104
5.1.3 Slewing Range Estimation and Model Updating 108
5.2 Quality Estimation in Blending 109
5.2.1 Grade Variability Modelling 110
5.2.2 Stockpile Voxelization for Quality Prediction 111
5.3 Experiment and Result 123
5.3.1 Cubic Stockpile Voxelization 123
5.3.2 Quality Volume Calculation in Cubic Model 125

5.3.3 Quality Predication from Cubic Voxel Models 127
5.3.4 Sickle-shape Stockpile Voxelization 131
5.4 Summary 136

6 Conclusion and Future Work 139
6.1 Conclusions 139
6.2 Future Work 141

References 143

Appendix A 3DOF Laser Scanning System 149

List of figures

Fig. 1.1 A normal iron ore exportation procedure 3
Fig. 1.2 A Stockpile with layers and a cutting geometry caused by a BWR . . . 4

Fig. 2.1 The ideal cross sections of stockpiles after stacking 10
Fig. 2.2 A rail mounted BWR operated at the Brockman 4 mine in the Pilbara region of Western Australia 11
Fig. 2.3 The ideal cross sections of stockpiles after stacking 12
Fig. 2.4 3D stockpile management model for quality control 24

Fig. 3.1 Upgrading a BWR into a mobile 3D laser scanner 28
Fig. 3.2 The KF algorithm for a linear dynamic system 30
Fig. 3.3 The UKF algorithm for a nonlinear dynamic system 33
Fig. 3.4 The structure of a typical Kalman filter for data fusion 33
Fig. 3.5 BWR coordination system and motion axes definition 34
Fig. 3.6 Data flow in the encoder module 37
Fig. 3.7 Data flow in the GPS module 39
Fig. 3.8 Simulated GPS and encoder data against the true trajectory in the first 200 s 41
Fig. 3.9 UKF localization results for the 1st dataset 42
Fig. 3.10 UKF localization results for the 6th dataset 43
Fig. 3.11 A 3D drawing of the indoor laser scanning system used for laboratory scale stockpile scanning 45
Fig. 3.12 Coordinator definition for stockpile modelling 46
Fig. 3.13 Experiment setup and dimension of the discharge chute 47
Fig. 3.14 1st layer of the cone stockpile 48
Fig. 3.15 2nd layer of the cone stockpile 49
Fig. 3.16 3rd layer of the cone stockpile 50

Fig. 3.17 Surface measured by the indoor 3DOF laser scanner 50

Fig. 4.1 The fitted Fourier curve of a single scan 56
Fig. 4.2 Locating the global minimum using optimized iteration searching . . . 58
Fig. 4.3 Point segmentation and boundary detection using image processing . . 59
Fig. 4.4 Point segmentation result 59
Fig. 4.5 Grid partitioning reduces the residuals and avoids Runge's phenomenon 62
Fig. 4.6 Over-fitting is detected automatically through the comparison of the surface normal vectors before and after modelling 63
Fig. 4.7 A (6^{th}, 1×1) B-spline surface model 67
Fig. 4.8 Stockpile modelling procedure from laser measurement data 67
Fig. 4.9 Experiment setup for the bench scaled stockpile in the laboratory . . . 70
Fig. 4.10 Variation in the layers of the stockpile during the experiment 73
Fig. 4.11 Systematic errors may occur at some positions when laser scans the aluminium prism 74
Fig. 4.12 Fit a single scan in the standard prism data using an 8^{th} order Fourier series 75
Fig. 4.13 The triangular prism modelled by the Fourier and the universal Fourier functions 75
Fig. 4.14 R-squared and residuals when fitting a single scan obtained at the stacking phase 77
Fig. 4.15 R-squared and residuals when fitting a single scan obtained at the reclaiming phase 77
Fig. 4.16 Large residuals always locate around sharp corners 78
Fig. 4.17 The laboratory scaled stockpile modelled by the Fourier and the universal Fourier functions 78
Fig. 4.18 Fitting a profile from the full scale stockpile using a 8^{th} Fourier series . 80
Fig. 4.19 Fitting a profile from the full scale, simulated stockpile using a 8^{th} Fourier series 80
Fig. 4.20 A zoomed view of the imperfect boundary detection results for the 4^{th} layer at the stacking phase 81
Fig. 4.21 Detecting boundary from the simulated stockpile data 82
Fig. 4.22 Laser measurement against the ideal prism surface. The point measurements are plotted in grey 83
Fig. 4.23 3^{rd} polynomial model of the triangular prism created from 8×8 patches 83
Fig. 4.24 Polynomial surface models obtained using the grid partitioning method 85

Fig. 4.25 Surface rending of the full scale stockpile 87
Fig. 4.26 A polynomial surface model of the 4^{th} layer from the full scale data . . 88
Fig. 4.27 A polynomial surface model of the 13^{th} layer from the full scale data. . 88
Fig. 4.28 The (7^{th}, 15×15) surface model of the ideal stockpile 91
Fig. 4.29 The (7^{th}, 15×15) surface model created for the noise measurement data 91
Fig. 4.30 A comparison of two same degree B-spline models from different wireframe model 92
Fig. 4.31 B-spline surfaces model of a partially reclaimed stockpile 93
Fig. 4.32 B-spline and polynomial model comparisons of the partially reclaimed stockpile after 15 cuts 95
Fig. 4.33 The B-spline surface model of the 15^{th} cut 98
Fig. 4.34 The B-spline surface model of the noise measurement data 98

Fig. 5.1 Ideal torus generated through superimposing the rotation motion of the BW and the slewing motion of the boom 103
Fig. 5.2 The maximum cutting depth (H) of the BW in regard to the bank surface 105
Fig. 5.3 Landing the bucket wheel on the stockpile 106
Fig. 5.4 Evaluating the landing point set using a stockpile management model . 107
Fig. 5.5 Updating the shape of the stockpile after the BW cut out the stockpile using the trajectory generated from the BWR kinematic model 110
Fig. 5.6 A quality distribution model of a one-layer stockpile 111
Fig. 5.7 A cubic voxel model created for the bench scale stockpile 114
Fig. 5.8 QVOs inside a voxel 115
Fig. 5.9 Table of the 2D region R used for automatic double integral calculation 116
Fig. 5.10 Identification of reclaimed voxel based on the trajectory of the bucket wheel 118
Fig. 5.11 Calculating the volume of a QVO object using the QMC method 120
Fig. 5.12 Partitioning a voxel into octants and linking them with the quality distribution model 122
Fig. 5.13 Quality calculation using the QMC method for the 2^{nd} cut 122
Fig. 5.14 A 40 *mm*-resolution voxel model superimposed onto the bench scale stockpile 124
Fig. 5.15 A 1 *m*-resolution voxel model superimposed onto the full scale stockpile 124
Fig. 5.16 Standard voxel models for quality calculation 126
Fig. 5.17 Material removed in the first cut 128

Fig. 5.18 Quantity of the material recovered in the 1st case 128
Fig. 5.19 Voxels recovered in each cut 129
Fig. 5.20 Quantity of the material recovered in the 2nd case 130
Fig. 5.21 Automatic landing and reclaiming simulation 132
Fig. 5.22 The volume of the 2nd cut calculated using QMC method 133
Fig. 5.23 Validate the potential landing point from the B-spline model 134
Fig. 5.24 Voxelization of the top bench based on the real cutting trajectory 134
Fig. 5.25 Stockpile after the reclaiming 135

Fig. A.1 Coordinator defined for kinematic analysis 150

List of tables

Table 3.1 Parameters of the BWR 39
Table 3.2 Noise characters used in the GPS module 41
Table 3.3 Average RMSE of the UKF estimation 44
Table 3.4 Cone shape stockpile stacked using quartz aggregate. 47

Table 4.1 Particles used to create stockpile layers 70
Table 4.2 Fitting accuracy versus computation time for a single scan 76
Table 4.3 Volume calculated from different wireframe models 79
Table 4.4 Ground detected from the boundary detection algorithm 81
Table 4.5 Polynomial surface modelling results 84
Table 4.6 Surface modelling accuracy versus calculation time when apply grid partitioning to the 15th reclaiming data 84
Table 4.7 Volume calculated from the surface model 86
Table 4.8 Surface modelling accuracy versus calculation time when apply grid partitioning to a full scale stockpile 89
Table 4.9 Volume of polynomial models of the full scale data 90
Table 4.10 B-spline surface modelling results 93
Table 4.11 The volume calculated from the B-spline surface model 94
Table 4.12 Surface modelling accuracy versus calculation time when apply grid partitioning to a full scale stockpile 96
Table 4.13 The volume of the full scale B-spline models 97

Table 5.1 Voxel modelling using different resolutions 124
Table 5.2 Volume calculation results for the standard prism 126
Table 5.3 Volume of each layer calculated from the cubic voxel model 126
Table 5.4 Quality data used in the simulation 127
Table 5.5 BWR Parameters used in case study 127

Table 5.6 Quality of reclaimed material for the 1st case using cubic voxels . . . 129
Table 5.7 Quality of reclaimed material and their percentages in the 2nd case using cubic voxels 130
Table 5.8 Quality of reclaimed material for the 1st case using sickle-shape voxels 133
Table 5.9 Quality of reclaimed material for the 2nd case 136

Table A.1 LMS200 scanning configurations 149
Table A.2 Link analysis of the 3DOF laser scanning system 151

List of acronyms

BW	Bucket Wheel
BWR	Bucket Wheel Reclaimer
CAD	Computer Aid Design
DCM	Direction Cosine Matrix
DGPS	Differential Global Positioning System
DOF	Degree of Freedom
ECEF	Earth Centred Earth Fixed
EKF	Extended Kalman Filter
FIFO	First in, First out
GA	Genetic Algorithm
GP	Goal Programming
GPS	Global Positioning System
GPU	Graphical Processing Unit
KF	Kalman Filter
LiDAR	Light Detection and Ranging

LRF	Laser Range Finder
LTP	Local Tangent Plane
MSE	Mean Squared Error
NED	North East Down
PF	Particle Filter
QMC	Quasi-Monte Carlo
QVO	Quality Volume Object
RMSE	Root Mean Square Errors
SSE	Sum of the Squared Error
UKF	Unscented Kalman Filter
UT	Unscented Transformation
UWB	Ultra-wide Band
VRR	Variance Reduction Ratios

Chapter 1

Introduction

The problems and aspects of iron ore production, transportation and blending operations, which involve engineering and economic applications, often evoke immense interest from researchers. This chapter firstly provides an introduction to this study and then explains the motivation for pursuing the research work. The research objectives and the scope of the study are followed. Finally, the structure of this thesis is presented.

1.1 Iron Ore Exportation

Australia is one of the major iron ore producers in the world and iron ore mining is a primary industry and contributor to the Australian economy. According to the statistical data, 554,288 kilotons of iron ore and concentrate were produced from 2012 to 2013 and 527,109 kilotons, equalling 95.1% of the total production, were exported overseas [1]. Nearly all the ore sold in the market is fed into blast furnaces for steel making. Traditionally, iron ore was sold at prices that were set in advance in long-term contracts between the suppliers and buyers (steel makers). Also, customers took the responsibility for shipping the ore after the purchase. However, the exporting business has changed in nature since the demand greatly outpaced the supply, especially driven by the rapid booming of the steel market in China from 2009. Although China's consumption of iron ore slumped since 2014, most steel makers in China still use spot prices at the point of purchase and they also want suppliers to deliver ore to their mills directly.

A finely tuned blast furnace is inflexible in terms of changes in grades. Iron ore fed into the furnace must be prepared within a very tight burden specification that contains not only the iron content but also any major contaminants, such as silica, phosphorus and alumina. Therefore, the grade consistency is a main quality criterion in price and quantity negotiations, and is closely monitored by customers on a short-term basis (i.e. the ship-by-ship variability). However, because the mineral composition of raw iron ore varies even when the ore is mined from the same source and there exist strong cross-correlations across minerals in the ore body, great efforts are needed to plan the mine production so as to deliver a steady stream of product that is close to the target grade.

1.2 Mining Operation and Quality Control

The iron ore production encompasses a broad spectrum of activities. Generally, it can be divided into four major operations: finding, mining, processing and delivering [2]. Before operating a mine, the tonnage and distribution of ore are explored through a range of geological, geophysical and metallurgical techniques. Such information will assist the suppliers to create a lifetime production plan. This lifetime plan is then separated into yearly, monthly and even daily plans to achieve the pre-determined target tonnage and grade requirements. These subsidiary plans indicate the specific areas, which have similar geology, to be mined each time, in a particular sequence. Furthermore, all the plans are updated continuously in light of changing knowledge about the ore deposit and operating requirements.

Holes are drilled in an appropriate pattern and filled with an explosive to fulfil the requirements of the daily production plan. The blasting breaks the material into an appropriate size for the digging process. Samples are taken after the blasting to provide a more accurate estimation of the ore grade than the one obtained from previous exploratory operations. Ore extracted from the mine is transported to the processing plant via haul trucks. At the plant, the ore is crushed into small size particles and separated into the lump (with an approximate particle size between 7 *mm* ~ 25 *mm*) and fines products (with an approximate particle size less than 7 *mm*). In some cases, a gravity separation system may also be involved to extract top quality iron ore pellets (haematite) from the fines product [3]. Because the grades between the lump and fines products are always different, they are stacked separately.

In accordance with exporting requirements, train loading is scheduled and the stockpiled iron ore is recovered, then transported to the port. At the port, offloaded iron ore can be mixed with other high- or low-grade raw material to adjust the averaged quality. Tertiary or quaternary crushing may also be applied when needed. Again, processed ore is stacked into stockpiles accordingly. Sold iron ore are then recovered and transported by ship to customers. Occasionally, instead of having two storage facilities, mined iron ore is loaded directly onto trains and transported to the port. At the port, iron ore is processed and stacked into stockpiles. A simplified transportation arrangement after the ore is blasted, demonstrating the flow of the ore, is shown in Fig. 1.1.

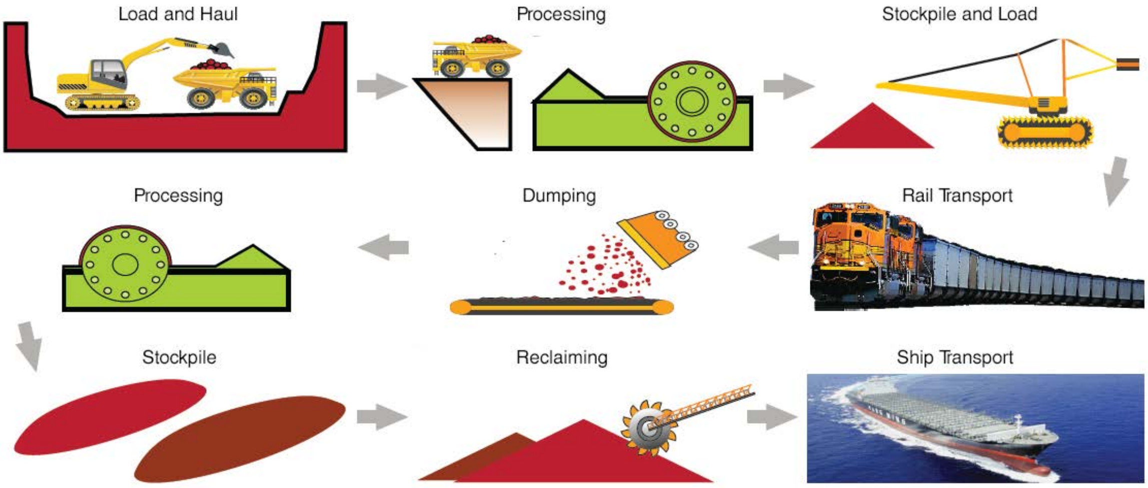

Fig. 1.1 A normal iron ore exportation procedure.

Finding, mining, processing and delivering operations construct a multi-level supply chain to maintain the quality of the delivered product within acceptable tolerances of the target grade. In most cases, other than the previously mentioned mine planning, ore processing, rail scheduling, stockpile blending is also conducted in the supply chain to adjust the quality. A stockpile is the simplest storage form for bulk material and it exists between delivery and reception to provide sufficient reserves for continuous operations, i.e. to serve as a buffer for iron ore shipments at exporting ports. Additionally, stockpiles are always built at the processing plants to blend ore with different grades (potentially from multiple pits) in order to meet the predefined target grade.

Blending is generally achieved through stacking iron ore into different geometric shapes layer-by-layer and reclaiming the stockpiles slice-by-slice. Therefore, stacking and reclaiming are collectively named blending throughout this thesis. For instance, a chevron stockpile, which is one of the most common stacking methods in iron ore exporting, is formed by moving the stacker forwards and backwards over the predefined length at an almost constant speed. The boom lifts a little at each end. Ideally, materials poured from the end of the boom form a thin layer with a triangular cross-section. Layers are stacked on top of each other after the zigzag motion is completed (see Fig. 1.2 a). When the stockpile is recovered using a Bucket Wheel Reclaimer (BWR), which has a rotating wheel with buckets mounted at the tip of the boom, the horizontal motion of the BWR and the circular motion of the bucket wheel result in a sickle-shaped cutting geometry (see Fig. 1.2 b). Materials in different layers are almost simultaneously scooped up by buckets and mixed inside the wheel. As a result, the variation in the quality of the recovered material is reduced.

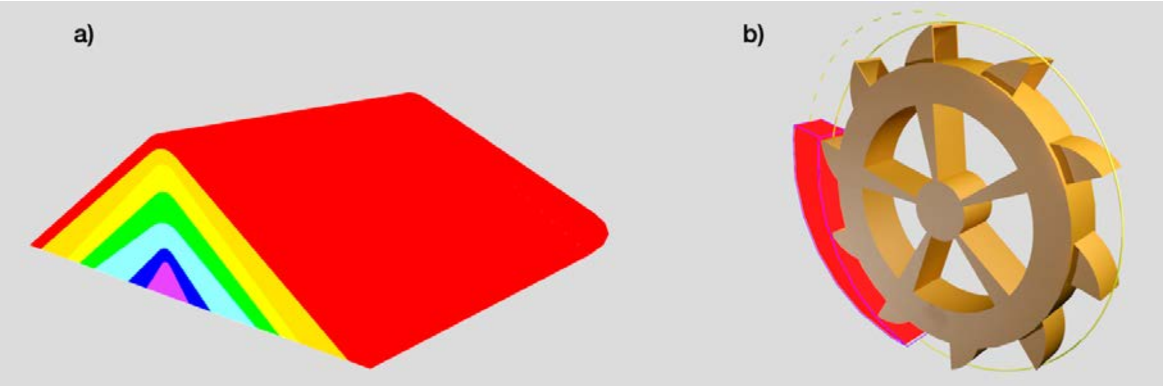

Fig. 1.2 A Stockpile with layers and a cutting geometry caused by a BWR. a) The ideal cross-section of a chevron stockpile. Layers with different quality grades are represented by different colours. b) The bucket wheel and a sickle-shaped cut.

1.3 Motivation

Blending aims to distribute ore selectively so as to improve the homogeneity of that specific stockpile. Obviously, the chemical properties inside each layer, the geometric shape of each layer, the number of layers and the cutting geometry of the reclaimer will determine the final blending results. However, the mineral composition of the ore may be not known with the highest degree of accuracy before blending due to the limitations of current sampling and analysis techniques. For instance, the chemical composition cannot be accurately analysed until the sampled iron ore is crushed. Therefore, there is always a delay of several hours before obtaining the most accurate analytical results. Frequently, to save storage space and maximize the production rate, stockpiles have to be built using prior quality data. Such prior data can be inaccurate and inappropriate because they are obtained before the iron ore is processed. Thus, stacking may be unable to smooth out the quality fluctuations of the stockpile. For instance, when the train delivery of iron ore is crushed and screened into the lump and fines products, the separation will cause systematic differences in the chemical compositions of the two products. Both pieces of quality information are needed to direct these two products to specific stockpiles. Conversely, there is only one set of data that is obtained before crushing and screening. The use of such inappropriate quality data may cause the optimization algorithm to fail and the quality of a stockpile not to be known exactly after stacking.

It is not surprised that the performance of a blending plant is poorer than expectations. On-site investigations indicate that stockpiled products are currently being reclaimed at only approximately 50% of their potential engineering productive rates [4]. There exist many sources of disruption and irregularity in the blending process, key issues being that the quality of a stockpile cannot be controlled accurately at the stacking phase; the quality of reclaimed material cannot be predicted before reclaiming and the reclaimer is operated semi-automatically. Thus, the first cut into a stockpile has to be decided and activated manually, mainly based upon driver's experiences. To adjust the quality of recovered material regarding the end objective, the reclaiming has to be suspended frequently whilst waiting for the quality information. If any changes in quality are needed, the reclaimer has to move to another position to recover different grade material. Again, the decision is made through the imperfect quality information of the stockpile. Meanwhile, because the cut is conducted by human operators, it inevitably introduces more uncertainties into quality adjustments.

There is a real need to enhance blending efficiency with a capability to predict and control the quality grade of stockpiled products, thereby increasing the productivity and export potential, and reducing costs. The current research focus is to build a stockpile that satisfies a particular target grade through scheduling the stacking sequence using optimisation theory. Generally, a stockpile is modelled by an objective function with a set of constraints in such mathematical optimisation approaches. On the contrary, this research intends to create a new 3D stockpile management model featured with highly accurate 3D volumetric stockpile models from real-time measurement data, precise quality data from chemical analysis and machine operation models. Such a novel management model can be used not only for highly accurate quality grade prediction and control but also assist in the decision-making process to achieve stacking/reclaiming strategies pro-actively and with much higher efficiency than current selective stacking approaches.

1.4 Objectives

Achieving customer acceptable quality specifications has been the main focus for both academic research and industry practice. Although various approaches have been reported for this purpose, none of them has associated the stockpiling modelling and machine operations together to form such an innovative and comprehensive system as is proposed in this project. There is a definite lack of 3D real-time stockpile models for more efficient and effective blending algorithms with consistent product quality grade planning and control capability. Therefore, the general aim of this research is to develop a 3D stockpile management model to deliver the relatively consistent grade of bulk solids required by customers in a highly efficient and low cost manner. More specific objectives for this study are as follow:

1. To map the stockpile in real time using laser scanner
   Contemporary measurement data is essential for stockpile modelling purposes. This project aims to upgrade a stacking/reclaiming machine to a mobile laser scanner to measure the stockpile profiles while it is being stacked/reclaimed. Through capturing the dynamic profile data of the stockpile, the geometric shapes of a stockpile can be profiled in detail. Meanwhile, to map the stockpile, the mobile laser scanner needs to be localised. An Unscented Kalman Filter will be applied to obtain accurate positional estimations from a GPS receiver and encoders.

2. To build accurate 3D mathematical models using measurement data
   Continuously updating the geometric shapes of a stockpile will result in a huge amount of 3D data points. It is expected to identify stockpile regions from point cloud data automatically and handle them mathematically. The modelling error in volume is expected to be less than 0.5%. Thus, these models can be visualized and utilized easily, not only for quality control, but also for other relative applications, such as collision detection. Besides, data to be stored will be much less. Two different mathematical models are presented in the thesis for this purpose.

3. To enable automatic blending using 3D stockpile models
   Most reclaimers currently operated in the stockyard are semi-automatically controlled. Stockpile models and BWR operations are not tightly coupled with each other. This study aims to couple them together to achieve automatic blending which is able to convert the ‘selective stacking’ mode into a ‘proactive stacking/reclaiming’ mode. Thus, detailed knowledge of a stockpile can be updated and learned through controlling

the trajectory of the stacking/reclaiming machine. Meanwhile, the trajectory of the BWR can be predicted and planned using dynamic stockpile models which will enable fully automatic control of the BWR. A 3D stockpile management model that links a stockpile and a BWR will thus be studied.

4. To estimate the quality in blending using voxels
   Both stacking and reclaiming operations can be considered as discrete operations because the geometric shape of a stockpile changes step by step. Additionally, the quality of the discharged material from the conveyor belt during stacking is not uniform. Therefore, a better way to estimate the quality of a stockpile or recovered material is to use the discrete voxel space. Two different voxel models and quality calculation procedures are investigated and detailed in the thesis.

1.5 Thesis Structure

Chapter 2 provides literature review and motivation for this thesis. Through reviewing stockpile modelling algorithms, paying special attention to applications in blending optimisation and automatic algorithms employed in BWR automation, the need to build a novel 3D stockpile management model is exemplified.

Chapter 3 details the development of a mobile laser scanning device and experimental facilities built in a laboratory environment to scan a scaled-down chevron stockpile. An Unscented Kalman filter (UKF) based sensor data fusion algorithm is proposed to improve the positioning accuracy of the end-effector (the bucket wheel) of a BWR. A simulation study is presented to demonstrate the localization results. An indoor experimental environment for modelling data collection is also detailed in this chapter.

Chapter 4 addresses the stockpile modelling. Whilst a variety of approaches are available for surface reconstruction from point cloud data, this study focuses on the building of mathematical models in real time without human supervision. These models are proven to be generated automatically almost in real time using a variety of point data.

Chapter 5 investigates the 3D stockpile management model. The stockpile models proposed in Chapter 4 are used to solve BWR automation problem. The joint angles of BWR and slewing range of the boom are calculated from the 3D stockpile. This will provide a true automation in quality control. Stockpiles are therefore voxelized into two formats for quality estimations. The advantages of these voxelization methods are discussed and the quality of reclaimed material is calculated accordingly.

Chapter 6 presents conclusions and points out the contributions. Additionally, it outlines directions for future research which may further benefit the industry.

Chapter 2

Literature Review

The nature and quality of a stockpile plays a key role in bulk material handling. Stockpiles are where bulk materials are buffered and quality adjustments are normally performed. This chapter provides a review of the work in the field relevant to stockpile management. The review focuses on blending optimisation and quality estimation for a stockpile. Then it extends to a broad spectrum of relative techniques in bulk material handling, such as machine automation and stockyard management. The literature reviewed in this chapter helps to identify the need to build a 3D stockpile model for stockyard management and the importance of applying this model in quality estimation for blending control.

2.1 Stockpile Blending

Bulk materials, such as iron ore, limestone and coal, are never consistent in terms of quality, even they are mined from the same source. Such raw materials, with different chemical compositions, need to be blended into one in order to meet the required specification before further use. Stockpile blending is one of the few techniques available that converts heterogeneous raw materials into a relatively stable homogeneous product. It is considered to be indispensable in bulk material delivery and preparation. In industry practice, the sequence of operations in building a stockpile is described by two terms: blending and grade targeting. Blending refers to mechanical operations, including stacking and reclaiming. Grade targeting refers to the decisions that have been made prior to commanding the machine operations [5]. For example, to direct ore to a specific stockpile so as to improve the homogeneity of quality of that stockpile or to recover material from multiple stockpiles during the ship loading operations, in order to meet the required quality and quantity combinations. Essentially, stockpile blending aims to meet the predefined target grade and reduce the variations in quality of any given stockpile.

Stacking is the beginning of a blending process. Currently, in the mining industry, stockpiles are normally created in a longitudinal direction and stacked layer by layer through automatic control of the trajectory of a stacking machine. Besides the most popular chevron method used in the majority of the iron ore exporting facilities in Australia, other methods include cone-shell, strata and windrow stacking [6]. Each method has its unique stacking trajectory that creates a certain pattern in the cross-section of a stockpile (see Fig. 2.1). It should not be too hard to deduce the moving path of the stacker from the cross section of a stockpile. For example, a chevron stockpile is created through driving a stacker slowly at an almost constant speed from one end of the stockyard to the other. Ideally, poured material has an inverted V-shaped pattern over the entire length of the stockpile. Before turning the stacker back at each end, the boom lifts a little to create a space for adding a new layer onto the pile.

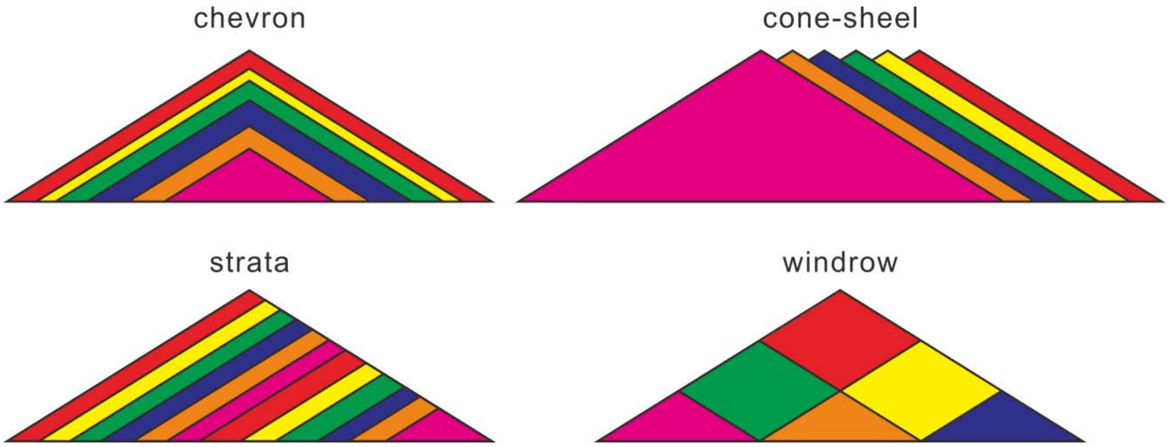

Fig. 2.1 The ideal cross sections of stockpiles after stacking.

Reclaiming allows material to be mixed to improve the homogeneity in quality. In iron ore handling, a boom-type reclaimer with a bucket wheel, which has the combined features of a stacker and a reclaimer, is commonly used (see Fig. 2.2). Its boom slews across the body of a pile and the buckets on the rotating wheel scoop materials from the pile simultaneously. Hence, recovered materials from different layers are mixed inside the wheel.

General reclaiming methods include long travel, bench (terrace) and pilgrim step reclaiming. A chevron stockpile is normally reclaimed by the bench (terrace) or pilgrim step reclaiming.

Fig. 2.2 A rail mounted BWR operated at the Brockman 4 mine in the Pilbara region of Western Australia. Image source: Wikipedia, under GNU Free Documentation Licence.

In bench reclaiming, the lateral motion of the boom is performed perpendicularly to the stacking direction. The slewing speed of the boom is controlled to achieve a constant conveying output. The slewing movement of the boom and the circular movement of the bucket wheel result in a sickle-shaped cut. After the bucket wheel cuts through the pile, the slewing motion stops and the machine advances along the stacking direction. Then the boom is reversed back from its stopped position to make a new cut. In most cases, the swing motion mechanism repeats until the material above the specified height of the stockpile is totally recovered. As a result, such operations cause a flat bench on the stockpile. The bucket wheel is lowered to another height to create another bench.

Pilgrim step reclaiming is, in principle, built upon bench reclaiming. However, only a limited number of cuts are conducted at each bench height [7]. It starts from the topmost bench with an even number of cuts. After that, the reclaimer travels back and lowers the bucket wheel to resume a sequence of new cuts. When bucket wheel is down to the lowest bench and pre-set the cuts are completed, the reclaimer will travel to the first tranche of the stockpile and use the same method of reclaim. Since a single sickle-shaped cut obtained from bench or pilgrim step reclaiming contains materials of different grades (from different layers) and these materials are mixed inside the rotating bucket wheel, reclaiming will improve the homogeneity of a stockpile.

According to the blending operations, the quality of a stockpile is tightly connected with its geometric shape. More specifically, it is determined by the geometric shapes of its layers because the material quality of each layer is different. The reasoning behind is that the quality of a single element from the chemical analysis is represented as a weight percentage of the whole composition and the density of the ore can be considered as a constant after crushing and screening. In this thesis, a stockpile is considered to have four phases across its life cycle, as shown in Fig. 2.3. These phases are stacking, awaiting reclaiming, reclaiming and awaiting stacking. At the stacking and reclaiming phases, the geometric shapes of a stockpile change continuously with the machine movement. Therefore, to calculate the quality of a cut or a stockpile accurately, it is necessary to record such changes faithfully. While a stockpile is at awaiting reclaiming or awaiting stacking phase, it is the best opportunity to integrate the recorded geometric information with the chemical analysis results to estimate the quality of a stockpile. Obviously, the estimation results will guide operations conducted at stacking or reclaiming phase. Thus, the quality management can be controlled effectively and efficiently.

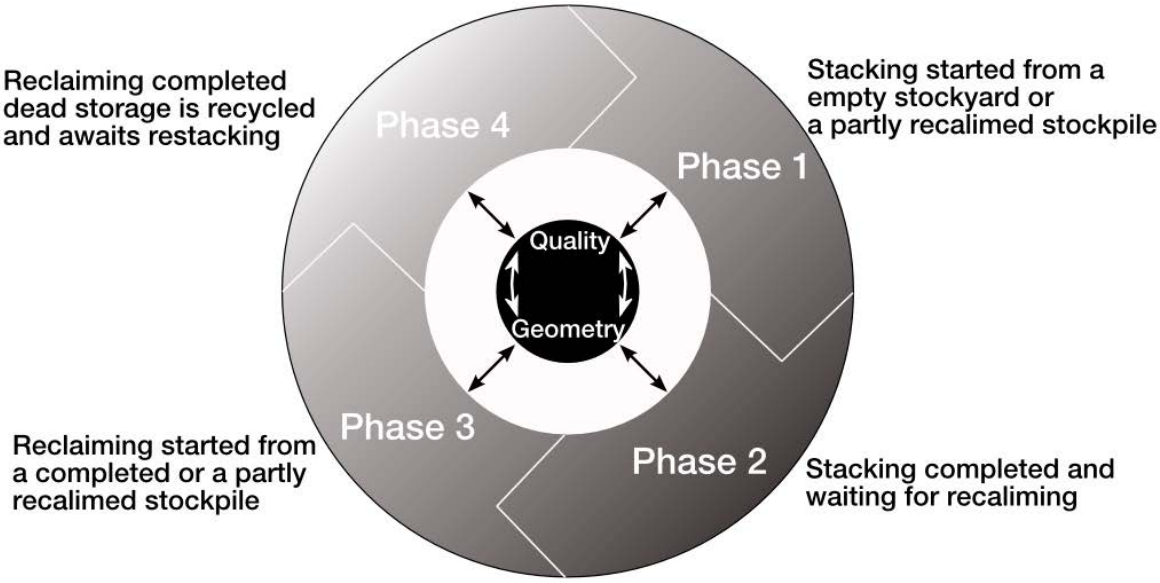

Fig. 2.3 The ideal cross sections of stockpiles after stacking.

Grade targeting is essential in blending because it is how quality control takes place. To meet the quality specification required by a client, material stacked onto the stockpile or recovered from the stockpile needs to be carefully arranged in appropriate proportions. At the stacking phase, decisions are made based on the knowledge of the quality of the current materials and the ore already in the stockpiles. It aims to assign the current materials selectively onto a specific stockpile without causing significant changes in the grade of that stockpile. In turn, mine production scheduling and train sequencing are also involved as control factors for such selective stacking operations. At the reclaiming phase, grade targeting is achieved through moving BWRs in the stockyard to reclaim different materials. Again, decisions are made based on the knowledge of the stockpiles and required product quality. Approaches used to optimise the blending and assist the decision making in grade targeting are reviewed in the next section.

2.2 Stockpile Modelling

Obtaining the best results from minimum blending is vital because blending raises operating costs and lowers system efficiency. Therefore, stockpile models have been developed to analyse blending activities and guide grade targeting operations. Generally, two types of modelling approaches have been introduced for blending optimisations and quality estimations. The first one treats the quality of iron ore as a function and uses mathematical equations to describe a stockpile. The second one extracts geometric features and builds a volumetric model of a real stockpile.

2.2.1 Mathematical Model

A statistical approach was first suggested by Gerstel to estimate the quality after blending in 1977 [8]. In his bed blending theory, the material flow into and out of a stockpile was named input and output flow, consecutively. These material flows were considered as discrete signals for the estimations of the quality variations. Several assumptions were made to describe the characteristics of such signals, including the average, standard deviation, the variance and the covariance. An exponential function was used to approximate the covariance function, to estimate the standard deviation of the signal. Gerstal defined a factor called blending efficiency, which was the quotient of the standard deviations of the input and output signals, and suggested that it is inherently connected with the number of layers in a stockpile. Furthermore, he pointed out that stockpiles can be used to control the long-term fluctuations in bulk material handling.

Soon after, Gy presented a new variographic theory for bed blending, to suppress the continuous input variations for a steady output quality grade [9]. He claimed that Gerstel wrongly assumed that the standard deviations of the input and output signals are uncorrelated with each other. However, some assumptions in both blending theories do not hold true in real operations, such as that all cross-sections of a stockpile are identical, all layers have the same uniform thickness and that materials in each layer are uniformly distributed along the pile length. Additionally, both authors suggested that stockpile blending was only effective for adjusting long-term variations, not for short-term ones. However, with the further understanding and developments in mathematical optimisation and scheduling since this date, their proposals have been superseded.

In 1996, Everett presented a simulation model to schedule iron ore handling procedures and improve performance in quality control. He introduced a stress vector to describe the deviations of four quality elements (iron, silica, alumina and calcium oxide) in iron ore [10]. The quality of the arrived iron ore is evaluated by its stress vector and aggregation of the stress vectors will finally result in a stockpile being in ‘pain’. Accordingly, the best strategy is to minimize the increment in the stress vector of a stockpile when it is stacked. In the meantime, he also applied this stress vector approach to ship loading operations. Through selecting the optimum mix from multiple stockpiles in a stockyard, the ship-to-ship variability in quality is also minimized. Simulation results indicated that this approach had cumulative effects in reducing the short-term variations in iron ore handling.

Building on the previous research, Everett further explored the stress vector approach in iron ore production scheduling. He created a diagram that contains four stages to describe the production sequence from a mining site to a ship, schematically [11]. He suggests that opportunities to adjust the quality of the final products exist throughout these stages: for example, to select specific mine blocks at multiple mining sites, or to schedule train sequences to transport ore from source mines to the port. Again, the key selection criterion at each stage is the quality composition, which is reflected as a stress vector. Through scheduling individual operations at each stage, the stockpiles built at the port will have a uniform composition in accordance with the predefined specifications for shipping. Additionally, a recent paper, published by Everett in 2010, reported a simulation model designed for short-term grade control during ore handling [12]. It simulated real day-to-day operations of an iron ore mining company in Western Australia. Optimizing decisions in the process are made by human operators, based on the optimisation results deduced by the stress vector algorithm. Everett's research proves that stockpiles can be used to adjust the short-term grade constancy, which is believed to be a great contribution to stockpile blending.

Kumral designed a stockpile model to minimize the grade variations in stockpile output in 2006 [13]. He called the blending efficiency, which is defined by Gerstel [8], VRR (Variance Reduction Ratios) and used it to evaluate the homogenization effect of a stockpile. To obtain a sufficient number of VRRs, a stockpile is partitioned into a number of discrete blocks. The VRR of each block is predicted through multiple regression modelling. A genetic algorithm (GA) is employed to determine optimal stockpile parameters, including the stockpile length, the number of layers and the speed of a stacker. These parameters are given in terms of the number of blocks that minimize the VRR. Two case studies were presented to validate his optimisation algorithm. According to the simulation results, he suggested that windrow stacking would result in a much greater variance reduction effect than chevron stacking does. However, such a conclusion has been challenged by Robinson at the end of Kumral's paper [14].

Wharton described three case studies in blending optimisation using linear programming techniques provided by the Whittle Strategic Mine Planning package [15]. Extractive blending is defined as a process that uses blending to meet quality constraints prior to future processes. Materials are taken from different stockpiles and are represented by tonnage and grade, which forms the basis for the linear programming problem. Constraints for the linear programming optimisation are: the product limits, the minimum or maximum element grade limits and the stockpile quantity limits. All case studies are based on practical stations on existing mine sites and each case study has a specific aim: to improve the throughputs, reduce costs and increase recoveries. The results demonstrate that extractive blending based on linear programming techniques can improve the quality of the input material.

Lyu et al. incorporated a goal programming (GP) model to a coal blending management system. The model assists the manager to determine the appropriate quantities of coal recovered from different stockpiles to meet the environmental and boiler performance requirements. In this paper, the quality of stockpiles and the quality requirements for boilers are assumed to be known in advance. The optimisation aims to blend materials recovered from different stockpiles to minimize the deviation requirements of coal with a view to maintaining uniform usage of stockpiles for all boilers [16]. They introduced a number of real operation constraints into the GP model and solved it using a mathematical programming software package called ‘LINDO’, which is available on the commercial market. Lyu et al. believe that their model is also applicable to assist with the coal distribution system, namely, to assist in the decision-making process in stacking operations.

Mathematical models have demonstrated their capability to improve the homogeneity of a stockpile through selective blending operations. A stockpile is considered as an abstract concept and is described through one or more objective functions in these modelling approaches. With operational constraints, the objective function(s) is/are then solved using mathematical optimisation algorithms. However, they are still insufficient for realistic problems because quality data in current mathematical models are assumed to be available with the highest degree of accuracy before stacking, despite current limitations in sampling and chemical analysis techniques.

As pointed out by Everett, the quality composition of the ore cannot be accurately assayed until it is crushed [17]. A complete element analysis needs two to three hours. In turn, there is always a delay of several hours in obtaining the grade information of the ore. Conversely, to save storage space and enhance the effective time management of the machinery, materials have to be stacked right after the iron ore is processed (i.e. after crushing and screening, or after gravity separation). Consequently, the quality information used in these selective stacking approaches is normally imperfect or insufficient because they are obtained before such processing. For example, crushing and screening will yield lump and fines products and the grades of these two products are different. However, there is only one type of quality data before the iron ore is crushed. Thus, the use of such imperfect or insufficient quality data may wrongly estimate the quality of a stockpile and cause optimisation algorithms to fail. If a stockyard receives materials from different sites, such estimations are liable to be biased since there exist large differences in ore grades. Furthermore, since mathematical models cannot represent the real geometric shape of the stockpile, no correction can be made to improve the accuracy of the estimation even after the chemical analysis results are acquired. Another problem inherent in these mathematical models is that they require a very tight operational coupling between mining, delivering, sampling and blending operations. A minor perturbation may disrupt the entire optimisation process and lower operational efficiency.

Of course, mathematical models are designed for assisting decision-making but not for machine automation. In these models, stockpiles are abstract concepts and represented in tabular or pictorial formats with quality data attached to them. Consequently, these models are not able to guide the machine operations because the geometric parameters of actual stockpiles are not known. A stockpile is believed to have an almost uniform quality in each grade after stacking. Namely, the stockpile meets a certain quality specification. Thus, machines can simply reclaim that stockpile until the required quantity (mass) is reached. However, real reclaiming operations are much complex than such assumptions allow, as inaccurate quality data are used at the stacking phases. Quality control is also needed during reclaiming phases and so detailed operational procedures will be discussed in the ‘machine operation control’ (Section 2.3) of this thesis.

2.2.2 Geometric Model

Geometric models intend to represent real stockpiles using geometric shapes and they are normally created in order to calculate the quality of a stockpile. Robinson and Ross introduced three differential equations to approximate a semi-infinite chevron stockpile (with one end open) and solved these differential equations using a numerical approach [18]. To simplify the question, the repose angle of the stockpile was assumed to be of 45°. Thus, a multilayer stockpile can be modelled through changing the parameters of three equations. The quality of a stockpile portion is determined by the volume of each layer inside that portion and the grade of that layer. This modelling approach introduces a novel idea for stockpile quality calculation. However, the geometric model is based on the theoretical shape of a stockpile. No real measurement data are involved in the modelling. To accommodate this model to a real stockpile with an arbitrary repose angle, they advised a change in the density of the material. For example, if the repose angle of a stockpile is 35° and the density of the material is 2000 kg/m3, the modified density would be $2000\tan(35)$ kg/m3 according to their suggestions. Clearly the adjustments are notional, designed for theoretical models rather than actual models.

Pavloudakis and Agioutantis ignored the two conical ends of a chevron stockpile and assumed it has perfect isosceles triangular cross-sections along its stacking (longitudinal) direction [19]. Thus, a chevron stockpile is modelled as a triangular prism. To calculate the quality after stacking, the stockpile model was partitioned into a group of sub-prisms evenly along its longitudinal axis, a process which is called the ‘method of section’ in this paper. Every sub-prism or section is considered as a quality unit in the blending operations. Therefore, the quality of a pile is a combination of the grades of all the sections. The quality grades of these sections are simulated from the daily average properties plus normally distributed noise. Also, they introduced the ‘method of bench’ through dividing a stockpile along its vertical axis to estimate the quality of recovered material at the reclaiming phase. The name, bench, comes from the bench reclaiming method because it results in a bench after materials above a certain elevation are recovered by a BWR. They also suggested the most economical way to accomplish a stockpile was to use three bench levels. The quality of the reclaimed material was also estimated through combining the method of section and the method of bench for comparison purposes. They also concluded that the increase in the number of layers improved the blending efficiency and such an improvement is more obvious in windrow stockpiles with the bench reclaiming method. Additionally, Lu and Myo described an algorithm to optimise the BWR reclaiming trajectory to meet the target grade required by customers [20]. In their paper, a stockpile was also modelled as an isosceles triangular prism. However, such triangular prism models are far from a good representation of a real stockpile. Specifically, the two conical ends of a stockpile cannot be adequately described by a triangular prism.

In the commercial context, QMASTOR [21] and Indurad [22] choose laser or radar to perceive the stockpile and thereby to model stockpiles. 3D models were used to predict the quality grade of the stockpile and avoid collisions between stockpiles and BWRs. Also, a 3D stockpile model was developed and was stored with information for each cubic meter in regard to quantity and quality [23]. Even though no published paper that describes these systems can be found, it is evident from their websites, images, videos and contact emails that these systems are either highly customized, which means they are not mobile and thus be configured according to site specifications, or they are working off-line without the ability to update information in real time.

An advantage of volumetric models, when they are compared with the mathematical models, is that the quality of the stockpile can be calculated in more accurate manner when the quality assay results are available. It is easy to draw such a conclusion because the chemical composition is presented as a percentage of the weight and the density of the material can be considered as a constant after crushing and screening. However, current geometric modelling approaches are not able to record the real shape of a stockpile or update this shape continuously. Conversely, as discussed in the ‘stockpile blending’ section, a stockpile has four phases and these phases switch from one to another in blending operations frequently. Such switch between phases results in significant changes in geometric shapes and also changes the quality of the stockpile. For precise calculations, a geometric model is required to represent not only the external shape but also the internal shapes (layers) of a stockpile faithfully and update these shapes immediately after the blending operations. Without such ability, the quality of the stockpile is difficult to estimate over time, using current geometric models.

Again, geometric models are not tightly associated with machine automation. In the literature, a number of authors considered the machine's operating mechanism and used such operational procedures in their quality calculation. Stockpile models were partitioned into a sequence of sections by orthogonal planes that lie parallel to the horizontal and vertical axis of the stockpile. The chemical grades in these sections were calculated separately because each section was considered to be recovered as an entity during reclaiming. However, these simple shapes (triangular or trapezoidal prisms) are not good approximations of a real cut created by a BWR. Furthermore, current geometric models are not associated with machine operations. Consequently, BWRs are still operated manually or semi-automatically in stockyards.

2.3 Machine Operation Control

Full automation characterizes the latest developments in nearly all industrial fields, as it does in bulk material handling. Bucket Wheel Reclaimers (BWRs) which can be used for both stacking and reclaiming are one of the most popular choices for iron ore exporting. These machines are versatile in size and style for different applications. Since the 1980s, BWRs have been adapted to automatic operations. In the case of a stacker, the machine was able to follow a predetermined travel program to build chevron, cone-shell, strata and windrow piles [24]. In terms of these reclaimers, semi-automatic operations have been achieved using a positional sequence control system, which contains contactless control circuits and digital position measurement sensors [25]. Currently, most BWRs operated in Australia are supplied with encoders to measure the travelling distance, slewing and luffing angles. The position of the bucket wheel (BW) in 3D space can be calculated directly from encoder measurements. Also, measurement data are delivered to the feedback control programs to control the motion of the BWR. However, the operation is not fully automatic. The first cut into a stockpile has to be activated by human operators because it is not possible to predict whether there will be collisions between the wheel and the stockpile body under such control logic. Only after the first cut, can the BWR follow a specific reclaiming pattern to recover materials from a stockpile.

When a stockpile is recovered using the bench reclaiming method, an operator selects a landing point on the stockpile's surface manually and approaches the BW to that point with great care. When the contact between the BW and the stockpile surface is about to occur, the operator activates the circular motion of the buckets to make sure the buckets can pick up materials from the stockpile simultaneously with the landing. Normally, the rest of the operations are controlled automatically until the height of the BW is changed. The slewing range is determined by the feedback from the loading sensor. The lateral motion begins to stop until a lack of resistance is detected from the sensor. After a single cut, the BWR is advanced with a fixed cutting depth (i.e. 0.9×bucket width) to perform a new cut. The BW is lowered to start a new reclaim when all materials at that terrace are recovered. Again, the operator needs to choose the right landing point for the new reclaim. When other reclaiming methods are used, the moving trajectory of the BWR may be different but the operating procedures are similar to the bench reclaiming method.

Research in the field of BWR automation is very limited in the literature. To land the BW onto the stockpile automatically, Choi et al. extracted 2D contour map from 3D laser scanning data and used inverse kinematic equations to calculate the joint angle of the BWR from the contour map [26, 27]. The points along the contour lines were evaluated over the slewing trajectory of the BW. The validated landing points will not cause collision between the wheel body and the 2D contour map. Such idea was adopted by Lee et al. in 2006. They built a contour map from scanning data to optimize the trajectory of a BWR in terms of the safety, energy consumption and transfer time [28]. Obviously, these 2D stockpile models are not focused in blending optimisation and the quality of a stockpile cannot be calculated from 2D contour maps. Additionally, the boom and BW are assumed to be on the same slewing plane in these papers. Thus, the 3D collision detection problem is simplified as a 2D case. Conversely, in practice, to reduce the cutting resistance, the BW is tilted at a small angle. Therefore, such 2D approximation may be not able to identify all potential collision points in 3D space.

To achieve the contractual grade consistency required by the client with the minimum travelling distance, Lu and Myo employed a 3D stockpile model (a triangular prism) and partitioned it into a number of sections which are called voxels in their paper. A voxel is assumed to have excavated by the BWR in one cut and the quality variations of these voxels are assumed to satisfy a normal Gaussian distribution [20, 29]. Together with other operational constraints, a BWR trajectory optimisation system was developed. Thus, the system they have developed assists the BWR to reclaim stockpiles (two in their papers) selectively, in terms of the quantity requirements. However, these voxels (triangular/trapezoidal prisms) are different from the sickle-shaped cuts caused by the BWR and the two conical ends of a stockpile are not involved in the modelling.

There is definitely a lack of a novel stockpile model that is able to guide the reclaiming operations. The main reason for such need lies in the low recovering rate and operating efficiency of the system at the reclaiming phase. As pointed out by Lu, on-site investigations show that stockpiled products have currently been reclaimed at only approximately 50% of their potential engineering productive rates [4]. Because the quality of a stockpile is not known exactly after stacking, quality control is still a complex process at the reclaiming phase. To monitor the quality of recovered material regarding the final objective, the reclaiming has to be suspended frequently whilst waiting for the quality assay results. If any changes in quality are needed, it has to move to another position to recover different grade materials. Again, such decisions are made by humans using imperfect quality information. Furthermore, because the first cut is controlled by human operators, it inevitably introduces more uncertainties into the adjustments. Therefore, the entire operation is working in an inefficient and high-cost mode.

2.4 Stockyard Management

Other than optimizing the blending operations, some researchers aim to optimize the entire operation of iron ore handling. A port simulation model, including both mine sites and export ports, was introduced by Dahal et al. in 2003. This simulation model contains most of the handling facilities, such as stockpiles, conveyors, stackers and reclaimers, and a group of real operational constraints. The optimisation problem aims to find a sequence of feasible daily activities for the processing plant and material-movement systems that meet the overall production targets [30]. They suggest this problem will have two conflicting criteria: to minimise the total operating cost and to maximise component utilisation. A metaheuristic approach, based on a GA, was proposed to provide an optimized solution for these two criteria. Ayu and Mantoro studied the disturbance in train transportation which may affect daily stockyard operations at an exporting port [31]. They built a three-step system to simulate operations in a stockyard. The stockpiling system is the intermediate link between the train and ship loading systems. Their stockpile model is relatively simple in comparison with other modelling approaches. The ore has to follow a First in, First out (FIFO) strategy. Additionally, a completed stockpile is not allowed to receive new arriving material and an incomplete stockpile cannot be recovered. Restrictions specified in this paper limit its application to real operation environment.

Most recently, He et al. pointed out that yard crane scheduling has been studied consistently, but few scholars have considered energy-saving in their management models. Thus, they integrated a GA and the particle swarm optimisation algorithm that considers the trade-off between efficiency and energy consumption for yard crane scheduling [32]. The seaport container terminal simulated in their study, which is divided into many blocks and owns many yard cranes, is quite similar to an iron ore exporting terminal. Therefore, their scheduling model and algorithm are applicable to BWR movement optimisation. However, the quality and quantity constraints also need to be added into the management model.

Innes et al. developed an approach to track and fuse information on excavated materials throughout the process chain, in a mine site, using a decentralized sensor network [33]. The sensor network contains multiple sensors to track the excavated material. For example, GPS receivers and suspension strut pressures are mounted onto haul trucks. Further to this, the load and bucket volume fill level sensors are mounted on the buckets of an excavator. The ore tracking system is formulated with a dynamic state vector to enable material at each stage to be recorded. An augmented state Kalman filter with constrained system models was used to fuse data from information sources. They believed this method allowed probabilistic reconciliation of the materials, whilst ensuring that the total mass in correlated states remained constant. The data fusion approach reported by Innes et al. with the purpose of accurately tracking the ore, will undoubtedly lead to great financial benefits to the mining industry. However, the cost of building such a network from the mine site to the export port could be an issue. Meanwhile, this approach is not applicable after iron ore is stacked onto stockpiles.

Similar to most mathematical modelling approaches, a stockpile in above reviewed stockyard management systems is only an abstract concept. The general aim of these studies is more likely to increase productivity and lower costs rather than achieving the target grade in effective and efficient manner.

2.5 Research Gap

This section first summarises the literature review and outlines the research gaps. Then, it presents the innovations in this study.

2.5.1 Summary

Existing work in the field has demonstrated the need for building a real-time 3D stockpile management model to track for quality during the entire life cycle of a stockpile. This chapter first describes the stockpile's functions and details how such functions are achieved in daily operations (Section 2.1).Then, current research interests are catalogued into three sections and presented separately (Section 2.2, Section 2.3 and Section 2.4). Section 2.2 reviews the current stockpile modelling approaches and points out their incompatibilities. Section 2.3 presents the progress in machine automation and indicates the need to integrate both stockpile and machine operation to achieve full automation in stockpile blending. Section 2.4 introduces optimisation algorithms used for stockyard management and transportation scheduling and identifies their limitations in bulk material handling.

The classification method used in the literature may be not very rigorous. There are some overlapping areas in stockpile modelling, machine automation and stockyard management, as the quality control and optimisation can be conducted at every level throughout the delivery chain. It is also worth pointing out that there still exist other modelling algorithms. For example, the use of mathematical models to predict spontaneous combustion in coal stockpiles [34], to simulate the deterioration of stockpiled coal [35]and to estimate the temperature change behaviour of a coal stockpile using statistical analysis techniques [36]. However, they are obviously beyond the scope of this research. To the best of the author's knowledge, there are limited studies looking into achieving pre-defined grade constancy with great accuracy through stockpile blending. Although considerable stockpile models and management systems have been developed, it is still necessary to build a highly accurate 3D real-time volumetric model which is able to represent a stockpile dynamically and continuously guide the blending operations throughout a stockpile's life-cycle.

To summarize, the research gaps identified in this study are:

- A real-time measuring device and stockpile modelling method is needed for accurate quality estimation in stockpile blending operations.

- A novel 3D stockpile management model that links the stockpile and BWR is needed for efficient and effective quality control in stockpile blending operations.

2.5.2 Innovations

In this project, a mobile laser scanning device is proposed to measure a stockpile accurately. A BWR can be upgraded into a mobile scanner after installing such a device and can then scan the profiles of a stockpile continuously in stacking/reclaiming operations. Also, two geometric modelling algorithms will be presented to create dynamic models of a stockpile from 3D surface measurements. Unlike previous stockpile management modelling approaches, the quality of a stockpile in this project is not considered as an entity, it is estimated through creating a group of quality volumetric pixels (voxels). The quality of each voxel is calculated from its own geometric shape and the geometric shapes of the layers inside. No project has been identified to implement such a deep insight into stockpile management previously.

This research also presents an algorithm to calculate the BWR joint angles for machine automation. Through combining the 3D stockpile and BWR models, the collision free trajectory can be computed and the initial location of the BWR, along with the slewing and luffing angles during the reclaiming, can be obtained in advance. Thus, the quality of recovered material can be estimated and the machine is able to perform automatic missions using the calculated results, which will lead to real-time optimum stacking/reclaiming operations with consistent product grade control.

The overall block diagram of the proposed 3D stockpile management model is shown in Fig. 2.4.

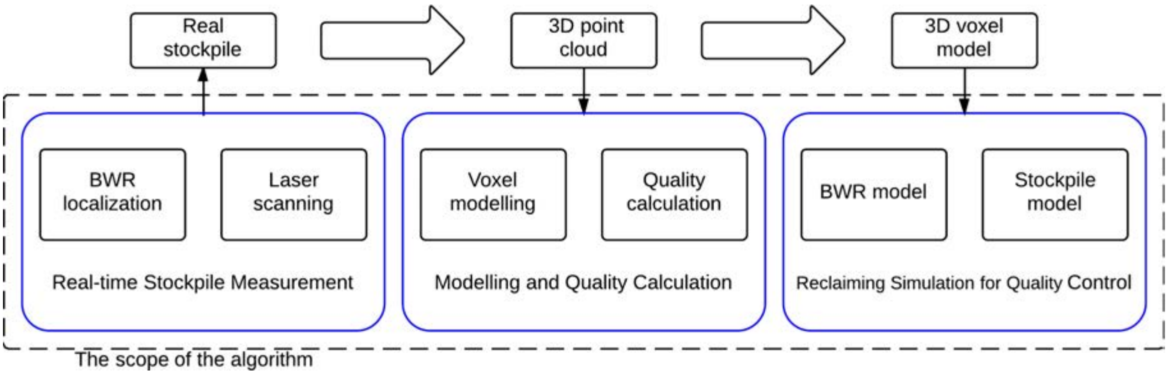

Fig. 2.4 3D stockpile management model for quality control.

Chapter 3

BWR Localization for Stockpile Scanning

To build an accurate and up-to-date 3D model of a stockpile, a measuring device is needed to scan the stockpile's surface continuously. A cost saving solution is to mount a 2D scanning device onto a BWR. Thus, the BWR can drive the scanning plane and measure the stockpile during stacking or reclaiming operations. This chapter details the laser scanning system design and a mobile robot localization algorithm, designed to improve the positioning accuracy for future modelling purposes. Additionally, an indoor laser scanning system used for the laboratory experiment is presented.

3.1 Mobile Laser Scanning

There is no doubt that all processes require infrastructure to be operated cost-effectively. Therefore, the stockpile scanning system in this study is designed with a mind to utilizing existing facilities as much as possible. Considering its popularity and mobility, a BWR is the best choice for the scanning mission. Therefore, a BWR has been selected to be upgraded into a mobile laser scanner to measure the most recent shapes of a stockpile.

A laser range finder (LRF) is an excellent choice to measure the environment due to its high accuracy in terms of both range and bearing measurements and its lower dependency on any given surface's texture. LRFs have been widely used for mobile robot navigation and mapping in various sceneries. For example, in the literature review, 2D contour maps of stockpiles are extracted from laser measurements [27, 28]. Additionally, Newman et al. [37] have reported that LRFs provide accurate measurements in outdoor environments. More importantly, Scheding et al. used a LRF sensor to map a dusty underground mining tunnel [38].

Ryde and Hillier also point out that although radar sensors are robust in rain and mist conditions whilst suspended dust conditions, they provides lower range and angular precision and scanning rate than the laser systems [39]. They examined the performance of two LRFs and one millimetre-wave radar in a test chamber, which is able to generate dust and rain of varying densities. The results shows that both LRFs fail to acquire a target at a 25 *m* distance from the sensor when the visibility of the environment is less than 10 *m*, while the millimetre-wave radar does not. However, in a separate experiment, they installed these sensors onto a P&H 2100 BLE electric face shovel for terrain mapping. Results indicates that measurements from millimetre-wave radar contain significant data noise with uncertainty in the ground plane (typically near 0.5 *m* and up to 1.25 *m* in some instances). This uncertainty in measurement and low cloud density made identification of objects less than 2 *m* in size difficult in the radar data [39]. Conversely, both LRFs demonstrate high precision and accuracy for environment modelling. Although these measurements are susceptible to corruption in environments with high mist and dust loading, they still believe that LRFs are best sensors in terms of price/performance ratio for outdoor mapping.

Supported by these results, the sensor considered for this study is a 2D LiDAR (Light Detection and Ranging). It emits a narrow laser beam and sweeps the beam towards to the objects to be scanned, which results in a fan-shaped scanning plane. When the scanner is mounted at the end of the boom of a BWR and faced toward a stockpile, the motion of the boom is exploited to move the scanning plane and produce a de-facto 3D scanner (see Fig. 3.1). Under such configuration, the laser beam can cover the entire stockpile at the stacking phase.

The measuring accuracy of the 3D scanner is not only determined by the LiDAR itself but also by the positioning accuracy of the end-effector (where the LiDARdar is mounted on the BWR, in this study, it is the centre of the bucket wheel). When the BWR is stationary, the noise from the LiDAR is the main characteristic that pollutes the measurement. However, when the BWR is moving whilst simultaneously scanning a stockpile, the measurement accuracy is largely affected by errors generated from the BWR positioning system. According to the feedback from industry partner, MatrixGroup, to enable automatic operation and avoid collisions, most BWRs operated in Australia are supplied with encoders to measure the travelling, slewing and luffing motions. Thus, the positioning information of the end-effector can be calculated in real-time. However, encoders' measurements suffer from quantization errors and degrade without boundary over time. With the travelling encoder, errors are eliminated by placing many calibration points along the moving track. With the slewing and luffing angular encoders, no calibration can be applied due to the technical difficulties in mounting extra calibration devices to such large-scale machinery. As a consequence, the estimated position errors of the end-effector are more than 30 *cm*, resulting in a significant corruption of the LiDAR measurements. Furthermore, this error range does not contain the sources caused by the imperfect mechanical linkage and the vibration of the boom during machine movements. Such positioning accuracy is not favourable for stockpile modelling. Therefore, a localization algorithm is first studied.

The capability of a mobile robot to elaborate the sensor measures and find out its position with respect to a coordinate system is called localization. Once the robot is localized, it is able to build a map of its surroundings. The localization is a key problem for mobile robots and many approaches have been developed and evaluated. One of these approaches is to use Kalman filtering techniques that fuse sensory data according to their statistical properties. A Kalman filter (KF) is an optimal recursive estimation method that can be applied in real-time processing to handle noisy measurements. Its success has been well proved using both indoor and outdoor mobile robots [40–42]. Therefore, the author proposed an UKF (Unscented Kalman Filter) based sensor data fusion technique. The UKF fuses GPS and on-board encoder sensor data to provide a better position estimation of the end-effector for stockpile modelling. Fig. 3.1 indicates the proposed mounting position of the GPS and laser sensor, as well as the encoders used to measure the joint angles of a BWR.

3.1.1 Kalman Filter

A Kalman filter addresses a general problem of estimating a state vector that is governed by linear dynamic system equations. The vector X, consisting of n variables, describes some properties of the system, i.e. the location of the BWR in 3D space, consisting of three variables x, y and z coordinates. In Kalman filtering, the state of the vehicle at a specific time is predicted using a dynamic model based on the previous state information and the control input. Then, the measurements from the sensors are employed to update the estimation of the vehicle's state. The translation from sensory measurements to the vehicle state is made

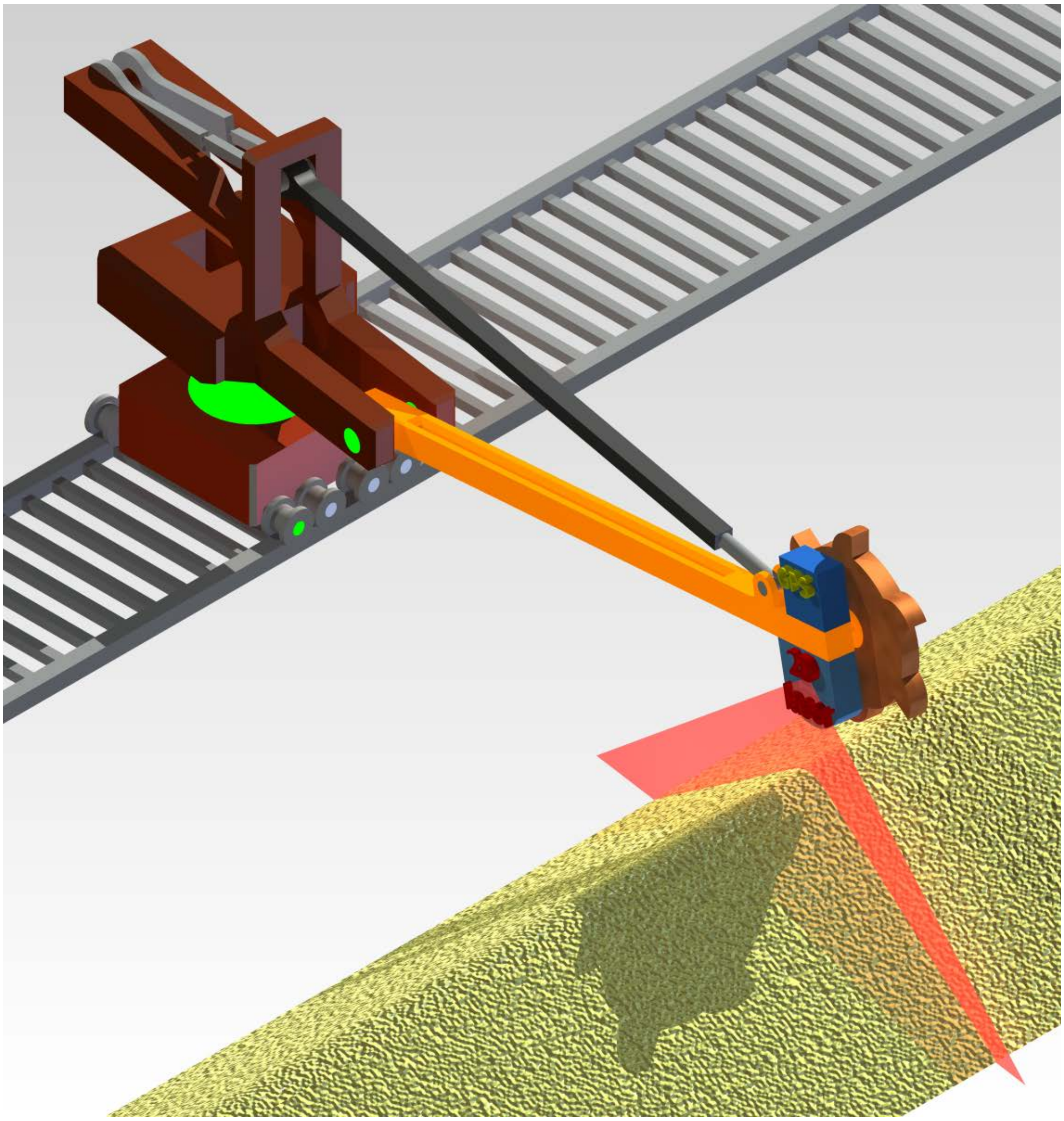

Fig. 3.1 Upgrading a BWR into a mobile 3D laser scanner. The green parts illustrate how the position of the end-effector is measured through encoders. The GPS and laser sensors are mounted at the same position. The fan-shaped scanning plane is illustrated in red.

by a sensor or measurement model. Kalman filtering is also a data fusion technique because both the dynamic and sensor models are interpreted through sensory information.

Dynamic Model. The dynamic model describes how the true state of the system changes through time due to its dynamics. Given an $n \times 1$ state vector (X) of a linear system, its true state at time k, X_k, depends on its previous state X_{k-1}, the control input, U_k, at time k, and some Gaussian noise at time $k-1$.

$$X_k = AX_{k-1} + BU_k + W_{k-1} \tag{3.1}$$

where A is an $n \times n$ state transition matrix that transforms the previous state to the current state. B is an $n \times l$ control matrix that maps the control input vector U_k (consisting of l variables) to the state vector. Although U_k is sometimes provided by a robot's odometry, these odometry measurements are still treated as control signals in most mobile robot applications. W_{k-1} is also an $n \times 1$ vector that represents process noise terms for each element in the state vector.

Measurement Model. The measurement model describes the relationship between the sensor measurement and the state vector. The KF uses this model to correct the state prediction when sensor measurements are acquired. The true measurement vector ($m \times 1$) at time k, depends on the state of the system X_k and measurement noise at time k.

$$Z_k = CX_k + V_k \tag{3.2}$$

where C is an $m \times n$ transformation matrix that maps the state vector to the measurement domain. V_k is a noise vector containing m noise terms.

Noise Characteristics. A very important assumption in Kalman filtering is that the linear dynamic system is corrupted by independent, white, zero-mean, Gaussian noise. Thus, the system noise W_k in eq. 3.1 and the measurement noise V_k in eq. 3.2 are random variables that satisfy independent, white, zero-mean Gaussian probability distributions. The system noise W_k and the measurement noise V_k are described as:

$$\begin{gathered} W_k \sim N(0, Q_k) \\ V_k \sim N(0, R_k) \end{gathered} \tag{3.3}$$

where Q_k and R_k denotes the process noise covariance matrix and measurement noise covariance matrix of the Gaussian distribution, respectively.

Kalman Filter Algorithm. The KF algorithm can be broken down into two phases: the prediction and the correction phase. At the prediction phase, the belief of state vector $\overline{X}_k$ at the current state is estimated using the previous state $\overline{X}_{k-1}$ and the control input. Also the covariance $\overline{\Sigma}_k$ that indicates the confidence of the state estimation is calculated through the linear matrix A. At the correction phase, the Kalman gain K_k is firstly calculated and then the state estimation $\overline{X}_k$ and covariance $\overline{\Sigma}_k$ is refined using measurement data and the Kalman gain, respectively. The KF algorithm is depicted in Fig. 3.2.

```
Kalman Filter Algorithm
$(X_k, \Sigma_k) = KF(\overline{X}_{k-1}, \overline{\Sigma}_{k-1}, U_k, Z_k)$
Prediction:
    $\overline{X}_k = A\overline{X}_{k-1} + BU_k$
    $\overline{\Sigma}_k = A\overline{\Sigma}_{k-1}A^T + Q_k$
Correction:
    $S_k = (C^T\overline{\Sigma}_k C^T + R_k)$
    $K_k = \overline{\Sigma}_k C^T S_k^{-1}$
    $X_k = \overline{X}_k + K_k(Z_k - C\overline{X}_k)$
    $\Sigma_k = (I - K_k C)\overline{\Sigma}_k$
```

Fig. 3.2 The KF algorithm for a linear dynamic system with Gaussian state transitions and measurements.

3.1.2 UKF

The success of a KF depends on the accuracy of its prediction model. It has been pointed out that the use of a KF in a nonlinear system directly will cause significant errors in predicting the state of the system [43]. The simplest and most widely used approach is to linearize the nonlinear function using the Taylor expansion, which is called the Extended Kalman Filter or EKF. EKF has become a very popular tool for the state estimation for nonlinear systems in robotics [41, 44].

The use of linear Taylor expansions to approximate state transition and measurement matrices has limitations. The performance of such linearization depends on two main factors: the degree of nonlinearity of the system and the degree of uncertainty of the state vector.

Generally, the greater the amount of the state vector is affected by nonlinearities in the state transition and measurement matrices; the less certainty there is in the state vector; the wider the Gaussian behaviour of the noise; thus the less likely it is that the posterior belief can be estimated using an EKF [44]. Conversely, a particle filter (PF) estimates the sequence of hidden system states based on the observed measurements only and has proved to be very successful in the estimation of nonlinear, non-Gaussian state-space systems [45, 46]. This is mainly because it does not rely on any local linearization techniques or crude functional approximations. However, the computational complexity is the main issue that prevents its implementation in real-time applications.

Recently, an Unscented Kalman filter (UKF) has been proven to be able to deliver better estimation results than the EKF [47, 48]. A UKF performs a stochastic linearization through an unscented transformation (UT). The UT generates a set of weighted sigma points, which are located at the mean and symmetrically along the main axes of the covariance, to represent the Gaussian distribution and linearize the nonlinear system function. The use of these weighted sigma points in UT propagates more accurate mean and covariance results than the use of the first-order Taylor expansion in the linearization. A UKF can be considered as a KF based on the UT.For a nonlinear dynamic system governed by nonlinear functions G and H, can be described as:

$$\begin{aligned} X_k &= G(X_{k-1}, U_k) + W_{k-1} \\ Z_k &= HX_k + V_k \end{aligned} \tag{3.4}$$

Again, X_k is an n-dimensional state vector and U_k is an n-dimensional control vector. The UT creates $2n$+1 sigma points $\chi^{[i]}$ to represent the propagation of the state vector through the nonlinear function G according to the following equation [48]:

$$\begin{cases} \chi^{[0]} &= \mu & i = & 0 \\ \chi^{[i]} &= \mu + (\sqrt{(n+\lambda)\Sigma})_i & i = & 1, ..., n \\ \chi^{[i]} &= \mu - (\sqrt{(n+\lambda)\Sigma})_{i-n} & i = & n+1, ..., 2n \end{cases} \tag{3.5}$$

where $\lambda = \alpha^2(n+\kappa) - n$, with α and κ being scaling parameters that determine the spread of sigma points around the μ. Commonly, α is set to be a small positive value (i.e. 1e-3) and κ is set to be 0. The weight $w_m^{[i]}$ used to calculate the mean is:

$$\begin{cases} w_m^{[0]} &= \frac{\lambda}{n+\lambda} & i = & 0 \\ w_m^{[i]} &= \frac{1}{2(n+\lambda)} & i = & 1, ..., n \end{cases} \tag{3.6}$$

The weight $w_c^{[i]}$ used to calculate the covariance is:

$$\begin{cases} w_c^{[0]} & = & \frac{\lambda}{n+\lambda} + (1-\alpha^2+\beta)) & i = & 0 \\ w_c^{[i]} & = & \frac{1}{2(n+\lambda)} & i = & 1,...,n \end{cases} \tag{3.7}$$

The parameter β aims to incorporate additional knowledge of the distribution underlying the Gaussian representation. An optimal choice is $\beta = 2$ if the distribution is an exact Gaussian. When these sigma points are passed through G, the mean and the covariance of resulting Gaussian representation can be calculated according to eq. 3.8:

$$\begin{aligned} \gamma^{[i]} &= G(\chi^{[i]})) \\ \mu' &= \sum_0^{2n} w_m^{[i]} \gamma^{[i]]} \\ \Sigma' &= \sum_0^{2n} w_c^{[i]} (\gamma^{[i]} - \mu')(\gamma^{[i]} - \mu')^T \end{aligned} \tag{3.8}$$

At the prediction stage, the UKF algorithm firstly utilizes the UT eq. 3.6 to generate sigma points of the previous belief $\overline{X}_{k-1}$ and then propagates these sigma points through noise-free state estimation function G. Secondly, the predicted mean and covariance of these sigma points are computed. The noise matrix Q_k is added to model the additional uncertainty whistle calculating the covariance. Finally, a predicted observation $\overline{\gamma}_k$ is calculated for each sigma point and then it is used to calculate the predicted observation $\widehat{Z}_k$. At the correction stage, the uncertainty of the $\widehat{Z}_k$ is first calculated. Secondly, the cross-covariance between the state and the observation is computed and the Kalman gain is obtained. Finally, the state estimation and the covariance are updated. The innovation procedure is identical to the one used in the Kalman filter. The UKF algorithm is depicted in Fig. 3.3.

3.1.3 UKF Sensor Data Fusion for BWR Localization

Because BWRs are heavily engaged and stretched to their limits in production, it should be expected that fewer hardware changes will need to be made to upgrade a BWR into a mobile laser scanner with localization capability. Additionally, in contrast with encoders, the accuracy of the GPS degrades neither over time nor distance. Due to their complementary characters, the integration of GPS and encoders through Kalman filtering techniques is a

Unscented Kalman Filter Algorithm

$$(X_k,\Sigma_k) = UKF(\overline{X}_{k-1},\overline{\Sigma}_{k-1},U_k,Z_k)$$

Calculate sigma points:

$$\chi^a_{k-1} = \left[\overline{X}^a_{k-1}\ \ \mu^a_{k-1}+\sqrt{(n+\lambda)\Sigma^a_{k-1}}\ \ \mu^a_{k-1}-\sqrt{(n+\lambda)\Sigma^a_{k-1}}\right]$$

Prediction:

$$\overline{\chi}^a_k = G(\chi^a_{k-1},U_k)$$

$$\overline{X}_k = \sum_{i=0}^{2n} w_m^{[i]}\overline{\chi}_k^{a[i]}$$

$$\overline{\Sigma}_k = \sum_{i=0}^{2n} w_c^{[i]}(\overline{\chi}^a_k-\mu_k)(\overline{\chi}^a_k-\mu_k)^T+Q_k$$

$$\overline{\gamma}_k = H(\overline{\chi}_k), \qquad \hat{Z}_k = \sum_{i=0}^{2n} w_m^{[i]}\overline{\gamma}_k^{[i]}$$

Correction:

$$S_k = \sum_{i=0}^{2n} w_c^{[i]}(\overline{\gamma}_k^{[i]}-\hat{Z}_k)(\overline{\gamma}_k^{[i]}-\hat{Z}_k)^T+R_k$$

$$\Sigma_k^{x,z} = \sum_{i=0}^{2n} w_c^{[i]}(\overline{\gamma}_k^{[i]}-\overline{X}_k)(\overline{\gamma}_k^{[i]}-\hat{Z}_k)^T$$

$$K_k = \Sigma_k^{x,z}\,S_k^{-1}$$

$$X_k = \overline{X}_k + K_k(Z_k-\hat{Z}_k)$$

$$\Sigma_k = \overline{\Sigma}_k - K_kS_kK_k^T$$

Fig. 3.3 The UKF algorithm for a nonlinear dynamic system.

perfect match to improve the position estimations of the BWR in 3D space. Fig. 3.4 shows a structure of a UKF based GPS/encoder fusion.

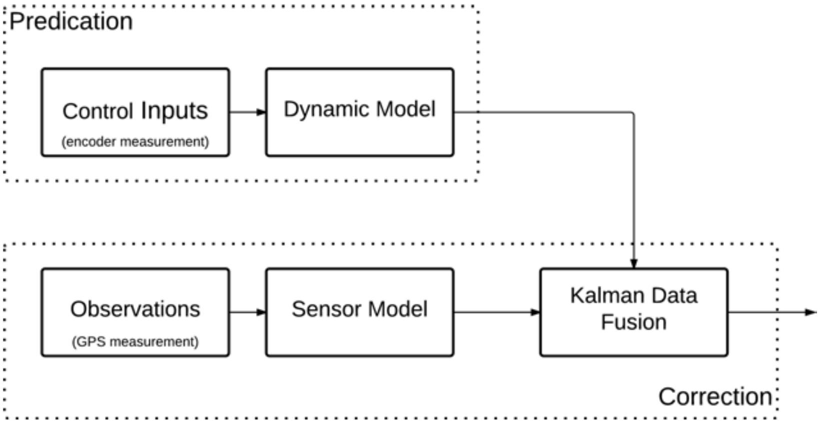

Fig. 3.4 The structure of a typical Kalman filter for data fusion.

BWR Odometer Motion Model. A kinematic model of a BWR was studied by Lu in 2009 [49]. Both forward and reverse kinematic equations have been deduced and proved to be efficient and accurate for BWR motion control [50]. The forward kinematic equations [49] are used as a dynamic model for Kalman filtering in this study.

$$\begin{aligned} x(t) &= \sin\theta_2(t)(L_5\cos\theta_2 + L_4) \\ y(t) &= L_5\cos\theta_2(t)\cos\theta_3(t) + L_4\cos\theta_2 + d1 \\ z(t) &= -L_5\cos\theta_3(t) - L_2 - L_3 \end{aligned} \tag{3.9}$$

where θ_i is the angle between x_{i-1} and x_i measured about z_i. L_i is the distance from z_i to z_{i+1} measured along x_i. d_i is the distance from x_{i-1} to x_i measured about z_i. The x_i, y_i and z_i represent the BWR motion axes, respectively, which are defined in Fig. 3.5.

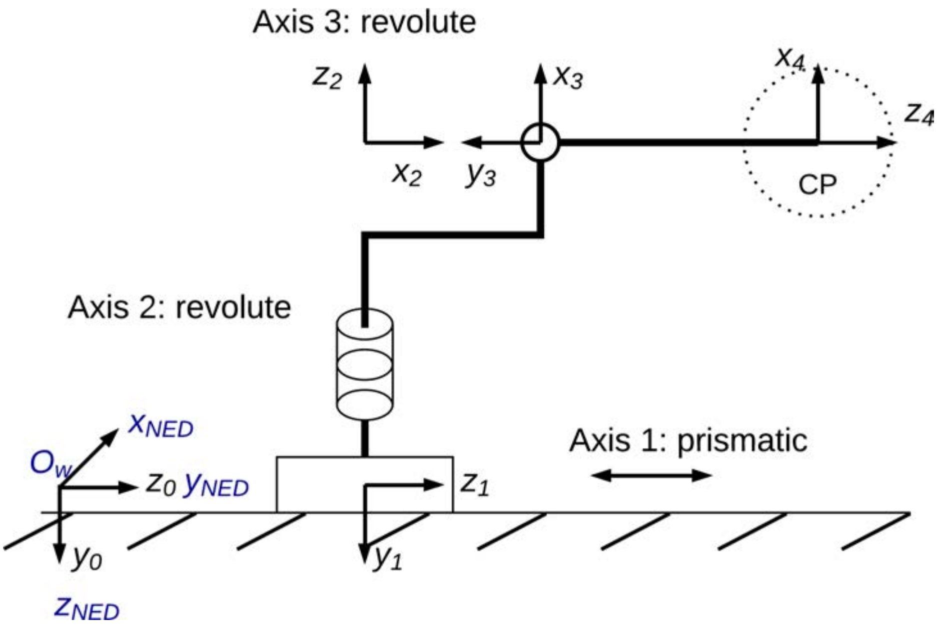

Fig. 3.5 BWR coordination system and motion axes definition, original image adopted from Lu's work [49].

This kinematic model of the BWR is defined in a world coordination frame which is centred at O_w as shown in Fig. 3.5. To simplify the transformation matrix in the measurement model, the coordinate definition follows the North-East-Down (NED) coordinate system. The NED system is Local Tangent Plane (LTP) coordinate system and its x axis points toward the ellipsoid north and the y axis points toward the ellipsoid east. The z axis points downward along the ellipsoid normal. Thus, the state vector for the end-effector position is $X = [x_{NED}, y_{NED}, z_{NED}]^T$. The relative difference between any two poses is represented by a concatenation of three motions: a translation (d_1) and two rotations (θ_2, θ_3). Consequently, the true position, X_k, obtained from X_{k-1} by the encoder measurements which are used for calculating the BWR motion, is:

$$\begin{bmatrix} x_k \\ y_k \\ z_k \end{bmatrix} = \begin{bmatrix} x_{k-1} \\ y_{k-1} \\ z_{k-1} \end{bmatrix} + \begin{bmatrix} \sin\theta_2(t)(L_5\cos\theta_2 + L_4) \\ L_5\cos\theta_2(t)\cos\theta_3(t) + L_4\cos\theta_2 + d1 \\ -L_5\cos\theta_3(t) - L_2 - L_3 \end{bmatrix} \tag{3.10}$$

where d_1, θ_2, θ_3 is the increment measured by on-board encoders from time $k-1$ to time k. Thus, the motion information U_k in eq. 3.1 is transformed into odometer information. Obviously, the BWR motion model is nonlinear. Equation 3.10 can be simplified as:

$$X_k = F(X_{k-1}, U_k) + W_{k-1} \tag{3.11}$$

However, in computer based systems, calculations are performed in discrete time. Therefore, it is necessary to transfer dynamic matrix F to state transition matrix Φ. The transformation can be approximated by the power series expansion of the exponential function [51]:

$$\Phi_k = e^{F(t_{k-1})\Delta t} = I + F(t_k)\Delta t + \frac{(F(t_k)\Delta t)^2}{2} \tag{3.12}$$

where I is the identity matrix and Δt is the sampling interval. Thus, eq. 3.11 can be rewritten into:

$$X_k = \Phi(X_{k-1}, U_k) + W_{k-1} \tag{3.13}$$

The system noise W_k is modelled on the assumption of three independent sources of error, one for a translational encoder, two for angular encoders. The covariance Q_k is:

$$Q_k = \begin{bmatrix} \sigma_{d_1}^2 & 0 & 0 \\ 0 & \sigma_{\theta_2}^2 & 0 \\ 0 & 0 & \sigma_{\theta_3}^2 \end{bmatrix}$$

Sensor Measurement Model. Measurements from GPS receivers are normally given in the Earth-Centred-Earth-Fixed (ECEF) coordinate system. Conversely, the coordinate system used in BWR localization is the NED frame as shown in Fig. 3.5. A simple technique to perform the transformation (from the ECEF to the NED) is through the application of an appropriate Direction Cosine Matrix (DCM), which is detailed in several textbooks, such as [52] and [53]. However, due to the limitation of the experimental venue, only a simulation study was performed. Therefore, it is assumed that the GPS measurements are also given in the same NED coordinate as the BWR. Thus, the transformation matrix H is a 3 × 3 identity matrix. The measurement model can be expressed as:

$$Z_k = H(X_k) + V_k \tag{3.14}$$

The noise covariance matrix R_k for noise vector V_k is:

$$R_k = \begin{bmatrix} \sigma_x^2 & 0 & 0 \\ 0 & \sigma_y^2 & 0 \\ 0 & 0 & \sigma_z^2 \end{bmatrix}$$

UKF Data Fusion. The UKF based localization algorithm starts with the construction of the argument state vector $X_k^a = [X_k^T, W_k^T, V_k^T]^T$. The initial estimate of the argument state vector X_0^a is:

$$\begin{aligned} X_0^a &= [X_0^T, 0, 0]^T \\ \Sigma_0^a &= \begin{bmatrix} \Sigma_0 & 0 & 0 \\ 0 & Q & 0 \\ 0 & 0 & R \end{bmatrix} \end{aligned} \tag{3.15}$$

The sigma points constructed using the UT for X_k measured by encoders are given by eq. 3.11:

$$\begin{cases} \chi_{a,k-1}^0 & = & \overline{X}_k^a & i = & 0 \\ \chi_{a,k-1}^i & = & \mu_{k-1}^a + (\sqrt{(n+\lambda)\Sigma_{k-1}^a})_i & i = & 1,...,N \\ \chi_{a,k-1}^i & = & \mu_{k-1}^a - (\sqrt{(n+\lambda)\Sigma_{k-1}^a})_i & i = & N+1,...,2N \end{cases} \tag{3.16}$$

where N is the dimension of the argument state vector. In this case, $N = 9$. As described in the section 3.1.2, the rest of the implementation of the UKF is quite straightforward. The constructed sigma points are passed through a motion model and the Gaussian statistics are computed using eq. 3.8. Then the estimation is updated in the measurement model and the state-measurement cross-covariance matrix S_k is used to calculate the Kalman gain. The rest is virtually identical to the KF correction step.

3.2 Simulation Framework

After consulting with MatrixGroup, informedit is confirmed that it is currently not possible to mount a laser scanner on a BWR and scan a real stockpile for the required experiments because it is hard to find the right experimental venue and a spare BWR for the research. Thus, a simulation system is proposed at this stage to evaluate the UKF localization algorithm. The simulation system contains an encoder, a GPS and a UKF module. Both the GPS and encoder modules take the real trajectory of the end-effector as an input. Pseudo-random noise is then added to simulate the sensor measurement. The UKF localization module integrates the sensory measurements and updates the position estimation using a UKF.

3.2.1 Encoder Module

A three-step procedure is employed to simulate encoder measurements (see Fig. 3.6). Firstly, the real end-effector trajectory is converted into joint measures and these measures are rounded down regarding to their resolutions. Secondly, Gaussian noises are added to these datasets individually. Finally, these noisy data are rounded down again to simulate the encoders' measurements.

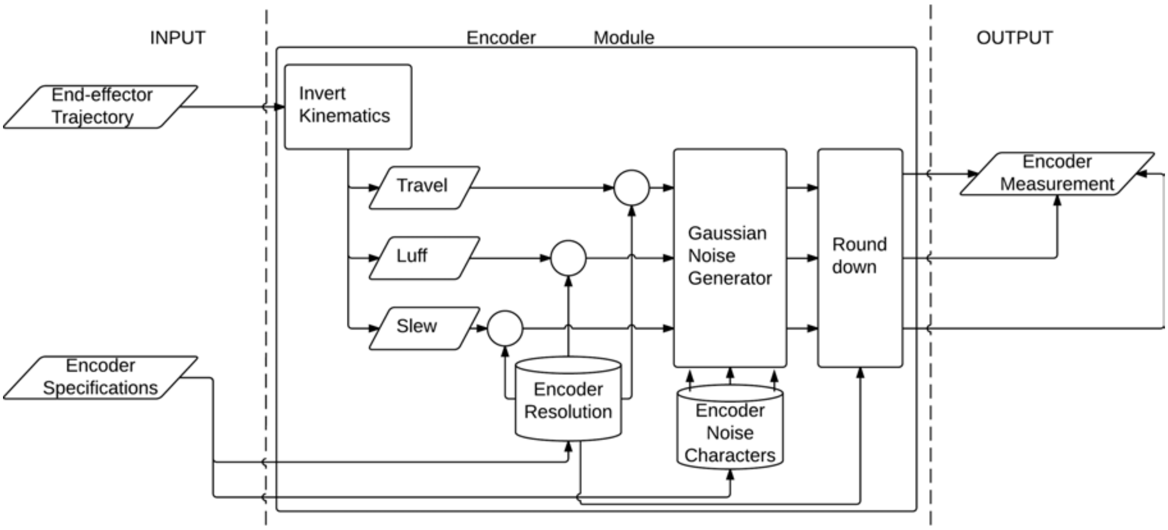

Fig. 3.6 Data flow in the encoder module.

3.2.2 GPS Module

When a GPS receiver operates in the yard, its errors can be considered to contain Gaussian and non-Gaussian characteristics. Most common errors, such as atmospheric errors and user equipment errors are Gaussian-based; while environmental noises, such as impulsive noise, ultra-wideband noise, demonstrate the non-Gaussian behaviour. These two different types of noises are simulated separately.

A differential GPS is a technique that applies corrections from a reference station to a normal GPS receiver. That is to say, it works at the differential mode when corrections are available and at the normal mode when connections are lost. Therefore, to simulate DGPS measurements faithfully when it is operated in the stockyard, these two scenarios are both considered in the GPS module. Gaussian noises are compensated when the receiver acquires the correction signal broadcasted from the reference station. However, the compensation suffers a certain degradation due to the separation between the reference station and the receiver. When corrections are available, the degradation can be described by a function of the distance between the reference station and the receiver [54]:

$$\sigma_{correction}(95\%) = 0.41 + 0.2S \tag{3.17}$$

Equation 3.17 means that 95% of the DGPS error is approximately equalled to 0.41 *m* plus 0.2 *m* for each 100 *km* distance from the reference station. When the connection between the receiver and the reference station is lost, the standard deviation of the GPS error is:

$$\sigma_{no\_correction} = \sigma_{ephemeris} + \sigma_{ionosphere} + \sigma_{troposphere} \tag{3.18}$$

where $\sigma_{ephemeris}$ means the ephemeris error, $\sigma_{ionosphere}$means the ionosphere error and $\sigma_{troposphere}$ means the troposphere error. The ephemeris error is caused by the difference between the expected and actual orbital position of GPS satellites. The ionosphere and troposphere will slow down radio waves and cause time delays between signal transmission and reception. In the simulation, only ephemeris, ionosphere and troposphere errors are considered because they are the major error sources [52]. Further information regarding these three errors can be found in the following texts [52, 53] The Gaussian noise is simulated by:

$$\sigma_{Guassian} = \frac{l}{3}(\frac{\sigma_{no\_correction} - \sigma_{correction}}{4-12}) + \sigma_{ave} \tag{3.19}$$

where 12 represents that the maximum number of satellites that can be seen in the sky and 4 represents the minimum number of satellites that can be seen in the sky. l is the number of satellites locked by the GPS receiver. σ_{ave} is the average GPS positioning accuracy without selective availability, which is 15 m in this paper. The standard deviation of Gaussian noise is divided by three, based on the three-sigma rule, which means the error produced has about a 99.7% chance to be within the maximum error. Non-Gaussian noise considered in the GPS module is mainly based on the working environment of the BWR. Operated in a stockyard with numbers of heavy-duty machines, major noise sources could consist of impulsive noise, motor ignition noise and ultra-wideband (UWB) noise. All these noise sources applied in the simulation are based on the models conducted by Liu and Amin [55]. The data flow of the DGPS module is shown in Fig. 3-7.

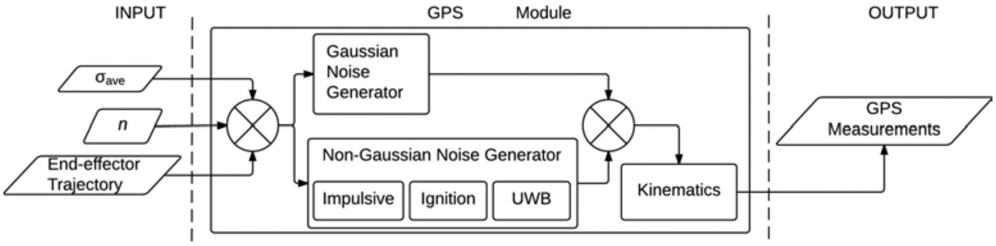

Fig. 3.7 Data flow in the GPS module.

3.3 Simulation Results

Two real trajectories of the BWR were prepared for the simulation. The first one comes from Lu's study [50] and the second one is derived from the bench reclaiming strategy. With the second dataset, it is assumed that the boom of the BWR raises from 0° to 10° and then slews from one side of the stockpile, with a slewing angle of 90 degrees. Afterwards, the machine is advanced for a new cutting depth (0.8 m) and the boom reverses back after the travelling motion. The trajectory was generated by replicating such procedures five times. These two trajectories were the inputs of the UKF simulation system. The dimensions of the BWR used in the simulation are listed in Table 3.1.

Table 3.1 Parameters of the BWR (unit: m)

d_0	L_2	L_3	L_4	L_5
0	6	5	5	50

Similar to the trajectory data, a group of two encoder specifications were created. The first one is provided by the industry partner, MatrixGroup. In this set, the travelling encoder has a resolution of 0.5 *mm*. The slewing encoders can measure up to 0.001° and the luffing encoder is limited to approximately 0.01° due to the slop in the linkages. In the second set, the resolution of travelling, slewing and luffing encoder is 1 *mm*, 0.02° and 0.01°, respectively.

With the GPS module, the BWR was assumed to be operated at the Rio-Tinto Cape Lambert facility, which is one of major upgrading works performed by MatrixGroup. The position of the Cape Lambert facility is $20°39'35.06''$ S; $117°4'42.59''$ E in the WGS84 coordinator system and the nearest reference station is about 31km away in Karratha ($20°42'24.840''$ S; $116°46'26.152''$ E). Two GPS receivers were chosen for the simulation: the first one refers to OEMV-1 from NovAtel. The accuracy for this receiver is 1.5 *m* when working under a single point L1 mode. The second one is a generic DGPS with 5 *m* positioning accuracy. Three different configurations were used to generate GPS measurements:

1. The first assumed that the OEMV-1 receiver was used to receive L1 signal and corrections from the reference station. Meanwhile, six satellites were locked by the receiver.

2. The second assumed that OEMV-1 was working under the local DGPS mode. The rover (receiver) was assumed to receive corrections from the local reference station. It offers 40 *cm* positioning accuracy in real time. In this case, the ionospheric and tropospheric errors were not considered.

3. The third was generated based on the generic DGPS system with 7 satellites in the sky.

Table 3.2 shows the noise characters used in the GPS module regarding the above configurations. Paired with the real trajectory and the GPS configuration, a collection of six datasets were obtained to examine the UKF localization algorithm. Fig. 3.8 plots the simulated GPS and encoder measurements of the first dataset in the x, y and z-axis, separately.

In the simulation, all sensors are assumed to be sampled every 1 *s*. The positioning error/accuracy is expressed in the root mean square errors (RMSE) based on distance error. The localization program was set to run 10 times to average the RMSE and the results are listed (see Table 3.3). Fig. 3.9 and 3.10 illustrate the GPS and encoder measurements against the UKF estimations of the 1^{st} and the 6^{th} dataset.

Table 3.2 Noise characters used in the GPS module (unit: m)

Configuration		1	2	3
Gaussian	σ_{max}	11.942	N/A	15.472
	σ_{min}	1.972	N/A	5.472
	$\sigma_{Gaussian}$	2.5	0.4	2.08
Non-Gaussian	$\sigma_{middleton}$	9.99E-06	9.99E-06	9.99E-06
	σ_{cauchy}	0.25	0.25	0.31
	$\sigma_{ignition}$	0.293	0.293	0.285
	σ_{UWB}	0.4	0.4	0.42

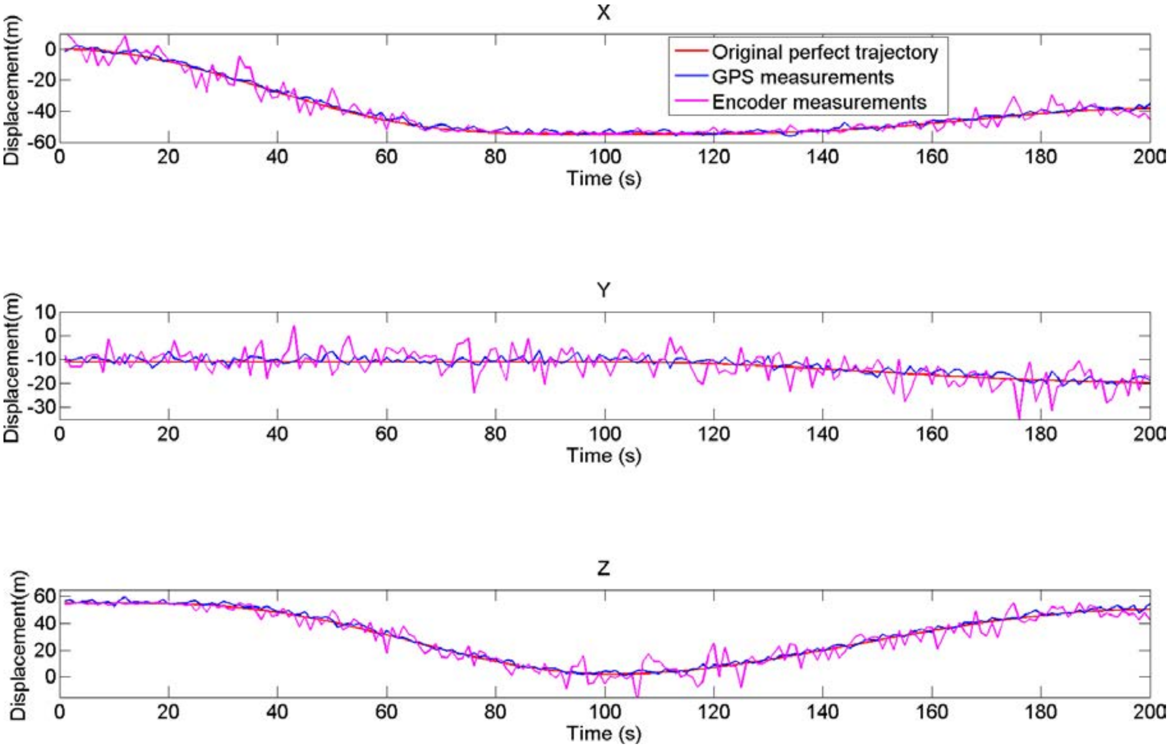

Fig. 3.8 Simulated GPS and encoder data against the true trajectory in the first 200 s.

According to the simulation results, implementing UKF is able to provide more accurate position estimations from noisy measurements. The maximum position errors obtained in the simulations were mostly detected at the very beginning of the filtering (from 0 to 5 s). The reason behind this is the sudden changes in the encoder data. Because both θ_2 and θ_3 are assumed to be 0 at the beginning and increase gradually, even a small error caused by random noise will result in large variations in measurement data. Another interesting finding is that UKF provided good estimations regardless of different GPS' error ranges. All the reporting errors are of the same order in magnitude, giving a useful consistency of results. This may be

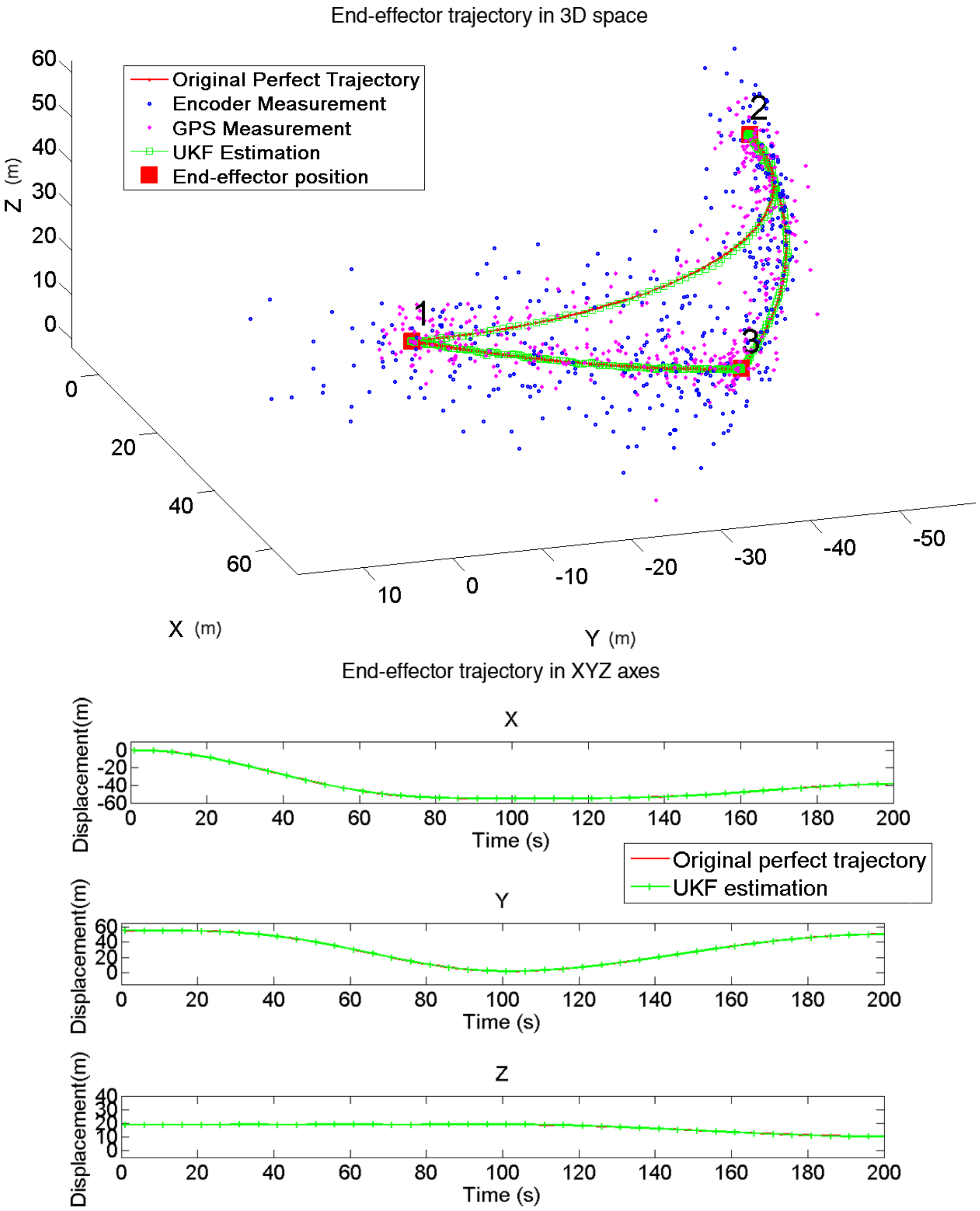

Fig. 3.9 UKF localization results for the 1st dataset.

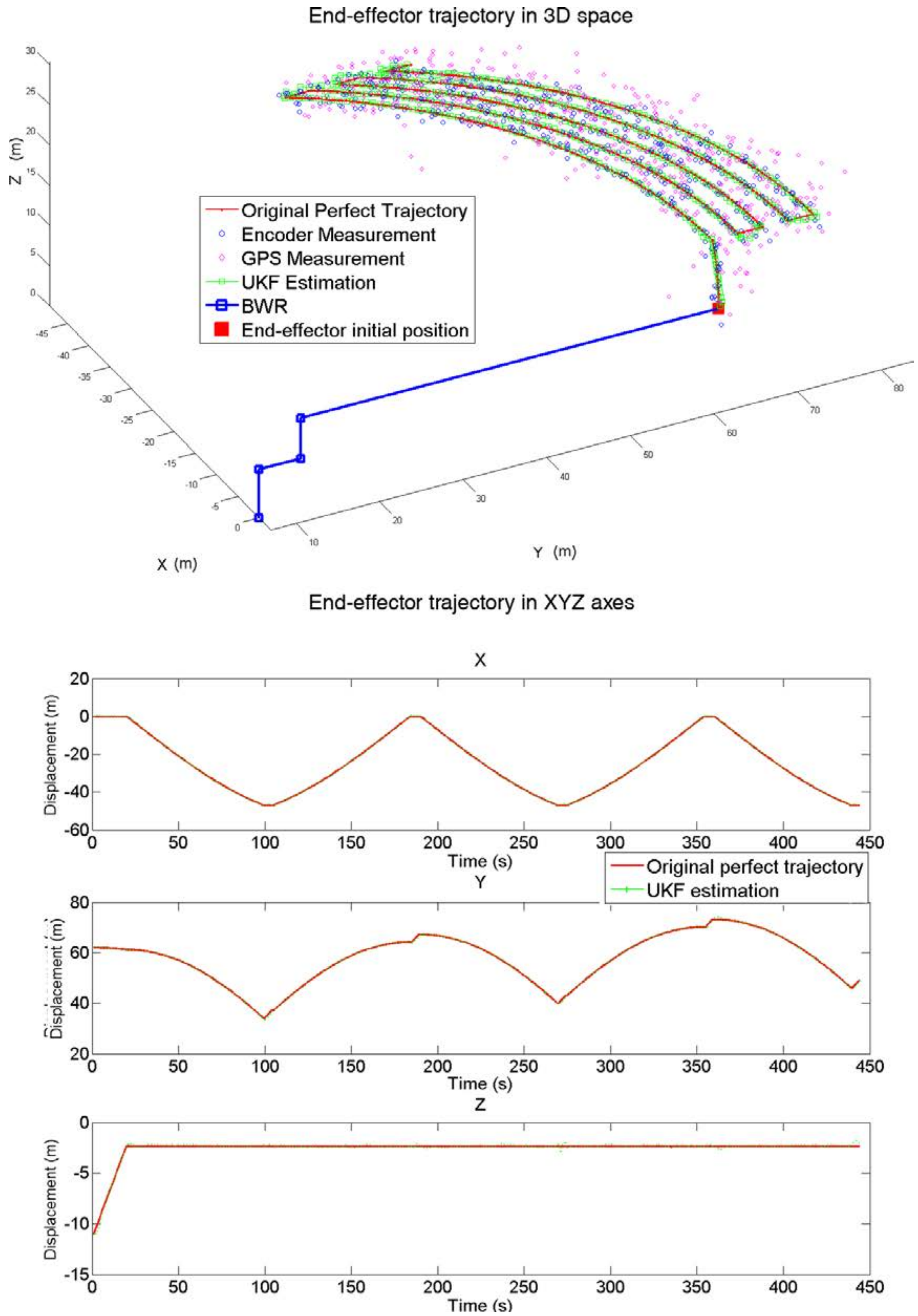
End-effector trajectory in 3D space

End-effector trajectory in XYZ axes

Fig. 3.10 UKF localization results for the 6th dataset.

Table 3.3 Average RMSE of the UKF estimation

Dataset	Real trajectory	Encoder specification	GPS configuration	RMSE Encoder (cm)	GPS (m)	UKF (m)
1	1	1	1	66.11	1.47	15.60
2	1	1	2	67.42	1.24	15.58
3	1	1	3	64.74	3.02	15.69
4	2	2	1	122.43	4.02	26.64
5	2	2	2	121.69	3.35	27.20
6	2	2	3	120.69	6.65	27.48

because the RMSEs of the GPS receivers are very close to each other. In the simulation, the UKF is able to reduce measurement noise and the positioning accuracy of the end-effector (bucket wheel) can be improved to around 15 *cm*, which is believed to be a desirable situation for stockpile scanning and modelling. Because the laser sensor is proposed to be mounted close to the end-effector, its position can be also estimated using the same UKF.

3.4 Indoor Laser Scanning System

For data collecting purposes, a 3DOF scanning system designed for monitoring the ship loading process was adopted to scan the laboratory scale stockpiles. This system was designed to detect obstacles above the deck of a cargo ship and supervise product levels within each cargo hold using lasers [56]. It has a similar scanning mechanism of the proposed mobile laser scanner for this project.

3.4.1 Mechanical and Electrical Aspects

Major components for this system include a pan&tilt platform QPT-50, a linear track, a motor with controller, an optical distance sensor O1D100 and a 2D laser range finder LMS200. As shown in Fig. 3.11, the QPT-50 together with a track roller is mounted on an aluminium linear track and driven by a chain pulley system. The pulley system is controlled by the EPOS 24/5 motor controller. The LMS200 manufactured by Sick was mounted on the QPT-50. Thus, the mechanism allows the LMS200 to scan objects underneath the linear track in both forward and reverse directions. The optical distance sensor (O1D100) is fixed on one end of the frame to measure the displacement of the LMS200 along the track.

The LMS200 is operated as a time of flight sensor. It sends out an infra-red laser pulse and measures the time taken for the pulse to be reflected and returned to the sender. The measured range is proportional to the time of flight of the pulse. A rotating mirror (with a speed of 75 Hz) housed inside the LMS200 reflects the laser beam to allow it to scan objects in front of the device. The LMS200 can be configured to scan a 100° or 180° sector with 0.25°/0.5°/1° in angular resolution. With an angular range of 180° and scanning resolution of 1°, it is capable of completing 13575 measurements per second. The O1D100 is an industry level punctual distance sensor. Its sampling rate is adjustable with the maximum of 50 Hz. However, the high sampling rate will also decrease the measurement accuracy. Therefore, for the work described throughout this thesis, its sampling rate is 15 Hz.

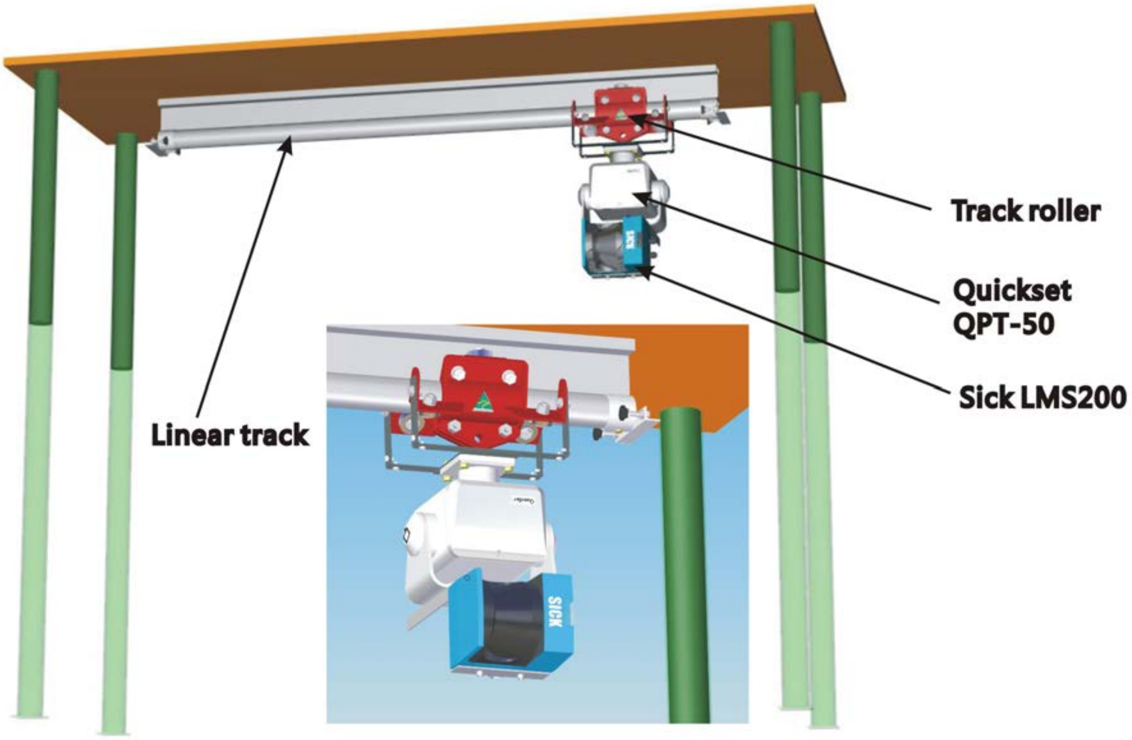

Fig. 3.11 A 3D drawing of the indoor laser scanning system used for laboratory scale stockpile scanning [56]

Both the LMS200 and the O1D100 are connected to a computer through RS232 protocols. An internal computer timer is created to synchronize the measurement data from both sensors. The recorded data are then represented in a 3D Cartesian coordinate system on the computer screen in real time through a GUI which is implemented in C#. Fig. 3.12 illustrates the orientations of the x, y and z-axes, as defined for scanning in the laboratory environment.

Based on this coordinate definition, the plane that lies in parallel to the YZ plane and passes through the centre of the stockpile is named the coronal plane. The plane that parallels to the XY plane and passes through the centre of the stockpile is named the sagittal plane. The plane that parallels to the XZ plane and passes through the bottom surface of the stockpile is named the transverse plane. More detailed coordinate definitions and kinematic equations of the laser scanning system are presented in Appendix A. The GUI plots the scanning data in real time and exports the data into three separated txt files (each file contains the measurements for one axis) after scanning.

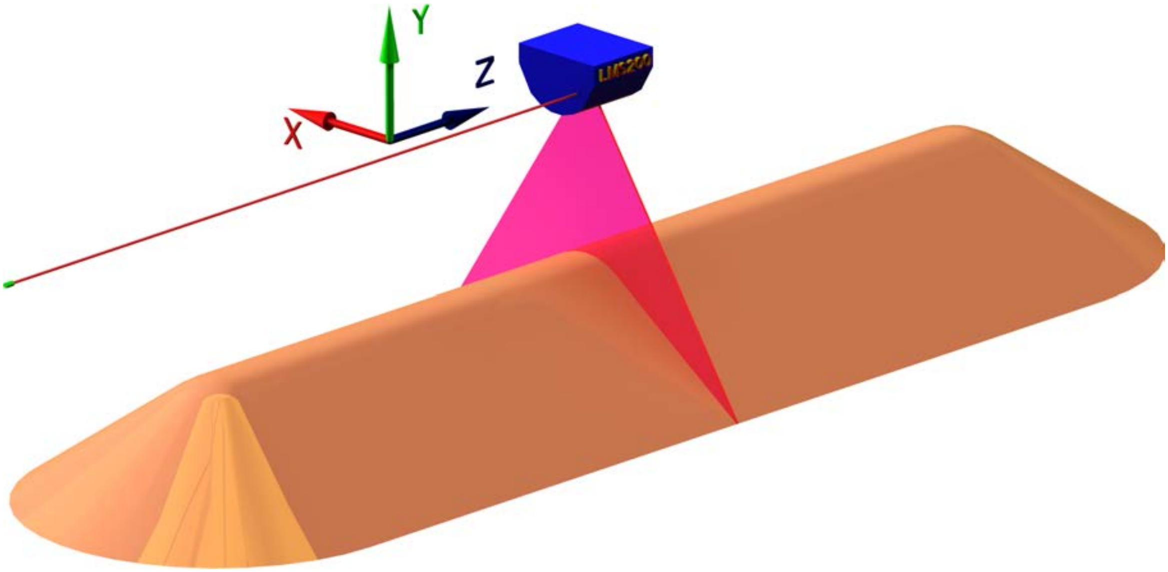

Fig. 3.12 Coordinator definition for stockpile modelling.

3.4.2 Preliminary Experiment

A pilot experiment was designed to build a cone shape stockpile for testing and calibration purpose. The stockpile was stacked using round quartz aggregate with a rough diameter of 7 mm but in three lots to create three layers. A temporary discharge chute with a frame was attached to the track roller to generate the material flow. The chute can hold a 6.6 kg quartz gravel maximum and the initial drop-height between the chute and supporting platform is 17.3 cm (see Fig. 3.13). In the experiment, a human operator fed pebbles into the chute manually and opened it once it was full. The observed average flow speed was 0.43 $kg/second$. When the stockpile was scanned by the laser, the chute and the frame were removed from the track roller. The scan range and the angular resolution used in the experiment is 100° and 0.25°, respectively.

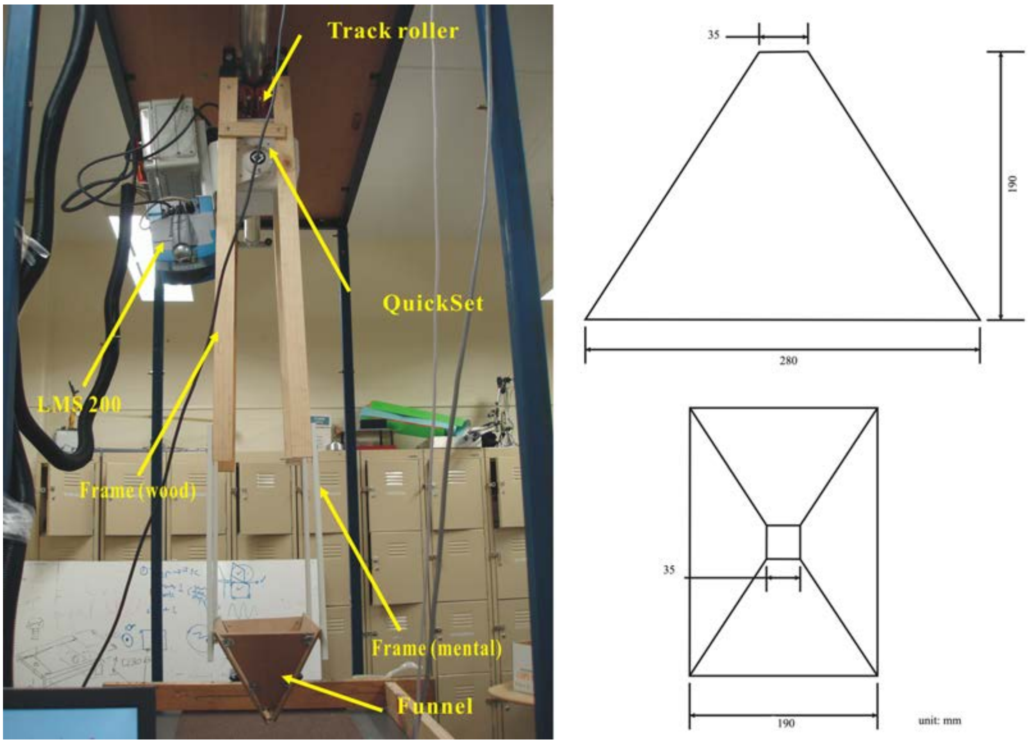

Fig. 3.13 Experiment setup and dimension of the discharge chute.

Table 3.4 shows the geometric shape and the weight of the stockpile measured by the human operator. Fig. 3.14, 3.15 and 3.16 draw the 3D surfaces of the three layers using the laser measurement data. For comparison purposes, the actual image and data cloud are also presented.

Table 3.4 Cone shape stockpile stacked using quartz aggregate.

Layer No.	Diameter (cm)	Height (cm)	Weight (kg)	Falling height (cm)
1	37	9.6	6.6	17.3
2	45	12	6.6	28.5
3	56	14.3	6.6	28.5

The preliminary experiment also identifies an inclined plane angle of 1.7° between the surface obtained from the laser measurement and the tabletop (the supporting platform), which can be seen in Fig. 3.17. The error source for such an inclined angle could be the imperfect

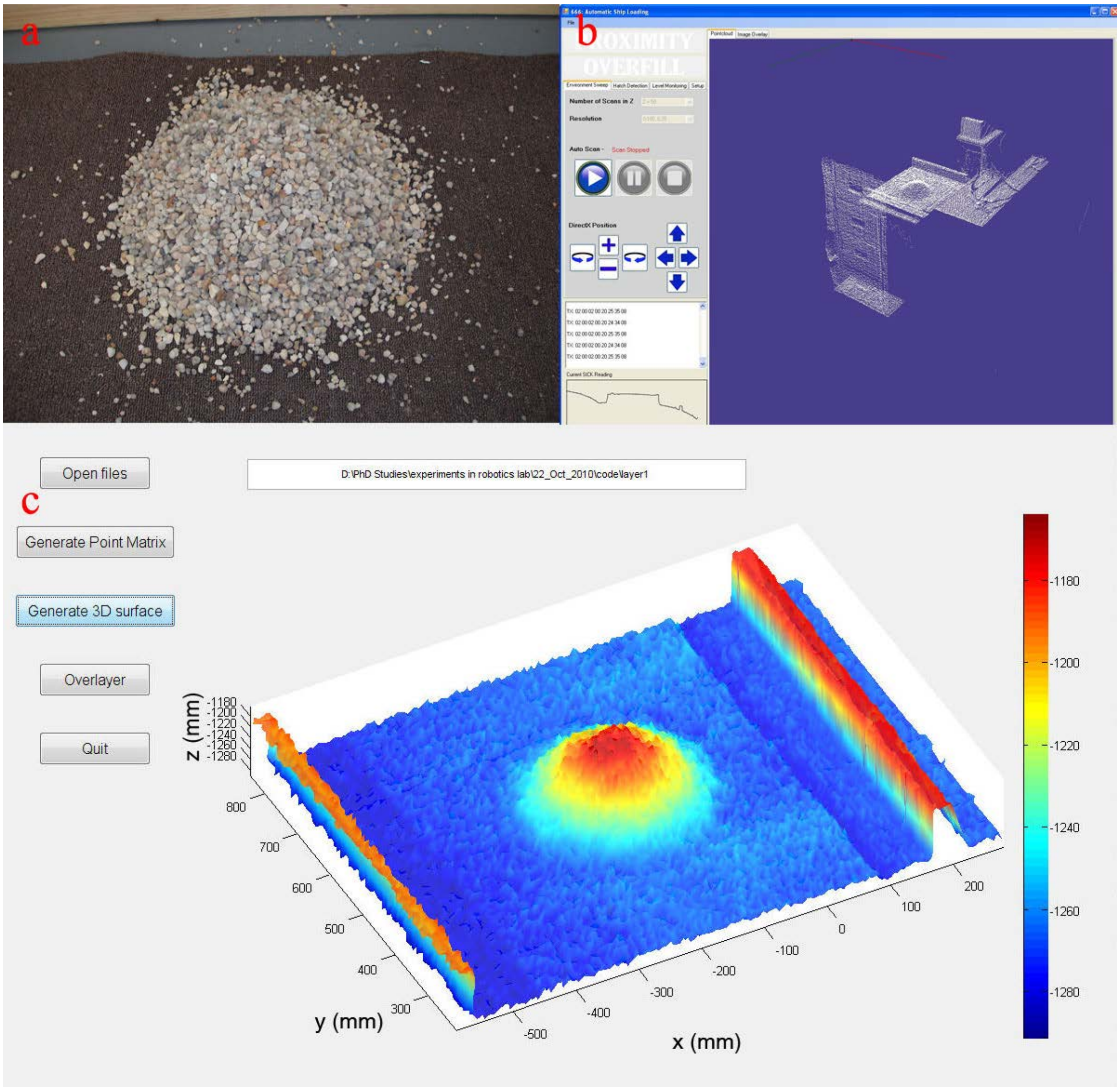

D:\PhD Studies\experiments in robotics lab\22_Oct_2010\code\layer1

Fig. 3.14 1st layer of the cone stockpile. a) real stockpile b) point data c) triangular surface.

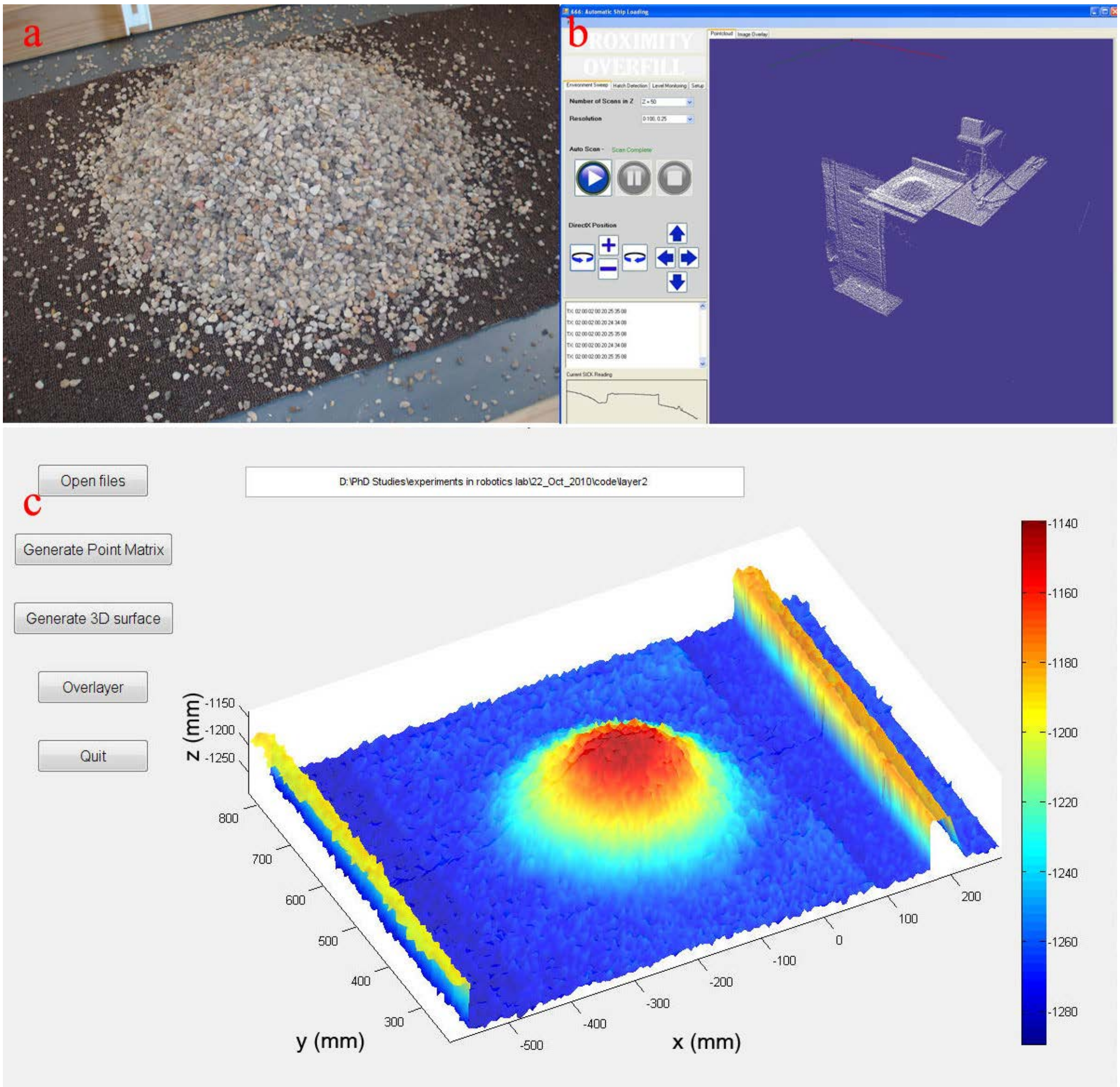

Number of Scans in Z: Z = 50
Resolution: 0.100, 0.25

```
TX: 02 00 02 00 20 25 35 08
TX: 02 00 02 00 20 24 34 08
TX: 02 00 02 00 20 25 35 08
TX: 02 00 02 00 20 24 34 08
TX: 02 00 02 00 20 25 35 08
```

D:\PhD Studies\experiments in robotics lab\22_Oct_2010\code\layer2

Fig. 3.15 2nd layer of the cone stockpile. a) real stockpile b) point data c) triangular surface.

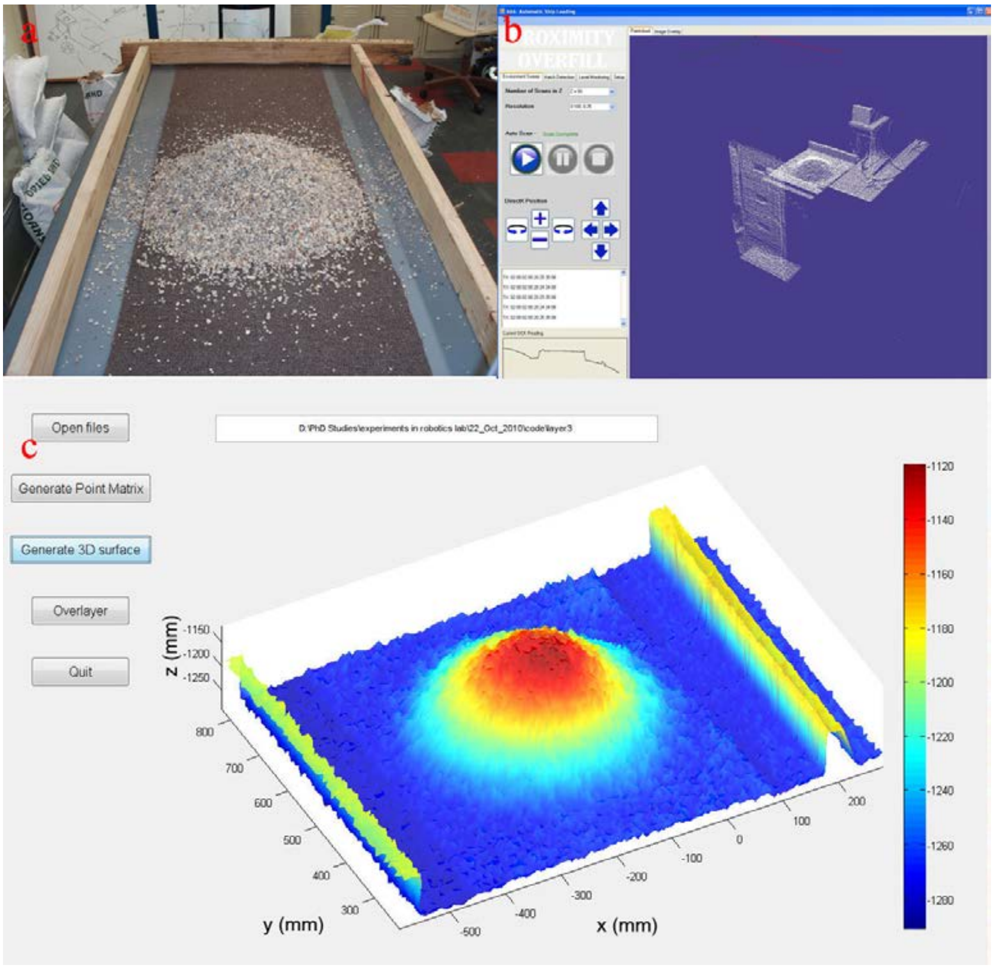

D:\PhD Studies\experiments in robotics lab\22_Oct_2010\code\layer3

Fig. 3.16 3rd layer of the cone stockpile. a) real stockpile b) point data c) triangular surface.

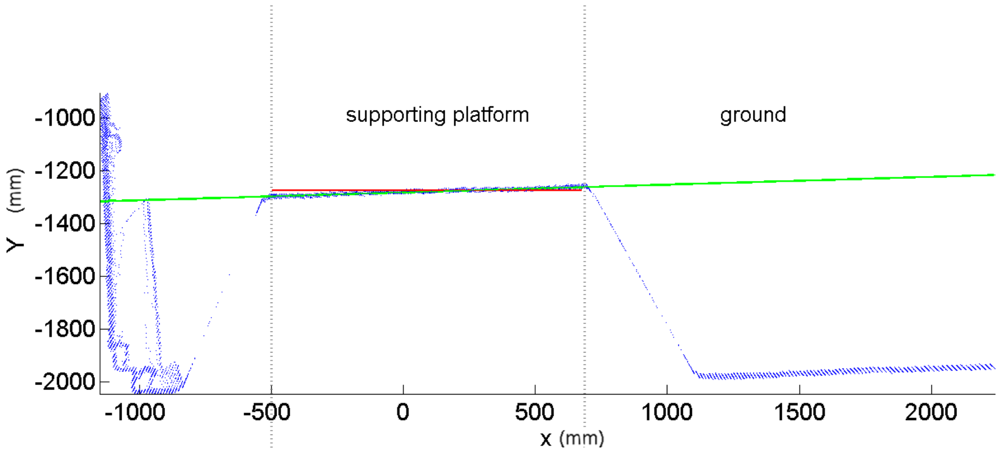

Fig. 3.17 Surface measured by the indoor 3DOF laser scanner. The red line indicates the true surface while the green line shows the fitting result.

mounting conditions or the measurement noise from the QPT-50 (to allow the LMS200 to face towards to the ground, the QPT-50 has to be rotated with an angle of 90°). This angle is compensated for before the laser measurements were converted from the polar coordinator to the Cartesian coordinator.

Laser measurement noise is also observed in the experiment. For example, in Fig. 3.17, points obtained from the tabletop are not on the same plane. Assuming the tabletop is a perfectly smooth surface, the standard deviation of the laser measurements are 1.45 *cm* on average. Also, it appears that the false returns (may also call phantom points [57] or mixed pixels [58]) occur when the laser beam hit the edge of an object. As shown in Fig. 3.17, these false returns exist on the both sides of the supporting platform. This is because that only a portion of the beam is reflected from platform, while another portion is reflected from the ground. Thus, it will create some phantom points between the two surfaces.

The results indicated that laser scanning performed quite well on determining the shape of the stockpile. Geometric information can be acquired more easily than the use of other sensors, such as a digital camera. Meanwhile, due to the wide availability in outdoor LiDAR scanners, algorithms developed in the study can be applied to real operation environments.

3.5 Summary

In this chapter, a BWR is proposed to be upgraded into a mobile laser scanner to measure the profiles of a stockpile when it stacks or reclaims the stockpile simultaneously. An UKF based sensor data fusion is detailed to localize the laser scanner. Simulation results indicate that the employment of a UKF can improve the positioning accuracy to better than 20 *cm*, which is acceptable and feasible considering the size of a real stockpile. In the meantime, an indoor laser system which has similar scanning mechanism of the mobile scanner is presented in the chapter. Preliminary experiments have been conducted to evaluate the laboratory scanning system. Point data collected after scanning show a good accuracy in terms of range and bearing measurement.

Chapter 4

Stockpile Modelling from Point Cloud Data

Point-sampled objects are flexible for handling highly complex or dynamically changing shapes. However, a loose representation for a stockpile with multiple layers will occupy valuable computer storage space. Additionally, such a data structure cannot be utilized for other applications directly, such as to assist in the collision detection between a BWR and a stockpile, or to estimate the quality of a stockpile from chemical analysis results, directly. This chapter describes a sequence of algorithms for automatic generation of mathematical surface models from 3D point clouds. These algorithms are evaluated by a variety of point clouds collected from different sources. The results prove the efficiency and accuracy of the proposed modelling algorithms.

4.1 Problem Statement

A point-based geometric representation of a stockpile is obtained through measuring the surface of a stockpile using a de-facto 3D Lidar scanner, as described in Chapter 3. Point data acquired after scanning are organized as three separate column vectors. Each column vector with O elements represents one axis in the Cartesian coordinate system. Therefore, a point representation of a stockpile in the 3D Cartesian space is a $O \times 3$ matrix $P(p_x, p_y, p_z)$. This matrix is so called a point cloud in this thesis.

A single scan is defined as an array of points obtained after one complete sweep of the laser beam. For instance, when the LMS200 performs a 100° sweep with an angular resolution of 0.25°, it will result in 401 points and these points form a single scan. Because the longitude movement of the BWR is much slower than the speed of light, these points are on the same plane that lies in parallel to the sagittal plane. Therefore, a point cloud that represents a complete measurement of a surface of a stockpile contains a collection of single scans and the planes formed by these single scans are parallel to each other. Accordingly, a column vector in a point cloud can be converted into an M-by-N matrix, where N is the number of the single scans in a point cloud and M is the number of points in one single scan. Obviously, O equals to $M \times N$. Thus, a point cloud is converted into three 2D measurement matrices X, Y and Z and each matrix represents the x, y and z coordinates respectively.The goal of surface modelling is to create a mathematical function S from a point cloud automatically to approximate the true stockpile surface. Based on the coordinates defined in Fig. 3.12, the surface model can be represented as a function $p_y = S(p_x, p_z)$.

The modelling procedure consists of three steps. The first step employs a curve fitting operation for every single scan completed by the laser. It aims to filter out the measurement noise and store scanning data using mathematical functions. At this step, each fitting operation requires a real-time response and noise filtering should not create a significant shrinkage effect. A wireframe model is generated after this step. The second step retrieves the point data from the wireframe model and partitions the point cloud into two subsets using image processing techniques: the ground and the stockpile subset. Points belonging to the ground represent the ground plane which also yields the height of the stockpile. Points in the stockpile subset will be used for surface modelling. The execution time of the segmentation algorithm also needs to meet the real-time stockpile modelling requirement. The last step builds a mathematical surface model from the point data. Only the coefficients of the mathematical functions are stored after modelling. Again, a good trade-off between the computation time and modelling accuracy is expected.

4.2 Wireframe Modelling from Raw Scanning Data

A real stockpile is around 100 ~ 200 m long and may contain more than 100 layers. When it is scanned by a LiDAR, it could result in much more than thousands of points. Therefore, it would be better to store these raw measurements using mathematical functions in real time for further processing. Therefore, a wireframe model is designed. In this model, every single scan accomplished by the LMS200 is fitted into the model by a Fourier series. Therefore, a single scan can be described by $2l+2$ coefficients, where l is the number of the terms in the Fourier expansion, which is also known as an order of the Fourier series. For this reason, a 4^{th} term Fourier series is called a 4^{th} order Fourier series, or a 4^{th} Fourier series for short. In turn, a wireframe model created by a group of 4^{th} Fourier functions is called a 4^{th} Fourier model in short. Another benefit of Fourier approximation is that it acts as a low-pass filter that smooths the measurement noise but will not produce an obvious shrinkage effect. A Fourier series representation of a single scan is given by:

$$\begin{aligned} y &= f(x, a_0, a_1, ..., a_n, b_1, ..., b_n) \\ &= a_0 + \sum_{n=1}^{l} (a_n \cos n\omega x + b_n \sin n\omega x) \end{aligned} \tag{4.1}$$

where $a_0, a_1, ..., a_n, b_1, ..., b_n and \omega$ are the Fourier coefficients. A least square regression for Fourier coefficients estimation is to minimize the residual sum of squares E:

$$E^2 \equiv \sum_{i=1}^{M} w(x_i)(f(x_i - y_i))^2 \tag{4.2}$$

where M is the number of measurements taken by the LMS200 in a single scan, $w(x_i)$ is the weight function and default value is 1. This minimum requires:

$$\begin{aligned} &\frac{\partial E}{\partial a_0} = 0, \frac{\partial E}{\partial a_1} = 0, ..., \frac{\partial E}{\partial a_n} = 0 \\ &\frac{\partial E}{\partial b_1} = 0, ..., \frac{\partial E}{\partial b_n} = 0 \\ &\frac{\partial E}{\partial \omega} = 0 \end{aligned} \tag{4.3}$$

Equation 4.3 can be solved using the trust-region-reflective method [59], which is an improved version of the Newton iterative method. To shorten the runtime of the iterative searching, an initial value of a_0 and ω is estimated, while other high order coefficients are not, because from the signal processing point of view, the shape of the signal is largely determined by the direct component a_0 and fundamental frequency ω. The initial guess is based on the ideal triangular prism model of a real stockpile. Because the height of a stockpile and the repose angle of a particular bulk material are always easy to obtain in advance, the initial value of a_0 and ω can be solved if the cross-section of a stockpile is considered as a non-periodic triangular wave. By setting the searching range in the iteration, the speed of convergence of the trust-region-reflective method is further improved. Fig. 4.1 plots a single scan and the Fourier curve fitted by an 8th order Fourier series.

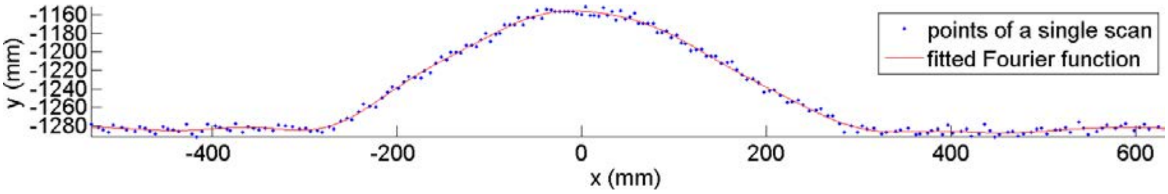

Fig. 4.1 The fitted Fourier curve of a single scan. The sum of squared error (SSE) is 2.422×10^3 and the R-square is 0.9949.

A linear stockpile stacked using the chevron method has two semi-conical ends and a middle section. The parasagittal cross sections (sliced by the planes lying in parallel to the sagittal plane) of the middle section always have similar shapes. Furthermore, due to the noise of the laser range measurements, the parasagittal cross sections are not aligned according to the coronal plane. This is because both the x and y coordinates of a single scan are converted from the range measurement. These errors will shift each scan slightly along the x and y axis in a random manner. Thus, a universal Fourier model is generated to further filter out such errors and to reduce the parameters in a wireframe model.

In the universal Fourier model, parasagittal cross sections which are highly similar in shapes are described by one Fourier series. In other words, a collection of N_u single scans is represented by one Fourier series. For example, if a stockpile is at the awaiting reclaiming phase, its profiles along the entire middle section will have similar shapes and be fitted by one Fourier series using the universal Fourier model. If a stockpile is at the reclaiming phase, the unreclaimed section still can be described by one Fourier series. Using this model, the number of parameters needing to be stored and processed can be reduced greatly. To obtain such a generic Fourier curve, it is necessary to minimize the residual sum of squares E for a collection of N_u single scans:

$$E^2 \equiv \sum_{k=1}^{N_u} \sum_{i=1}^{M} w(x_{k,i})(f(x_{k,i} - y_{k,i}))^2 \tag{4.4}$$

where $f(x_{k,i})$ is the Fourier series and defined by Eq. 4.1 and $w_{k,i}$ is the weight function and its default value is 1. Again, to minimize E is to assign the gradient defined in Eq. 4.3 to zero. In real practice, the Fourier curve determined by the trust-region-reflective algorithm sometimes fails to find the global minimum in resolving these nonlinear equations. The iteration terminates when a local minimum is found. For this specific problem, an optimized iterative searching strategy is proposed. Because the fundamental frequency ω for each single scan is obtained during the Fourier modelling procedure, a searching range [ω_{min}, ω_{max}] can be defined. For a ω within this range, the gradient equations can be rewritten as:

$$
\begin{aligned}
\frac{\partial E}{\partial a_0} &= \frac{\partial \sum\limits_{k=1}^{N_u} \sum\limits_{i=1}^{M} (f(x_{k,i} - y_{k,i}))}{\partial a_0} = 0 \\
\frac{\partial E}{\partial a_n} &= \frac{\partial \sum\limits_{k=1}^{N_u} \sum\limits_{i=1}^{M} (\cos n\omega (x_{k,i} - y_{k,i}))}{\partial a_n} = 0 \\
\frac{\partial E}{\partial b_n} &= \frac{\partial \sum\limits_{k=1}^{N_u} \sum\limits_{i=1}^{M} (\sin n\omega (x_{k,i} - y_{k,i}))}{\partial b_n} = 0
\end{aligned}
\tag{4.5}
$$

A matrix representation of Eq. 4.5 is:

$$
\begin{aligned}
D &= \begin{vmatrix}
N_u M & \sum\sum C\omega x_{k,i} & \cdots & \sum\sum Cl\omega x_{k,i} & \sum\sum S\omega x_{k,i} & \cdots & \sum\sum Sl\omega x_{k,i} \\
\sum\sum C\omega x_{k,i} & \sum\sum C\omega x_{k,i} C\omega x_{k,i} & \cdots & \sum\sum C\omega x_{k,i} Cl\omega x_{k,i} & \sum\sum C\omega x_{k,i} S\omega x_{k,i} & \cdots & \sum\sum C\omega x_{k,i} Sl\omega x_{k,i} \\
\vdots & \vdots & \vdots & \vdots & \vdots & \vdots & \vdots \\
\sum\sum Cl\omega x_{k,i} & \sum\sum Cl\omega x_{k,i} C\omega x_{k,i} & \cdots & \sum\sum Cl\omega x_{k,i} Cl\omega x_{k,i} & \sum\sum Cl\omega x_{k,i} S\omega x_{k,i} & \cdots & \sum\sum Cl\omega x_{k,i} Sl\omega x_{k,i} \\
\sum\sum S\omega x_{k,i} & \sum\sum S\omega x_{k,i} C\omega x_{k,i} & \cdots & \sum\sum S\omega x_{k,i} Cl\omega x_{k,i} & \sum\sum S\omega x_{k,i} S\omega x_{k,i} & \cdots & \sum\sum S\omega x_{k,i} Sl\omega x_{k,i} \\
\vdots & \vdots & \vdots & \vdots & \vdots & \vdots & \vdots \\
\sum\sum Sl\omega x_{k,i} & \sum\sum Sl\omega x_{k,i} C\omega x_{k,i} & \cdots & \sum\sum Sl\omega x_{k,i} Cl\omega x_{k,i} & \sum\sum Sl\omega x_{k,i} S\omega x_{k,i} & \cdots & \sum\sum Sl\omega x_{k,i} Sl\omega x_{k,i}
\end{vmatrix} \\
U &= \begin{vmatrix} a_0 & a_1 & \cdots & a_l & b_1 & \cdots & b_l \end{vmatrix}^T \\
V &= \begin{vmatrix} \sum\sum y_{k,j} & \sum\sum C\omega x_{k,i} y_{k,j} & \cdots & \sum\sum Cl\omega x_{k,i} y_{k,j} & \sum\sum S\omega x_{k,i} y_{k,j} & \cdots & \sum\sum Sl\omega x_{k,i} y_{k,j} \end{vmatrix}^T
\end{aligned}
\tag{4.6}
$$

where C represents cos and S represents sin. $\sum\sum$ means $\sum\limits_{k=1}^{N_u} \sum\limits_{i=1}^{M}$. Thus, the remainder of the Fourier coefficients can be calculated by:

$$
U = (D^T D)^{-1} D^T V \tag{4.7}
$$

Also, U can be considered as a function of ω:

$$
U = F(\omega) \tag{4.8}
$$

Based on Eq. 4.7 and 4.8, the global minimum can be found using iteration searching when the trust-region-reflective method fails to identify the global minimum (see Fig. 4.2).

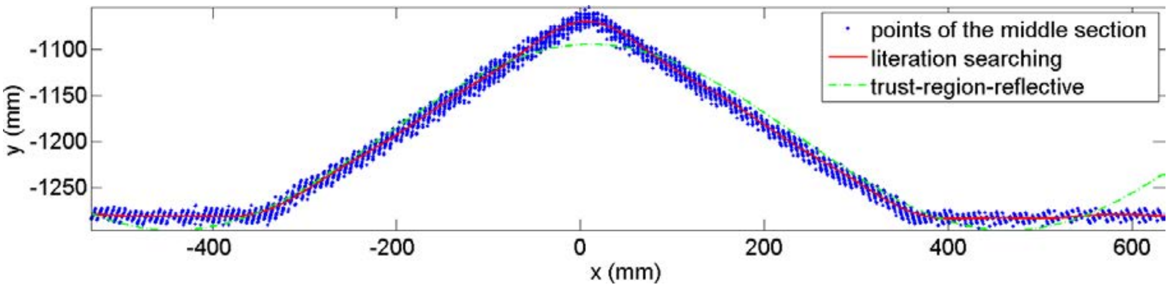

Fig. 4.2 Locating the global minimum using optimized iteration searching. The middle section of the stockpile contains 68 single scans.

The data regenerated from the wireframe model has the same structure as the original scanning data. Therefore, it is still called the point cloud but denoted by $P_w(P_{w\_x}, P_{w\_y}, P_{w\_z})$. The letter after the underscore in the subscript denotes the axis of abscissas. Again, P_w can be converted into three 2D matrices: X_w, Y_w and Z_w.

4.3 Point Cloud Segmentation

For modelling and quality estimation purposes, a point cloud has to be segmented in order to detect the stockpile surface (region) and the ground (region). A highly precise and accurate detection algorithm is not necessary for this application because the bottom region of a stockpile near the ground will not be reclaimed using a BWR due to safety reasons. Conversely, the segmentation algorithm needs to be fast and fully automatic. The proposed method is based on mathematical morphology operations, which have been proven to be successful by the author to detect objects from sonar images [60].

The boundary detection algorithm takes the matrix Y_w as an input and converts it into a grey image through Eq. 4.9. Then, the grey image is thresholded into a binary image using the Otsu's algorithm [61]. After thresholding, mathematical morphology erosion and dilation are applied to separate and label foreground regions from the binary image. With the understanding that the largest foreground object in the binary image is the stockpile, the rest of the foreground objects are assigned collectively to be the background object (ground). Finally, the edge of the stockpile is detected through tracking the boundary of the foreground object. The detection result is mapped into X_w and Z_w matrices directly, since their indices are the same. Thus, the point cloud data can be partitioned into two submatrices: the stockpile surface submatrix (F_s) and the ground submatrix (B_g). The overall procedure of the proposed segmentation method is shown in Fig. 4.3 and the detection result is plotted in Fig. 4.4. Although the proposed segmentation method seems simplistic, it is fast and effective. Also, it is applicable to differently shaped stockpiles through changing the structuring element in the mathematical morphology operations. More results will be presented in the experiment and result section of this chapter.

$$Y_{grey} = \frac{255Y_w}{max(Y_w) - min(Y_w)} - min(Y_w) \tag{4.9}$$

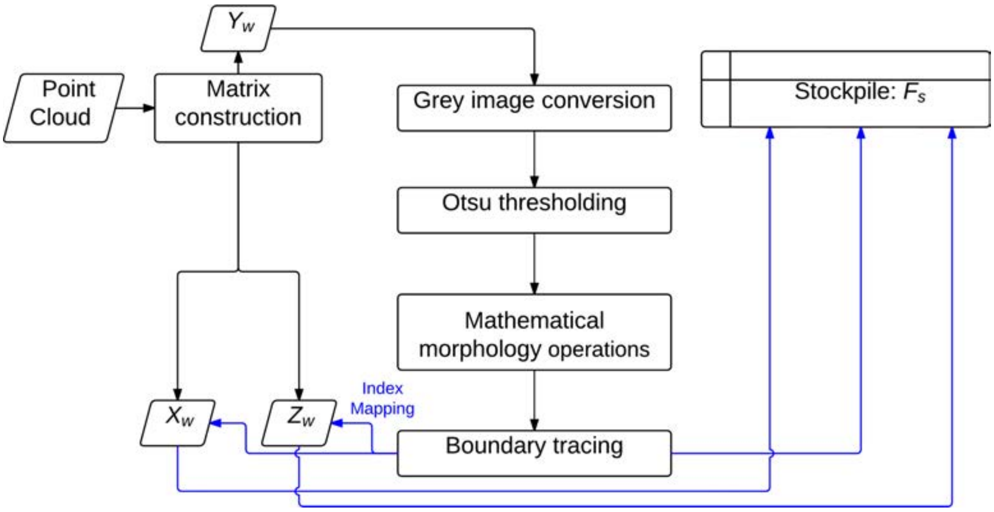

Fig. 4.3 Point segmentation and boundary detection using image processing.

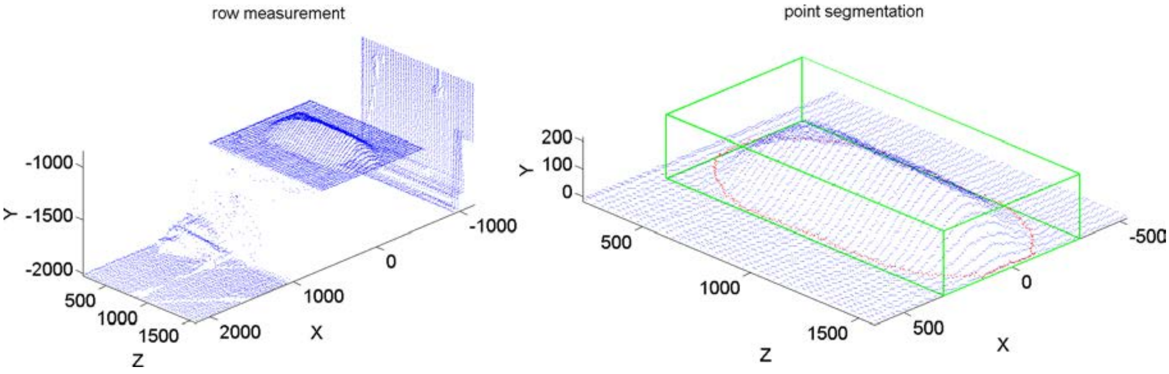

Fig. 4.4 Point segmentation result. The identified boundary is highlighted in red. The minimal bounding box created based on the stockpile boundaries is highlighted in green. Points inside the bounding box belong to the stockpile region subset S_r.

After segmentation, the average distance D_{avg} between the ground and the laser is calculated from B_g. Thus, the transverse plane of the stockpile is determined and elevation of the stockpile is obtained through coordinate transformations. Meanwhile, the y coordinates in B_g are all marked as zero during the transformations. A minimum bounding box for F_s is created and the points inside the minimum bounding box form a new subset (S_r), called the stockpile region subset (see Fig. 4.4). Points in this subset will be used for the stockpile modelling. The relationships between these point sets are: $F_s \subset P$, $B_g \subset P$, $F_s \cap B_g = \varnothing$, $F_s \cup B_g = P$, $F_s \subset S_r$.

4.4 Surface Modelling

The objective of surface modelling is to utilize geometric information for stockpile quality estimations and BWR automation. Consequently, the modelling algorithm is expected to have an ideal trade-off between the modelling accuracy and computational efficiency. More importantly, for such an industrial applications, the modelling is expected to reduce computation time and achieve near real-time implementation. Therefore, surface reconstruction algorithms created for medical imaging or computer aided design (CAD), which focus on the representation of highly detailed geometric features and incurs a huge runtime cost, such as matching cubes [62] and ball pivoting [63] are not considered. In this section, two different mathematical models (polynomial approximation and B-spline interpolation) are presented. The distinction between the two methods is that the approximation aims to find a function to conform as closely as possible to the given point cloud, while the interpolation tries to find a function that passes through the given data points as much as possible. The reasons for creating two mathematical models will be given at the end of this chapter.

4.4.1 Polynomial Approximation

Polynomial approximation aims to generate a polynomial surface function using the least square method from laser measurement (the subset S_r). The polynomial function S of an ordered pair p and q along the x and z axis is:

$$y = S(x,z) = \sum_{i=0}^{p} \sum_{j=0}^{q} a_i a_j x^i z^j \tag{4.10}$$

where $a_i a_j$ is the coefficient of the polynomial function; x, y and z are laser measurement in the Cartesian coordinator and $x = S_{r\_x}$,$y = S_{r\_y}$,$z = S_{r\_z}$. The order means the highest order power in a univariate polynomial function. Although p and q are not necessary to be equal, they are assigned to be identical here because no obvious difference is observed between a same-ordered pair and a differently-ordered pair during modelling. The degree of the polynomial surface will be the polynomial order p minus one ($d = p - 1$). In this thesis, the term order is used to describe a specific polynomial function while the term degree is used to present a model after fitting. For example, a 6th degree polynomial surface model is created from the 7th order polynomial function. A least square regression for polynomial surface fitting is to:

$$E \equiv \sum_{k=1}^{n} w(x_k, z_k)[\sum_{i=0}^{p}\sum_{j=0}^{q} a_i a_j x^i z^j - y]^2 = min \tag{4.11}$$

where $w(x_k, z_k)$ is the weight function and its default value is equal to 1. To minimize the squared residual, the partial derivatives are set equal to be 0. The derivatives can be rewritten into a form similar to Eq. 4.6 and yield to a Vandermonde matrix:

$$\begin{vmatrix} 1 & x_1 & z_1 & x_1 z_1 & x_1^2 z_1 & x_1 z_1^2 & \cdots & x_1^{p-1} z_1^{q-1} \\ 1 & x_2 & z_2 & x_2 z_2 & x_2^2 z_2 & x_2 z_2^2 & \cdots & x_2^{p-1} z_2^{q-1} \\ \vdots & \vdots & \vdots & \vdots & \vdots & \vdots & \ddots & \vdots \\ 1 & x_n & z_n & x_n z_n & x_n^2 z_n & x_n z_n^2 & \cdots & x_n^{p-1} z_n^{q-1} \end{vmatrix} \begin{vmatrix} a_0 a_0 \\ a_1 a_1 \\ \vdots \\ a_{p-1} a_{q-1} \end{vmatrix} = \begin{vmatrix} y_1 \\ y_2 \\ \vdots \\ y_n \end{vmatrix} \Rightarrow D \times U = V \tag{4.12}$$

Similar to the Fourier model, the coefficient matrix U can be calculated using the matrix notation listed in Eq. 4.7.

Generally, the use of a higher order polynomial function will improve the fitting accuracy. However, Runge's phenomenon [64], which describes the oscillation around the edges of the data when constructing a polynomial interpolating using high order functions, is observed frequently when the order of the function is higher than ten. Also, due to the geometric complexity of a real stockpile during blending, the use of one polynomial function may not obtain the best modelling result. To avoid Runge's phenomenon and improve the modelling accuracy, the matrix S_r is subdivided into a set of rectangular patches (R_p) through a checkerboard pattern and then each patch is fitted by a polynomial function. In this chapter, the size of each patch is calculated based on the size of the measurement matrix. Because the geometric complexity of each surface patch is reduced after subdivision, even a low order function can produce a good fit. As shown in Fig. 4.5, Runge's phenomena happen around four corners of the stockpile region when a 10th order polynomial function is used. Conversely, Runge's phenomenon is not obvious in the (6th, 4×4) polynomial model and the residuals of this model are much less than the 9th degree polynomial model.Surface models created using this method are referred to as $n_p \times n_p$ patch polynomial models, where n_p is the number of the patches after the partition. Thus, the full name of a polynomial model will be a d^{th} degree, $n_p \times n_p$ grid polynomial surface model and the abbreviation is a (d^{th}, $n_p \times n_p$) polynomial model. Also, if a surface model is created from the measurement data directly, it can still be considered to be partitioned by a 1×1 grid.

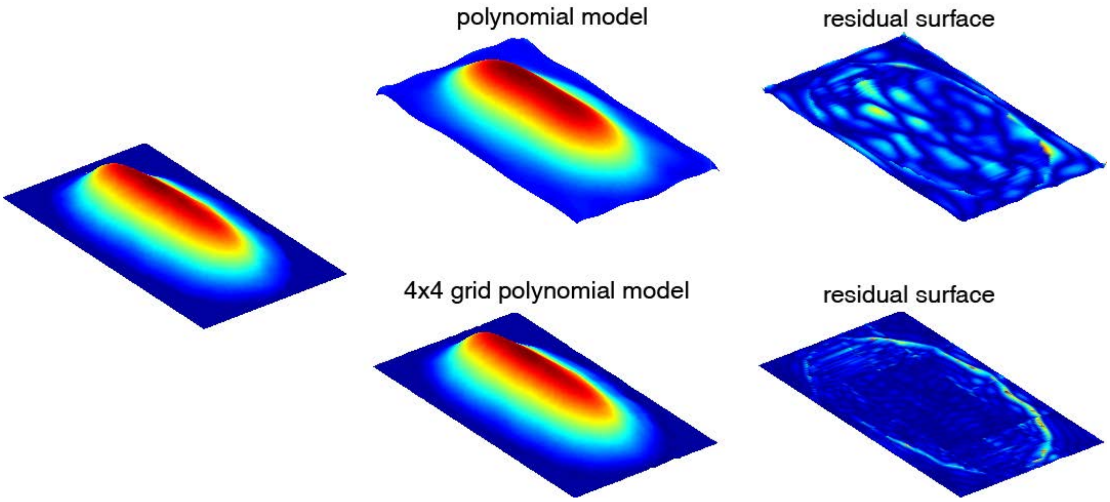

Fig. 4.5 Grid partitioning reduces the residuals and avoids Runge's phenomenon.

Grid partitioning improves the modelling accuracy but the over-fitting problem then arises. Since each patch contains only a small amount of data, the measurement matrix D is prone to be ill-conditioned or close to singular. If D is ill-conditioned or close to singular, the inversion of the Gramian matrix $(D^T D)^{-1}$ will add quite significant numerical noise to the solution and result in over-fitting. It has also been detected that when D is constructed from the patch which is located around the stockpile boundary, it is more liable to be ill-conditioned or close to singular. The main reason for such a situation is the nature of the measurement data. It is easy to imagine that a patch around the boundary of the stockpile always contains both the stockpile surface and the ground. The y coordinates for those ground (points) are all zeros and the y coordinates for the stockpile surface (points) are very close to zero. Furthermore, due to the sensor noise, these y coordinates may fluctuate by $10 \sim 20\ mm$ around the true measurements. The combination of these three conditions may cause an ill-conditioned or close to singular matrix and lead to an over-fitting problem.

To avoid the over-fitting caused by an ill-conditioned or close to singular matrix, point data on the surface patch are centred and normalized before fitting. However, over-fitting events still happen occasionally. In some extreme cases, the fitted model is very chaotic and peak-to-peak difference can reach up to three orders of magnitude (see Fig. 4.6). Therefore, a surface normal comparison algorithm is proposed to detect the over-fitted patch automatically. For a given rectangular patch R_p ($R_p \subset S_r$) with a centre point of o, its k-nearest neighbours can be calculated and a point set $N_{CenNeig}$ is constructed through gathering o and its k nearest points from R_p, where k is a user-specified parameter and its default value is 8. Then, a least square plane (the best fitting plane) is fitted from the point set $N_{CenNeig}$ and the normal vector $\hat{n}$ at the point o of the plane is called the estimated surface normal of the patch. Similarly, the estimated surface normal of the polynomial model can be also calculated. Because an over-fitted model contains too many idiosyncrasies and has a high variance in shape, the directions of these two estimated vectors will be different. The evaluation criterion is that if the angle between two vectors is larger than 5°, over-fitting is believed to have occurred. Under such circumstance, the order of the fitting function will be reduced by one until no over-fitting is detected.

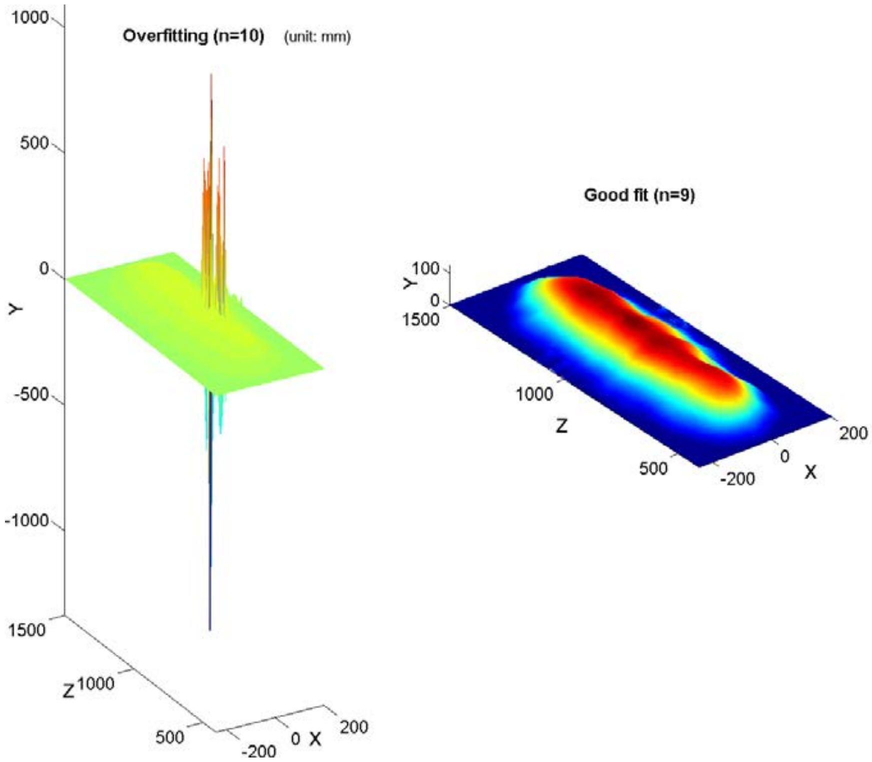

Fig. 4.6 Over-fitting is detected automatically through the comparison of the surface normal vectors before and after modelling. Also, through reducing the order of the polynomial function, over fitting condition can be avoid.

4.4.2 B-Spline Interpretation

The tensor product B-spline is one of the most popular surface interpolation methods in computer graphics and reverse engineering. It aims to produce an interpolated surface function that is continuous through to the second derivative and pass through all observation data. However, because the point cloud data obtained from laser scanning contain errors, a least square fitting process is still required for B-spline modelling. A tensor product B-spline surface $S(u,v)$ is defined by a 2D control net Q_{ij} ($0 \leqslant i \leqslant m$ and $0 \leqslant j \leqslant n$) together with a vector-valued function of two parameter B-splines, u and v (in this case, u and v represent the x and z axis, respectively):

$$S(u,v) = \sum_{i=0}^{m} \sum_{j=0}^{n} N_{i,d_i}(u) N_{j,d_j}(v) Q_{i,j} \tag{4.13}$$

where the d_i and d_j are the degrees for the surface function and $0 \leqslant d_i \leqslant m$ and $0 \leqslant d_j \leqslant n$ (of the spline order = $m+1$ or $n+1$). Again, m and n are assigned to be identical in this thesis. $Q_{i,j}$ are the control points and function $N_{i,d_i}(u)$ and $N_{i,d_i}(u)$ are the B-Spline basis functions. These basis functions can be defined reclusively through a sequence of non-decreasing real numbers called knot vector, i.e. knot vector $U = [u_0, \cdots, u_m]$ and $V = [v_0, \cdots, v_n]$. Each $u_i(v_j)$ is referred to as a knot and $u_i \leqslant u_{i+1}$, $i = 0, \cdots, m-1 (v_i \leqslant v_{i+1}$, $j = 0, \cdots, n-1)$. Such a recursive B-Spline function is called Cox-De Boor relations [65]. A basic spline function defined by the vector u is:

$$N_{i,d_0}(u) = \begin{cases} 0 & u_i \leqslant u \leqslant u_{i+1} \\ 1 & otherwise \end{cases} \tag{4.14}$$

$$N_{i,d_i}(u) = \frac{u - u_i}{u_{i+d_i}} N_{i,d_i-1}(u) + \frac{u_{i+d_i+1} - u}{u_{i+d_i+1} - u_{i+1}} N_{i+1,d_i-1}(u) \tag{4.15}$$

where $N_{i,0}(u)$ is a step function, equal to zero everywhere except on the half open interval $u \in [u_i, u_{i+1})$, and for a $d(d>0)$, $N_{i,d}(u)$ is a linear combination of two $(d_i - 1)$-degree basis functions [66]. According to such a definition, the knot vector U completely determines the functions $N_{i,d_i}(u)$ once the degree of the function is fixed. The knot vector can be either periodic or non-periodic (open). Regarding the geometric shape of a real stockpile, the knot vector used for the surface model is non-periodic and it is determined by the centripetal method [67]. The idea behind the centripetal method is that the normal acceleration (i.e., centripetal force) should not be too large and should be proportional to the change in angle when a car is driven through a sharp corner. Suppose there are m_u knots along the x axis of the stockpile region $[a,b]$ that was obtained from previous boundary detection results and $a = min(x)$, $b = max(x)$, the distance between two adjacent data points is measured by $|D_k - D_{k-1}|^\alpha$ rather than the true distance $|D_k - D_{k-1}|$. Usually, $\alpha = 1/2$ for square root. The total length of the data polygon L is:

$$L = \sum_{i=1}^{m_u} |D_i - D_{i-1}|^{\frac{1}{2}} \tag{4.16}$$

The ratio of the distance from the data point D_0 to D_k, denoted as L_k (k=1,...,m+d-1) over the total length is:

$$L_k = \frac{\sum\limits_{i=1}^{k} |D_i - D_{i-1}|^{\frac{1}{2}}}{L} \tag{4.17}$$

Therefore, the knots for vector u are:

$$\begin{cases} u_0 & = & a \\ u_k & = & a - L_k(a-b) \\ u_m & = & b \end{cases} \tag{4.18}$$

Similar spline definitions are also applicable to the vector v. Thus, $N_{i,d_i}(u)$ and $N_{j,d_j}(v)$ are obtained and the coefficients of the spline surface (control point $Q_{i,j}$ in a matrix format is:

$$Q = \begin{bmatrix} Q_{00} & \cdots & Q_{0n} \\ \vdots & \ddots & \vdots \\ Q_{m0} & \cdots & Q_{mn} \end{bmatrix}$$

And the point cloud data that represents the stockpile can be also arranged as a matrix:

$$P = \begin{bmatrix} Q_{00} & \cdots & Q_{0q} \\ \vdots & \ddots & \vdots \\ Q_{p0} & \cdots & Q_{pq} \end{bmatrix}$$

The least square error function that measure the square distance between the B-spline surface and a point cloud is:

$$E^2 \equiv \sum_{k_0=0}^{p} \sum_{k_1=0}^{q} \left| \sum_{i=0}^{m} \sum_{j=0}^{n} N_{i,d_i}(u_{k_0}) N_{j,d_j}(v_{k_1}) - P_{k_0k_1} \right|^2 \tag{4.19}$$

Similar to classic least square fitting, the solution to Eq. 4.19 is the control point matrix Q that minimizes E. The global minimum occurs when all its first order partial derivatives are zero:

$$\begin{aligned}
\frac{\partial E}{\partial Q_{k_0k_1}} &= \sum_{k_0=0}^{p} \sum_{k_1=0}^{q} \left(\sum_{i=0}^{m} \sum_{j=0}^{n} N_{i,d_i}(u_{k_0}) N_{j,d_j}(v_{k_1}) Q_{ij} - P_{k_0k_1} \right) N_{k_0,d_i}(u_{k_0}) N_{k_1,d_j}(v_{k_1}) = 0 \\
&= \sum_{k_0=0}^{p} \sum_{k_1=0}^{q} \sum_{i=0}^{m} \sum_{j=0}^{n} N_{i,d_i}(u_{k_0}) N_{j,d_j}(v_{k_1}) N_{k_0,d_i}(u_{k_0}) N_{k_1,d_j}(v_{k_1}) Q_{ij} \\
&- \sum_{k_0=0}^{p} \sum_{k_1=0}^{q} N_{k_0,d_i}(u_{k_0}) N_{k_1,d_j}(v_{k_1}) - P_{k_0k_1} = 0
\end{aligned} \tag{4.20}$$

Let $a_{k_0,i} = N_{k_0,d_i}(u_{k_0})$ and $a_{k_1,j} = N_{k_1,d_j}(u_{k_1})$, a matrix format for Eq. 4.20 is:

$$\frac{\partial E}{\partial Q_{k_0k_1}} = A^T A Q B^T B - APB = 0 \tag{4.21}$$

where A is a $(p+1) \times (m+1)$ and B is a $(q+1) \times (n+1)$ matrix, respectively. The solution for the coefficients matrix Q is:

$$Q = [(A^T A)^{-1}] P [B(B^T B) B^T]^T \tag{4.22}$$

Because a spline presents a sufficiently high degree of smoothness, a B-spline model offers great flexibility and precision for handling complex geometric shapes. Consequently, grid partitioning is not necessary for B-spline modelling. During the modelling, the stockpile region is fitted by two sets of basic spline functions in the x then the z direction, in order. The name of a B-spline surface model still follows the previous naming method. An m^{th} degree B-spline surface model or an m^{th} B-spline model in short means the order of the B-spline function is $m+1$. If the model is created after grid partitioning, it is called an (m^{th}, $n_p \times n_p$) B-spline model. Fig. 4.7 shows a stockpile surface model created using a six-degree spline function in both directions. The proposed over-fitting detection algorithm is also applicable to the B-spline modelling. However, no over-fitting problem occurs using the experimental data. The entire set of modelling procedures is summarized in Fig. 4.8.

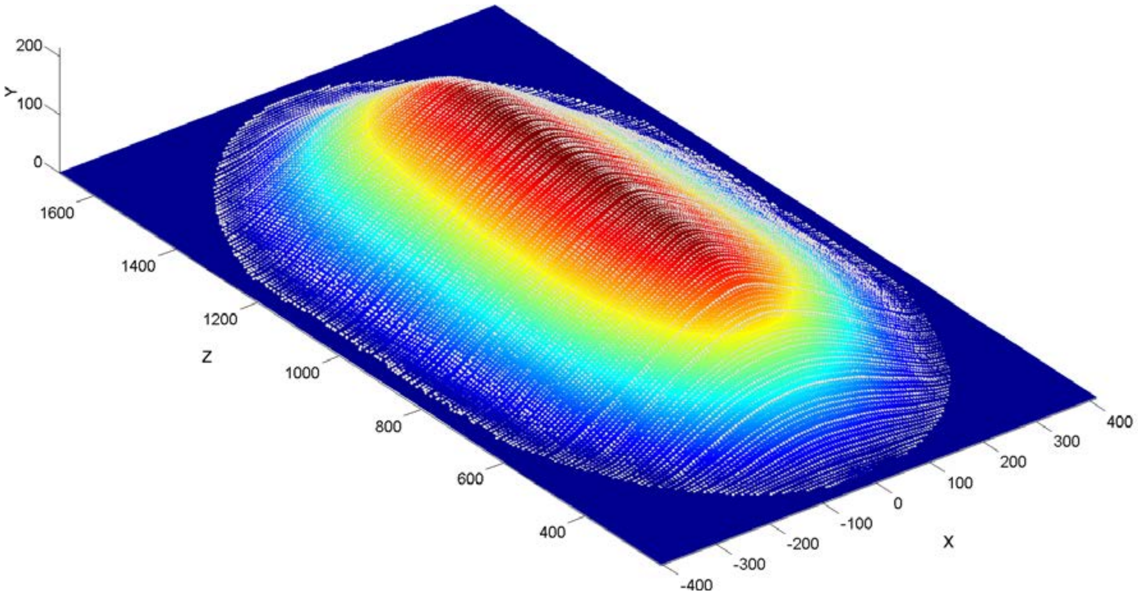

Fig. 4.7 A (6^{th}, 1×1) B-spline surface model. The point cloud is plotted as white dotted points against it (unit: mm).

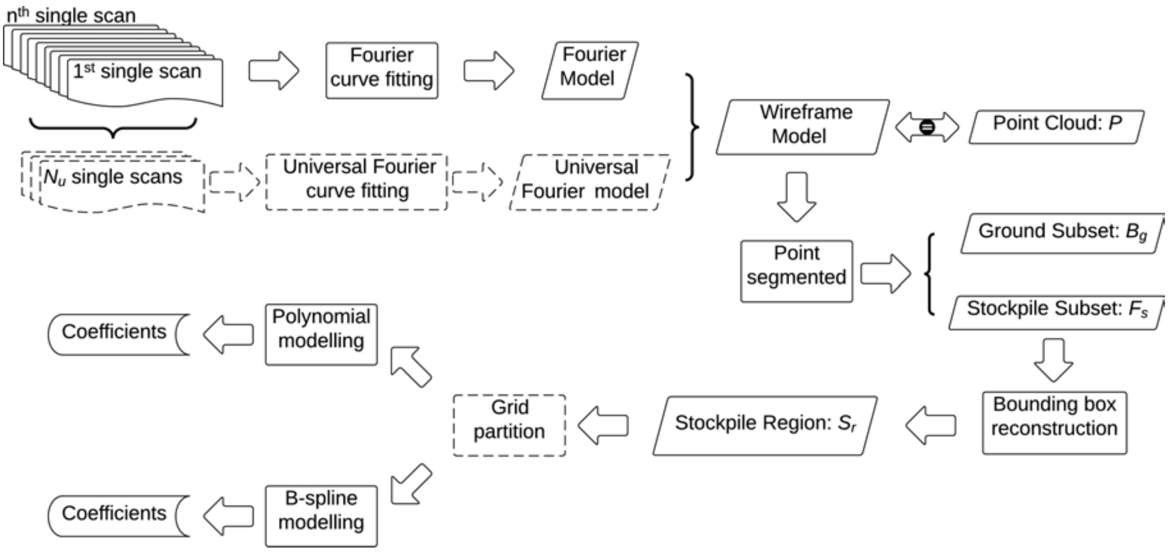

Fig. 4.8 Stockpile modelling procedure from laser measurement data. The data and operations illustrated by dotted lines are optional.

4.5 Experiments and Results

This section first outlines the experimental design and then presents the modelling results. A group of four datasets are prepared to evaluate the modelling algorithm. The parameters used to evaluate the surface modelling accuracy includes: the sum of squared errors (SSE)of prediction , the mean squared error (MSE) and the volume of the surface model.

4.5.1 Data Preparation

First, an isosceles triangular prism is selected as a standard modelling unit, which gives accurately known geometric shape and volume for comparison purposes. Another reason for making this decision is because that the triangular prism is a basic geometric object that is the most close to the shape of a stockpile. Also, it has been used by a number of researchers for stockpile modelling, i.e. Pavloudakis and Agioutantis [19] and Lu and Maung [29]. The triangular prism used for the experiment was made by bending a 1.5 mm thick aluminium sheet. The dimensions after blending are 617.50 $mm\times$ 174.10 $mm\times$1000 mm (W×H×L) and the volume is 53.753 cm^3.

Second, a laboratory scale chevron stockpile is built in the indoor environment through duplicating real blending operations. It is designed to have four layers and each layer is stacked with different sized particles. Detailed simulation procedures will be presented in Section 4.5.3. Both the triangular prism and the laboratory scale stockpile are scanned by the 3 DOF laser scanning system under the same configuration. The datasets obtained after scanning are called the standard prism data and the bench scale data, respectively. The aims of generating these two datasets are: to evaluate the proposed modelling algorithm using real laser scanning data and to compare the modelling accuracy (in volume) against the accurately known geometric shape.

Third, a dataset of a full scale stockpile provided by MatrixGroup is prepared. A 70 $m\times$155 m stockyard was sampled by surveyors at a 1 $m\times$1 m quadrat over a certain time period. The dataset consists of a sequence of 16 point clouds and each record represents the geometric shape of a stockpile after some blending operations. According to the changes in shapes, the stockpile is more likely to have been stacked using the windrow method rather than the chevron method. Also, since there are significant changes in shapes between each point cloud, it is believed that the survey was not conducted continuously. However, detailed information was not given to the author due to the firm's intellectual property protection strategy. This dataset is named the full scale data in the thesis and every point cloud in this dataset is considered to be a layer of the stockpile. Therefore, the full size stockpile has 16 layers and the dimensions of the last layer are 50 m×153 m×29 m (W×H×L). Since this dataset contains various shapes and the point density is much lower than that of the laser scanning data, the results from this dataset will provide more general insights of the proposed modelling algorithm.

Lastly, to examine the applicability of the proposed modelling algorithm further, an ideal stockpile model is generated by assuming that profiles of a stockpile along the z axis are all hyperbolic curves. The length of this model is 220 m and the height is 30 m. The repose angle of the stockpile (the angle between the side of a stockpile and the ground) is 35°. The LMS200 is assumed to be located 45 m above the ground to scan the stockpile using a 1° angular resolution along the coronal plane. The sampling distance between each single scan is 1 m. The simulation will create a perfect (noise free) point cloud, which is named the simulated stockpile. Also, through adding white Gaussian noise generated by random processes to each single scan (which is aimed to simulate the uneven stockpile surface and laser measurement noise) another point cloud called the simulated laser measurement is generated. This dataset is called the full scale simulation data. This dataset is used to examine the stockpile segmentation algorithm and compare the modelling accuracy in this thesis.

4.5.2 Experiment Design

To test the performance of the modelling algorithms against different sized particles, the laboratory scaled stockpile was designed to have four layers and each layer is stacked with different sized particles. According to the experimental results reported by Lee et al [68], these materials themselves will not affect the laser measurement accuracy. The maximum height of each layer was also predefined to avoid overlay regions between layers. Because errors from the laser are largely independent of the colour and texture, gravel used for landscaping is selected to build the laboratory scale stockpile. The particles used for the each layer are listed in Table 4.1. Among these particles, the sizes of basalt and quartzite are closet to the size of the real fines (iron ore) samples. Table 4.1 also shows the expected stacking height of these materials and measured height after a layer is completed.

Table 4.1 Particles used to create stockpile layers

Layer No.	Diameter (*cm*)	Height (*cm*)	Weight (*kg*)	Falling height (*cm*)
1	37	9.6	6.6	17.3
2	45	12	6.6	28.5
3	56	14.3	6.6	28.5

A platform, which has dimensions of 1800 *mm* length, 1000 *mm* in width and 1230 *mm* in height, was allocated beneath the 3 DOF laser scanning system to support the stockpile against the ground (see Fig. 4.9a). It is considered to be the ground plane in the point clouds collected from scanning. Reference lines were marked on both the platform and the ground to guide the stacking and reclaiming operations conducted by the operator. During the stacking operations, a cylindrical container was used to hold the gravel and moved in a zigzag motion, based on the central reference line, which represents the coronal plane, drawn on the supporting platform. Another two reference lines, vertical to the central reference line, were also highlighted on the platform. These two lines indicate the starting and ending points for the zigzag motion.

To simulate the reclaiming operation of a BWR, a simplified reclaiming arm, which has similar moving mechanisms to a BWR, was designed (see Fig. 4.9b). It was made by mounting a boom with a tube on the tripod. The bucket wheel can be simplified as a tube on the assumption that it rotates at a constant speed and recovers material evenly from the stockpile. The tripod itself has two joint movements: luffing and slewing. The travelling motion of the arm is achieved by moving the tripod base manually.

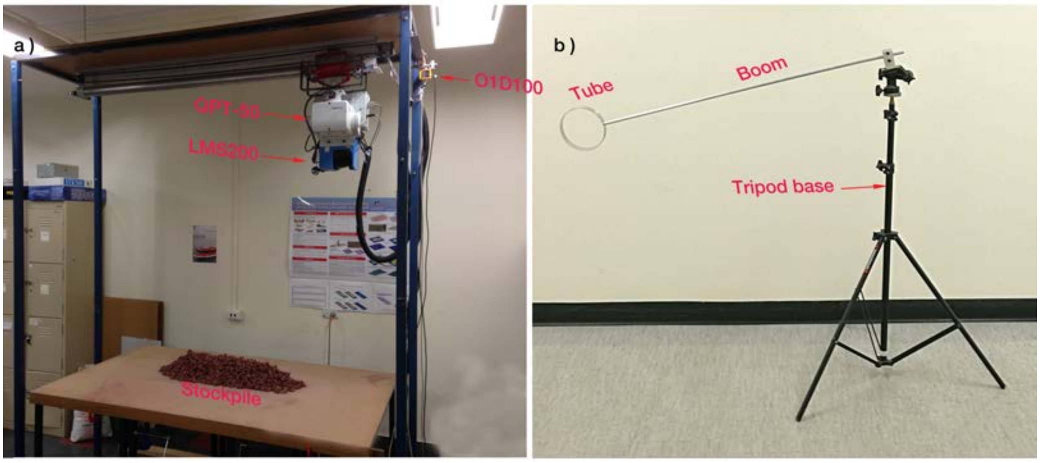

Fig. 4.9 Experiment setup for the bench scaled stockpile in the laboratory. a) A laboratory bench stockpile under the laser scanner. b) The reclaiming arm used in the experiment.

The LMS200 was configured to perform a 100° scan with an angular resolution of 0.25°. Also, according to the experiment results reported by Ye and Borenstein [58], the scanning was conducted after a three hour warm-up to reduce drifts in the laser measurements. During the scanning mission, the travelling velocity along the rack was controlled to be at 12 m/min, which is close to the average travelling speed of a BWR. The travelling displacement was sampled by the O1D100 at a 15 Hz rate.

In the experiment, the triangular prism was placed on the supporting platform and scanned by the laser first. Then, the laboratory scale stockpile was stacked layer by layer. The scanning was activated after each layer was completed. Last, reclaiming was conducted manually using the reclaimer arm. Again, the stockpile was scanned after each reclaiming step. The stacking and reclaiming procedures will be detailed in the next section.

4.5.3 Blending Simulation

The laboratory scale stockpile is created by a human operator through the following stacking and reclaiming operations to ensure it has a similar shape to a real stockpile. Because the discharge chute system used at the preliminary stage cannot provide a relatively constant material flow, it was not involved in the experiment.

Stacking and scanning

1. Lower the cylindrical container (full of gravel) at the starting point marked on the platform (the clear height between the cylinder container and stockpile surface is maintained to be around 30 *mm*).
2. Tilt the container gradually and allow particles to fall at a constant speed due to their own gravity.
3. Move the container linearly at a constant speed once particles start to fall.
4. Stop the motion when the container is empty and record its position.
5. Refill the container and repeat steps 1, 2 and 3 at the recorded point until the container reaches the ending point marked on the testing platform.
6. Reverse the moving direction and repeat steps 1, 2, 3, 4 and 5.
7. Stop the stacking operation until the pre-defined height is reached.

8. Repeat step 1~7 after scanning each time.

Four point clouds were obtained after stacking. These data are named according to the stacking sequence. For example, the 1st layer means the layer made by the red scoria.

Reclaiming and scanning

1. Adjust the luffing angle (the angle between the boom and the tripod centre axis) to 80 ° and select an initial reclaiming point manually.
2. Advance the centre of the tripod 30 *mm* along the stacking direction.
3. Rotate the arm around its central axis (slewing) and allow the tube to cut into the body of the pile.
4. Stop the slewing motion when the intrados of the tube is merged into the stockpile and remove particles picked up by the tube.
5. Rotate the boom in the opposite direction until the tube and stockpile are separated.
6. Repeat steps 3, 4, 5 and 6 until the tube has cut through the body without any obvious particles that block the tube. Then, advance the centre of the tripod another 30 *mm* to complete one reclaiming step.
7. Scan the stockpile and export the measuring data.
8. Make another nine reclaiming step and scanning the stockpile after reclaiming.
9. Return the arm to its initial position and change the luffing angle to 70°.
10. Make another five reclaiming steps and scan the stockpile accordingly.

Fifteen point clouds were collected during reclaiming. Each reclaiming step is considered as a cut from the stockpile. These point clouds are named in order according to the reclaiming steps. For example, the 1st cut is the first reclaiming step with a luffing angle of 80°, whilst, the 11th cut represents the first reclaiming step with a luffing angle of 70°. Fig. 4.10 depicts the stockpile in different states during the experiment.

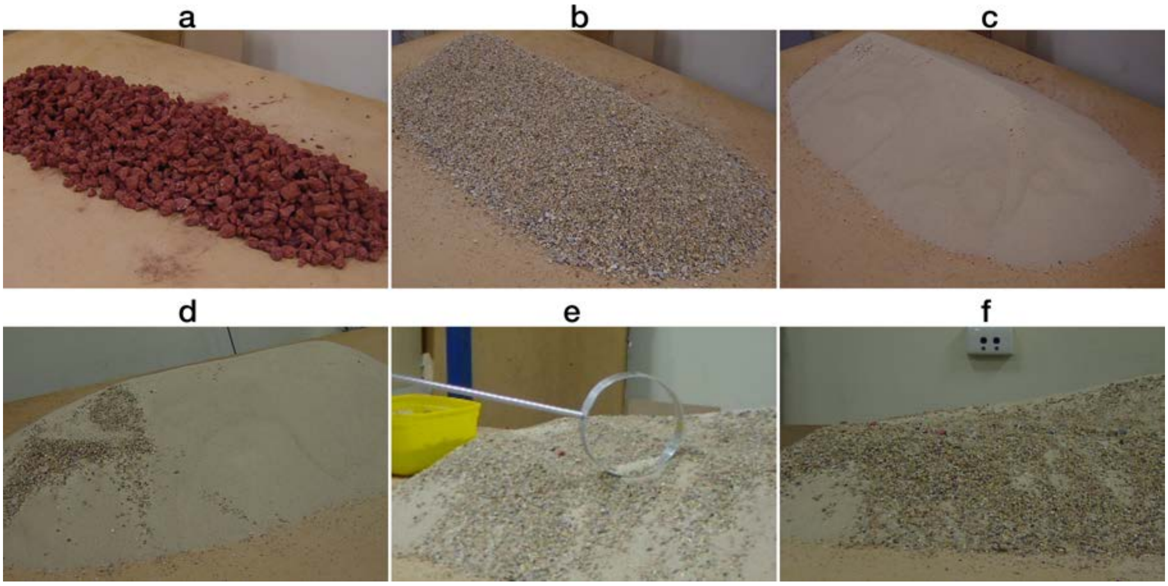

Fig. 4.10 Variation in the layers of the stockpile during the experiment. a) The 1st layer. b) The stockpile during the stacking. c) The 4th layer. d) The stockpile after the 1st reclaiming. e) The stockpile during the reclaiming. f) The stockpile after reclaiming.

4.5.4 Modelling Result

This section presents modelling results from all four datasets. The computation time and accuracy are compared and discussed because they are two crucial factors in evaluating the real-time performance of modelling algorithms. All these results are obtained from an Intel Q9400 Quad Core CPU with 4GB Ram in the Windows operation system.

4.5.4.1 Wireframe Modelling

Standard prism data. The average error range of the data collected in the laboratory is much larger than the one mentioned in the LMS200 specification. The main reason is because the LMS200 uses the time of flight to calculate the distance. A short range between the sensor and target object means a short time interval between the transmission and reception. Large errors could be created because the timing discriminator inside the LMS200 may not identify the time differences properly. In addition, it is believed that systematic errors are produced due to the high reflectivity of the aluminium sheeting. When the triangular prism was allocated at a certain position on the supporting platform, laser beams with oblique incidence angles to the prism may cause spurious points far from the true surface (see Fig. 4.11).

Such systematic errors only occurred at some locations and disappear if the position of the prism is changed. Furthermore, three one-layer stockpiles stacked by red scoria were created at different locations on the supporting platform for testing purposes. No systematic errors occurred when these stockpiles were scanned by the LMS200. All these results further support the author's suggestion that such systematic errors are mainly caused by the high reflectivity of the material only. However, the author would not to identify the true reason(s) behind this scenario because it falls outside the scope of this thesis. The point clouds used for evaluating the stockpile modelling algorithms are free from systematic errors.

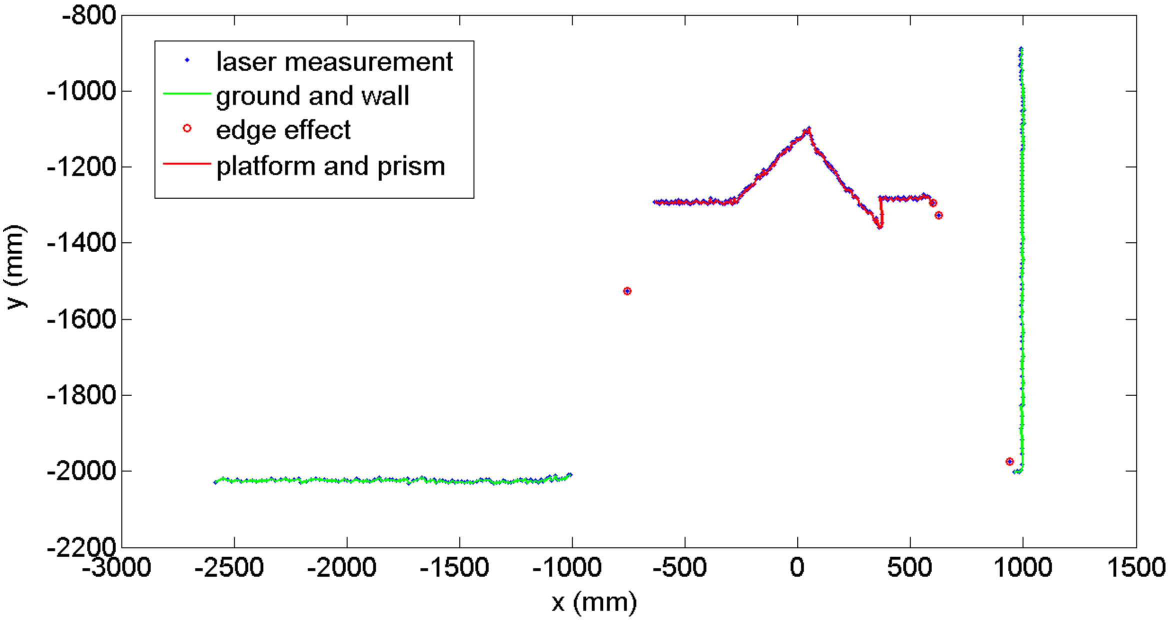

Fig. 4.11 Systematic errors may occur at some positions when laser scans the aluminium prism. Spurious points are observed on the lateral face from the positive direction of the x axis. The cross section measured is not in an isosceles triangle shape.

The profiles of the triangular prism are approximated quite well using Fourier series functions. Fig. 4.12 shows a correct single scan obtained from LMS200 and the fitting result using an 8th Fourier series function. Fig. 4.13 compares the 8th Fourier model with the 8th universal Fourier model. Because more measurement noise is removed from the universal Fourier model, its shape is closer to the surface of the real prism than the Fourier model achieves.

Bench scale data. Table 4.2 compares the accuracy against the calculation time of a single scan in a bench scale dataset using different order Fourier series functions. Generally, the use of a higher order function increases the accuracy at the expense of processing time. However,

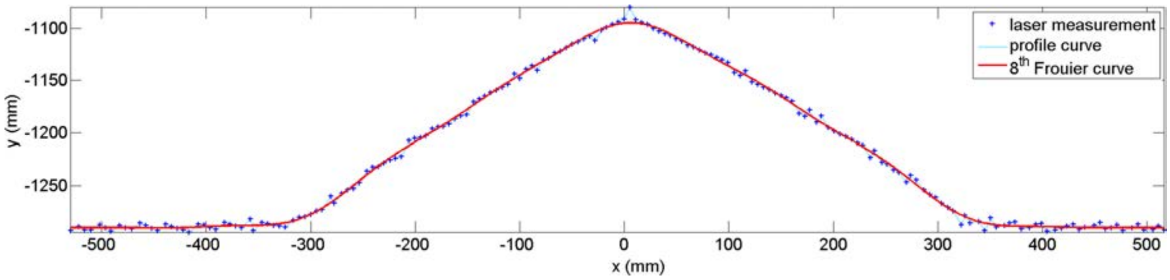

Fig. 4.12 Fit a single scan in the standard prism data using an 8th order Fourier series.

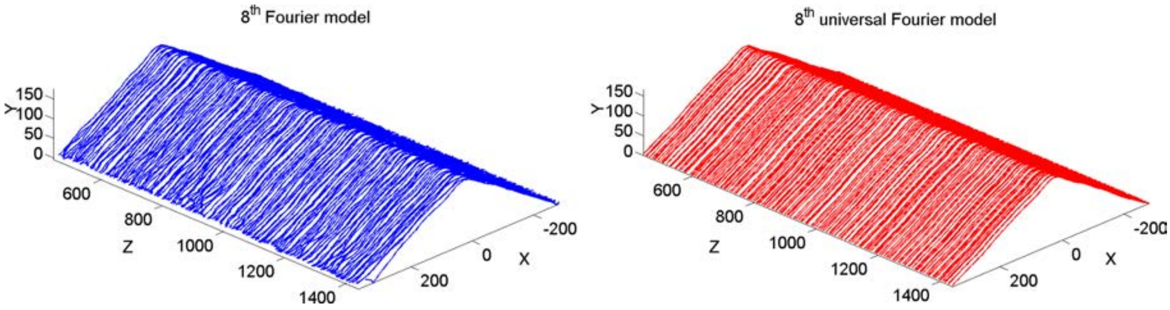

Fig. 4.13 The triangular prism modelled by the Fourier and the universal Fourier functions (unit: mm).

as shown in Table 4.2, the use of 6th- and 8th-order Fourier functions greatly improved the accuracy without causing an obvious upward trend in time consumption. The average time needed for fitting a single scan is better than 0.06 s. Clearly, the Fourier model is able to be created in real-time.

Additionally, it has been observed that the time cost for the 4th Fourier fitting was longer than the 8th Fourier function in some cases. This is mainly because a low order Fourier is not good at approximating a rough and rugged shape, i.e. a profile of the partially reclaimed section of a stockpile. Therefore, the fitting algorithm needs more evaluations to satisfy the stop criterion. Because the Fourier series is applied directly to the raw data as a smooth filter to the scanning data, large SSEs and MSEs are produced. The roughness of the stockpile surface and the noise of the LMS200 result in large residuals after fitting. The results show a clear decrease in MSE when the particle size of the stockpile is decreased (see Table 4.2). Over-fitting events frequently occur at the beginning and ending sections of the stockpile if the order of the Fourier series is higher than eight. The reason for such a phenomenon is the fitting function is excessively complex in comparison with the scanning data because the profile at the very beginning of the stockpile is more likely to be a straight line instead of an inverted U-shaped curve.

Table 4.2 Fitting accuracy versus computation time for a single scan. (unit: time s; MSE mm^2).

	4th Fourier		6th Fourier		8th Fourier	
	time	MSE	time	MSE	time	MSE
1st layer	0.0307	29.286	0.0225	29.420	0.0332	31.134
2nd layer	0.0288	20.861	0.0442	19.675	0.0278	17.725
3rd layer	0.0476	18.975	0.0368	13.703	0.0428	12.398
4th layer	0.0392	14.635	0.0278	13.684	0.0359	12.322
1st cut	0.0893	23.272	0.0795	13.000	0.0883	11.490
3rd cut	0.0415	27.941	0.0556	20.362	0.061	16.205
5th cut	0.0331	26.613	0.0499	14.661	0.0825	11.619
7th cut	0.0507	24.648	0.0725	12.626	0.0481	12.021
9th cut	0.0452	18.339	0.0612	13.327	0.0521	12.641
11th cut	0.0415	20.693	0.0646	15.537	0.0834	15.087
13th cut	0.0419	20.357	0.0538	12.361	0.0615	10.690
Average	0.0421	20.861	0.0498	13.703	0.0558	12.398

The coefficient of determination (R-squared) is the accuracy of the predictor of independent variables on dependent variables, which is a useful measure in determining the ‘goodness of fit’ in regression analysis. It ranges from 0 to 1 and $R^2 = 1$ indicates that the fitted function explains all variability. Fig. 4.14 and Fig. 4.15 plot fitting results using different Fourier series with respect to stacking and reclaiming phases. The coefficient of determination increases together with the increment in the order of the Fourier series. For example, R-squared increases from 0.9975 to 0.99793 when the order of the Fourier series function increases from 4 to 8. In the meantime, a decrease in residuals is also observed.

Another finding from Fig. 4.14 and Fig. 4.15 is that the large residuals always occur around the sharp edges in the laser measurement. Most of them exist in the top section of the stockpile (the crest of the wave) and the intersection between the side of a stockpile and the ground (the transition curve region). In mathematics, such a sharp edge is called a cusp and the curve is unable to be differentiated at the corner point. Therefore, large residuals are detected around these cusps when the curve is approximated by a differentiable function. Additionally, a stockpile stacked with large particles contains many empty holes and these holes will create a jagged array of peaks and valleys in laser measurements. Thus, large residuals also happen at these locations (see Fig. 4.16). Also, as shown in Table 4.2, the MSE of the 1st layer is almost double that of the rest layers. In other words, large particles may result in large modelling errors. This problem exists throughout the entire modelling procedure.

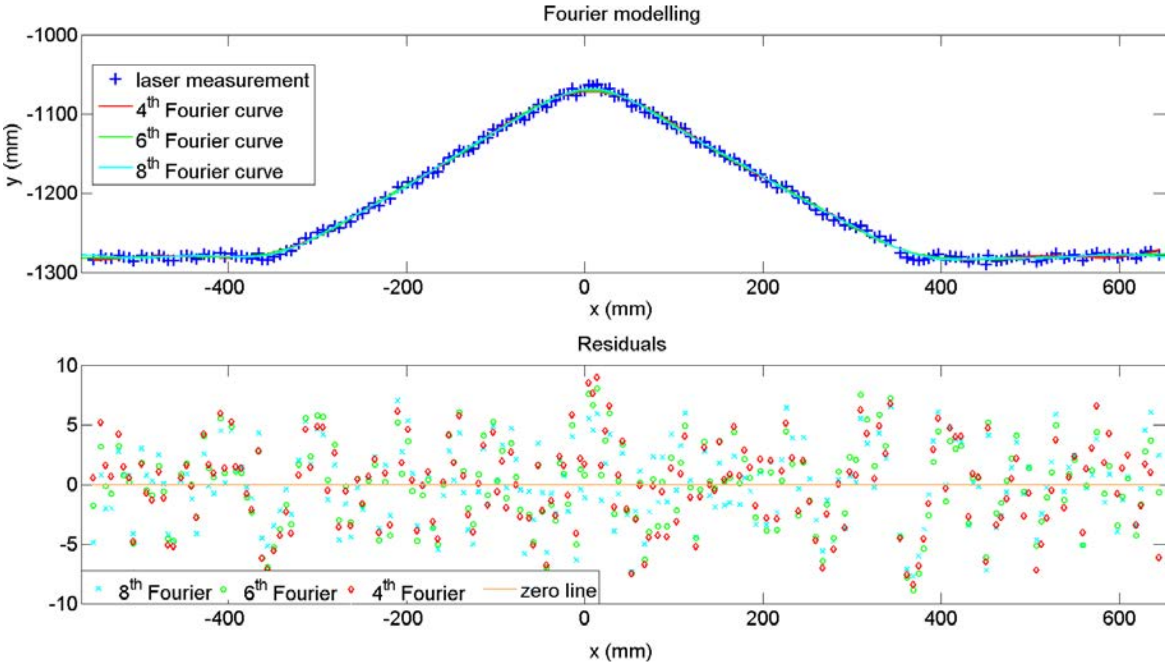

Fig. 4.14 R-squared and residuals when fitting a single scan obtained at the stacking phase.

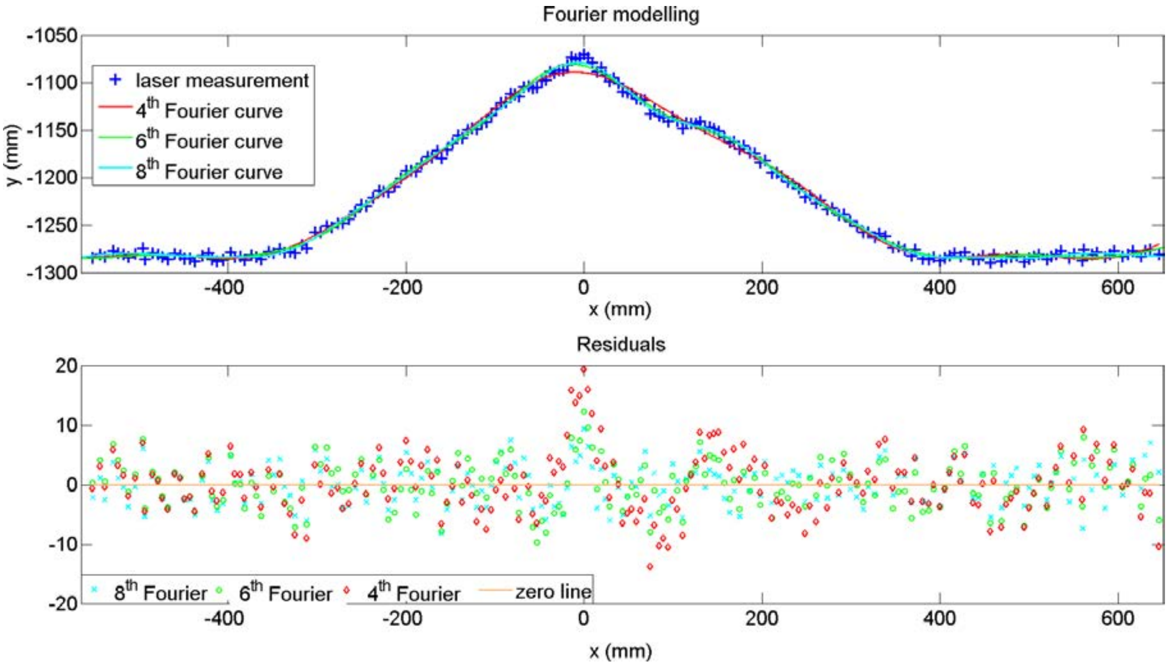

Fig. 4.15 R-squared and residuals when fitting a single scan obtained at the reclaiming phase.

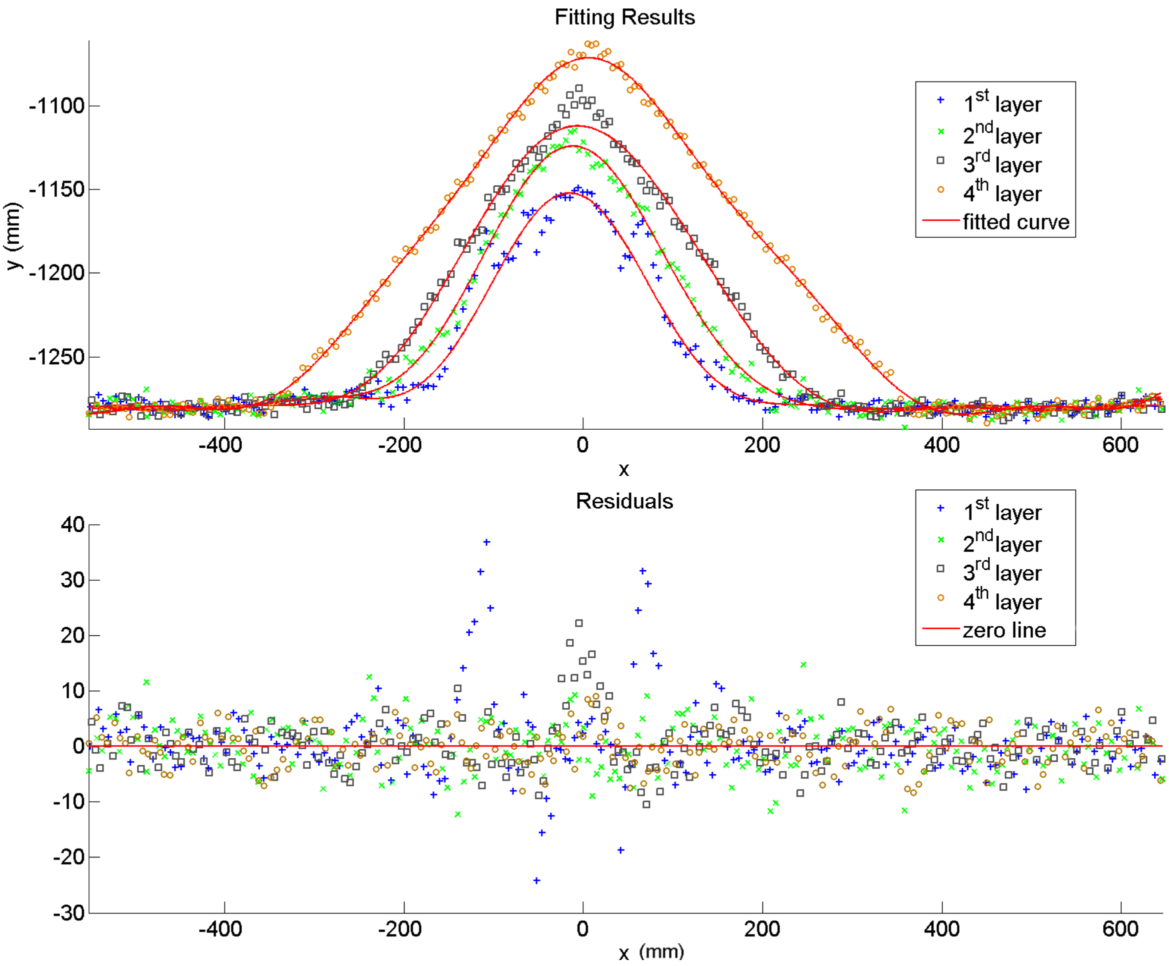

Fig. 4.16 Large residuals always locate around sharp corners.

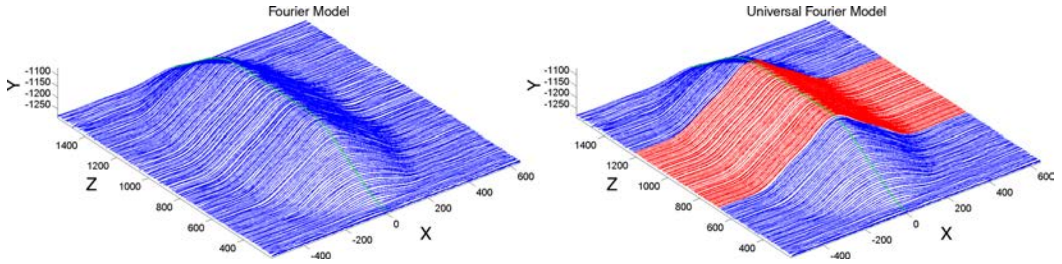

Fig. 4.17 The laboratory scaled stockpile modelled by the Fourier and the universal Fourier functions (unit: mm).

Fourier model versus universal Fourier model. Fig. 4.17 shows the Fourier model and the universal Fourier model generated by 6th order Fourier series for the 4th layer of bench scale stockpile. The average distance error is 0.824 *mm* for the Fourier model and 1.865 *mm* for the universal Fourier model respectively. Table 4.3 compares the average volume and error in percentage terms based on these two algorithms. The SSE and R-squared are not compared here for two reasons: first and foremost, the volume is more important to evaluate a stockpile model in this specific application. Secondly, the Fourier model and the universal Fourier model have the same features. These results prove that the use of a low order Fourier series decreases the fitting accuracy but does not introduce obvious errors in volume calculation. Meanwhile, according to these results, it can be concluded that the use of a universal Fourier model will lead to errors in volume calculation but within an acceptable range.

Table 4.3 Volume calculated from different wireframe models. (unit: volume decalitre, error %)

	Raw	4th-Fourier	Error	6th-Fourier	Error	4th-Universal	Error	6th-Universal	Error
1st layer	2.03666	2.03630	-0.0188	2.03705	0.0191	2.03730	0.0314	2.03692	0.0128
2nd layer	2.95675	2.95752	0.0260	2.95723	0.0162	2.95678	0.0010	2.95750	0.0254
3rd layer	4.30362	4.30049	-0.0727	4.30366	0.0009	4.30825	0.1075	4.30681	0.0741
4th layer	6.81162	6.79486	-0.2461	6.81197	0.0051	6.83791	0.3859	6.82877	0.2518
1st cut	6.65806	6.65041	-0.1149	6.65438	-0.0553	6.62722	-0.4631	6.62712	-0.4632
2nd cut	6.57272	6.56245	-0.1563	6.57028	-0.0371	6.57397	0.0190	6.57862	0.0897
3rd cut	6.48189	6.48437	0.0383	6.47964	-0.0347	6.41972	-0.9591	6.42362	-0.8990
4th cut	6.40154	6.40321	0.0261	6.40035	-0.0186	6.31811	-1.3033	6.33664	-1.0138

The wireframe models generated by the Fourier series demonstrate a high degree of accuracy and reasonable computation time for real time applications. Users are able to choose different orders of the Fourier series according to accuracy and time requirements. In this thesis, unless stated otherwise, the default order of the Fourier series functions is 8 in creating the wireframe models from the point clouds collected in the laboratory environment.

Full scale data. Due to the sampling resolution of full scale data, the modelling results are relatively poorer than that from the bench scale data. Fig. 4.18 shows the fitting result of a cross section of a layer in the full scale data. Sharp edges and corners cannot be preserved faithfully using a Fourier series. However, as illustrated in Fig. 4.18, less measurement noise is observed in the full scale data. This might be because the stockpile is sampled by surveyors using professional instruments. Since the full scale data has different noise characteristics in comparison with the laser scanning data, the wireframe modelling which is designed to filter out laser scanning noise is not applied in modelling. The full scale data are used for surface modelling directly.

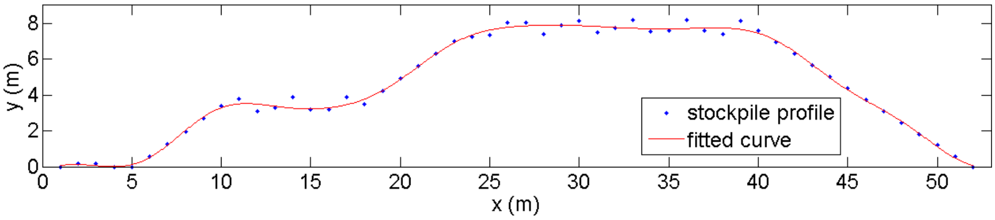

Fig. 4.18 Fitting a profile from the full scale stockpile using a 8th Fourier series. The SSE of the fit is 2.70 m^2.

Full scale simulation data. The simulation data provide another opportunity to evaluate the fitting accuracy because the true profiles of the simulated stockpile are known accurately. Fig. 4-19 plots the fitting result of a single scan in the simulated laser measurement data using the 8th Fourier series. The SSE and R-square are 11 mm^2 and 0.9987, respectively. The computation time is 0.03 s.

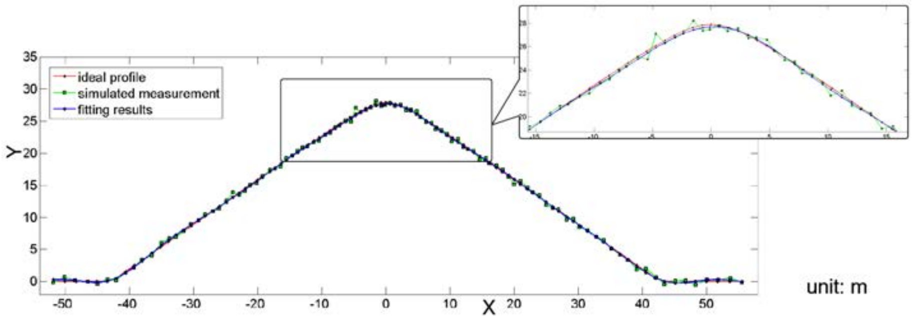

Fig. 4.19 Fitting a profile from the full scale, simulated stockpile using a 8th Fourier series. The SSE of the fit is 11 mm^2.

Results obtained from the data collected in the real scanning and simulation prove that the proposed wireframe modelling algorithm meets the design requirement for real time processing. The wireframe model created is able to preserve the real geometric shape of the stockpile with great accuracy.

4.5.4.2 Boundary Detection

Only the bench scale and the full scale simulation data are used for the evaluation of the boundary detection algorithm because the ground measurements in the full scale data equal to zero exactly and the geometric shape of the triangular prism is different from a real stockpile, which require different structuring elements in mathematical morphology operations.

Bench scale data. The boundaries of the stockpile are detected successfully from all 19 point clouds in the bench scale data. The average run time of the segmentation operation is 0.04 *s*. The detection results from each point cloud are slightly different due to the laser measurement noise. The distance measured from the centre of the LMS200 to the supporting platform in the experiment is 1285.3 *mm*, while the average distance calculated from the detection results is 1281.37 *mm*. Considering the error range of the LMS200 is 10 ~ 20 *mm* and the size of the bench scale stockpile, this result is promising. Table 4.4 compares the distance calculated from the segmentation results.

As shown in Fig. 4.20, the detection result is not perfect. Inaccurate detections are normally located around the conical ends of the stockpile. The maximum segmentation error (the segmentation error is the y coordinate of the point that belongs to the stockpile but is classified wrongly as the ground) is up to approximately 13.2 *mm*. On average, the ground is shown as 4 *mm* higher than its true level.

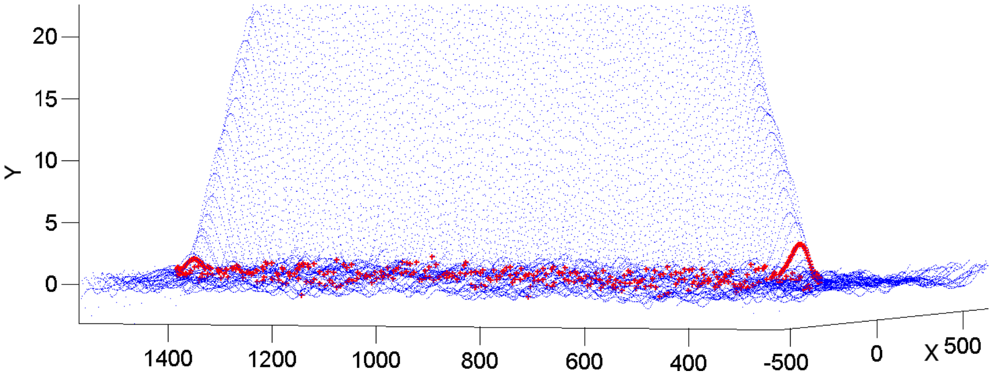

Fig. 4.20 A zoomed view of the imperfect boundary detection results for the 4th layer at the stacking phase. Detected boundary points are shown in red (unit: mm).

Full scale simulation data. The true boundary of the simulated (noise free) stockpile can be located in a straightforward way because the *y* coordinates of those points on the ground are all zero exactly. Therefore, the boundary detection is applied to the simulated laser measurement data (Gaussian noise). Fig. 4.21 compares the detected boundary of the simulated laser

Table 4.4 Ground detected from the boundary detection algorithm. (unit: *mm*)

	Stacking phase				Reclaiming phase				
Dataset	1st layer	2nd layer	3rd layer	4th layer	1st cut	3rd cut	5th cut	7th cut	9th cut
Ave.	1281.18	1280.76	1280.91	1281.37	1283.31	1280.75	1283.07	1281.48	1282.72
Std.	1.96	1.90	1.88	2.66	3.72	1.91	3.73	2.03	2.63

measurement data against the true boundary. The maximum segmentation error for the ideal model is 0.94 m and the average segmentation error is 0.49 m with a standard deviation of 0.16 m. Also, the maximum segmentation error for the simulated laser measurement data is up to 1.55 m and the average segmentation error is 0.43 m with a standard deviation of 0.31 m. An important reason for such large errors is the pseudo-Gaussian noise generator. For each single laser scan, the random number generator is called once. Thus, there is no correlation between each scan after the simulation. When the x and y coordinates in the point cloud are separated from the laser range measurement, errors exist in both axes and the true boundary is difficult to detect from the height measurement only.

Clearly, the boundary detection algorithm is not highly precise and accurate. However, it is efficient and effective. Additionally, because the adjacent region between the stockpile and the ground is considered to be a dead region and never recovered by a BWR, the proposed boundary detection algorithm is sufficient for this application.

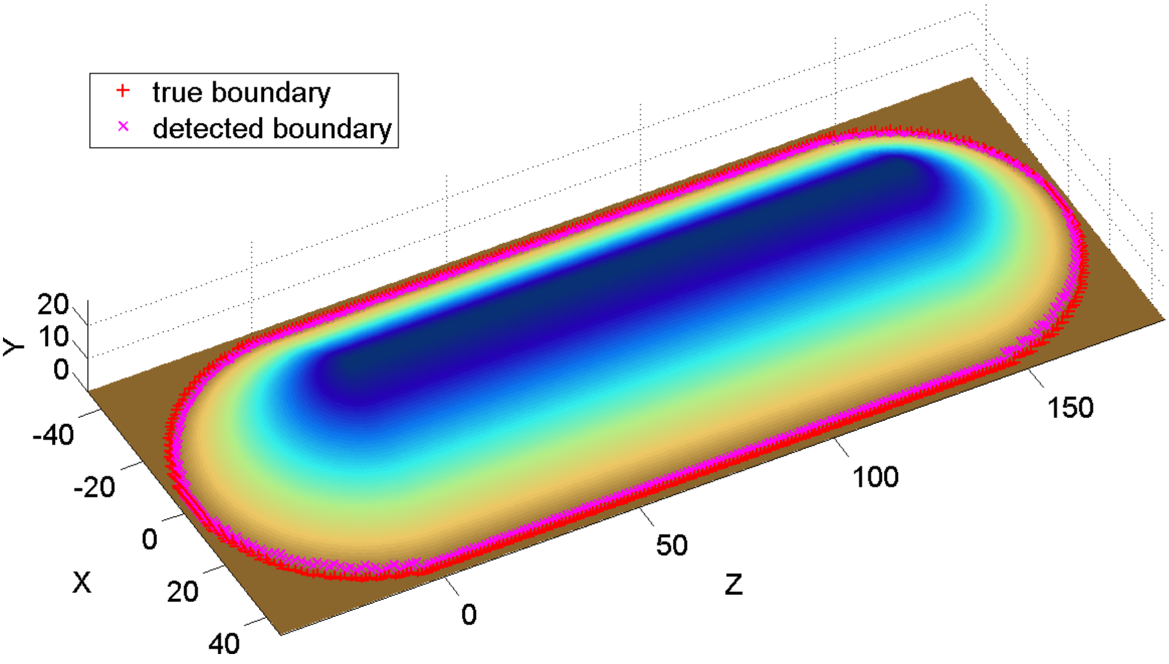

Fig. 4.21 Detecting boundary from the simulated stockpile data (unit: mm).

4.5.4.3 Polynomial Surface Modelling

Standard prism data. The triangular prism serves as a standard geometric object to evaluate the accuracy of the proposed modelling algorithm because its shape and volume are known accurately before scanning. Fig. 4.22 compares the laser measurement data against the perfect prism surface. Due to the measurement noise, almost half of the total points are located outside of the ideal prism surface. Thus, the base of the prism seems to be expanded when it is represented by the point cloud. Fig. 4.22 shows the surface model created through partitioning the Fourier wireframe model of the prism into 8 × 8 patches. The order of the polynomial function used to fit these patches is 3. Runge's phenomenon will happen if the order of the fitting function is higher than 3. Obvious oscillations can be observed around the edges of most surface patches. The volume of the polynomial surface model is 53.626 cm^3 with a percentage error of -0.236%. When the 8th universal Fourier model is used, the volume of the polynomial surface model is 53.605 cm^3, resulting in a percentage error of 0.276%.

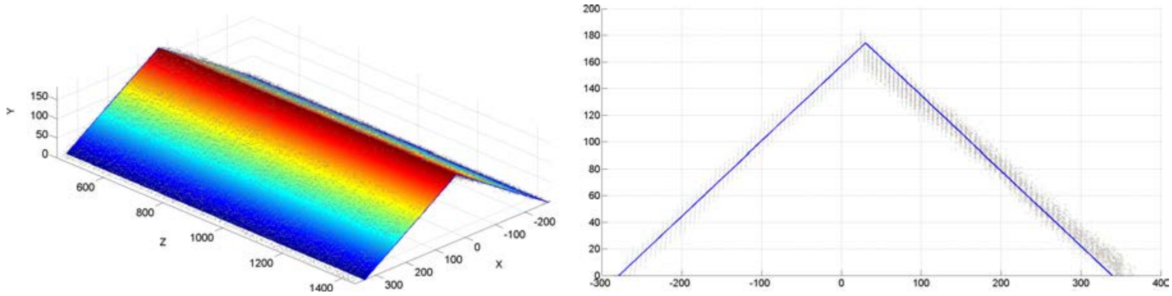

Fig. 4.22 Laser measurement against the ideal prism surface. The point measurements are plotted in grey (unit: mm).

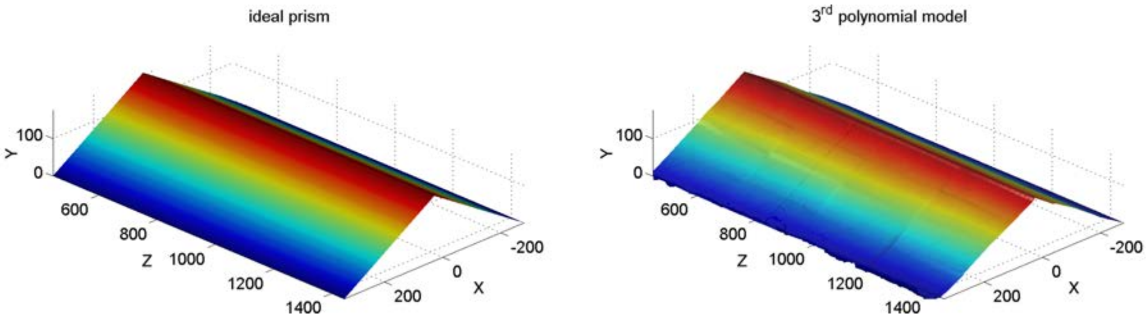

Fig. 4.23 3rd polynomial model of the triangular prism created from 8 × 8 patches (unit: mm).

Bench scale data. Previous results indicate that a high-order Fourier series can improve the fitting accuracy but will not cause obvious increments in computation time. By contrast, opposite outcomes are detected in the surface model. As shown in Table 4.5, the time consumption of a low-order polynomial is much less than that of a high-order polynomial function. For example, the calculation time jumps from 6.51 s to 54.24 s when the order of the polynomial function increases from 6 to 9. However, the average modelling time is still promising for this application because the use of a high-order function will generate a highly accurate model. However, such an improvement is not obvious if the order increases from 8 to 10, as can be seen in Table 4.5. The SSE and MSE calculated here show the discrepancy between the wireframe model and the fitting results. If the order of the polynomial functions is large than 10, Runge's phenomenon will happen and may introduce more errors into the modelling.

Table 4.5 Polynomial surface modelling results. (unit: time s, SSE $mm^2 \times 10^6$, MSE mm^2)

Dataset	6th poly			8th poly			10th poly		
	time	SSE	MSE	time	SSE	MSE	time	SSE	MSE
1st layer	6.51	1.466	396.32	21.52	0.2895	78.26	54.24	0.2438	65.91
2nd layer	6.42	1.175	289.41	29.65	0.2457	60.52	53.84	0.2235	55.05
3rd layer	7.27	1.154	251.53	32.66	0.1745	38.03	60.65	0.0994	21.67
4th layer	8.11	1.145	190.71	33.76	0.2514	41.87	68.23	0.1961	32.66
1st cut	8.74	1.280	213.19	21.52	0.3081	51.32	74.31	0.2473	41.19
3rd cut	9.74	0.835	139.07	29.65	0.3123	52.02	81.18	0.1783	29.70
5th cut	9.51	0.851	141.74	32.66	0.3341	55.65	79.54	0.2092	34.84
7th cut	9.83	0.891	148.40	33.76	0.3707	61.74	81.12	0.2246	37.41
11th cut	9.66	0.839	139.74	21.52	0.3960	65.96	80.45	0.2984	49.70
15th cut	9.98	0.967	161.06	29.65	0.8346	139.01	83.34	0.2151	35.83
Average	8.71	1.0438	175.89	29.23	0.31126	58.08	81.03	0.21769	36.62

Table 4.6 lists the time consumption and modelling results for the 15th cut, after applying the grid partitioning method. The orders of the polynomial functions are 6th, 8th and 10th, respectively. Based on these results, it can be verified that the grid partitioning method increases the modelling accuracy greatly without significant computational cost.

Table 4.6 Surface modelling accuracy versus calculation time when apply grid partitioning to the 15th reclaiming data. (unit: time s, SSE $mm^2 \times 10^6$, MSE mm^2)

Polynomial	6 × 6			7 × 7			8 × 8		
	time	SSE	MSE	time	SSE	MSE	time	SSE	MSE
6th	11.48	1.48	2.47	11.66	0.93	1.56	12.15	0.89	1.49
8th	37.92	1.39	2.33	38.50	1.25	2.10	39.95	1.38	2.31
10th	94.23	0.92	1.55	95.67	0.60	1.01	99.40	0.59	0.99

Fig. 4.24 plots three models for comparison purposes. Out of the three models shown in Fig. 4.24, one over-fitting event is detected when the stockpile is partitioned into 8×8 patches and modelled through the 8^{th} polynomial function. This raises the SSE to 1.384×10^4 mm^2. However, the over-fitted surface patch is identified automatically and, through reducing the order of the polynomial function to 7, a correct model is created. The SSE of this model is reduced to $1.16 \times 10^4 mm^2$.

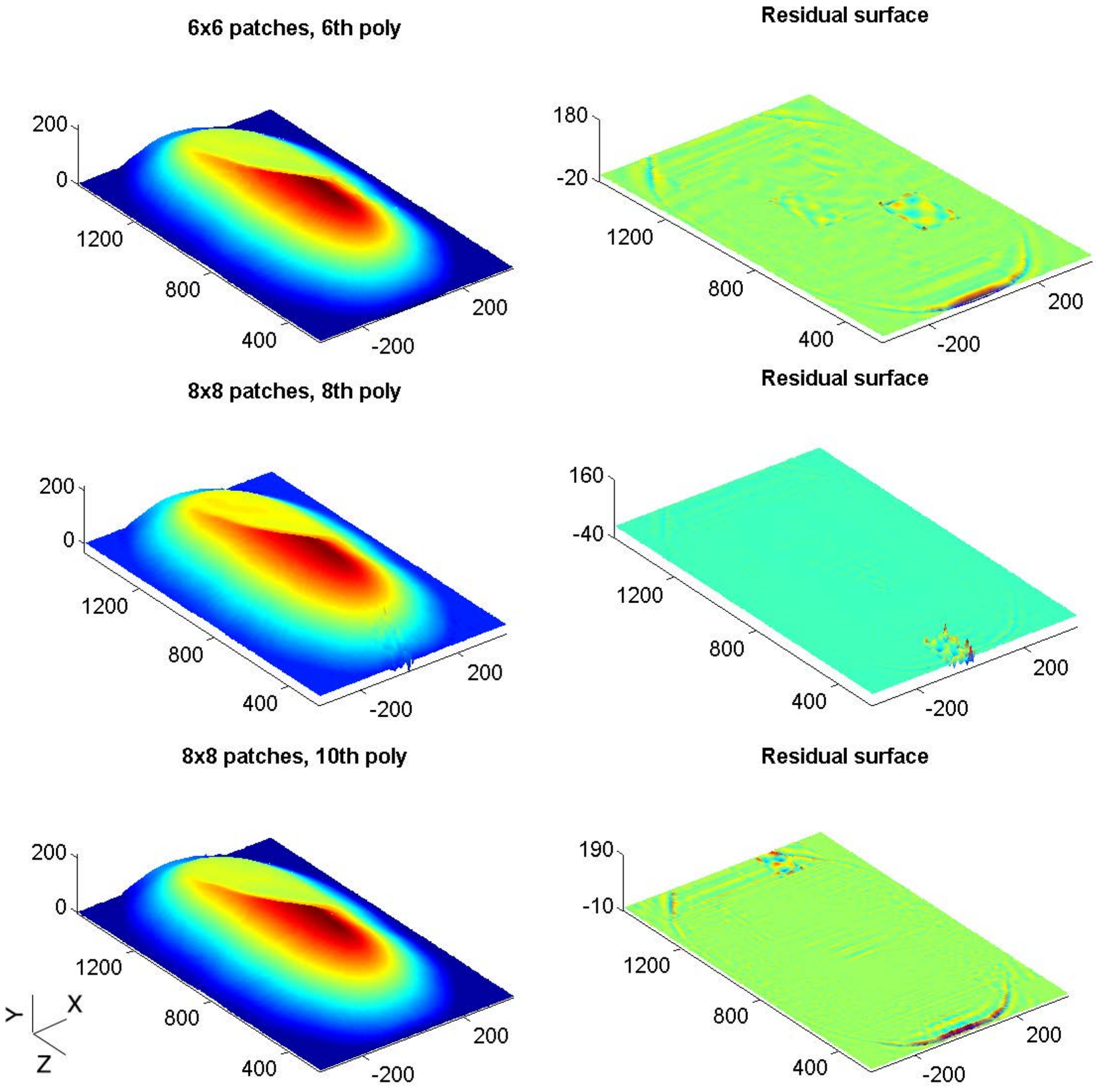

Fig. 4.24 Polynomial surface models obtained using the grid partitioning method (For display purposes, the over-fitted surface patch remains unfixed, unit: mm).

In the laboratory scale dataset, if the ground section is more than 90% in a patch, over-fitting is liable to happen. Therefore, the authors would suggest that the minimum size of each patch should be larger than 82 *mm* in width and 142 *mm* in length (9 × 9 patches) to avoid over-fitting problem. The surface normal comparison algorithm detected all over-fitted patches successfully in the bench scale data. 95% of these over-fitted surface patches are fixed through reducing the order of the polynomial function by 1. The rests are avoided when the order of the fitting function is reduced by 2. Therefore, in some cases, a polynomial mode of a stockpile may be represented by different ordered polynomial functions.

Table 4.7 compares the average volumes calculated through different polynomial surface models. The error in percentage is compared against volumes obtained from original laser measurements, which are listed in Table 4.3. These results clearly prove that the grid partitioning method improves the modelling accuracy. A low-order function can approximate the geometric shape of a stockpile as well as a high-order function through applying the grid partitioning method. Volumes calculated through surface models are reasonably good unless over-fitting event happens. For example, when the stockpile is segmented into 9 × 9 patches and fitted by the 9th polynomial function, the volume of the 4th layer is 68296.03 cm^3 and the percentage error is 0.264%. This is caused by two over-fitted patches: the (5, 6) and the (5, 7) patch. No over-fitting occurred when these two surface patches were fitted by the 8th polynomial function. The volume of the final model is 68121.60 cm^3 which yields a percentage error of 0.007%.

Table 4.7 Volume calculated from the surface model. (unit: volume decalitre, error %)

Dataset	(5th, 1×1)	Error	(5th, 6×6)	Error	(7th, 6 × 6)	Error	(7th, 9 × 9)	Error	(9th, 9 × 9)	Error
1st layer	2.05970	1.130	2.03988	0.158	2.03729	0.031	2.03894	0.112	2.03872	0.070
2nd layer	2.96619	0.319	2.96166	0.166	2.96132	0.155	2.95656	-0.006	2.95697	0.008
3rd layer	4.30596	0.054	4.30213	-0.034	4.30223	-0.032	4.30318	-0.010	4.30333	-0.007
4th layer	6.78327	-0.416	6.80376	-0.115	6.80568	-0.087	6.80934	-0.034	6.82960	0.264
1st cut	6.62244	-0.535	6.6464	-0.174	6.64957	-0.127	6.65080	-0.109	6.65366	-0.066
2nd cut	6.54419	-0.434	6.56060	-0.184	6.56160	-0.169	6.56475	-0.121	6.56701	-0.087
3rd cut	6.46606	-0.244	6.46985	-0.186	6.47072	-0.172	6.47203	-0.152	6.47228	-0.148
4th cut	6.41672	0.237	6.39386	-0.120	6.39451	-0.110	6.39594	-0.087	6.39672	-0.075

Full scale data. Fig. 4.25 illustrates the geometric shape of layers in the full scale dataset. From this image, it is possible to determine that from the 1st layer to the 7th layer, the stockpile was at the stacking phase, while from the 8th layer to the 10th layer, the stockpile was at the reclaiming phase. Then, stacking operations are conducted from the far end of the partially reclaimed stockpile. This operation creates two separated stockpile regions and these two regions are rejoined gradually during the stacking procedure to form one stockpile.

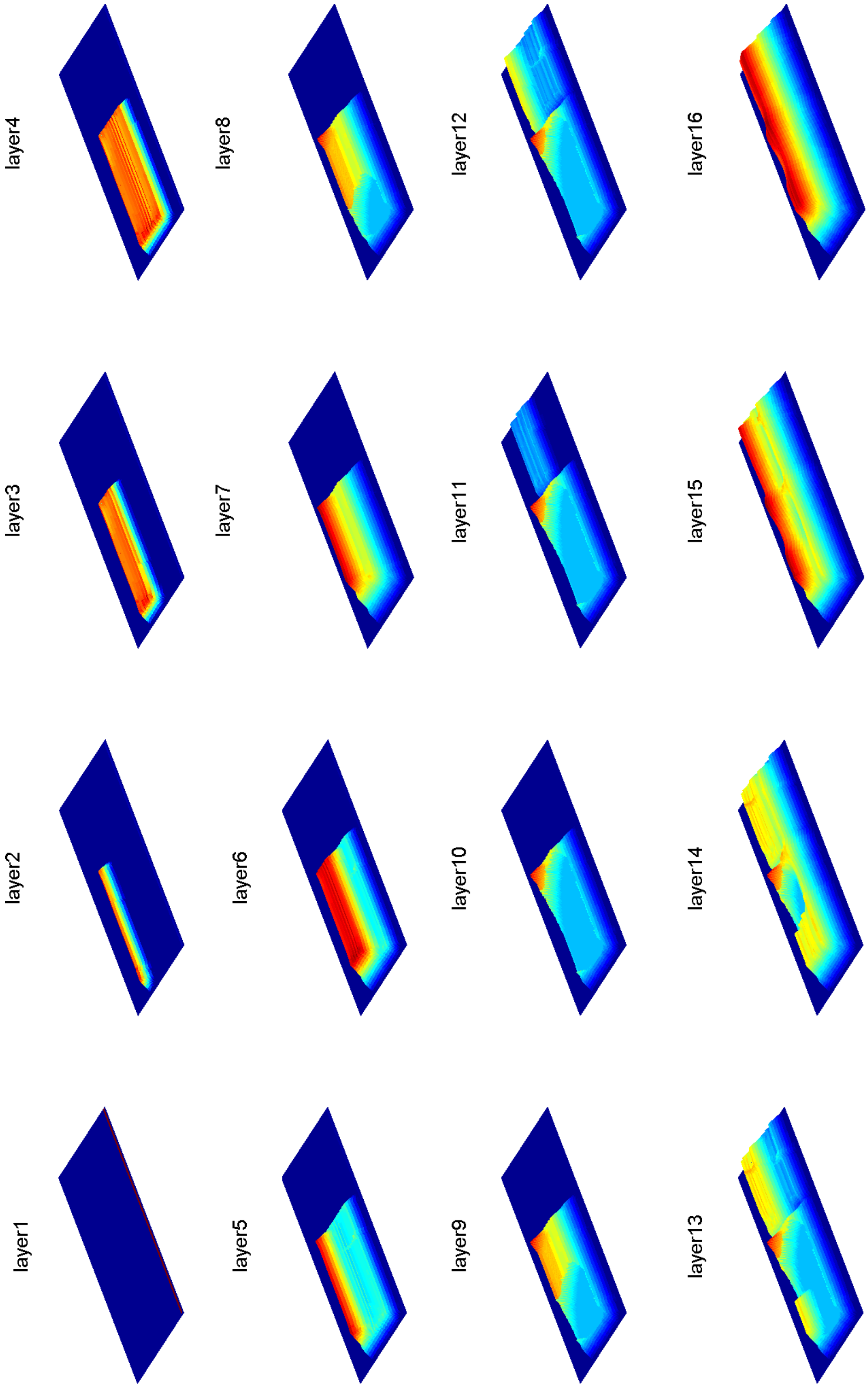

Fig. 4.25 Surface rending of the full scale stockpile.

Because both modelling algorithms are designed for high-resolution scanning data, the modelling accuracy degrades at the full scale data (with a point-to-point resolution of 1 *m*), even when high order polynomial functions are used (see Fig. 4.26 and Fig. 4.27). However, the grid partition algorithm is still applicable to this dataset. For example, when a 10th polynomial function is applied to fit the 13th layer of the stockpile directly, the two separated regions are connected after modelling. Meanwhile, there exist very large residuals along the sickle-shaped cutting surface created by a BWR and Runge's phenomenon is also present around the boundary region of the stockpile. Conversely, when the layer is subdivided into 15×15 patches and each patch is fitted by a 6th degree polynomial function, the model is improved significantly in terms of both geometric shapes and residuals.

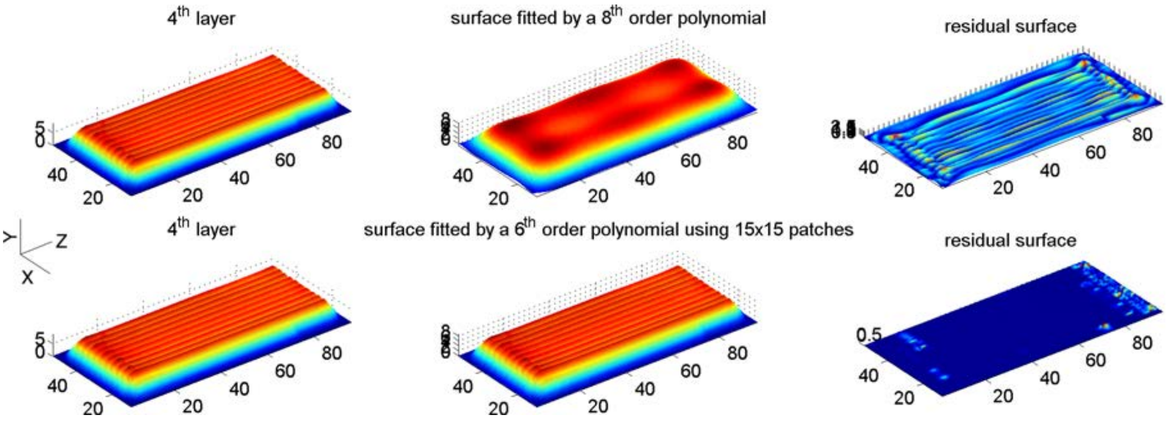

Fig. 4.26 A polynomial surface model of the 4th layer from the full scale data (unit: m).

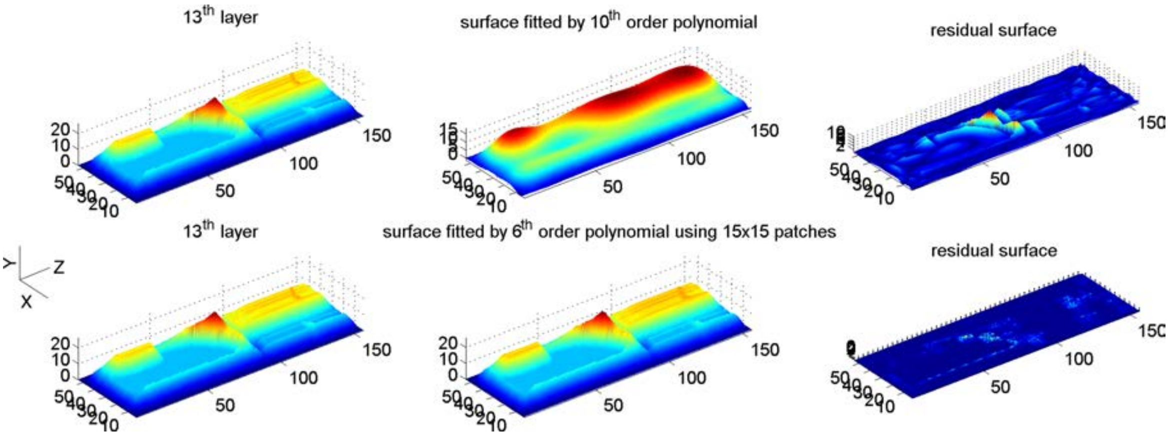

Fig. 4.27 A polynomial surface model of the 13th layer from the full scale data (unit: m).

Table 4.8 lists the computation time and the modelling results from the 3rd layer to the 16th layer. The 1st layer is in a cuboid shape with exact dimensions of 2 *m*× 153 *m*× 0.34 *m*

$(W \times L \times H)$, which means it only contains two measurements in x axis. The dimensions of the X matrix constructed from the 1st layer are not suitable for grid partitioning due to the lack for the differentiation. Therefore, it was ignored for modelling purposes, as was the 2nd layer.

Table 4.8 Surface modelling accuracy versus calculation time when apply grid partitioning to a full scale stockpile. (unit: time s, SSE m^2, MSE cm^2)

Layer	(6th, 8×8)			(6th, 10×10)			(6th, 15×15)			(8th, 15×15)		
	Time	SSE	MSE	Time	SSE	MSE	Time	SSE	MSE	Time	SSE	MSE
3	2.82	8.17	27.75	3.49	8.35	28.37	6.16	0.80	2.72	18.98	0.37	1.26
4	3.89	149.57	346.22	4.11	14.96	34.63	6.8	0.89	2.06	21.12	3.8	8.8
5	3.63	117.66	245.13	4.32	21.82	45.45	6.88	7.15	14.89	21.82	3.18	6.62
6	3.58	86.44	180.08	4.31	19.75	41.14	6.95	3.83	7.97	21.93	3.15	6.57
7	3.57	65.21	135.84	4.33	20.00	41.67	7.08	2.09	4.36	21.89	1.94	4.04
8	3.57	197.33	411.11	4.31	91.16	189.92	7.03	27.65	57.6	21.93	29.48	61.43
9	3.57	164.19	342.07	4.32	125.46	261.37	6.96	38.99	81.22	21.94	172.14	358.63
10	3.61	217.18	452.47	5.74	122.88	255.99	7.13	71.18	148.29	26.53	38.48	80.17
11	5.09	586.53	751.97	5.86	389.28	499.07	8.56	135.68	173.95	26.97	176.49	226.26
12	5.2	669.46	825.27	6.21	390.81	481.77	8.55	191.13	235.61	27.85	203.68	251.09
13	5.69	652.92	789.70	5.93	385.22	465.92	8.9	180.67	218.51	27.85	153.22	185.32
14	5.22	565.25	683.66	6.67	340.05	411.29	8.54	149.71	181.07	28.70	102.82	124.36
15	5.3	301.37	364.51	6.45	117.73	142.40	8.87	62.35	75.41	27.53	22.32	26.99
16	5.29	291.94	353.10	6.65	76.67	92.73	8.58	39.04	47.22	27.25	14.76	17.86
average	3.76	207.255	358.803	5.035	104.445	166.16	7.105	39.015	66.505	24.235	25.90	44.21

There are obvious degradation trends in the modelling accuracy that start from the 8th layer because the stockpile contains two separated regions. One region is partially reclaimed and the other is being stacked using the windrow method. Thus, large residuals will be observed around the sickle-shaped cutting region caused by the BWR and the gaps between the two regions. With more materials stacked onto the stockpile, these regions are filled and the modelling accuracy is improved. These results demonstrate strong evidences that the grid partitioning algorithm is able to improve the modelling accuracy even when the point resolution is low. During modelling, over-fitting events happen quite frequently. Other than the boundary region, these over-fitting events are also happened around the sickle shaped cut created by the BWR. Most over-fitted patches were detected automatically and all detected over fitting events are fixed through lowering the order of the fitting function by one. However, a total of 6 missing detections were reported when generating Table 4.8. Because of the low point-to-point resolution, the point set $N_{CenNeig}$ contains a large region. The distances between two adjacent points in both directions are all 1 m. If the point set determined from k-nearest neighbour algorithm contains 5 points, which means a central point with four neighbours, the bounding rectangular of the point set will be 4 m^2. Given such a large surface patch, the normal vectors of the planes fitted from two $N_{CenNeig}$ point sets may be in a nearly parallel condition and cause a miss detection.

Table 4.9 shows the volumes of all the (7th, 15 × 15) polynomial models generated from the full scale dataset.

Table 4.9 Volume of polynomial models of the full scale data. (unit: volume m^3, error %)

Layer	Volume of the layer	Volume of the model	Error
3	13523.64	13456.23	0.50
4	22263.67	22218.41	0.20
5	31425.70	31378.39	0.15
6	40838.28	40798.71	0.10
7	51806.42	51764.77	0.08
8	44576.43	44534.78	0.09
9	41850.85	41809.20	0.10
10	33865.67	33824.02	0.12
11	44363.11	44291.84	0.16
12	58170.99	58000.70	0.29
13	68351.16	68198.32	0.22
14	80577.99	80420.41	0.20
15	92812.83	92643.52	0.18
16	104017.15	103845.30	0.17

Full scale simulation data. Fig. 4.28 and Fig. 4.29 illustrates the (7th, 15 × 15) polynomial surface models created from the ideal stockpile and noise measurement data, respectively. Similar to other datasets, large residuals are located around the boundary area of the stockpile. The SSEs and MSEs for these two models are 17.52 m^2 and 8.27 cm^2, and 182.81 m^2 and 86.21 cm^2, respectively. The average modelling time is less than 50 s. The results obtained from this simulation dataset further demonstrate the efficiency and effectiveness of the polynomial modelling algorithm.

No over-fitting problem happened to the ideal stockpile data but it happened twice to the noise measurement data. Both of these two over-fitted conditions were detected automatically and eliminated after the order of the polynomial function was reduced by 1. The volume calculated from the ideal stockpile data is 230396.43 m^3. The volumes of the two surface models (see Fig. 4.28 and Fig. 4.29) are 230398.54 m^3 and 230455.28 m^3, respectively. The percentage errors are 0.0009% and 0.0255%.

All of these results prove that the polynomial function can approximate stockpile surfaces with a great degree of accuracy in terms of both geometric shapes and volumes through the grid partitioning method.

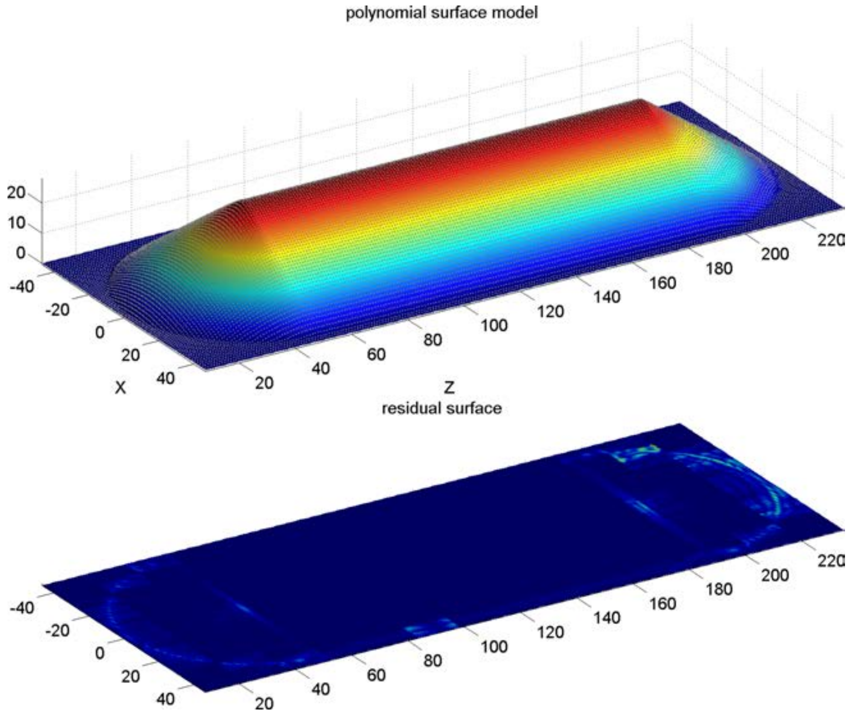

Fig. 4.28 The (7th, 15 × 15) surface model of the ideal stockpile. The original point cloud data are plotted as grey dot points.

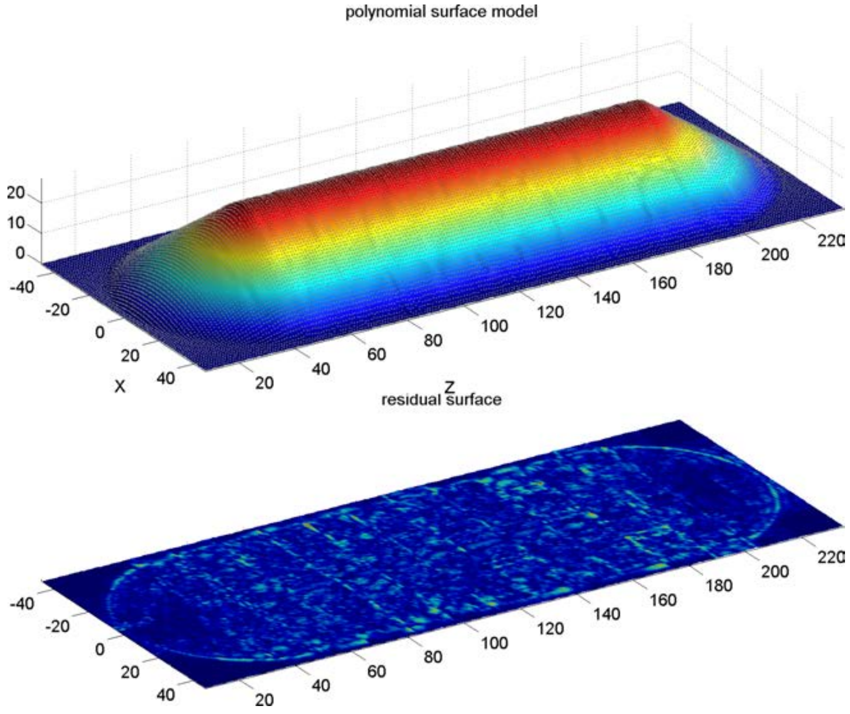

Fig. 4.29 The (7th, 15 × 15) surface model created for the noise measurement data. Points in the wireframe model are plotted as grey dot points. The residuals are calculated against the ideal stockpile (unit: mm).

4.5.4.4 B-spline Surface Modelling

Standard prism data. Benefited from its elasticity, a spline offers great flexibility and precision in fitting the constraints. However, it is not robust in dealing with measurement noise. As pointed out by Lee and Ehsani [68], the distance data obtained from the LMS200 fluctuate with a peak-to-peak value of about 20 *mm* when it is used to measure an intended distance of 4.0 *m*. Such drifting is relatively large in terms of the dimensions of the triangular prism. Thus, the B-spline model, created from the 8th Fourier model of the prism seems to be slightly ridged. Conversely, the surface model created from the 8th universal Fourier model is better than the former model in representing the true geometric shape of the triangular prism (see Fig. 4.30).

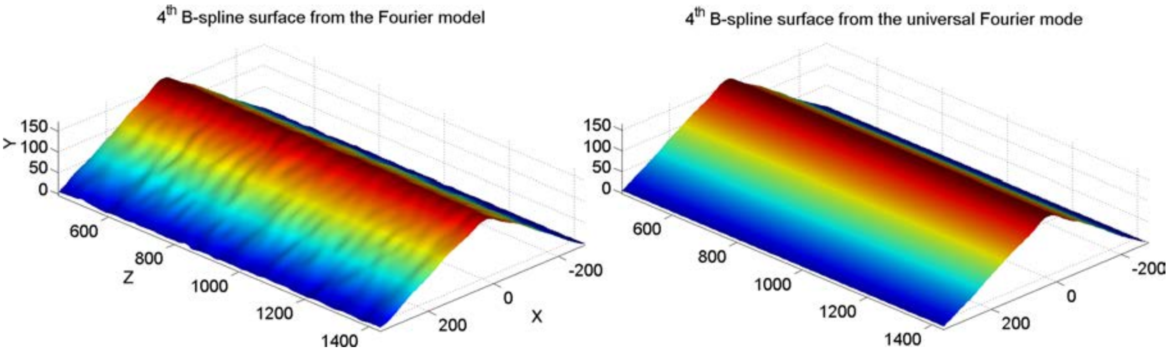

Fig. 4.30 A comparison of two same degree B-spline models from different wireframe model (unit: mm).

The volumes of these surface models are 53.186 cm^3 and 53.194 cm^3, yielding a percentage error of 1.056% and 1.041%, respectively. The percentage errors are not as good as for the polynomial model (nearly quintupled). However, these results are obtained in less than 1 *s* and grid partitioning is not applied.

Bench scale data. A great advantage of B-spline interpretation is the capability that approximates the true surface using lower order basic functions. Even without applying the grid partitioning algorithm, tensor product B-spline function can model the stockpile quite well (see Fig. 4.31). No over-fitting was recorded throughout the entire modelling process.

According to the results shown in Table 4.10, B-spline interpretation is more accurate than polynomial approximation. On average, the SSE of the B-spline modelling is reduced by 2 orders of magnitude in comparison with the polynomial modelling. In most cases, a high order function provides a better fit but such improvement is not obvious in B-spline

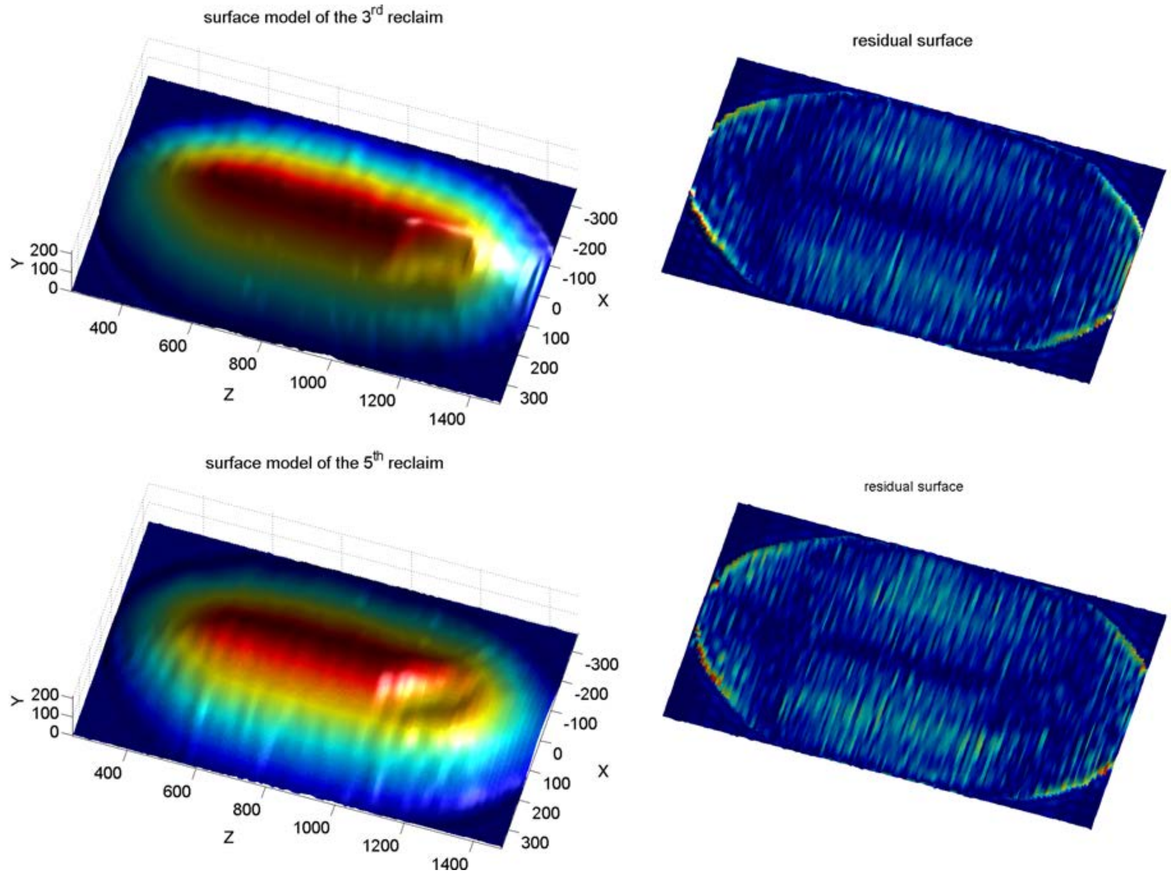

Fig. 4.31 B-spline surfaces model of a partially reclaimed stockpile (unit: mm).

Table 4.10 B-spline surface modelling results. (unit: time s, SSE $mm^2 \times 10^4$, MSE mm^2)

Dataset	3rd degree model			4th degree model			5th degree model		
	time	SSE	MSE	time	SSE	MSE	time	SSE	MSE
1st layer	0.020	8.24764	6.61	0.018	8.08009	6.48	0.019	8.27607	6.64
2nd layer	0.020	3.21134	2.35	0.020	3.21634	2.36	0.021	3.19362	2.34
3rd layer	0.016	3.81988	2.53	0.019	3.78650	2.50	0.018	3.78543	2.50
4th layer	0.019	6.22702	3.83	0.018	6.19193	3.81	0.017	6.12973	3.77
1st cut	0.019	9.75717	5.12	0.016	9.47729	4.98	0.019	9.34739	4.91
3rd cut	0.016	1.03298	5.49	0.017	10.00849	5.24	0.018	9.89061	5.20
5th cut	0.016	8.24758	4.33	0.016	8.06272	4.24	0.017	8.04801	4.22
7th cut	0.016	8.18758	4.30	0.017	8.10974	4.26	0.017	8.09962	4.25
11th cut	0.016	81112.67	4.26	0.016	8.08878	4.25	0.016	8.03360	4.22
15th cut	0.016	8.51591	4.47	0.017	8.40249	4.42	0.016	8.32858	4.38
Average	0.017	8.21758	4.32	0.017	8.08443	4.26	0.017	8.07382	4.23

interpretation. Taking the 2nd layer as an example, the SSE of the 3rd degree model is 3.21134×10^4, while the SSE of the 5th degree model is 3.19362×10^4, which means only 0.55% less than the 3rd model. Also, in some cases, a high order basic function even results in a large SSE. For example, the SSE of the 1st layer fitted by the 6th order basic functions is $8.2476 \times 10^4 mm$, while the SSE of the 4th order basic functions is $8.247 \times 10^4 mm$. This is mainly because of the physical texture of the 1st layer. The layer stacked by red scoria is quite loose and coarse. However, a higher degree B-spline surface is smoother than a low degree one. Thus, residuals of the 6th spline model are large than that of the 4th spline model. Lastly, the computation time improves significantly. The average modelling times for different order B-spline functions are quite close. When they are rounded up to the 4th decimal place, they are almost of the same value.

There is no doubt the accuracy of a B-spline model can be further improved by grading portioning. Fig. 4.32 compares the (5th, 10 × 10) B-spline surface model against the (5th, 10 × 10) polynomial and the (5th, 1 × 1) spline surface model of the 15th cut. The SSEs for those models are: 10597.28 mm^2, 34308.53 mm^2 and 83285.84 mm^2, respectively. Table 4.11 shows the volumes calculated using different B-spline models. An error is detected in (5th, 1 × 1) models. The volume of the 4th cut is large than that of the 3rd cut due to large residuals. This should not happen in reality. However, the calculation results of the (5th, 6 × 6) and (5th, 9 × 9) are in accordance with the real scenario. These results also indicate that the grading partitioning method is more effective and powerful in improving the modelling accuracy than the use of high order B-spline function.

Table 4.11 The volume calculated from the B-spline surface model. (unit: volume $10^4 \times cm^3$, error %)

Dataset	(5th, 1 × 1)	Error	(5th, 6 × 6)	Error	(5th, 9 × 9)	Error
1st layer	2.04861	-0.556	2.03683	-0.0225	2.03731	-0.0078
2nd layer	2.97298	-0.555	2.95621	-0.0116	2.95633	-0.0075
3rd layer	4.32688	-0.575	4.30177	-0.0083	4.30181	-0.0720
4th layer	6.85902	-0.729	6.80876	-0.0085	6.80891	-0.0063
1st cut	6.60787	-0.754	6.65753	-0.0078	6.65796	-0.0014
2nd cut	6.52264	-0.762	6.57206	-0.0101	6.57246	-0.0040
3rd cut	6.32370	-0.764	6.48121	-0.0104	6.48151	-0.0057
4th cut	6.35275	-0.762	6.40064	-0.0137	6.40116	-0.0056

Full scale data. Low point resolution is also a challenge for B-spline modelling if the point cloud is not segmented. According to previous results obtained from the bench scale dataset,

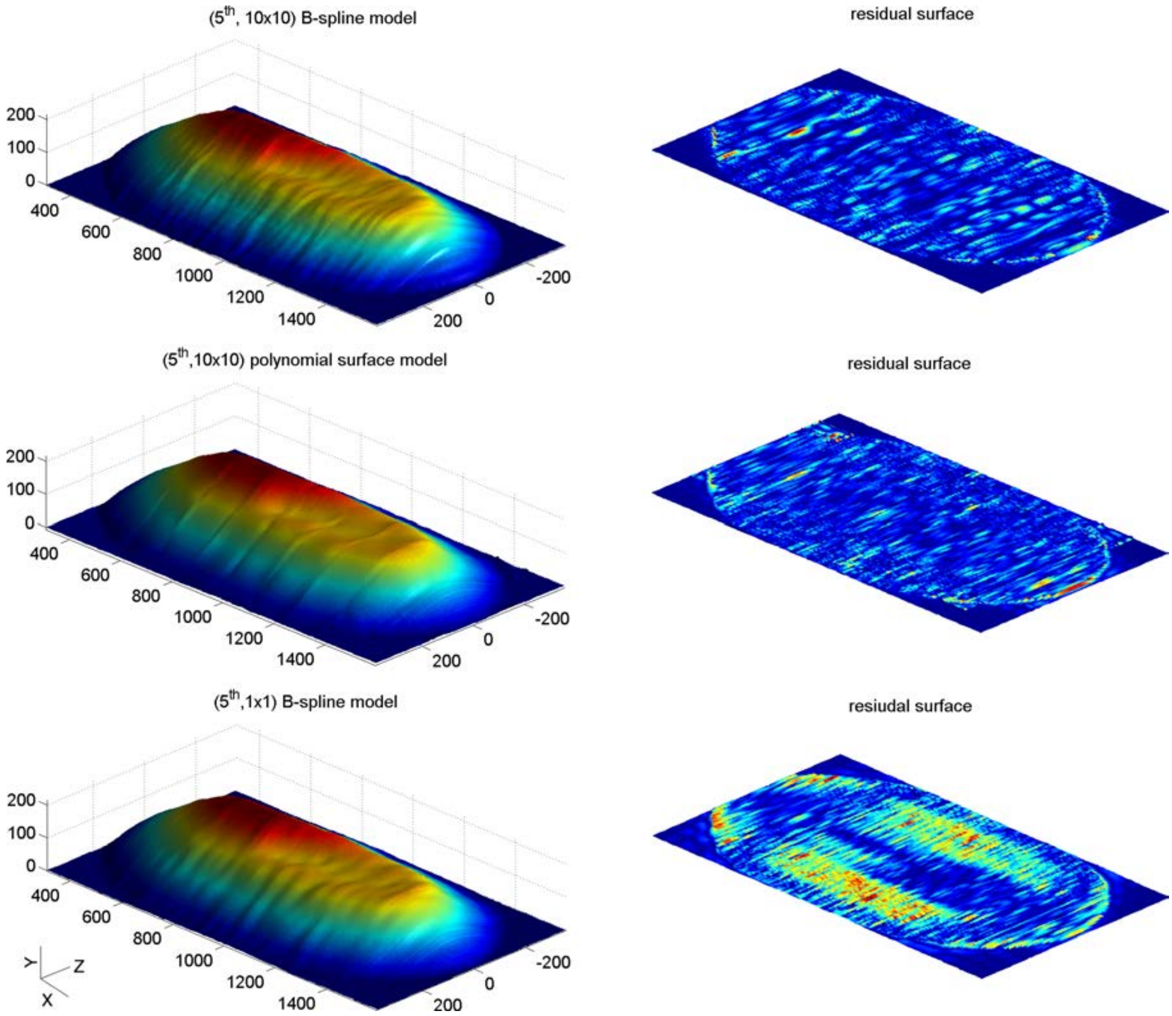

Fig. 4.32 B-spline and polynomial model comparisons of the partially reclaimed stockpile after 15 cuts (unit: mm).

instead of increasing the degree of the B-spline surface model, the grid partitioning method is applied to all the point clouds in this dataset. The modelling results shown in Table 4.12 and Table 4.13 list the volume calculated from all (3rd, 10×10) B-spline models. The percentage errors are calculated against the 'Volume of the layer' column listed in Table 4.9. For comparison purposes, the SSEs of these models are also listed here. From the results, it can be observed that the percentage errors of the (3rd, 10×10) B-spline models and the (7th, 15×15) polynomial models are very close. However, except for the 1st layer, the B-spline models are more accurate than the polynomial models.

Table 4.12 Surface modelling accuracy versus calculation time when apply grid partitioning to a full scale stockpile. (unit: time s, SSE m^2, MSE m^2)

Layer	(4th, 3×3)			(3rd, 4×4)			(3rd, 5×5)		
	Time	SSE	MSE	Time	SSE	MSE	Time	SSE	MSE
3	0.033	170.84	0.058	0.054	56.56	0.019	0.083	8.82	0.003
4	0.032	840.34	0.195	0.055	591.77	0.137	0.086	186.27	0.043
5	0.032	761.21	0.159	0.053	498.40	0.104	0.084	344.08	0.072
6	0.032	697.14	0.145	0.053	408.49	0.085	0.081	357.67	0.075
7	0.032	294.31	0.061	0.055	269.59	0.056	0.081	106.74	0.022
8	0.032	669.63	0.140	0.055	473.11	0.099	0.084	231.85	0.048
9	0.035	786.90	0.164	0.055	444.95	0.093	0.086	236.54	0.049
10	0.034	642.93	0.134	0.056	366.87	0.076	0.088	205.81	0.043
11	0.033	2839.18	0.364	0.056	1373.81	0.176	0.087	705.59	0.091
12	0.035	3182.89	0.392	0.057	1370.45	0.169	0.089	850.69	0.105
13	0.033	3340.31	0.404	0.057	1133.79	0.137	0.089	828.57	0.100
14	0.034	2248.58	0.272	0.056	1264.79	0.153	0.088	695.23	0.084
15	0.034	767.45	0.093	0.056	511.65	0.062	0.084	349.56	0.042
16	0.041	873.24	0.106	0.061	341.31	0.041	0.087	258.08	0.031
average	0.033	777.175	0.152	0.0555	485.755	0.096	0.086	301.08	0.0485

Fig. 4.33 compares two B-surface model of the 13th layer of the full size stockpile. The volumes of the stockpile calculated from these two models are: 68.1247 m^3 and 68.1260 m^3, respectively. The percentage errors are -0.030% and 0.028%, each. Although the SSE for the (4th, 3×3) model is larger than that of the (4th, 5×5) model, the volumes calculated from these models are very close to each other. The reason is that large residuals distributed around the sickle shaped cut of the (4th, 3×3) model will cause an increase in the calculation. Also, the removal of some geometric features (dents located around z = 30 m, z = 95 m and z = 120 m) from the model will reduce the volume in calculations. The combination of these two effects seems to be balanced in the volume calculation and reduce the percentage error. These results also support the fact that grid partitioning can improve the modelling

Table 4.13 The volume of the full scale B-spline models. (unit: volume m^3, error %, SSE m^2)

Layer	Volume of the model	Error	SSE B-spline	SSE Poly
3	13456.18	-0.50	1.032	0.370
4	22217.95	-0.21	1.626	3.802
5	31378.10	-0.15	2.582	3.179
6	40798.54	-0.10	2.437	3.151
7	51764.66	-0.08	2.444	1.938
8	44534.60	-0.09	29.876	29.485
9	41809.02	-0.10	37.342	172.144
10	33823.84	-0.12	35.301	38.481
11	44290.16	-0.16	127.60	176.485
12	57996.97	-0.3	157.562	203.681
13	68189.43	-0.24	154.399	153.221
14	80411.81	-0.21	149.778	102.821
15	92635.05	-0.19	46.927	22.316
16	103836.75	-0.17	22.238	14.764

accuracy. The average modelling times for these two models are still much faster than that of the polynomial modelling method.

Full scale simulation data. Fig. 4.34 illustrates the (4th, 10×10) B-spline model of the noise measurement data and its residual surface. The SSEs and MSEs for these two models measured against the ideal stockpile surface are 18.48 m^2 and 8.79 cm^2, and 186.47 m^2 and 88.71 cm^2, respectively. The average modelling time is 0.45 s. The volumes of these models are 230394.35 m^3 and 230443.47 m^3 and the errors in percentage are -0.0009% and 0.0242%, respectively. The results obtained from this simulation dataset further demonstrate the efficiency and effectiveness of the polynomial modelling. Generally, the B-spline modelling algorithm performs much faster than the polynomial modelling algorithm. It demonstrates better accuracy in modelling the stockpile using low order functions.

4.6 Summary

This chapter describes the automatic stockpile modelling algorithms designed for surface representation from laser scanning data. Four groups of datasets are employed to evaluate the algorithm. Out of these groups, two datasets are from laser scanning. A series of experiments were conducted carefully in a laboratory environment for the purposes of data collection.

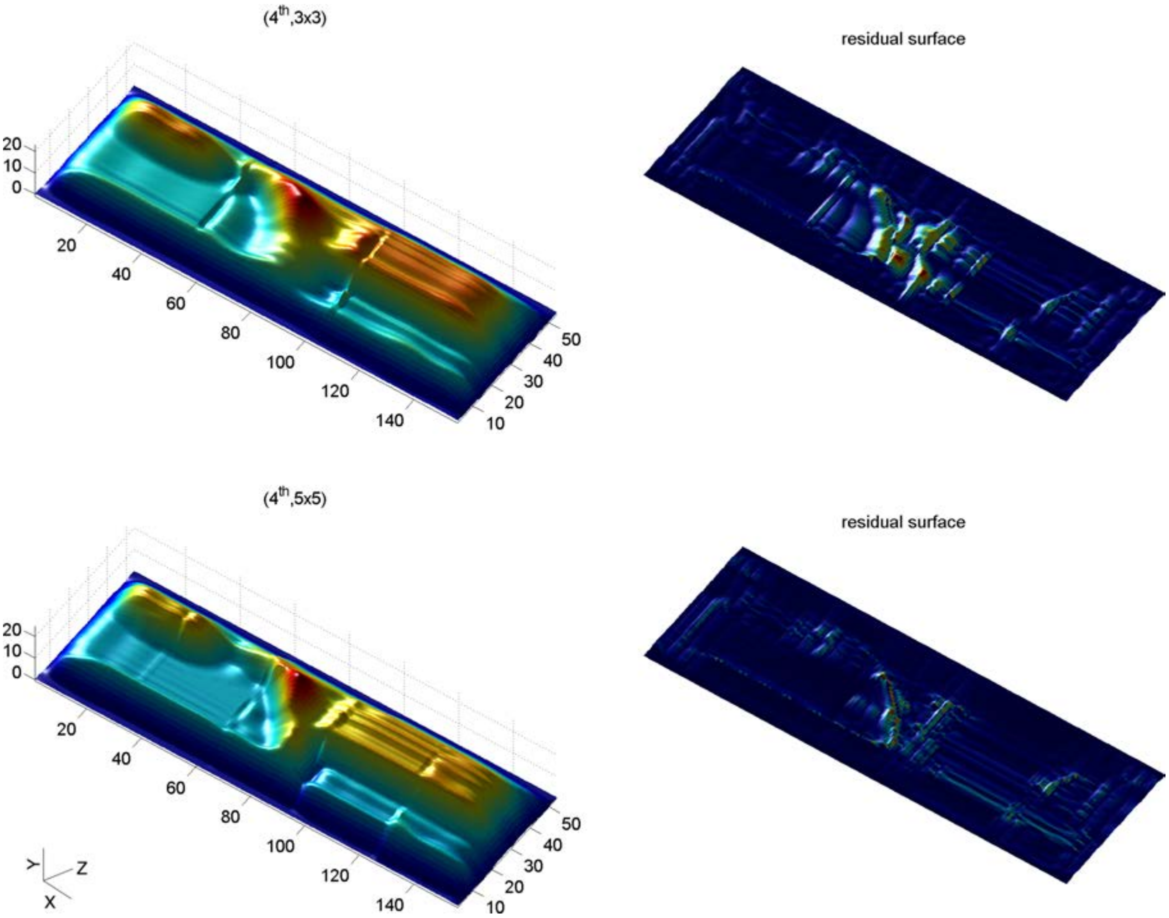

Fig. 4.33 The B-spline surface model of the 15th cut.

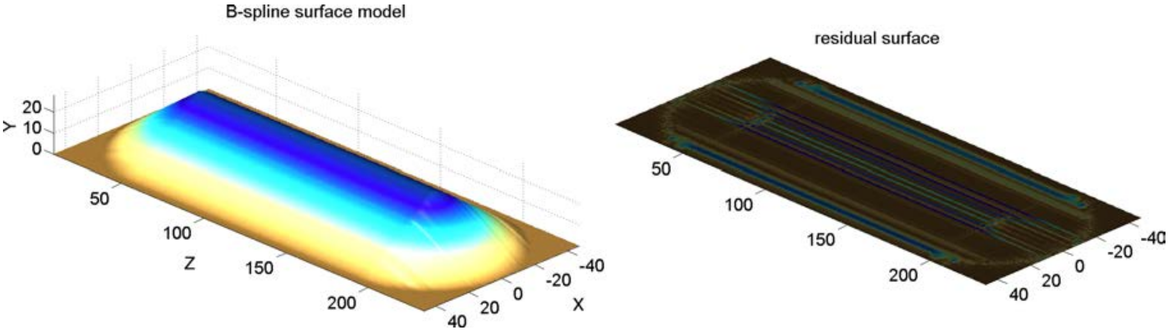

Fig. 4.34 The B-spline surface model of the noise measurement data (unit: m).

The other two datasets are from real measurement and computer simulation, respectively. There are 32 point clouds in total. These point clouds contain different geometric shapes and represent a variety of layers of a stockpile. The results obtained after evaluation prove the effectiveness and efficiency of the proposed modelling algorithms.

Laser scanning data can be processed and stored in real-time for future modelling purposes. The boundaries of the stockpile are detected successfully from the point clouds. Two different mathematical modelling approaches have also proven to be adequate, efficient and accurate for further applications in stockpile management. In Section 4.5, the polynomial and B-spline modelling algorithms are compared intensively against each other. In general, the B-spline approach is much faster and more accurate than the polynomial. However, polynomial approximation has a better performance in dealing with sensor noise than B-spline interpretation. To improve the modelling accuracy, the surface is partitioned into small patches. Meanwhile, such grid portioning also introduce over-fitting problems in polynomial modelling. The proposed surface normal comparison algorithm is able to detect most over-fitting events except for those which occurred in the full size dataset due to the low point resolutions.

Both polynomial and B-spline models can represent the geometric shapes of stockpiles faithfully and maintain a high degree of accuracy in volume calculations. With respect to the triangular prism, the percentage error in volume of the polynomial model is better than that of the B-spline model. However, for the bench and full scaled stockpile datasets, the percentage errors in volume are all less than 0.5%. Because these models are designed for industrial applications, which means there might be different requirements for the accuracy and execution time. Experimental results prove that increasing the order of the functions and the number of the surface patches in the partition will improve the accuracy. However, the cost is the program execution time. Therefore, these two parameters are suggested as needing and to be determined by the end user.

Clearly the number of the patches and the order of the function is in an inverse relation. When a surface is partitioned into more regions, both the geometric complexity of each patch and the number of points on the patch (used for surface fitting) are reduced. Thus, a low-order function is expected. Based on the bench scale dataset, the author would suggest the minimum size of a patch should no less than 82 mm along x axis and 142 mm along z axis. Also, according to the modelling results from the full-scaled datasets, the author suggests that the total patches should be less than 32 for a full size stockpile. Otherwise, over-fitting may occur frequently. In the meantime, the order of the polynomial and B-spline function should be less than 8 and 4, respectively. However, at this stage, it is very difficult to provide a universal guideline for the selection of surface patches and order of the surface function to avoid over-fitting due to the versatile geometry patterns of stockpile surface regions.

The volume calculated in this chapter is based on the Delaunay triangulation method. The point data are divided into triangles through connecting the data points as the vertices. By projecting these triangles onto the ground surface, a set of prisms is obtained. The volume under the surface is the sum of the volumes of these prisms. A major shortcoming of this method is that the accuracy is largely determined by the point resolution. A high-resolution point cloud will create more triangles and is able to approximate the true volume quite well. However, this method is still less accurate than the integral calculator. Given the polynomial function of a surface, the volume under the surface can be calculated directly using an integral calculator. The result obtained using double or triple integrals for a 3D object is believed to have the highest degree of accuracy. Due to the piecewise definition of the basic B-spline function, it is very hard to program an automatic integral calculator using digital computers. This is the most important reason that the author still reserves polynomial models even though B-spline modelling is much faster than the polynomial modelling approach.

Chapter 5

Quality Estimation and BWR Automation

Estimating the product quality beforehand or simultaneously with blending operations is crucial in improving fundamental stockpile management procedures. It allows the grade control and optimisation to be scheduled in advance. Together with the automated control of the BWR in reclaiming operations, the grades and tonnages of recovered material are predictable with a high degree of accuracy. Consequently, a proactive reclaiming pattern for BWR(s) that meets the set requirements in terms of both quality and quantity can be designed. Such a design will improve the effectiveness and efficiency in current bulk handling, and therefore increasing export potential and reducing costs. This chapter first describes a 3D stockpile management model and its application in BWR automation. Secondly, two voxelization algorithms and the procedures to estimate the quality in blending from the voxel models are introduced. Finally, the experiments and results are presented to demonstrate the quality estimation results from the proposed 3D stockpile management model.

5.1 3D Stockpile Management Model

In Chapter 3, a kinematic model suggested by Lu [50] is used to describe the movement of a BWR. This robotic model is further developed in this chapter, before being integrated into a 3D stockpile management model. Assuming that the bucket wheel is rotating at a constant speed and the material is being scooped evenly by the buckets during the reclaiming phase, the wheel with buckets can be considered as a circular ring. Also, if it is assumed that the boom of the BWR rotates perfectly according to its central axis, the slewing motion revolves the circular ring in 3D space and creates a non-degenerate torus surface out of the circular ring. In other words, given the slewing trajectory of the central point of the bucket wheel, the bucket wheel cutting trace (the toroidal surface) can be represented by a sequence of circles in 3D space because the centres of these circles are in accordance with the centres of the bucket wheel (see Fig 5.1). The major radius of the torus can be calculated using BWR kinematic equations, while the minor radius is the radius of the BW. Should the BW be tilted with a specific angle β, the projection of the circular ring to its rotating plane results in an ellipse and the revolving of the BW will generate an elliptic torus. The horizontal and vertical semi-axis of the elliptical cross-section is determined by the tilt angle and the radius of the BW.

Because both the stockpile and the BWR model have their own reference frames, a new global coordinate system (right-handed) is defined for 3D stockpile management modelling. The centre of the new coordinate is identical to the origin of the BWR kinematic model. The positive z axis normal to the crawler level forms the slewing axis. The positive y axis is in the direction of the BWR's advancement. The positive x axis is normal to the YZ plane. Consequently, once the distance between the stockpile boundary and the BWR centre is known, a 3D stockpile management model is generated after the coordinate transformation. For display purposes, the stockpile model is rendered as a smooth surface and the BWR model is plotted as solid lines. A graph for such a model will be given in the next section.

5.1.1 BWR Automation

A BWR is a combined machine that stacks and reclaims bulk materials. Automatic stacking is achievable based on the measurements from on-board encoders. Outputs from the wheel encoder(s) are used to control the travelling velocity and moving distance. Feedback from the luffing encoder determines the height of the boom-head which is also used to control the elevation of the discharge pulley to maintain a constant space between the stockpile and discharge point.

BWR Reclaiming is controlled semi-automatically or manually due to the reason identified in the literature section: the lack of real-time geometric knowledge of a stockpile and the lack of cooperation and interaction between the stockpile model and the BWR controller.

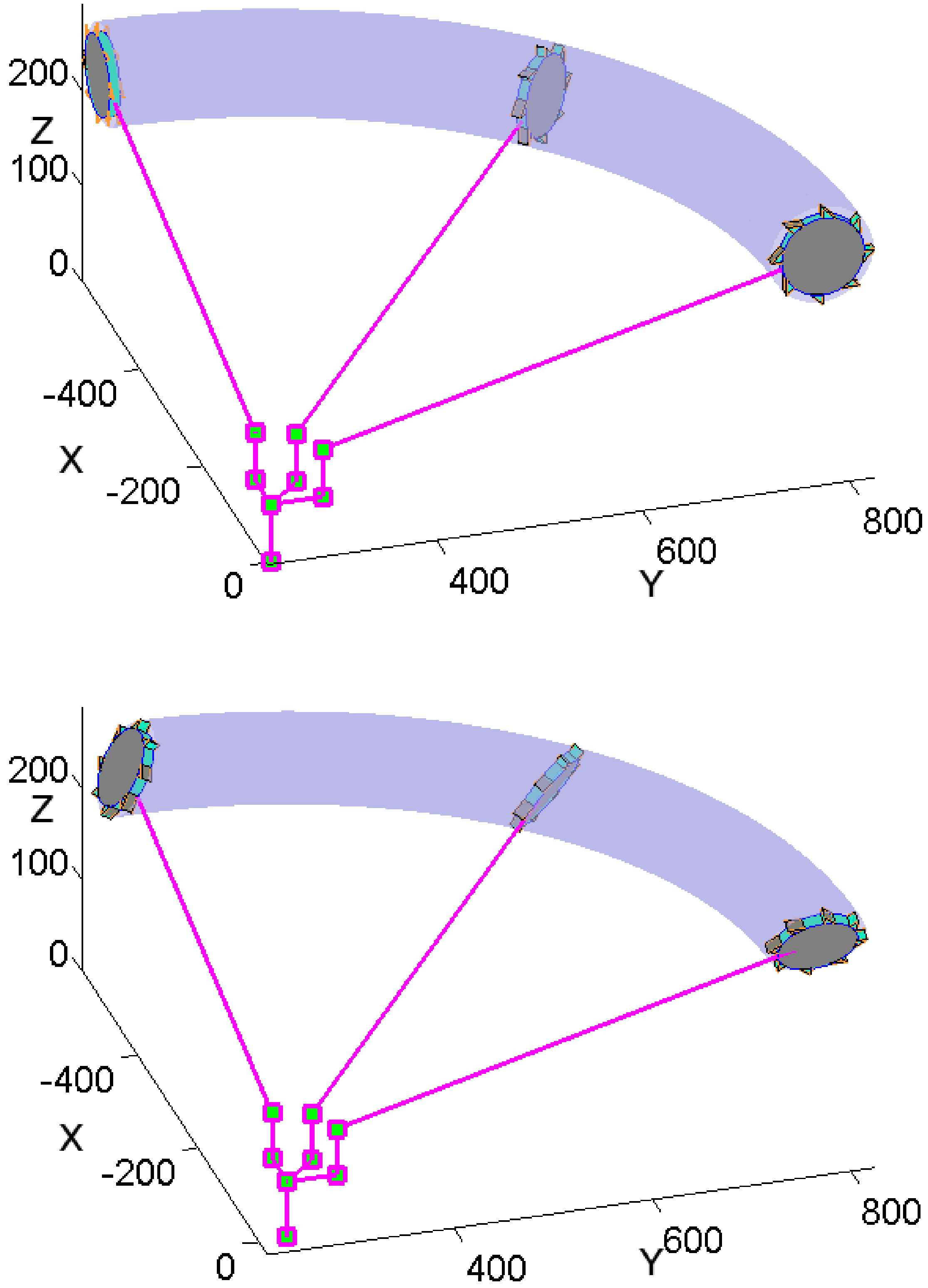

Fig. 5.1 Ideal torus generated through superimposing the rotation motion of the BW and the slewing motion of the boom. The magenta line with green squares indicates the boom of the BWR (unit: mm).

When a stockpile is recovered using the bench reclaiming (or terrace cutting) method, an operator selects a landing point on the stockpile surface manually, based on his experience, and then approaches the BW to that point with great care. When the contact is about to happen, the operator activates the circular motion of the buckets to enable buckets to pick up materials from the stockpile simultaneously with the landing. Normally, the rest operations are controlled automatically until the height of the BW is changed. The slewing range is determined by the feedback from the loading sensor. The lateral motion begins to stop until the resistance force is no longer detected by the sensor. If the BWR is controlled manually, the slewing range is based on human vision. Thus, when the bucket wheel is seen to be out of the stockpile completely, the operator stops the slewing motion. In either control logic, there is always extra fuel to be burnt because the lateral motion cannot be stopped immediately. After the first cut, the BWR is advanced with a fixed cutting depth (i.e. $0.9 \times$ bucket width) to conduct a new cut. When the BW is lowered to start a new reclaim, the operator needs to choose the correct landing point again. Therefore, BWR automation contains two tasks: to land the BW onto the stockpile without causing collision for all the cuts in one reclaim and to calculate the slewing range of each cut for the BWR controller. More importantly, landing is crucial for future quality control because the cutting depth of the BW is fixed in most cases.

The problem of BWR automation in this project is stated as the need to create a set of candidate points P_c from the stockpile model and validate a subset P_v that must not cause collision between the wheel body and the pile of all the cuts in one reclaim. Additionally, it covers the need to predicate the joint angles of the BWR $(d_1, \theta_2, \theta_3)$ to initialize the first cut for all the points in P_v. Meanwhile, it is necessary to calculate the slewing start and stop the angle of each cut for all the points in P_v. A cut means a revolving motion of the boom and a reclaim is a collection of cuts with equal cutting height.

5.1.2 Landing Point Estimation

An infinite number of points can be created from a mathematical stockpile model and every point could be a candidate point. It is neither feasible nor necessary to assess all these points. The candidate point set P_c is selected according to three criteria: the effective cutting depth, the facing direction and the square grid spacing. The effective cutting depth (D_e) is defined based on the maximum cutting height of a BWR, as shown in Fig. 5.2. Assuming that material inside the bucket starts to fall due to gravity at a certain angle ϕ, the maximum cutting height

H approximately equals $(R_v + R_k \sin\phi)\cos\beta$ and $D_e = max(P_{L\_z}) - H$. Additionally, because the BWR is normally mounted on rails or tracks, only one side of the stockpile is available for the landing mission. The first two criteria can be summarised as being only those points within the effective cutting region and facing the BWR mounting direction. However, there are still infinite points after thresholding. To obtain a finite set, the stockpile region on the XY plane is partitioned into a group of contiguous square cells (the grid partitioning method described in Section 4.4.1). Then, the centres of these grids are superimposed on the stockpile surface. Thus, a finite set P_c is created after such a grid reference method. Obviously, a small grid spacing (high resolution) will generate more points in the set.

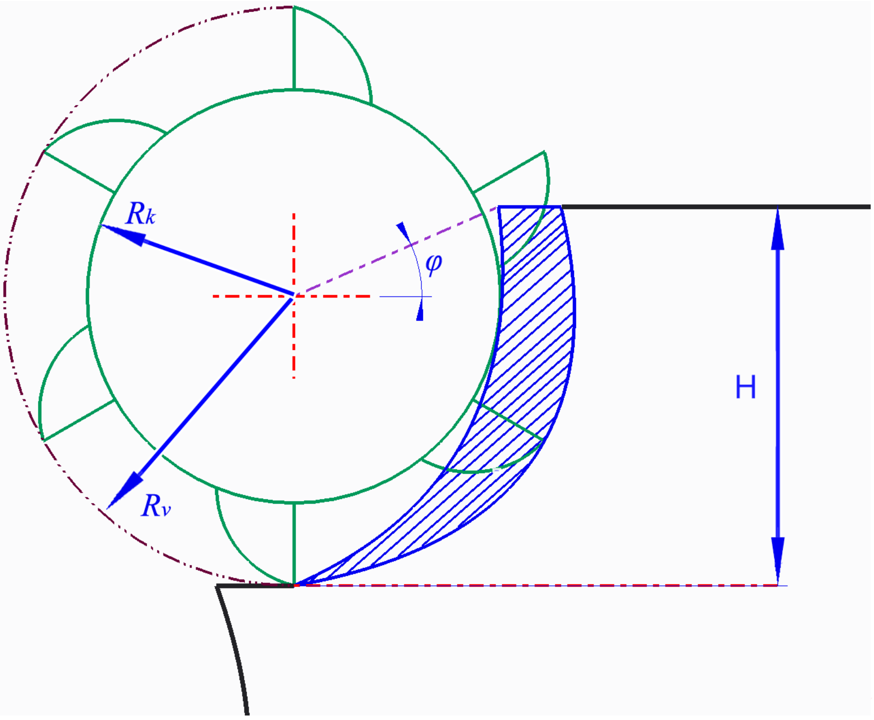

Fig. 5.2 The maximum cutting depth (H) of the BW in regard to the bank surface. ϕ is the angle at which material starts to fall from the bucket. The shadowed area indicates the material that is recovered by the buckets.

To calculate the joint positions of the BWR for a given query point p_q in P_c using inverse kinematic equations, the central point of the BW in 3D space needs to be identified. Furthermore, to calculate the centre of the BWR, the exact contact point between the BW and the stockpile must first be located. Due to the rotation of the BW, which creates another degree of freedom, the exact contact point between the BW and the stockpile surface cannot be solved using the kinematics of the BWR directly. However, the purpose of the auto-landing is not to locate the exact point on the BW that is tangent to the stockpile surface at p_q. Also, such a point does not always exist in reality due to the fact that the degrees of freedom of the BW are limited. Instead of creating more complex constraint functions to find such a tangent point, a simple way to approximate the position of the centre C_{bw} of the BW is to assume that the vector between two points (C_{bw} and p_q) is in accordance with the surface normal at point p_q (see Fig. 5.3). Therefore, $C_{bw} = p_q + R_v N_s$. The normal vector N_s at p_q can be calculated using the stockpile model. Once the C_{bw} is known, the d_1, θ_2, θ_3 can be solved using inverse kinematic equations. Thus, the initial cutting position of the BWR is known. The definition for d_1, θ_2, θ_3 and L_2~L_4 can be found in Lu's paper [50] and are shown in Fig. 5.4.

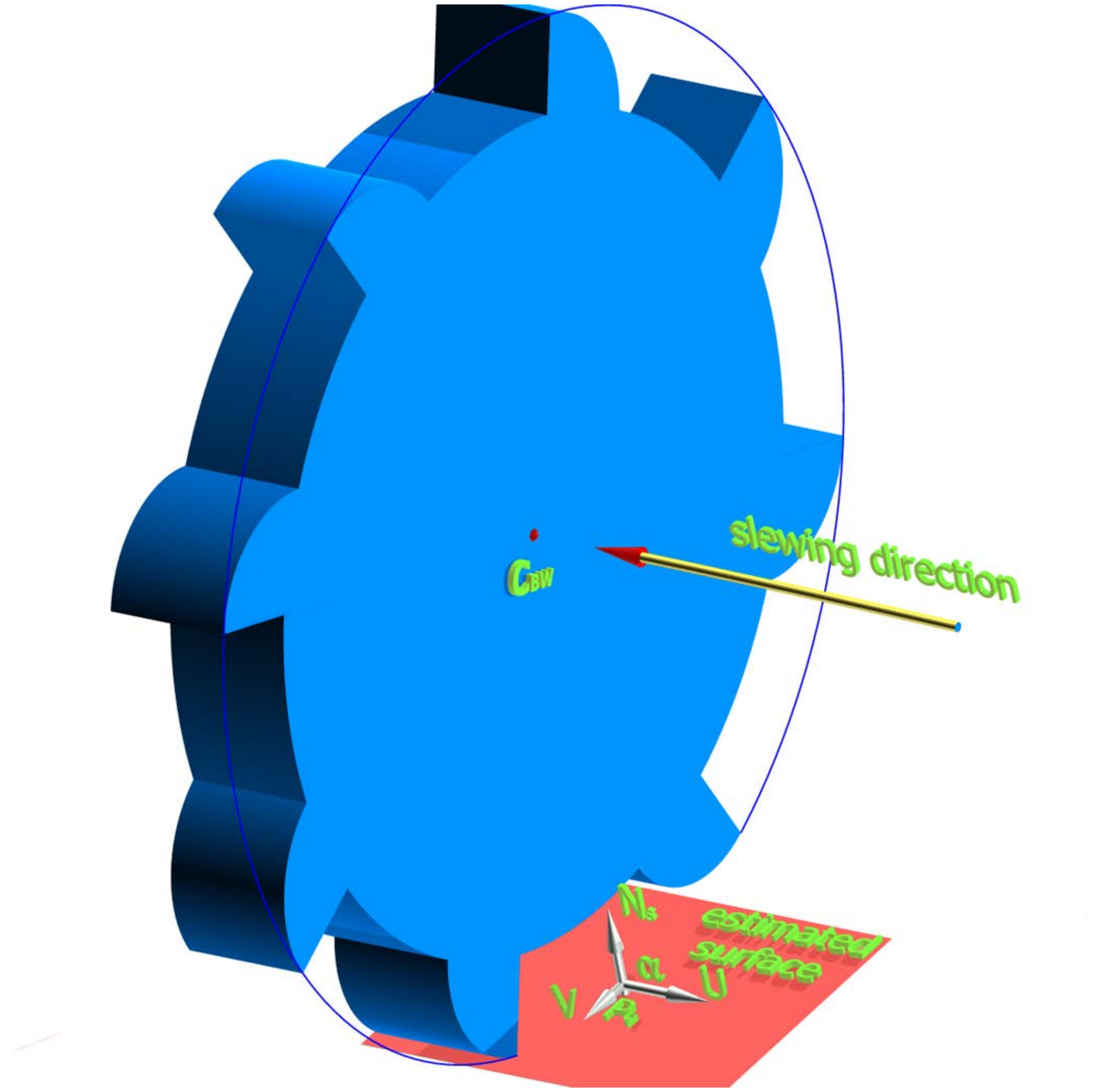

Fig. 5.3 Landing the bucket wheel on the stockpile. An ideal case when determining the BW's centre from the surface normal. The normal vector N_s of the least square surface at the point p_q is tangent vector U. U is in the opposite direction from the slewing direction of the bucket wheel at p_q. Vector V is directed towards the slewing axis of the BWR. The angle between N_s and U is α and $\alpha = 90°$.

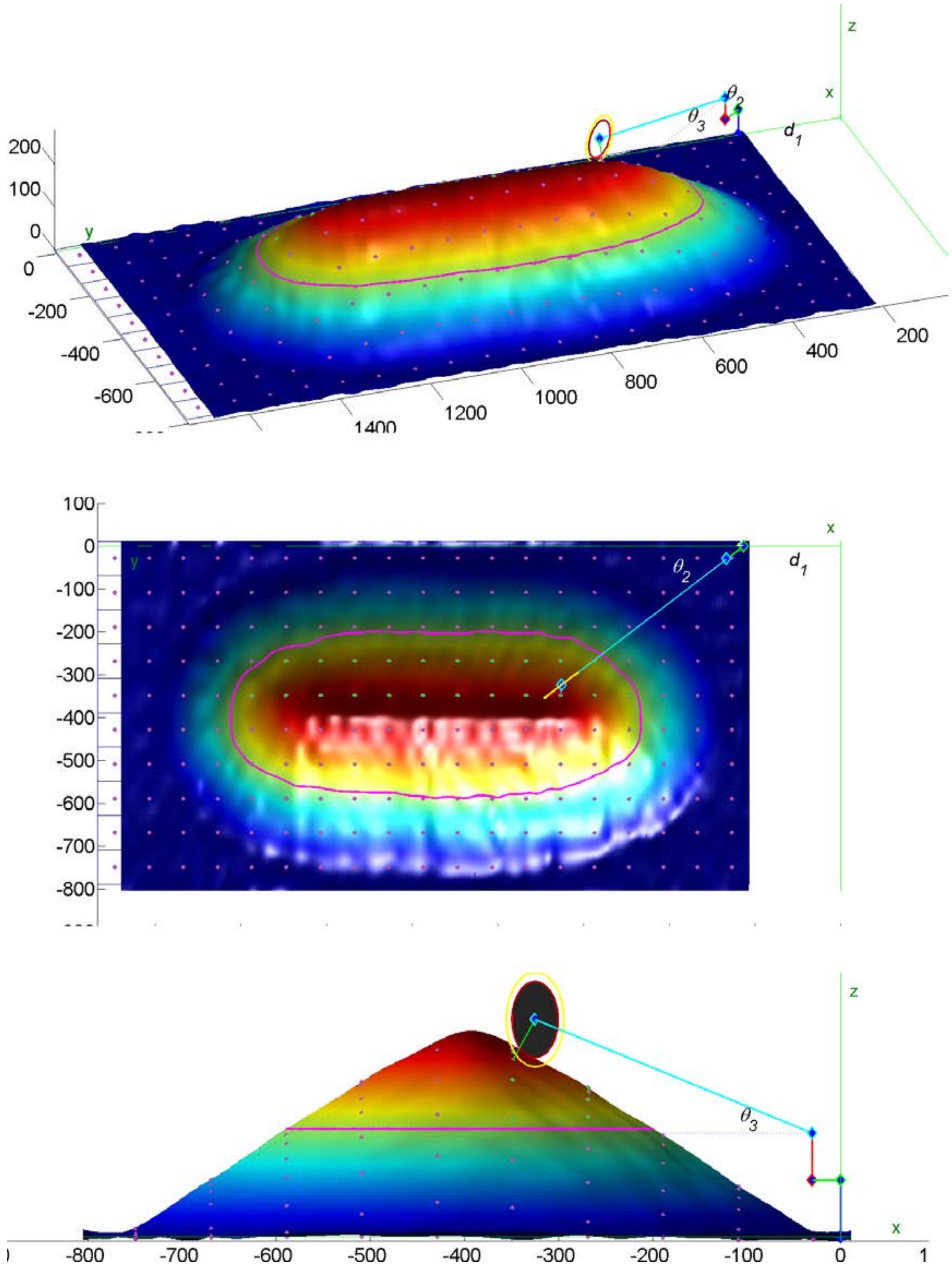

Fig. 5.4 Evaluating the landing point set using a stockpile management model. The stockpile is partitioned into a 19 ×10 patches. Each patch in the square grid is 80 *mm*. The query points are highlighted in green. The effective cutting region, determined by the maximum cutting height, is enclosed by a magenta curve (unit: mm).

To detect the collision between the wheel and the stockpile in one cut is to detect whether the points on the stockpile surface are also inside the torus generated by the revolving motion of the BW. If the cross-section of the toroidal surface is a circle, a point $p_s \in P_c(p_{s\_x}, ps\_y, ps\_z)$ lies inside the toroidal surface if:

$$\left(R_m - \sqrt{(p_{s\_x} - x_0)^2 + (p_{s\_y} - y_0)^2}\right)^2 + (p_{s\_z} - z_0)^2 < R_k^2 \tag{5.1}$$

where R_m is the major radius of the torus and $R_m = L_5 \sin\theta_3 + L_4$ and R_k is the radius of the wheel, which is equal to the minor radius of the torus. x_0, y_0 and z_0 are the centre of the BW in 3D, as determined previously. If the cross-section is an ellipse, a point is inside the elliptic torus if:

$$\frac{\left(R_m - \sqrt{(p_{s\_x} - x_0)^2 + (p_{s\_y} - y_0)^2}\right)^2}{(R_k \cos\beta)^2} + \frac{(p_{s\_z} - z_0)^2}{R_k^2} < 1 \tag{5.2}$$

where β is the zenith angle of the BW to the z axis in the stockpile management model.

5.1.3 Slewing Range Estimation and Model Updating

The slewing angle of the BWR will be calculated if no collision is detected in a single cut. Also, the recovered region needs to be replaced by the helical-shaped cutting surface (a part of the torus) for the next assessment. For these two purposes, the stockpile is presented as a set of points in 3D space calculated from its spline model. The elimination of recovered points from the stockpile is quite easy because Eq. 5.1 and 5.2 remain validated. The only change is to replace R_k by R_v. The cutting surface is the region that is enclosed by the intersecting curve between the torus ($T(s,t)$) and the B-spline stockpile model ($S(u,v)$), supposing that the torus is defined topologically as the product of two circles, s and t. The intersecting curve is an algebraic equation $T(s,t) - S(u,v) = 0$. Once the equation is solved, the cutting surface can be obtained to update the stockpile model. However, the relatively high degree of the algebraic representation of the stockpile surface may lead to an even higher degree algebraic curve. Because the algebraic degree and genus are too high to be solved mathematically, a numerical approach is proposed to determine the intersecting curve. After the intersecting curve is detected, the slewing range of the BWR can be also obtained.

This numerical approach separates the continuous slewing motion into a group of discrete angular steps. The range of the slewing motion created here is from 0 ° to 90 ° with a step size of 0.5 °, which is much larger than the actual slewing range in reclaiming operations. At each angular step, the origin of the BW (C_{bw}) is calculated using the BWR kinematic equations. Meanwhile, because a circle in the stockpile management model that represents the BW can be described using its parametric equation, a set of points P_{bw}, centred at C_{bw} with a radius of R_v, is created. Theoretically, the intersecting point(s) q $(q \in P_{bw})$ between the circle and stockpile surface satisfies $S(q\_x, q\_y) - q\_z = 0$. In other words, the Euclidean distance D between point(s) q and the stockpile surface $S(u, v)$ is/are zero. Because the circle is represented by a set of points, an approximation would be finding out the points from P_{bw} that have a minimum Euclidean distance to the stockpile surface and the minimum distance $min(D) \approx 0$. If the $min(D)$, obtained after calculation, is much large than zero, the circle is not intersected with the surface of the stockpile.

Because the BW will only intersect with the stockpile at two points at most, this numerical approach is sufficient to determine all the intersection points. Once the intersecting points are detected, P_{bw} can be separated into two subsets: inside and outside the stockpile. Points inside the stockpile and the two intersecting points will be inserted into the stockpile model. Points outside the stockpile are eliminated. Also, from 0 ° to 90 °, the intersecting conditions will change twice: from non-intersecting to intersecting and from intersecting back to non-intersecting again. Therefore, the iteration will stop if the 2^{nd} non-intersecting condition is detected. Thus, the actual slewing range within which the BW cuts into and moves out of the stockpile is obtained. Fig. 5.5 plots the shape of the stockpile after the first two cuts. The elimination and model updating procedure proceeds iteratively until a reclaim is completed or a collision has been detected. Thus, the slewing ranges of all the cuts in the reclaim are acquired and such information can be used as an input to the BWR controller and guide the motion of the BWR in real operational procedures.

5.2 Quality Estimation in Blending

The quality of an element acquired after the chemical analysis is expressed as a percentage by weight of the entire compound with the mean and standard deviation. Given the general knowledge that the stacked ore (after mechanical crushing and screening) is normally in the same size level, the density of the iron ore can be considered as a constant [69]. Therefore,

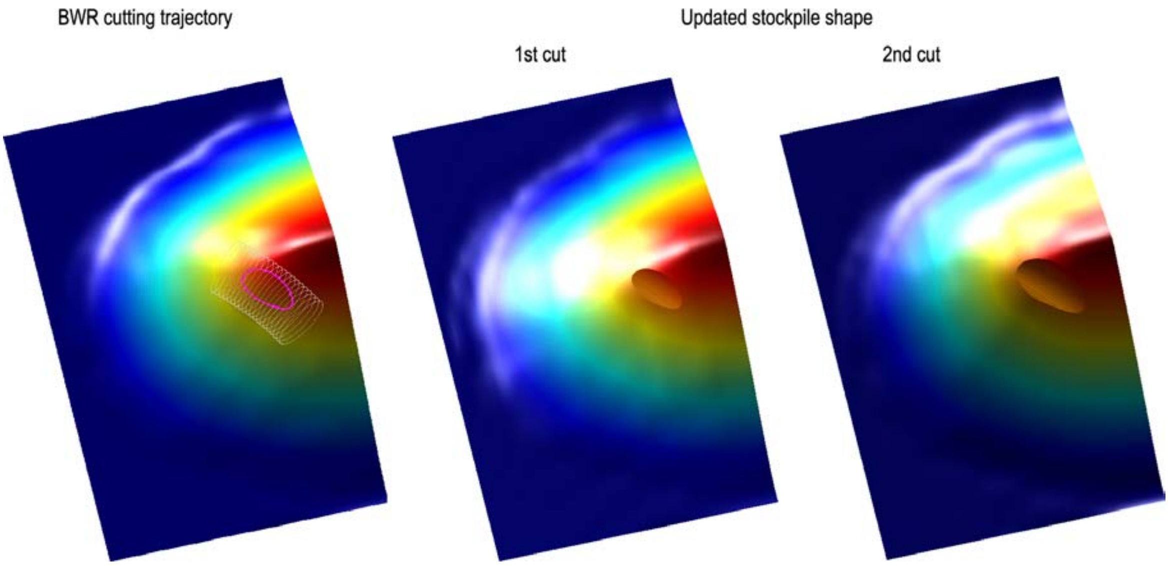

Fig. 5.5 Updating the shape of the stockpile after the BW cut out the stockpile using the trajectory generated from the BWR kinematic model. The closed magenta curve highlights the region that will be removed from the stockpile model.

the quality of a certain chemical component in a 3D space is linked with the volume of that 3D space. In this section, a model that simulates the grade variations is outlined first. Then, the two voxel models that link the geometric shape of the stockpile and the quality model used for quality estimations in blending are detailed.

5.2.1 Grade Variability Modelling

Because a homogeneous stockpile or a layer in the stockpile does not exist in reality, it is necessary to reflect the quality fluctuations in the chemical composition during the calculation. At this stage, due to trade secrets, the authors have no access to the real chemical assay results and long-term quality information. Therefore, the quality distribution model is based on the data and information provided by MatrixGroup. It is assumed that the fluctuations in quality along the stacking direction are satisfied with a normal distribution. The assumption is generally true because the previous handling processes will improve the homogeneity of the stacked material and the variation in grade will fluctuate slowly compared with the length of the stockpile. To embed the quality information into the geometric model, the stockpile is considered to be cut through by a group of equidistant parasagittal planes along the y axis of the 3D stockpile management model. The distance between the adjacent parasagittal planes is assumed to be a user-specified parameter here, although, in the next two sections, it is determined according to the size of the voxel.

For a slice in the stockpile, a bounding box, called a cuboid, is created from the outmost layer of the stockpile. The bounding box intersects with all the layers in the stockpile and the quality of an intersection between the bounding box and layer is assumed to be homogeneous. Under this assumption, the mean and standard deviation of every single element (i.e. Fe, Al or Si) are entered into a subroutine to generate pseudo-random numbers that follow the specified normal distribution. The output data from the subroutine are used to represent chemical variations when predicting the quality of the material. The quality values are then assigned to the cuboids along the stacking direction for quality predictions (see Fig. 5.6).

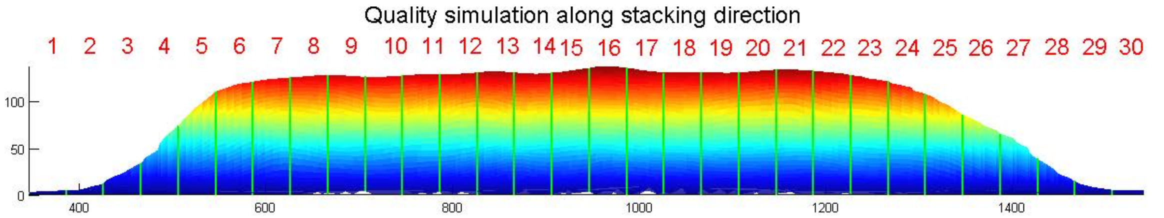

Section	1	2	3	4	5	6	7	8	9	10	11	12	13	14	15
Fe %	53.0796	47.3493	52.1889	58.9240	57.6546	51.6622	62.1656	61.0741	61.2505	53.6750	64.0830	61.3446	74.3919	64.1880	64.8479
Section	16	17	18	19	20	21	22	23	24	25	26	27	28	29	30
Fe %	57.0540	47.5840	54.0592	51.3300	52.6984	60.5993	52.7491	50.3605	53.7901	55.5441	59.5699	49.9544	58.9203	57.2308	66.0302

Fig. 5.6 A quality distribution model of a one-layer stockpile (unit m). The stockpile is manually partitioned into 30 sections by a group of equidistant parasagittal planes along its stacking direction. For each slice, the quality properties are simulated by a sequence of normally distributed numbers. For example, the percentages of Fe are listed.

5.2.2 Stockpile Voxelization for Quality Prediction

Two voxel models are designed in the study. The first is the cubic voxelization and the second is the sickle-shape voxelization. Between these two models, the sickle-shape voxel is designed especially for reclaiming operations.

5.2.2.1 Cubic Voxelization and Quality Estimation

In this model, a stockpile is represented as a group of 3D grid of voxels (volumetric pixels) other than a surface and edges. Each voxel is in a cubic shape and has an individual sequence number and is linked with a specific quality cuboid in the quality distribution model according to its geometric position. The benefit of this model is that it can be created directly from the wireframe model. These voxels are the basic quality units for the quality estimation during the blending. Through tracking the positions of these voxels, the quality of the reclaimed material can be predicted. The combination of the cubic voxel stockpile model and BWR model is called a cubic stockpile management model in this thesis.

Cubic voxelization is a procedure that represents an object by a set of discrete volumetric elements (cubes). It is achievable through geometric modelling techniques, such as Octree encoding [70]. In a regular octree structure, each node represents a cubic region. The node at the top of the structure is called the root and the root octant surrounds the entire domain of the object. The root octant is then divided into eight octants recursively until a sufficient resolution attained. As a result, each node has exactly eight children, except for the leaf nodes.The nodes at the bottom level of the tree structure are called leaf nodes or voxels. However, for this particular application, the hierarchical relations between nodes are not necessary. Therefore, the voxelization of the point cloud data is performed by calculating the geometric positions between octants. Given the wireframe model of the outermost layer of a stockpile F_s and the level of the Octree structure t_l, the side length L_C of the root octant is:

$$L_c = max[(x,y,z)_{max} - (x,y,z)_{min}] \tag{5.3}$$

The side length of the voxel o_l is $L_c/2^{t_l}$. The coordinates of the voxels' centres are:

$$(x,y,z)_c = (x_{min} + (i_l + \frac{1}{2})o_l, y_{min} + (j_l + \frac{1}{2})o_l, z_{min} + (k_l + \frac{1}{2})o_l) \tag{5.4}$$

The bounding coordinates of these voxels are:

$$\begin{cases} (x_c,y_c,z_c)_{min} & = & (x_{min} + i_l o_l, y_{min} + j_l o_l, z_{min} + k_l o_l) \\ (x_c,y_c,z_c)_{max} & = & (x_{min} + (i_l+1)o_l, y_{min} + (j_l+1)o_l, z_{min} + (k_l+1)o_l) \end{cases} \tag{5.5}$$

where i_l,j_l,k_l is the index of the voxel and:

$$(i_l, j_l, k_l)_c = ((\frac{x - x_{min}}{o_l}), (\frac{y - y_{min}}{o_l}), (\frac{z - z_{min}}{o_l})) \tag{5.6}$$

Thus, a voxel model is created out of the wireframe model of a stockpile directly after both the side lengths and the centres of the voxels are known. In this voxel model, o_l is also called the voxel resolution of the model. Also, if needed, the side length of the octants in all the levels between root and leaf can be also calculated. A primary property to describe the state of a voxel is empty or occupied, which means the voxel is free or occupied by point/points, respectively. Based on the geometric positions of the points and the voxels, the state of a voxel can be determined in a straightforward manner. If there is no point, there is no voxel. However, because the point data is a spare representation of a stockpile, the original scanning data may be insufficient for high resolution voxel modelling. The problem, is essentially twofold: firstly, if the point resolution in either x, y or z axis is smaller than the voxel resolution, voxels after modelling may be isolated from their neighbours. Secondly, because points are obtained from stockpile surface only,no voxel will exist inside the stockpile after the modelling. To generate a solid and watertight voxel model, the following two steps that insert points into the scanning data are introduced:

- Point interpolating
  This operation aims to increase the point resolution.The interpolation can be done using the previously developed wireframe or surface modelling algorithm if the point resolution is lower than the voxel resolution. It is also worth to mention that a wirefram model improves the point resolution along x and z axis only, while a surface model increases the resolution in 3D space.

- Bench filling
  This operation aims to generate more points inside the 3D space enclosed by the stockpile surface and the ground. It inserts a sequence of virtual planes, parallel to the ground, called benches to the point cloud. The distance between each plane is slightly less than the voxel resolution. Then, the boundary of the intersecting region between a bench and the stockpile is approximated using the boundary detection algorithm, described in the pre-processing stage. After a set of edge points are obtained, a convex hull is created from these edge points. Finally, the virtual bench is represented by a set of points and the points inside the convex hull are inserted into the point cloud.

Thus, a solid voxel model can be obtained after point interpolating and bench filling. Fig. 5.7 illustrates the voxel model generated from the 8$^{\text{th}}$ wireframe model.

A cubic voxel model has a similar effect to the grid partition method. Instead of separating the stockpile region based on the size of a measurement matrix, the stockpile region is divided by its dimensions. Also, a stockpile is represented as a group of identical cubes after voxelization. These voxels are easily linked with the quality model because a group of voxels

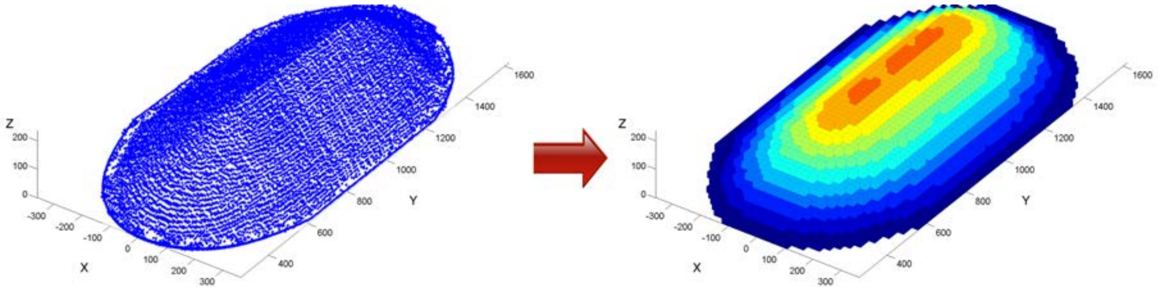

Fig. 5.7 A cubic voxel model created for the bench scale stockpile (unit: mm).

whose centres lies on the same plane form one cuboid (the quality unit). Thus, a cubic voxel model is a perfect fit for polynomial surface modelling and quality calculations using integral calculators.

Due to the fact that a stockpile is always stacked with multiple layers, these layers may cut through a voxel and separate the voxel into a sequence of subspaces. Furthermore, materials in different layers may have different chemical composition, which means the quality grades in these subspaces are also different. Therefore, the quality of a voxel should be calculated based on the volumes of these subspaces. Consequently, the volume of each portion of the layer needs to be calculated separately. An intersection between a voxel and a layer is called a quality-volumetric object (QVO) in this thesis. Thus, a voxel could contain multiple QVOs.

Fig. 5.8 a) shows the intersection between the three-layer stockpile and the voxel results in three surface patches, which are highlighted in brown, blue and purple colours, respectively. These surface patches partition the voxel into three QVOs. Thus, the volumes that required to be calculated include: the volume between the bottom facet of the voxel and the first layer, the volume between the first and second layer and the volume between the second and third layer. In this thesis, the sum of the volume of these quality-volumetric objects is called the quality volume of a voxel or quality volume in short.

A convenient method to calculate the volume of such quality-volumetric objects is to use the double integral from the polynomial model. The spline model is not suitable here because it is a piecewise-defined function which requires much more complex code than the polynomial

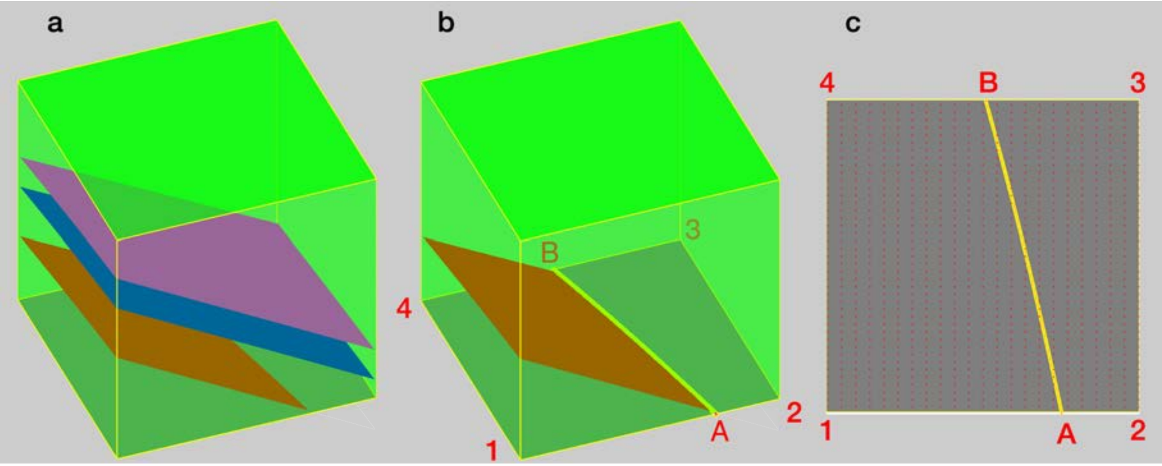

Fig. 5.8 QVOs inside a voxel. a) QVO created by layers. b) The quality volume between the 1^{st} layer and the bottom of the voxel. c) The 2D region R_{1AB4} used in volume calculations. The intersection curve C_{AB} between the 1^{st} layer and the bottom of the voxel is highlight in yellow.

model. The quality volume for a voxel is:

$$\begin{cases} V_{sn} = \iint\limits_R [S_n(x,z) - o_l b_h] dA & S_n = 1 \\ V_{sn} = \iint\limits_R [S_n(x,z) - o_l b_h] dA - V_{sn-1} & S_n = 2, \cdots, N \end{cases} \tag{5.7}$$

where S_n is the index of the layer, $S_n(x,z)$ is the polynomial function of the layer, o_l is the side length of the voxel, b_h is the index of the bench height and R is the bounded region determined by the surface patch and the voxel. The only unknown is the 2D region R.

To calculate the double integral automatically, the region R bounded by the stockpile layer and the voxel can be classified into two formats: a cubic or a general region. If there is no intersection between the stockpile layer and the bottom facet of the voxel, R is a cubic region bounded by the edges of the voxel. The calculation of the double integral can be done simply. Conversely, if any layer intersects with the bottom facet of the voxel, R is a general region and one side is the intersection curve of the two surfaces, as shown in Fig. 5.8 b). With the general region, the intersection curve function is needed for the double integral calculation.

A numerical approach is used to find the intersection curve. It firstly converts the laser scanning data from a 3D point format into a triangular mesh surface. Secondly, the intersection line between a triangular surface and a horizontal plane is calculated separately. Again, the detection results are represented as a set of points and the intersection curve is the union of these point sets. Fig. 5.8 c) is the top view of the voxel. The detected intersection curve C_AB is highlighted in yellow. Thirdly, a thresholding is applied to determine the appropriate fitting function for the point set. If the standard deviation in the x coordinates of these points is less than 10 mm, these points are believed to be on a straight line and will be fitted as a straight line (a 1st order polynomial function). Otherwise, they are considered as a curve and will be fitted by a 3rd order polynomial function. The following symbols are defined for the automatic calculation of the double integral. Vertices and edges on the facet of the voxel that intersects with the stockpile layers are named v_i and e_i in a counter-clockwise direction as shown in Fig. 5.9.

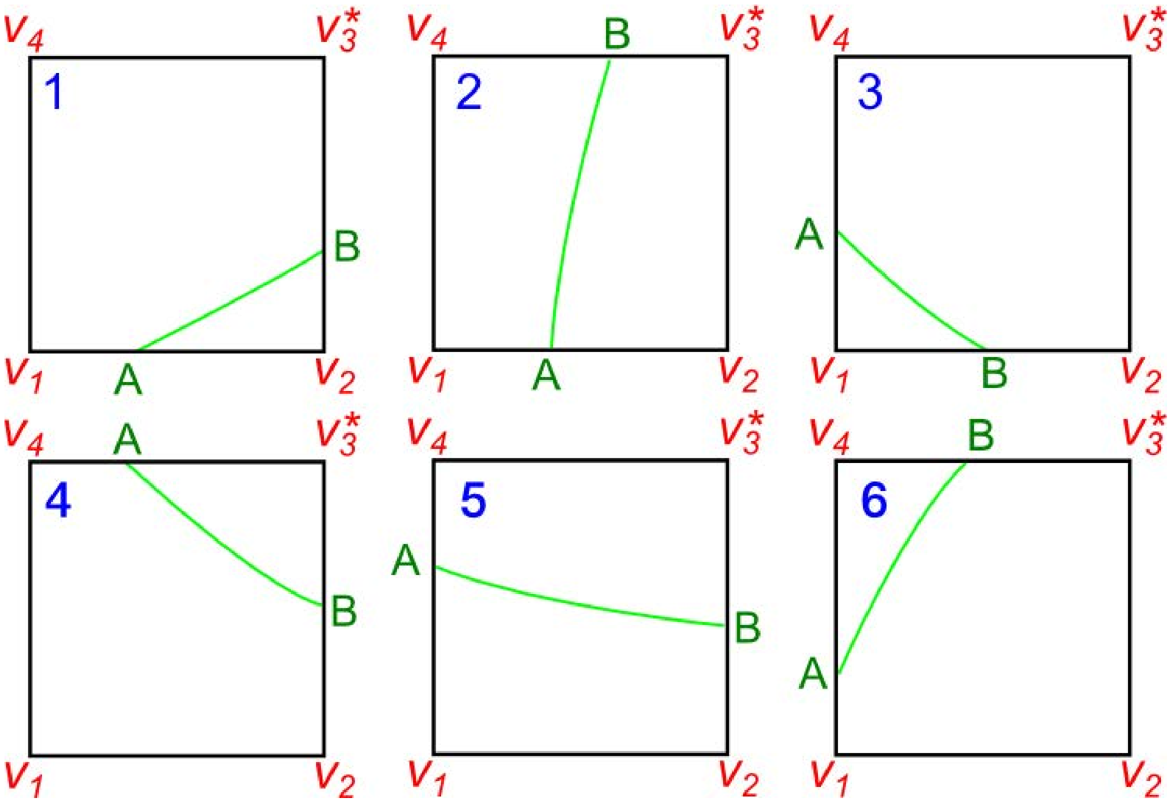

Fig. 5.9 Table of the 2D region R used for automatic double integral calculation. The P_{SV} is assumed to be located right on top of the v_3.

The index i starts from the bottom left vortex (x_{min}, z_{min}) and grows counter-clockwise. The end-points of the intersection curve are called v_A and v_B. Thus, the region R has four vertices: v_1, v_2, v_A and v_B and is called R_{12AB}. The summit point, which has the maximum elevation in the y coordinate of the layer within the voxel, is named P_S. The nearest neighbour vertex of the P_S is v_{inn} and a virtual point has the same x and z coordinates as the v_{inn} but on the stockpile layer is called P_{SV}. It is a virtual point because it may not exist in the laser scanning data but can be calculated from the surface model. With every single P_{SV}, there are six outcomes (C_4^2) that indicate the geometric position between the curve C_{AB} and the edge e_i (see Fig. 5.9). Based on the geometric position, the calculation can be classified into four cases and the calculator can be programmed based on these cases. For example, if the P_{SV} is collinear with the v_3, the quality volume of the first layer is:

1. If the v_A and v_B are on the e_1 and e_2, the region R is partitioned into two sub-regions. The first is $x = x_{v1}$, $x = x_A$, $z = z_{v1}$, $z = z_{v3}$ and the second is $x = x_A$, $x = x_B$, $z = h(x)$, $z = z_{v3}$. The volume calculated using the double integral is:

$$V_s = \int_{x_{v1}}^{x_A} dx \int_{z_v 1}^{z_{v3}} [f_n(x,z) - d_l b_h] dz + \int_{x_A}^{x_B} dx \int_{h(x)}^{z_{v3}} [f_n(x,z) - d_l b_h] dz$$

2. If the v_A and v_B are on e_1 and e_3, or on e_3 and e_4. Similar to the first case, the region R is partitioned into two subregions and the volume is:

$$V_s = \int_{x_A}^{x_B} dx \int_{z_{v1}}^{h(x)} [f_n(x,z) - d_l b_h] dz + \int_{x_B}^{x_{v2}} dx \int_{z_{v1}}^{z_{v3}} [f_n(x,z) - d_l b_h] dz$$

3. If the v_A and v_B are on e_1 and e_4, the volume is:

$$V_s = \int_{x_A}^{x_B} dx \int_{h(x)}^{z_{v3}} [f_n(x,z) - d_l b_h] dz + \int_{x_B}^{x_{v2}} dx \int_{z_{v1}}^{z_{v3}} [f_n(x,z) - d_l b_h] dz$$

4. If the v_A and v_B are on e_2 and e_3, the volume is:

$$V_s = \int_{x_A}^{x_B} dx \int_{h(x)}^{z_{v3}} [f_n(x,z) - d_l b_h] dz$$

Instead of traversing all the voxels, the author first apply a geometric constraint: the quality volume of the voxel that is not intersected with any layers (including the boundary of these layers) is equal to o_l^3. That means if a voxel is totally inside one layer, the quality volume is equal to the volume of the voxel. These voxels will not be calculated during the traversal. The traversal strategy created for quality calculation is called ‘column searching’. All voxels whose centres have the same x and y coordinates are considered as one column of voxels. The calculation starts from the top layers and then moves towards the bottom layer. For instance, to calculate the quality volume of these four voxels, as shown in the Fig. 6, the volume that under the 3rd layer (V_{layer3}) is calculated first. The quality volume of the 1st voxel (QV_1) equals $V_{layer3} - o_l^3[\frac{y_{centre_{voxel1}} - \frac{o_l}{2}}{o_l}]$. With the 2nd voxel, the volume between the 3rd and 2nd layer ($V_{layer32}$) is calculated using the triple integral, the quality volume of the 2nd voxel (QV_2) equals $V_{layer32} - QV_1$. The calculation of the 3rd voxel is similar to that of the 1st voxel. Furthermore, because the 1st voxel only contains the 1st layer, the quality volume equals the volume under the 1st layer.

Through traversing all the voxels, the quality volume of the entire stockpile can be obtained and the quality of the stockpile at the stacking phase is calculated once the compositions of each layer are identified through the chemical analysis. To predict the quality of recovered material using the cubic stockpile management model, it is assumed that a voxel is excavated entirely if its centre is inside the toroidal shell created by the slewing motion of the BWR model. Otherwise, it is believed to remain on the stockpile model. If an ideal BWR model is used, the detection can be conducted using Eq. 5.1 and 5.2. If the real trajectory is used, the previously introduced numerical approach can be applied to create a 3D convoy hull for the evaluation of the geometric position between the voxel and the cut. For example, supposing the centre trajectory of the BWR in a cut is estimated using UKF data fusion, for each central point, a circle in 3D space that represents the BW can be created out of it. Thus, each cut results in a set of points and the convex hull, which is the smallest convex region of the point set, can be calculated through the quickhull algorithm [71]. By tracking the position of the BWR and the voxel, the quality of reclaimed material is predictable. Fig. 5.10 illustrates the voxels that are recovered by a single slewing motion of the BWR.

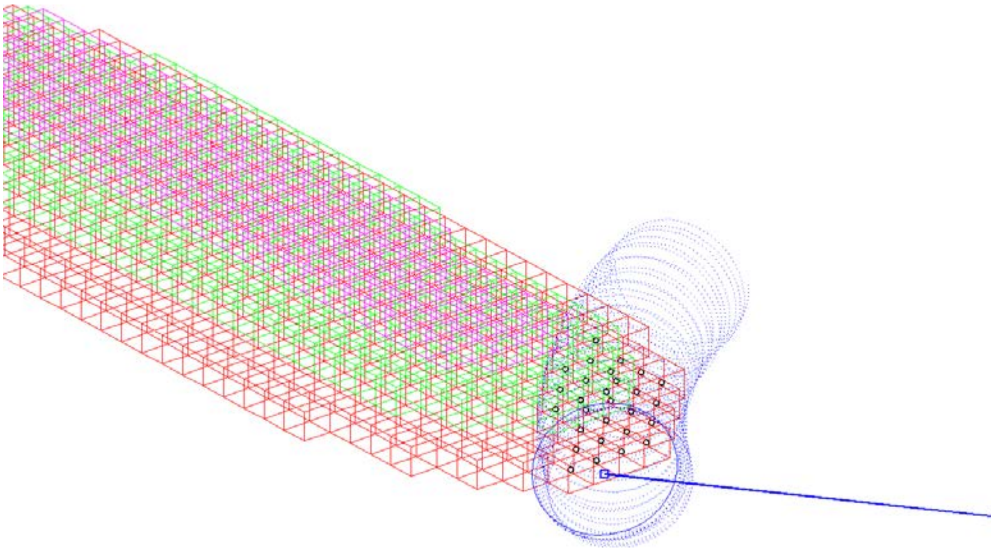

Fig. 5.10 Identification of reclaimed voxel based on the trajectory of the bucket wheel. The trajectory of the bucket wheel is plotted in blue. The centres of the scooped voxels are highlighted in black.

5.2.2.2 Sickle-shape Voxelization and Quality Estimation

A sickle-shape voxel is the intersection of the stockpile (the outermost layer) and a cut. Therefore, a sickle-shape voxelization has identical procedures as the slewing range estimation and model updating operation. Moreover, the boundary curve of each cut needs to be stored to illustrate the shape of each voxel when it is superimposed onto a stockpile model. Again, the voxelization can be based on two different data sources, the ideal trajectory calculated from the BWR kinematic model, or the real trajectory from the measurement data.

Similar to a cubic voxel, a sickle shape voxel may contain material from different layers, in other words, multiple QVOs. Due to the variability in shape of these objects, it is difficult to programme a universal algorithm to determine the integral region and perform the calculation automatically. Additionally, even if such a programme were developed, the complexity of the code would also prolong the calculation time. For these reasons, a Monte Carlo based integration method is selected for this study. Monte Carlo integration uses randomly generated points to approximate volume integrals of a 3D object. These points are randomly distributed inside a box enclosing an object of interest. The volume of the object is estimated as:

$$V_{obj} = V_{box}(N_{in}/N) \tag{5.8}$$

where V_{box} is the volume of the 3D bounding box of the object, N_{in} is the number of points that are contained within the object and N is the number of points generated in a random process.

A major source of error for such a method is the random nature of the sampling, because the pseudo-random points generated from the computer may not be distributed uniformly inside the bounding box. Quasi-Monte Carlo (QMC) techniques replace these pseudo-random numbers by deterministic sequences, which are constructed explicitly to minimize clumping through reducing the discrepancy of the point set. The use of such low-discrepancy numbers rather than pseudo-random numbers in the integral calculation increases the convergence rate and reduces the expected relative error. As pointed out by Davies and Martin, the error of the approximation by QMC methods is $O(N^{-1}\log^3 N)$ [72]. The implementation of the QMC method is quite simple. After generating a low-discrepancy set using Sobol's method [73], these points are shifted into the bounding box and then N_{in} is determined through point-membership classification based on the stockpile's surface and torus functions.

Fig. 5.11 shows the critical procedures in volume calculations using the QMC method. Given a voxel, whose upper surface is a part of the stockpile and lower surface is a part of the torus, a bounding box is created first, based on its geometric shape. Then, a low-discrepancy set with N points, generated by Sobol's method, is shifted into the bounding box using geometric transformations. Subsequently, based on algebraic functions of the stockpile and torus, the points are separated and the N_{in} is obtained. Finally, the volume of the voxel V_{voxel} is calculated using Eq. 5.8.

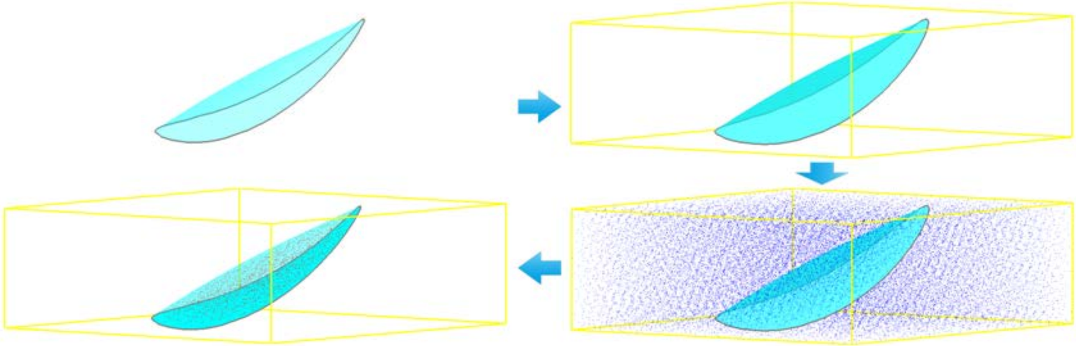

Fig. 5.11 Calculating the volume of a QVO object using the QMC method.

A matrix W is constructed for quality calculation. If a voxel only contains one QVO, and both the density of the QVO (ρ) and the weight in percentage of a certain element (w) are known, the quality of such an element in the voxel Q_{voxel} is equal to $\rho V_{voxel} w$. Because the quality of iron ore is evaluated by a number of elements, W is constructed as a row vector with we elements. For example, in this paper, the quality of iron ore is evaluated by three elements: Fe, Si and Al. Thus, W is a 1×3 vector $[w_{Fe}, w_{Si}, w_{Al}]$. At this stage, it is assumed that the QVO (or the layer) is homogeneous in quality (non-homogeneous cases will be discussed later). If a voxel contains v_q QVOs, such calculations will be performed v_q times to obtain the quality of a voxel. In turn, a $v_q \times w_e$ weight matrix is constructed and the quality of such a voxel is:

$$Q_c = \sum_{j=1}^{v_q} \rho V_{box} (\frac{N_{in(j)}}{N}) W_{(j,:)} \tag{5.9}$$

where ρ_j is the density of the j^{th} QVO object. V_{box} is the volume of the bounding box and $W_{(j,:)}$ means the j^{th} row of the weight matrix.

To link the geometric information with the quality simulation model, a sickle shaped voxel is further partitioned into o_s octants using the Octree decomposition method [70]. Again, octants which have the same y coordinates are grouped into a cuboid and the quality composition of the cuboid is assumed to be homogeneous. Meanwhile, the decomposition also subdivides a voxel into o_s sections and each section is encompassed by an octant (see Fig. 10b). Using the similar grouping strategy presented in 4.5.3, sections in the voxel are grouped into o_g cuboids. Because the voxel is further partitioned, another dimension is added to the weight matrix W. A 3D matrix $W[o_s \times v_q \times w_e]$ means the weight matrix has o_s sections, v_q QVO objects and w_e chemical components. The quality of the i^{th} section that contains v_q QVO objects, calculated using the QMC method, is:

$$Q_c = \sum_{j=1}^{v_q} \rho_i V_{box} \left(\frac{N_{in(i,j)}}{N}\right) W_{(i,j,k=1:w_e)} \tag{5.10}$$

where V_{oct} is the volume of the octant obtained after octree decomposition. $N_{in(i,j)}$ means the number of the points within the (i^{th}, j^{th}) QVO and k is the index of the chemical element in the weight matrix. $k = 1:3$ means the calculation includes all three chemical components. The quality of a voxel that contains o_s sections is:

$$Q_c = \sum_{i=1}^{o_s} \left[\sum_{j=1}^{v_q} \rho_i V_{box} \left(\frac{N_{in(i,j)}}{N}\right) W_{(i,j,k=1:w_e)} \right] \tag{5.11}$$

According to the previous assumptions in stockpile quality distribution, octants that have the same y coordinates form a segment and a layer inside this segment should have the same quality composition. Thus, when the programme chooses the quality value from the quality model, it only based on the number of the segments, not the number of octants. Two examples are given in the following section to explain the calculation procedure.

Example 1: estimating the quality of the first cut as shown in Fig. 5.5. This voxel only contains one QVO object and the density of the material, ρ, is assumed to be known. After octree decomposition, 18 octants are obtained and these octants are classified into 5 cuboids along the y axis (see Fig. 5.12). Thus, the voxel is partitioned into 18 sections and the weight matrix W is a $(3 \times 18 \times 3)$ matrix. Taking the first two octants at the bottom left, whose centre is (-328, 586, 168) and (-348, 586, 168) for example, the quality for each section inside the octant is $Q_1 = \rho V_{oct}(N(1,1)/N) W_{1,1,1:3}$ and $Q_2 = \rho V_{oct}(N(1,2)/N) W_{1,2,1:3}$ respectively. Because the 1st and 2nd sections belongs to the same segment, $W_{1,1,1:3}$ is equal to $W_{1,2,1:3}$. With the 3rd section, the quality $Q_3 = \rho V_{oct}(N(2,1)/N) W_{2,1,1:3}$. Because there is only one QVO, j always equals 1. The quality of the voxel is the sum of all sections $\sum_{i=1}^{18} Q_j$.

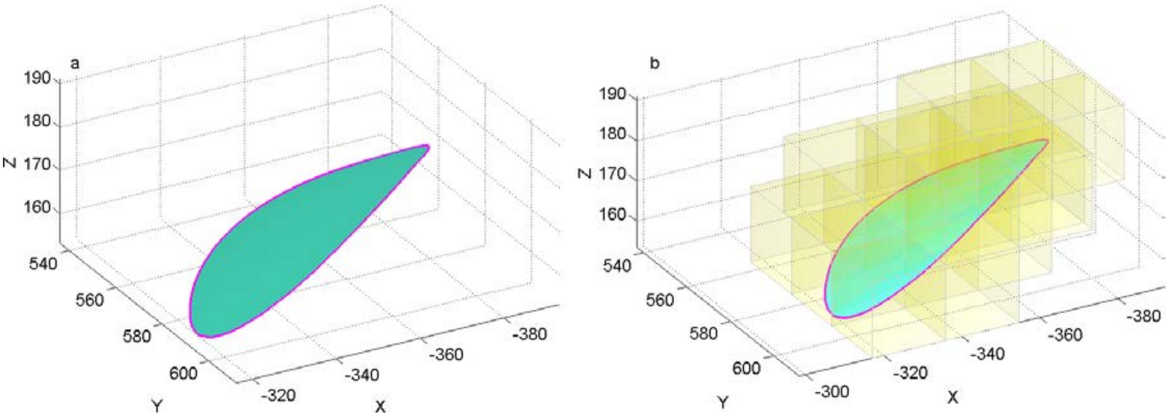

Fig. 5.12 Partitioning a voxel into octants and linking them with the quality distribution model (unit: mm).

Example 2: computing the quality of the second cut, as shown in Fig. 5.5. The shape of the voxel is shown in Fig. 5.13 and the boundaries of the cut are highlighted in magenta.

This voxel contains materials from two layers. Thus, it has two QVO objects (see Fig. 5.13). The voxel is divided into 16 sections by octants. Regarding its geometric position, a section may have one or two QVO objects. If the section only has one QVO object, similar calculation procedures mentioned in the *Example 1* can be used. For example, the quality of the bottom left section is $Q_1 = \rho_1 V_{oct}(N(1,1)/N)W_{1,1,1:3}$. If a section contains two QVO objects (the one with an octant highlighted in yellow, as shown in Fig. 5.13 b), the point-membership classification needs to be executed twice. The quality of the section is: $Q_1 = \rho_1 V_{oct}(N(6,1)/N)W_{6,1,1:3} + \rho_2 V_{oct}(N(6,2)/N)W_{6,2,1:3}$.

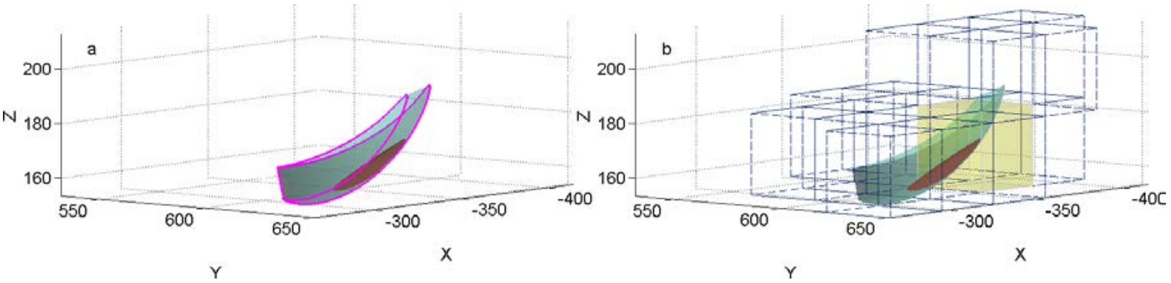

Fig. 5.13 Quality calculation using the QMC method for the 2nd cut. The 1st QVO is in dark red and the 2nd QVO is in light cyan. The octant intersecting with two QVOs is highlighted in yellow (unit: mm).

5.3 Experiment and Result

This section presents the experiments carried out to evaluate the 3D stockpile management model and the results obtained from the investigation. The data used in this section are the bench scale, standard prism and full scale datasets. Wireframe models were created from the bench scale dataset and point segmentation was applied to identify the boundary of each layer. With the full scale dataset, only the last four layers were selected for the validation. Thus, in this section, both the bench and full scale stockpile model contain four layers. The point resolution of the full scale dataset was increased to 0.25 m using the (4^{th}, 10×10) B-spline model before voxelization.

The cubic voxelization algorithm and integral calculator are first examined. Then, the sickle-shape voxelization algorithm is evaluated. The landing point validation and slewing range estimation are presented together with the sickle-shape voxelization because they can be integrated together.

5.3.1 Cubic Stockpile Voxelization

Fig. 5.14 and Fig. 5.15 illustrate two voxel models generated from the two datasets, respectively. Table 5.1 shows the modelling results of these two groups of datasets. It is clear that the increase in resolution will decrease the modelling speed. However, a model with a class of 3,408,497 voxels still can be obtained in less than 80 s. Therefore, the cubic voxel model is capable of modelling the stockpile for quality calculation quickly and effectively. The time cost to build a voxel model is promising when compared with the entire iron ore handling operation. The resolution of the model is flexible and adjustable, depending on the desirable quality management in reclaiming operations: small cubic voxels can approximate a cut better than large cubic voxels do.

A problem found in the experiment is to visualise all voxels using Matlab. If the model contains more than 20,000 octants, the model cannot be displayed properly. However, Kruger and Westermann introduced a GPU (graphical processing unit) acceleration approach to rend large-scale data sets using an ATI 9700 graphics card [74]. Because this graphics card is around two generations behind the current commodity model, the author believes that the rendering of the high-resolution voxel model is feasible using such techniques.

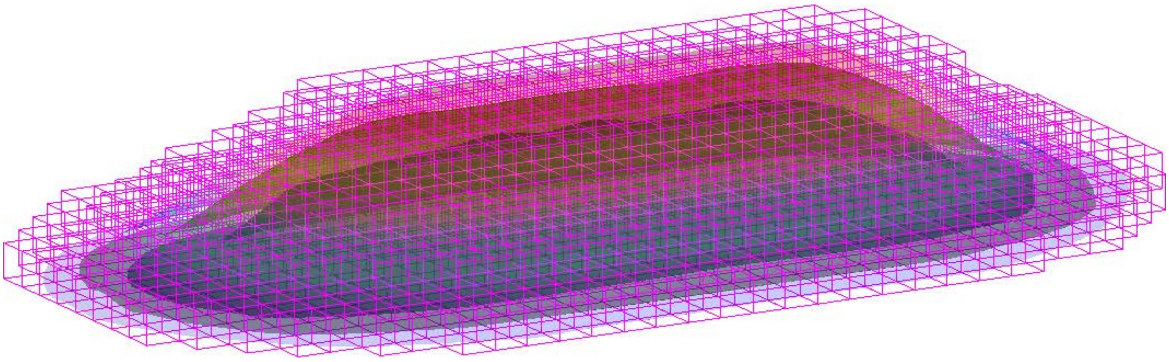

Fig. 5.14 A 40 *mm*-resolution voxel model superimposed onto the bench scale stockpile (unit: m).

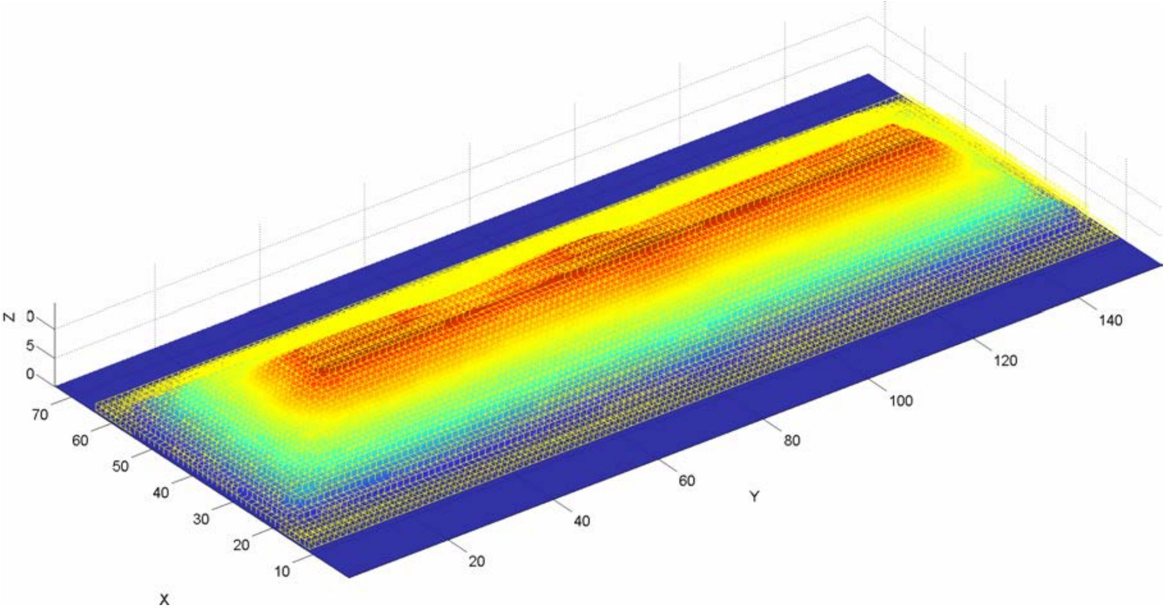

Fig. 5.15 A 1 *m*-resolution voxel model superimposed onto the full scale stockpile.

Table 5.1 Voxel modelling using different resolutions.

Dataset	Model No.	Resolution	Number of voxels	Modelling time
Bench scale data	1	60 *mm*	575	0.27 *s*
	2	40 *mm*	1,465	0.29 *s*
	3	20 *mm*	9,536	0.31 *s*
Full scale data	4	1 *m*	35,109	21.13 *s*
	5	0.5 *m*	264,978	42.62 *s*
	6	0.25 *m*	3,408,497	77.10 *s*

5.3.2 Quality Volume Calculation in Cubic Model

To evaluate the automatic volume calculation algorithm, the following steps were used. First, all the six models created in the previous section are employed to evaluate the intersection curve detection and automatic double integral calculation algorithms. The ‘column searching’ was executed more than 150,000 times. With all these trials, the proposed numerical approach located all the intersection curves (those that exist) and separated the straight lines and curves successfully. The double integration regions were identified properly and the calculations were performed accordingly.

Second, the performance of the volume calculation algorithm is evaluated using the 8^{th} wireframe model created from the standard prism data. Two different resolution (324 *mm* and 16.20 *mm*) voxel models were created from the wireframe model. The low-resolution model contains 8 voxels and the high-resolution model contains 14,875 voxels. The (2^{nd}, 8×8) polynomial model was used in the double integral. The total running times, including the voxel modelling and volume calculation, of the low and high resolution models are 3.24 *s* and 258.30 *s*, respectively. Table 5.2 compares the real volume with the calculation results. These results indicate that the proposed quality calculation algorithm is fast and effective. Also, the high resolution model is able to improve the calculation accuracy. Such an improvement is not obvious at the stacking phase, but it will increase the calculation accuracy at the reclaiming phase, because small voxels can provide a better approximation of the cut caused by the BWR than large voxels.

Lastly, the quality volume of each voxel in two cubic models is calculated. Instead of generating an individual surface function for each column of voxels during the traversing, a standard cubic model is created. The octants for the standard model are the determined by the 2^{nd} level of the octree. The octree structure is obtained based on the voxel resolution, which contains 7 levels and the 2^{nd} level node happens to partition the stockpile region into 2×4 patches. An (8^{th}, 2×4) polynomial model is generated for the integral calculator. This model, of course, contains all the layers of a stockpile (see Fig. 5.16). Therefore, eight polynomial functions are obtained for each layer and are used as standard functions in quality volume calculations. In other words, the surface functions of all the leaf voxels are the same if these voxels belong to a one node in the 2^{nd} level of the octree. The volume of each layer, calculated from the voxel model, is listed in Table 5.3. The quality calculation results are listed in the quality prediction section because it is hard to present such a large number of voxels at the same time.

Table 5.2 Volume calculation results for the standard prism. (unit: mm^3)

	Real	Low resolution	High resolution
Volume	53,753,375	53,259,921	54,031,070
Percent error	n/a	0.9180%	-0.5166%

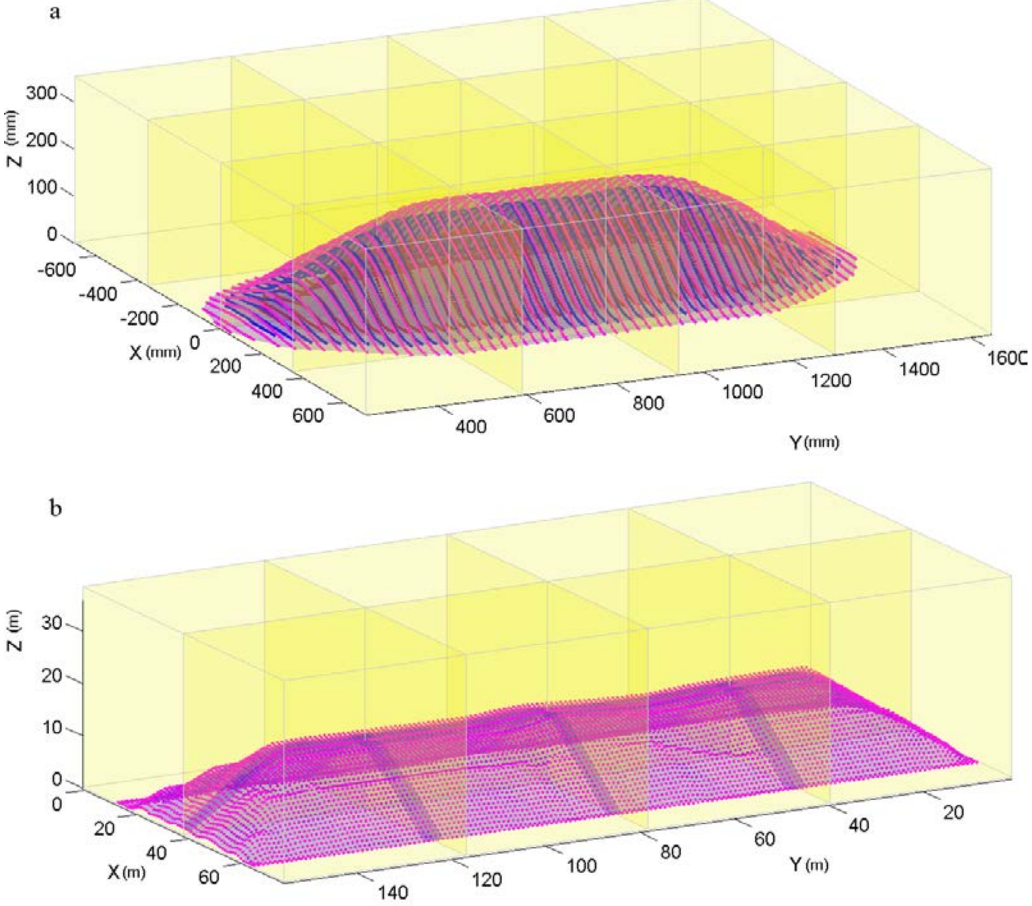

Fig. 5.16 Standard voxel models for quality calculation. Stockpiles are partitioned into eight cubic regions and each region is described by a polynomial function. a) The bench scale stockpile and its cubic model. Cubes created after voxelization are in transparent yellow with grey edges. b) The full scale stockpile and its cubic model. For display purposes, not all the layers in the stockpile are plotted.

Table 5.3 Volume of each layer calculated from the cubic voxel model.

Layer	Bench scale stockpile cm^3		Full scale stockpile m^3	
	Polynomial model	Cubic model	Polynomial model	Cubic model
1	20387.2	20393.1	68198.3	68202.7
2	29569.7	29572.4	80420.4	80425.6
3	43033.3	43037.1	92643.5	92649.4
4	68296.0	68303.3	103845.3	103850.1

5.3.3 Quality Predication from Cubic Voxel Models

Two specific cases were simulated to predict the quality of reclaimed material. The first one involves in the bench scale stockpile while the second involves in the full scale stockpile. The quality data used for the case studies are also provided by the MatrixGroup and are listed in Table 5.4. In the first case, the density of each layer is based on the material properties listed in Table 4.1. The parameters of the BWR models are listed in Table 5.5. The stockpile is assumed to be located on the left hand side of the BWR. All these parameters are, of course, subject to change to reflect the real operational environment.

Table 5.4 Quality data used in the case study.

Case	Layer	Density	Fe (%)		Si (%)		Al (%)	
			Mean	Var.	Mean	Var.	Mean	Var.
Bench scale	1	1.65 g/cm^3	52.13	5.06	3.86	1.32	1.17	0.53
	2	2.61 g/cm^3	58.68	7.06	4.38	1.45	1.54	0.84
	3	2.82 g/cm^3	57.77	6.82	3.96	1.26	2.31	0.96
	4	2.75 g/cm^3	58.19	7.13	4.54	1.32	1.66	0.75
Full scale	1	5.35 kg/m^3	56.23	6.56	4.98	1.53	0.24	0.081
	2	5.35 kg/m^3	60.77	4.32	5.33	1.23	0.35	0.063
	3	5.35 kg/m^3	51.43	5.18	7.66	1.08	0.41	0.023
	4	5.35 kg/m^3	62.05	7.46	5.08	1.34	0.21	0.015

Table 5.5 BWR Parameters used in case study.

Case	L_2	L_3	L_4	L_5	R_k	R_v	ϕ	β
Bench scale (cm)	6	5	5	50	4	5	20°	0°
Full scale (m)	6	5	5	50	7	10	15°	5°

The voxel resolution used for the first case is 20 *mm* and the total number of cutting steps is 15. Fig. 5.17 shows the voxel reclaimed in the first cutting step and Fig. 5.18 plots the quantity of each cut. As shown in Fig. 5.17, the BWR only recovers material from the 3rd and 4th layer during the reclaim because both the 1st and 2nd layers are below the bench height. The quality of reclaimed material is listed in Table 5.6.

The voxel resolution for the second case is 0.25 *m* and 10 reclaiming steps are simulated. Similar to the bench scale data, the BWR only cuts into two layers. Fig. 5.19 highlights

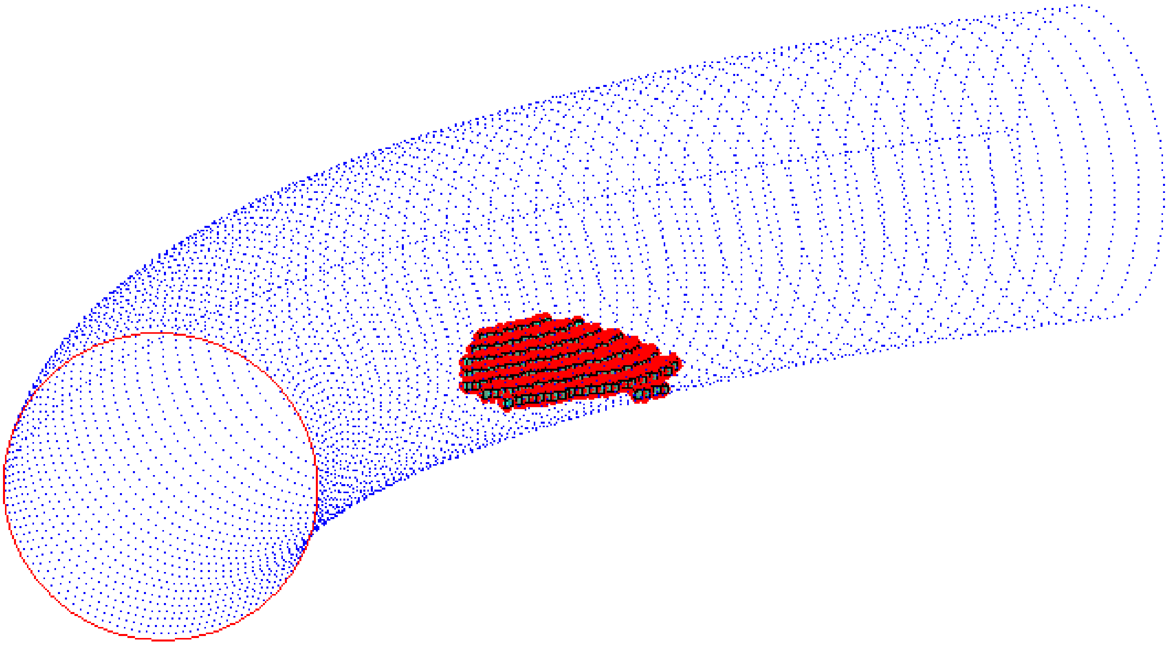

Fig. 5.17 Material removed in the first cut.

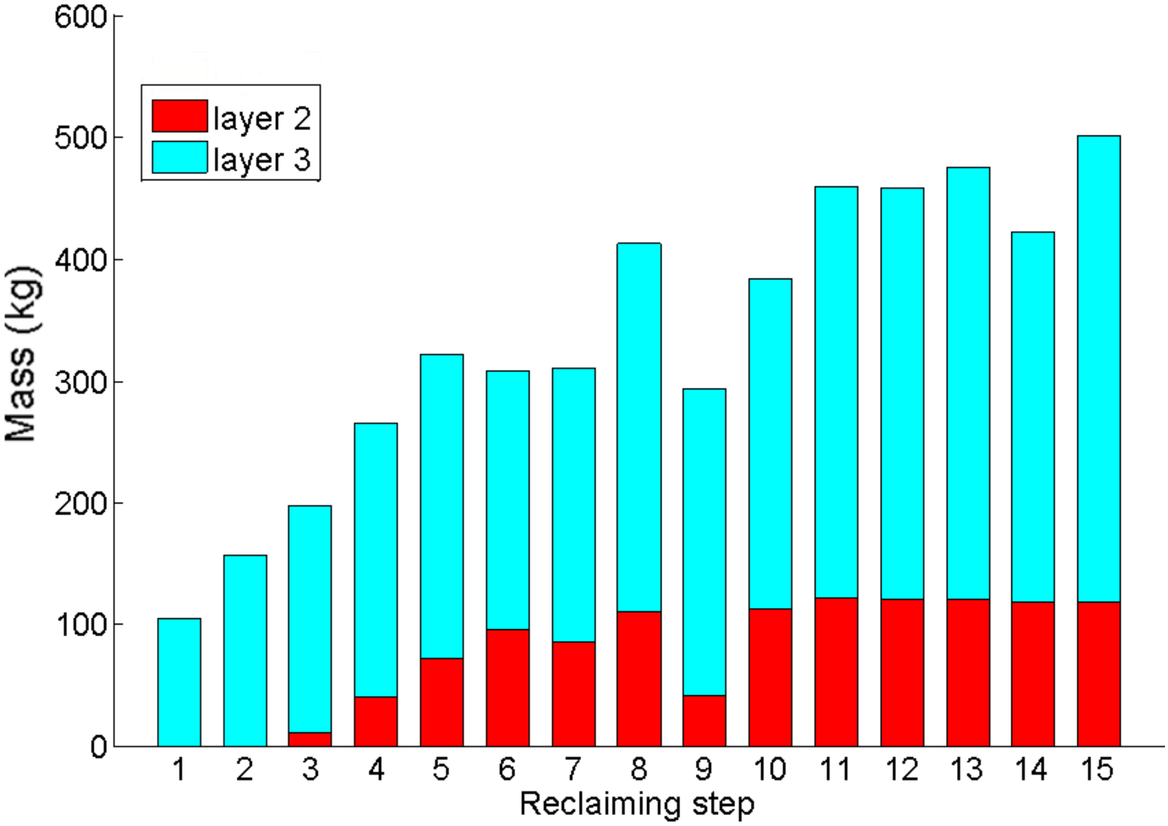

Fig. 5.18 Quantity of the material recovered in the 1st case. Each bar represents the total mass reclaimed and the materials recovered from different layers are stacked in each bar.

Table 5.6 Quality of reclaimed material for the 1st case using cubic voxels. (unit: g)

Step	Fe	Si	Al	Step	Fe	Si	Al
1	62.6	5.3	2.37	9	91.82	16.12	7.67
2	92.74	7.64	3.53	10	228.87	19.22	9.12
3	132.02	10.92	5.06	11	286.13	23.8	11.17
4	156.81	12.91	6.13	12	256.57	21.45	10.06
5	193.97	16.03	7.4	13	286.04	23.78	11.17
6	209.1	17.36	8.21	14	250.35	20.81	9.69
7	196.83	16.32	7.65	15	314.61	26.51	11.98
8	208.18	17.38	7.98		N/A		

the voxels that recovered by the BWR at each single step during the reclaiming. Fig. 5.20 illustrates the quality of the material in each cut, based on the data from Table 5.7.

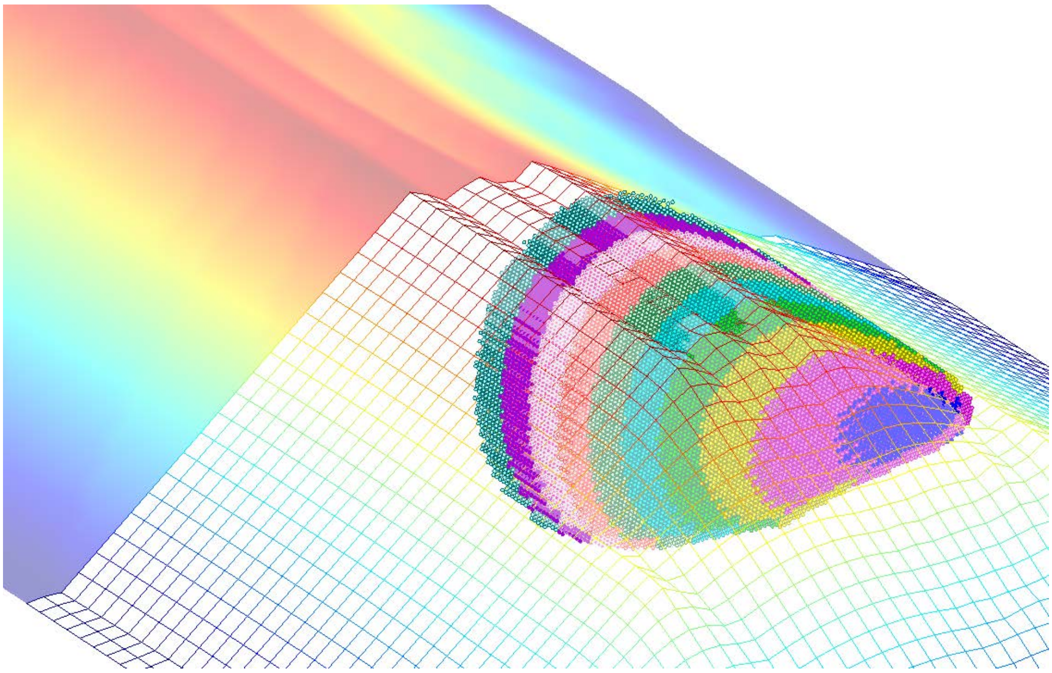

Fig. 5.19 Voxels recovered in each cut. The original stockpile is plotted as a surface mesh.

In a cubic voxel model, a sickle-shaped cut is approximated by a group of cubes. Therefore, the prediction accuracy can be improved through decreasing the size of the voxel. However, two problems will rise if the voxel size is too small: the computation time and the point resolution. The first problem is easy to understand as a high resolution model results in a large amount of voxels and this will prolong the calculation time. The second one is because small voxels require high resolution point data. However, the resolution of the scanning

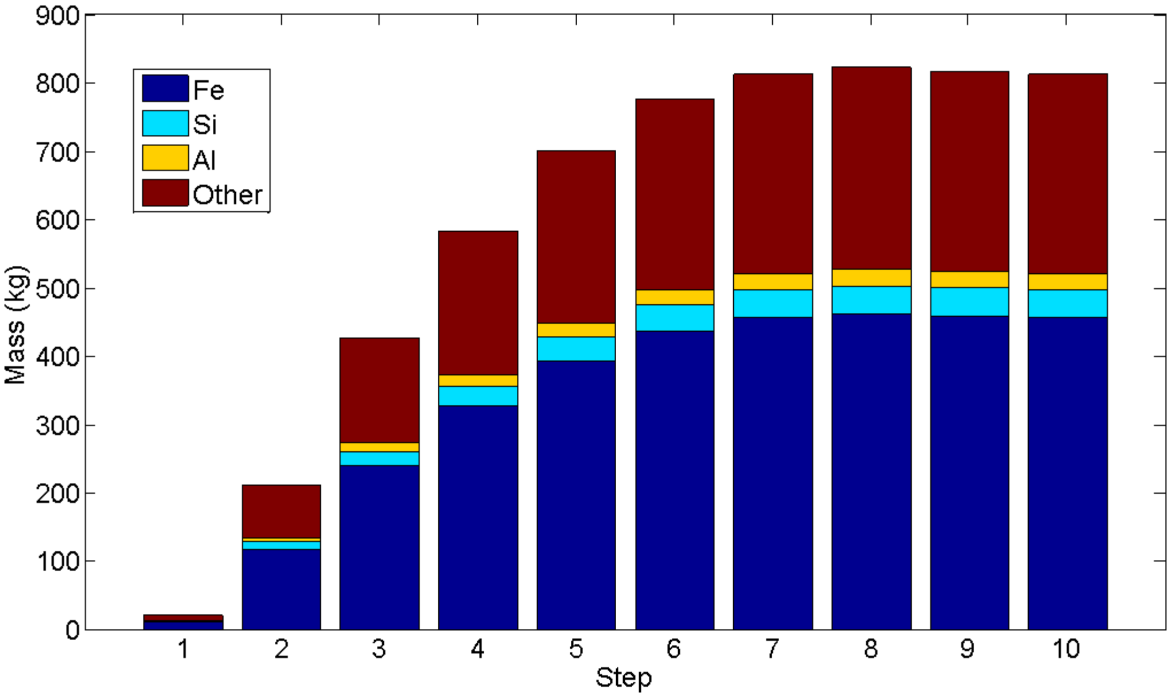

Fig. 5.20 Quantity of the material recovered in the 2nd case. The chemicals recovered in each step are stacked in each bar.

Table 5.7 Quality of reclaimed material and their percentages in the 2nd case using cubic voxels. (unit: *kg*)

Step	Fe	%	Si	%	Al	%
1	12.90	57.53	1.27	5.64	0.77	3.42
2	22.04	57.69	11.93	5.64	7.11	3.36
3	246.37	57.69	23.91	5.60	14.39	3.37
4	335.23	57.55	32.39	5.56	19.92	3.42
5	401.37	57.39	39.10	5.59	24.06	3.44
6	45.21	57.42	3.81	5.65	6.83	3.46
7	466.4	57.47	45.93	5.66	28.00	3.45
8	472.17	57.49	46.65	5.68	28.09	3.42
9	469.47	57.53	46.19	5.66	27.42	3.36
10	466.47	57.50	45.92	5.66	27.01	3.33

device is limited. Although it can be improved by using surface models to interpolate more points into the point data, due to the nature of the interpolation method itself, the proposed automatic integral calculator may be not able to detect the intersection curve between the stockpile surface and voxel plane accurately. Consequently, the quality volume calculated based on the intersection curve may be not accurate. This problem happened in the full scale stockpile when the voxel size was less than 0.2 *m*.

5.3.4 Sickle-shape Stockpile Voxelization

Two 3D stockpile management models are built for sickle-shape voxelization. In the first management model, the bench scale stockpile is coupled with the bench scale BWR model listed in Table 5.5. The stockpile is assumed to be located on the left side of the BWR, with a distance of 0 *mm* measured from the BWR slewing axis to the boundary of the stockpile region. The stockpile is assumed to be recovered by the BWR in two reclaims. The first reclaim contains 10 cuts and the second contains 5 cuts. The predetermined bench heights of two reclaims are 152.97 *mm* and 89.29 *mm*, respectively. The advancement between cuts is 9 *mm* ($0.9(R_v - R_k)$). After the first reclaim is accomplished, the BWR reverses and the BW is lowered to make the second one.

To locate the potential landing points for the initial cut, a reference grid with 20 *mm* spacing is superimposed onto the B-spline surface model. 83 candidature points are obtained and 38 points are validated to be effective landing points. The point with the largest cutting depth among these validated points is selected as the initial point for the first reclaim. Based on the inverse kinematic equations, the joint angle of the BWR can be acquired. Materials in the second layer are also scoped by the buckets after the 6th cut. The slewing range is detected and the model is updated after each cut. With the second reclaim, the latest surface model is evaluated to determine a new landing point. 55 candidature points are obtained and 27 points are validated to be effective landing points. Again, the one with the maximum cutting depth is selected. Only the material in the 4th layer is recovered for the 2nd reclaim. The states of the stockpile during the reclaiming are illustrated by a number of key frames in Fig. 5.21.

The side length of the cube used for the QMC calculation is configured to be 30 *mm*. Due to the fact that the size of each cut is not identical, this side length changes slightly with the cut. The low-discrepancy sequence filled into each voxel contains 32,768 points. The quality stockpile model is simulated based on the data listed in Table 5.4.

Fig. 5.22 shows the points identified to be inside the 2nd cut of the 1st reclaim when its volume is calculated using the QMC method. The final quality calculation results are shown in Table 5.8.

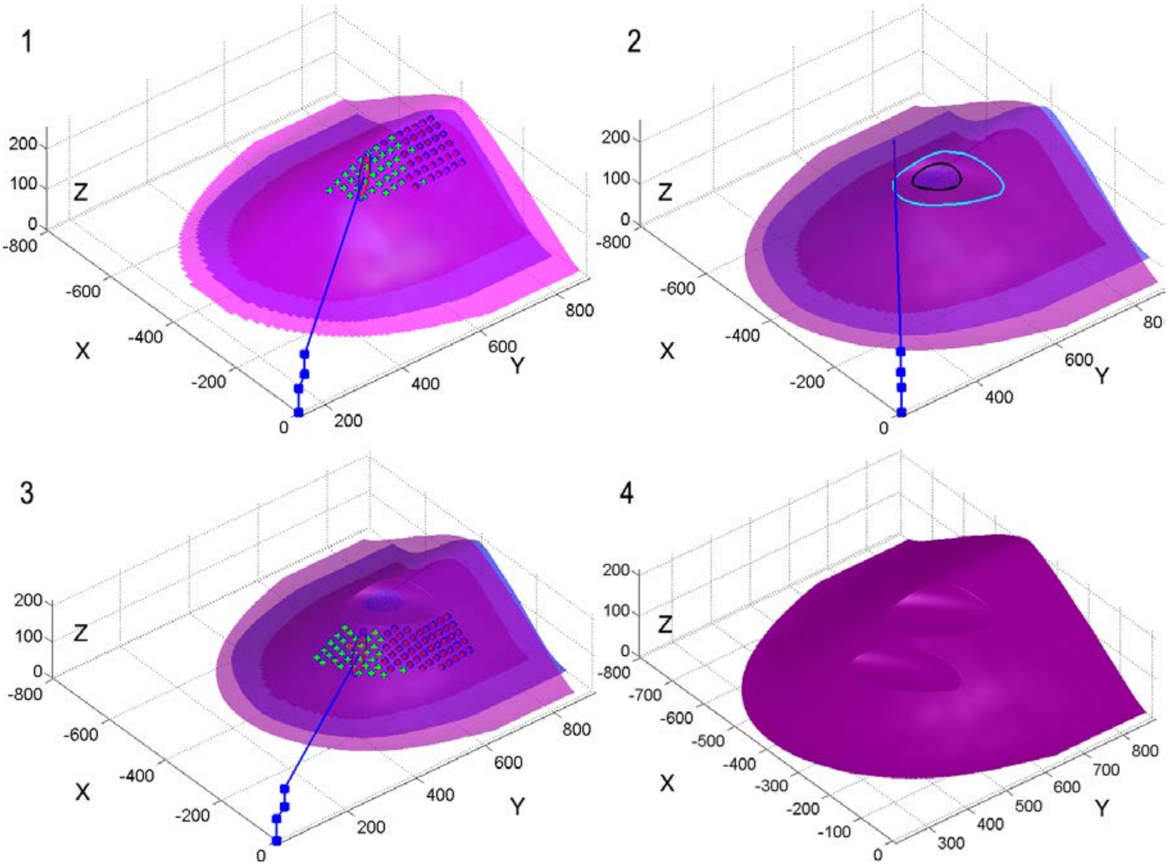

Fig. 5.21 Automatic landing and reclaiming simulation. Reclaim 1, Stage 1: determine the landing points. Reclaim 1, Stage 2: stockpile and BWR after 10 cuts. The boundary of the 10th cut for the 3rd and 2nd layer is highlighted in cyan and black respectively. The blue dot points are the overlapped region of the third and second layer. Reclaim 2, Stage 1: the landing point of the second reclaim. Reclaim 2, Stage 2: stockpile after the reclaim. The effective landing points are plotted in green '+'. The stockpile surface are rendered from its B-spline model (unit: mm).

The second management model is a combination of the full scale stockpile and BWR. The distance between the stockpile and BWR is 5 *m*. The maximum cutting height of the BWR model is 5.88 *m* and the maximum height of the stockpile is 28.94 *m*. The gridding resolution used to generate the landing point set Pc is 0.5 *m*. 600 points on the stockpile surface are generated and 100 points pass the collision assessment (see Fig. 5.23). The point with a cutting depth of 17.35 *m* is selected to activate the reclaiming operations. After the initial

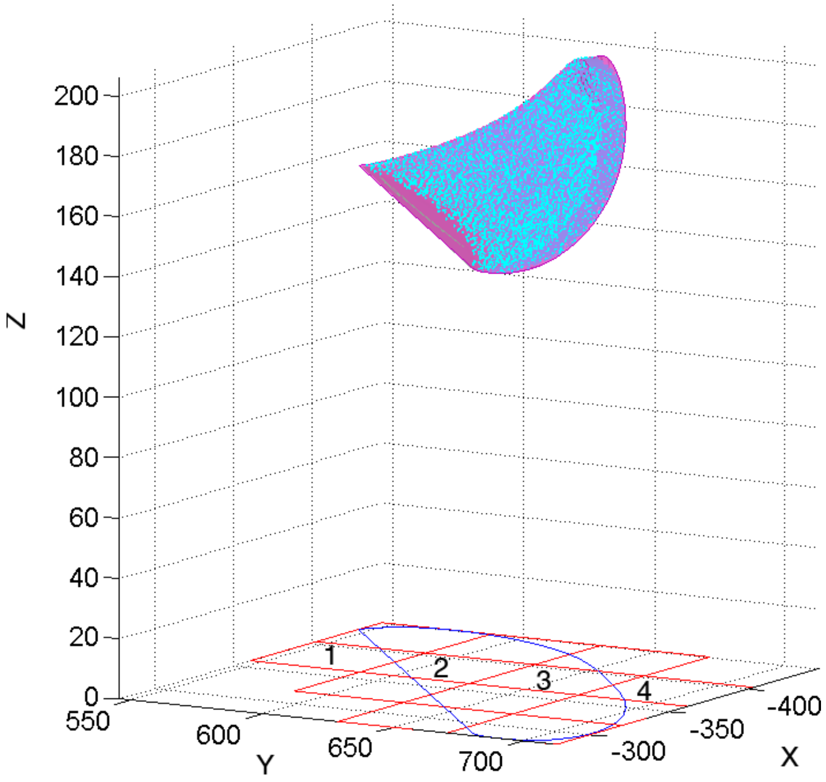

Fig. 5.22 The volume of the 2nd cut calculated using QMC method. 12 cubes are generated from the cut and are projected onto the XZ plane for display purposes. These cubes belong to 4 quality cuboids (unit: mm).

Table 5.8 Quality of reclaimed material for the 1st case using sickle-shape voxels. (unit: g)

voxel	Layer 2				Layer 3			
	Mass of the cut	Fe	Si	Al	Mass of the cut	Fe	Si	Al
1	0	0	0	0	43.86	24.99	1.23	1.06
2	0	0	0	0	44.06	25.50	1.56	0.61
3	0	0	0	0	58.28	33.10	3.08	0.77
4	0	0	0	0	70.74	40.46	2.66	1.06
5	0	0	0	0	82.25	49.11	3.98	1.38
6	0	0	0	0	93.52	54.56	4.56	1.17
7	4.10	2.29	0.12	0.10	100.73	63.08	4.83	1.34
8	18.72	11.91	0.71	0.34	95.70	58.35	4.97	2.27
9	40.64	23.66	1.78	0.90	83.21	46.55	2.77	1.21
10	61.90	39.56	2.89	1.81	72.31	37.97	2.89	1.03
11	0	0	0	0	52.31	23.14	1.45	0.68
12	0	0	0	0	65.19	26.13	1.57	1.02
13	0	0	0	0	79.02	34.34	2.67	1.23
14	0	0	0	0	93.34	41.13	3.78	1.65
15	0	0	0	0	102.56	50.12	4.89	1.43

position of the BWR and the slewing range of the BW are obtained, the top bench of the stockpile is voxelized in terms of the BWR reclaiming trajectory as illustrated in Fig. 5.24). Thus, the quality and quantity of each voxel can be computed using the QMC method accordingly. Fig. 5.25 draws the shape of the stockpile after 10 continuous cuts. The quality of recovered material in the first 10 cut is shown in Table 5.9.

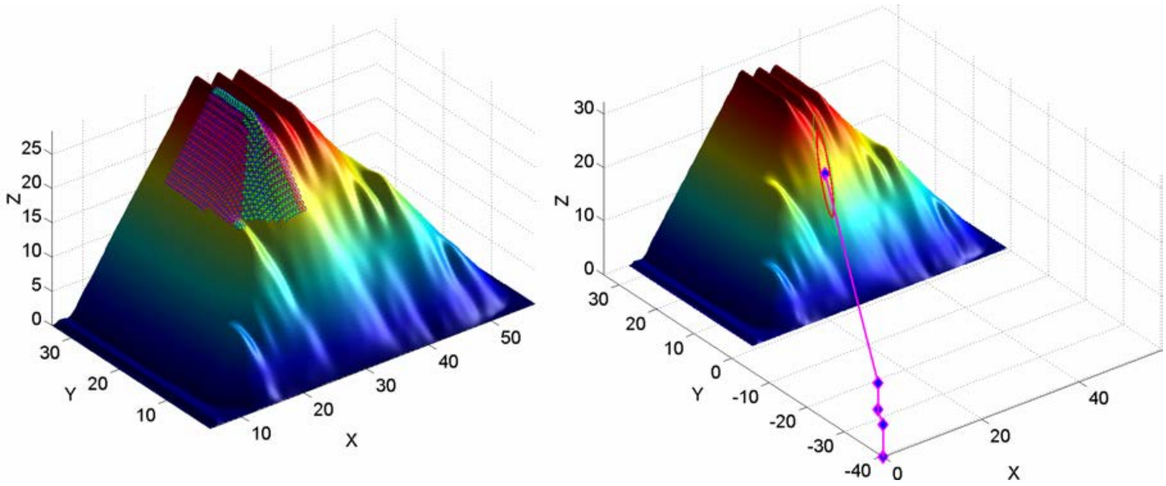

Fig. 5.23 Validate the potential landing point from the B-spline model. Effective landing points are plotted in green. The point selected for the initial cut has the maximum cutting depth. The position of the BWR determined form the point is shown on the right (unit: m).

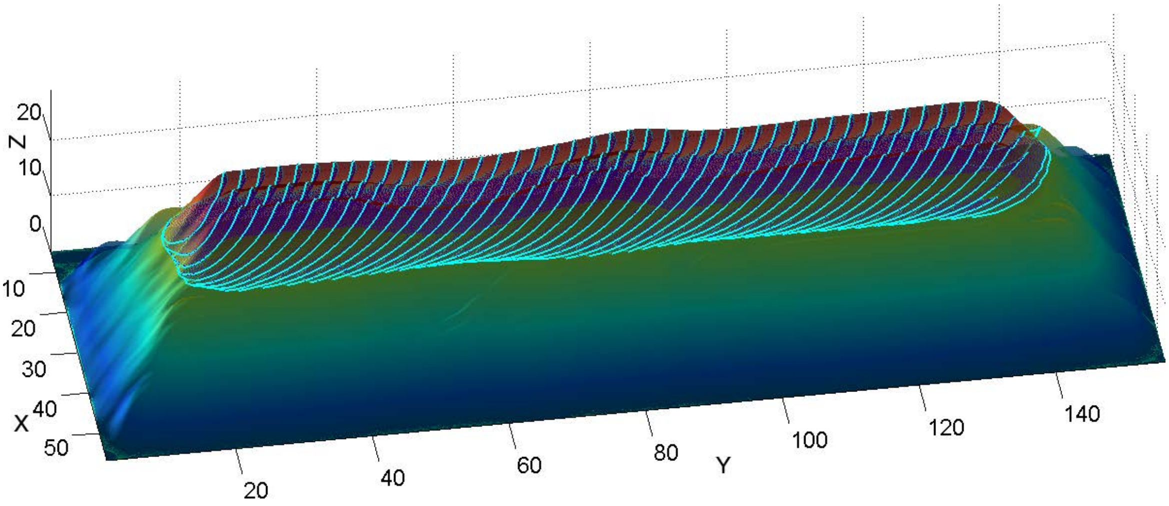

Fig. 5.24 Voxelization of the top bench based on the real cutting trajectory (unit: m).

Since the full scale stockpile is not stacked using the chevron method, the layers are overlapped at diverse points. Such overlaps are mainly existed in the first and second layers. These regions introduce errors to the final calculation results because the proposed algorithm assumes that such complex intersections between adjacent layers do not exist. However, in

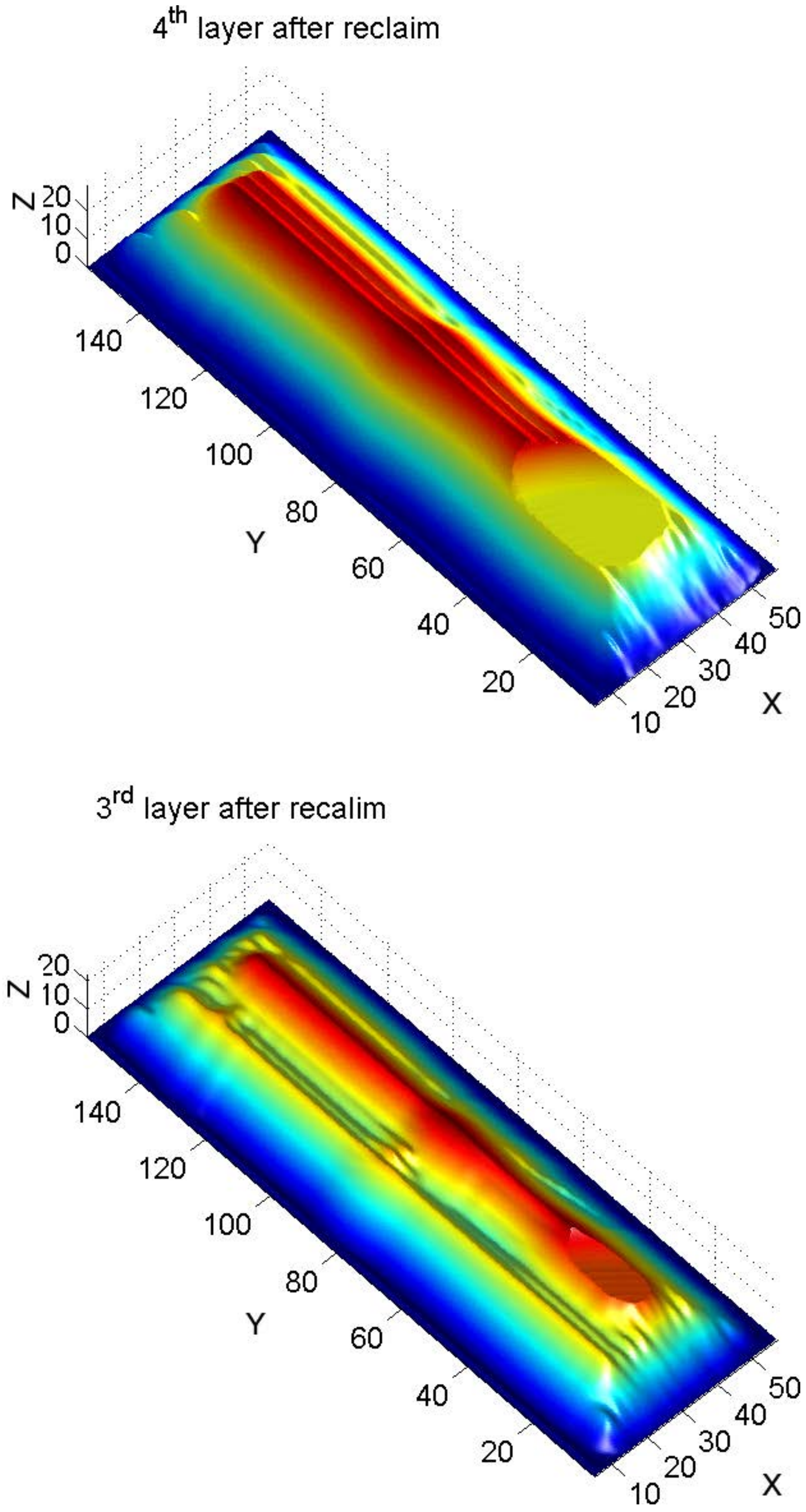

Fig. 5.25 Stockpile after the reclaiming. Only the 3^{rd} and 4^{th} layer are recovered by the BWR within the two reclaims. The geometric shapes of these two layers after the cut are plotted separately for display purposes (unit: m).

Table 5.9 Quality of reclaimed material for the nth2 case. (unit: kg)

voxel	Layer 3				Layer 4			
	Mass of the cut	Fe	Si	Al	Mass of the cut	Fe	Si	Al
1	0	0	0	0	852.59	531.43	39.85	2.37
2	0	0	0	0	1319.41	813.74	64.68	6.85
3	0	0	0	0	1713.36	1039.04	86.52	10.08
4	67.55	40.79	3.48	0.32	1811.63	1082.50	97.54	9.74
5	189.04	115.86	9.97	0.52	1773.62	1055.13	99.52	4.42
6	220.10	130.65	11.86	0.62	1768.30	1071.85	78.02	5.90
7	244.75	148.44	12.36	0.88	1755.98	1052.79	76.89	7.28
8	244.78	152.67	13.33	1.03	1737.98	1055.11	86.52	2.87
9	252.23	158.40	12.40	0.73	1692.67	999.57	100.35	9.29
10	245.21	148.74	13.93	0.88	1631.36	979.30	90.33	5.06

reality, these overlaps do not exist if the stockpile is scanned continuously. Additionally, if the stockpile is not stacked using the chevron method, a single cut may contain two separated 3D regions due to the shape of the stockpile surface. Under such circumstances, each region needs to be calculated separately.

5.4 Summary

This chapter details the building of a 3D stockpile management model and the procedures to apply this model for BWR automation and quality estimation in blending. The 3D stockpile management model is a combination of three individual models: a multilayer geometric stockpile model (polynomial or B-spline) generated from point clouds, a quality stockpile model simulated from quality data and a kinematic model outlined form a BWR. Using this model, the BWR can be controlled automatically without collision between the bucket wheel and the stockpile. Additionally, the quality of a stockpile in blending operations can be calculated from the geometric and quality information.

Two voxelization methods are introduced. The cubic voxelization is achieved through traditional octree decomposition algorithm. The intersections between the solid octants and layers are detected and the volumes of these intersections are calculated automatically using the integral calculator from polynomial surface model automatically. The quality of the material in blending can be estimated through linking the volume calculation results with the quality distribution model. The advantages of octree voxelization are fast and accurate.

The model can be created from a wireframe model directly and obtained in less than 2 *m*. Because the volume is calculated through integration techniques, results are more accurate than other methods. For example, the volume of the triangular However, to approximate a 3D sickle-shape cut resulted by a BWR using cubes with a great degree of accuracy, the cubes are required to be small enough, which results in a large amount of data to be processed by the proposed integral calculator. In the experiment, the integral calculator programmed in the Matlab requires around 2 *s* to accomplish one computation. Thus, increasing the number of voxels improves the accuracy, but elongate the overall execution time, which reduces the system efficiency.

The sickle-shape voxelization is to partition a stockpile based on the reclaiming trajectory of the BWR. A sickle-shape cut is an intersection between the outmost layer of a stockpile and a geometric shape created from superimposing the rotating motion of the buckets and the slewing motion of the wheel. Similar to cubic voxel, it may also intersect with internal layers of the stockpile. Through identifying these intersections and calculating their volume separately, the quality of a sickle-shape cut can be predicted accurately. In this chapter, a discrete numerical approach which converts the surface-to-surface intersection problem to curve-to-surface problem is applied to identify the sickle-shape voxels and those intersections. Experimental results indicate that this approach is able to find the intersections precisely. Meanwhile, the collision free reclaiming trajectory and slewing ranges of the BWR are also acquired during the voxelization procedure. The computational time for the sickle-shape voxelization is longer than cubic voxelization. The volume of the intersection is approximated by the QMC method. The advantage of this method is computational time and programming simplicity. It runs much faster than the integral calculator. The results obtained using the QMC are less accurate but closed to the results computed by integrals.

To summarise, the cubic voxelization and polynomial surface modelling is a perfect match to estimate the quality of a stockpile at stacking phases. Conversely, to predict the quality of recovered material at reclaiming phases, the sickle-shape voxel are suggested to be paired with either polynomial or B-spline surface model.

Chapter 6

Conclusion and Future Work

The work described in this thesis is concerned with the development of a 3D stockpile management model for BWR automation and quality calculation in blending. The following section first summarizes and draws conclusions according to the work presented in this thesis and then points out possible future work.

6.1 Conclusions

Stockpile blending is an effective method to adjust the quality and reduce the variability of the iron ore in a supply chain. However, it has been remained as a challenging problem to represent the geometric shapes of a stockpile and calculate the quality with the stockpile accurately and precisely in blending operations. The reasons for such situations identified in the literature section can be outlined as:

1. Inadequate understanding in the quality of a stockpile after stacking because no real-time measurement method is introduced to record the geometric shapes of a stockpile in blending operation, and the chemical compositions are not available with the highest degree of accuracy during stacking.

2. Insufficient knowledge during reclaiming operations because the BWR is controlled semi-automatically or manually and no dynamic link between the stockpile model and BWR model for quality calculation.

The main goal of this dissertation is to create a real-time 3D stockpile management model to address such inconsistencies and improve the efficiency and effectiveness in stockpile blending. The contributions can be surmise as follow:

1. A cost-efficient mobile laser scanning device based on a BWR was proposed to scan the stockpile when it is stacked/reclaimed. Such upgrading not only allows the dynamic shapes of the stockpile to be measured accurately in real-time but also provides precise positioning knowledge for other applications, i.e. collision avoidance.

2. Nearly real-time and automatic mathematical modelling from measurement data. This is the first time that layers inside a stockpile are recorded and represented faithfully in stockpile modelling. Experimental tests have proven the computational efficiency and accuracy of the proposed modelling algorithms.

3. Novel 3D stockpile management model for BWR automation and quality calculation. The combination of the geometric stockpile model and BWR model assist the BWR automation tasks, which have not been well researched in most studies. Through integrating the prior chemical analysis results into the 3D stockpile model layer-by-layer, the quality of a stockpile can be calculated accurately. The quality embedded 3D stockpile model associated with the cutting trajectory of the BWR allows the properties of the reclaimed material to be predicted with a great degree of accuracy continuously, which will upgrade the current ‘selective stacking’ to ‘proactive reclaiming’ in stockpile management.

Additionally, problems encountered in building the 3D stockpile management model were addressed and solved accordingly by the author. These problems include: finding the globe minimum for universal Fourier modelling through optimizing the searching strategy, improving the polynomial and B-spline modelling accuracy through grid partitioning, detecting the over-fitting automatically through comparing the surface normal and constructing the quality stockpile model and linking the model with BWR operation through geometric information.

The innovative and comprehensive 3D stockpile management model created in the study will reduce the handling costs and improve the efficiency of existing infrastructure in industries involved in bulk material handling (inclusive of minerals, grain, sugar and woodchips) fundamentally. Thus, it will increase the international competitiveness for Australia producers, particularly in the mining sector, in global trading business.

6.2 Future Work

A number of possible future studies from this thesis include:

1. Testing the UKF localization algorithm and stockpile modelling algorithms using real world data. Due to the time and physical constraints, the author was unable to upgrade a real BWR and use it for stockpile scanning. The data collected from the real operational environment will further provide a strong evidence for the proposed modelling algorithms and may also identify the potential challenges in building of such a 3D stockpile model. Additionally, experimental data can be used to evaluate whether a new algorithm is needed to reduce the position estimation errors caused by the vibrations of the boom. It is therefore expected to accomplish this mission when the external conditions are satisfied.

2. Researching automatic cloud data registration and alignment algorithms. When the bucket wheel is lowered to the stockpile at the reclaiming phase, beams from a single laser scanner may not able to cover the helical-shaped cutting surface or an entire stockpile. Multiple scanners may require for a full coverage of the stockpile. Therefore, it is necessary to align various views (3D point clouds) together to generate a complete point model.

3. Simulating the quality of a stockpile based on real chemical analysis results. In quality stockpile modelling, due to the lack of real chemical analysis results, the variations of a chemical content are assumed to be followed a normal distribution and are simulated separately. This simulation method may not be adequate because there are strong cross-correlations among the mineral contents in nature. Therefore, the quality stockpile model can be developed further to simulate the quality variations effectively using real mine production data, i.e. using the long-term historical chemical analysis results to create a best short-term simulation model. Another option is to apply chemical light spectrometric detectors to the flow of bulk material on the conveyor belt. Thus, the on-line chemical analysis results can be embedded into the geometric stockpile model.

4. Optimizing the reclaiming pattern to achieve the ‘proactive reclaiming’. Improving the product quality and maximizing the export throughout with minimal handling cost are crucial for the producers in bulk material handling. The research accomplished in this thesis creates an innovative management model to predict the quality of a stockpile or recovered materials accurately and continuously. Also, this model calculates the slew-

ing ranges and generates collision-free reclaiming trajectories for BWR automation. Therefore, it is possible to combine all these new features and generate an optimized reclaiming pattern for all BWR(s) operated in the stockyard to achieve the final quantity and quality objectives with minimal energy consumptions, which will make this work more valuable for industry applications. This is the main focus of the future research.

References

[1] Bureau of Resources and Energy Economics, *Resources and Energy Statistics 2013*. Commonwealth of Australia, 2013.

[2] T. Howard, M. Carson, and J. Everett, “Simulation modeling of iron ore product quality for process and infrastructure development,” in *Proceedings MODSIM 2005 International Congress on Modelling and Simulation*, 2005, pp. 1251–1257.

[3] R. O. Burt, *Gravity concentration technology*. Elsevier Science Pub. Co., Inc., New York, NY, 1984.

[4] T.-f. Lu, “Linkage grant (LP0989780), Part E: Project description,” 2008.

[5] G. Robinson, “How much would a blending stockpile reduce variation?” *Chemometrics and Intelligent Laboratory Systems*, vol. 74, no. 1, pp. 121 – 133, 2004.

[6] J. Bond, R. Coursaux, and R. Worthington, “Blending systems and control technologies for cement raw materials,” *Industry Applications Magazine, IEEE*, vol. 6, no. 6, pp. 49–59, Nov 2000.

[7] G. Knappe. (2011) Performance of bucket wheel reclaimers (method of calculation in principle). [Online]. Available: http://www.saimh.co.za/beltcon/beltcon8/paper820.html

[8] A. Gerstel, “Bed blending theory,” in *Stacking, Blending, Reclaiming of Bulk Materials*. Trans Tech Publications, 1977, pp. 321–341.

[9] P. M. Gy, “A new theory of bed-blending derived from the theory of sampling — development and full-scale experimental check,” *International Journal of Mineral Processing*, vol. 8, no. 3, pp. 201–238, 1981.

[10] J. Everett, “Iron ore handling procedures enhance export quality,” *Interfaces*, vol. 26, no. 6, pp. 82–94, 1996.

[11] J. Everett, “Iron ore production scheduling to improve product quality,” *European journal of operational research*, vol. 129, no. 2, pp. 355–361, 2001.

[12] J. Everett, T. Howard, and K. Jupp, “Simulation modelling of grade variability for iron ore mining, crushing, stockpiling and ship loading operations,” *Mining Technology*, vol. 119, no. 1, pp. 22–30, 2010.

[13] M. Kumral, “Bed blending design incorporating multiple regression modelling and genetic algorithms,” *Journal of the South African Institute of Mining and Metallurgy*, vol. 106, no. 3, pp. 229–236, 2006.

[14] G. Robinson, “Comment on the paper ’bed blending design incorporating multiple regression modelling and genetic algorithms’,” *Journal of the South African Institute of Mining and Metallurgy*, vol. 106, no. 3, p. 237, 2006.

[15] C. Wharton, “The use of extractive blending optimisation for improved profitability,” *Orebody Modelling and Strategic Mine Planning. Perth*, pp. 69–76, 2004.

[16] J. Lyu, A. Gunasekaran, C. Chen, and C. Kao, “A goal programming model for the coal blending problem,” *Computers & industrial engineering*, vol. 28, no. 4, pp. 861–868, 1995.

[17] J. Everett, “Computer aids for production systems management in iron ore mining,” *International Journal of Production Economics*, vol. 110, no. 1, pp. 213–223, 2007.

[18] G. Robinson, K. Ross, and B. S. Handling, “Blending in the ends of chevron stockpiles,” *Bulk Solids Handling*, vol. 11, no. 3, 1991.

[19] F. F. Pavloudakis and Z. Agioutantis, “Simulation of bulk solids blending in longitudinal stockpiles,” *International Journal of Surface Mining, Reclamation and Environment*, vol. 17, no. 2, pp. 98–112, 2003.

[20] T.-F. Lu and M. T. R. Myo, “Optimal stockpile voxel identification based on reclaimer minimum movement for target grade,” *International Journal of Mineral Processing*, vol. 98, no. 1, pp. 74–81, 2011.

[21] QMASTER, “Sms3d: the 3d stockpile modelling system,” QMASTER, accessed 2011-03-01. [Online]. Available: http://www.qmastor.com/Products/SMS3D.aspx

[22] indurad, “Online 3d heap, dome and stockpile/stockyard measurement,” indurad GmbH, accessed 2011-03-02. [Online]. Available: http://www.indurad.com/index.php?id=38

[23] Siemens, “Achieving the right quality mix,” Siemens Magazine: Metals and Mining, Siemens, accessed 2011-03-02. [Online]. Available: http://www.industry.siemens.com/industrysolutions/metals-mining/en/downloadcenter/customer_magazine/issue-2-2009/Documents/mm_2-2009.pdf

[24] M. Horn, S. Riede, and E. Schmitz, “Electrical equipment for stackers and reclaimers,” in *Stacking, Blending, Reclaiming of Bulk Materials*. Trans Tech Publications, 1977, pp. 346–357.

[25] E. Schmitz, “Automatic reclaiming of bulk solids,” in *Stacking, Blending, Reclaiming of Bulk Materials*. Trans Tech Publications, 1977, pp. 277–297.

[26] C. Choi, K. Lee, K. Shin, H. Ahn, and K. Lee, “Inverse kinematics of a reclaimer: redundancy and solution,” in *Systems, Man, and Cybernetics, 1997. Computational Cybernetics and Simulation., 1997 IEEE International Conference on*, vol. 3. IEEE, 1997, pp. 2883–2887.

[27] C. Choi, K. Lee, K. Shin, K. S. Hong, and H. Ahn, “Automatic landing method of a reclaimer on the stockpile,” *Systems, Man, and Cybernetics, Part C: Applications and Reviews, IEEE Transactions on*, vol. 29, no. 2, pp. 308–314, 1999.

[28] K.-H. Lee, H.-J. Bae, and S.-J. Hong, “Approximation of optimal moving paths of huge robot reclaimer with a 3d range finder,” in *Computational Science and Its Applications-ICCSA 2006*. Springer, 2006, pp. 151–160.

[29] T.-F. Lu and M. T. R. Myo, “Optimization of reclaiming voxels for quality grade target with reclaimer minimum movement,” in *Control Automation Robotics & Vision (ICARCV), 2010 11th International Conference on*. IEEE, 2010, pp. 341–345.

[30] K. Dahal, S. Galloway, G. Burt, J. Mcdonald, and I. Hopkins, “A port system simulation facility with an optimization capability,” *International Journal of Computational Intelligence and Applications*, vol. 3, no. 04, pp. 395–410, 2003.

[31] M. Ayu, T. Mantoro *et al.*, “Analyzing and managing the disturbance in a mining port stockyard system,” in *Industrial Electronics & Applications (ISIEA), 2010 IEEE Symposium on*. IEEE, 2010, pp. 323–328.

[32] J. He, Y. Huang, and W. Yan, “Yard crane scheduling in a container terminal for the trade-off between efficiency and energy consumption,” *Advanced Engineering Informatics*, vol. 29, no. 1, pp. 59–75, 2015.

[33] C. Innes, E. Nettleton, and A. Melkumyan, “Estimation and tracking of excavated material in mining,” in *Information Fusion (FUSION), 2011 Proceedings of the 14th International Conference on*. IEEE, 2011, pp. 1–8.

[34] K. Brooks, N. Svanas, and D. Glasser, “Evaluating the risk of spontaneous combustion in coal stockpiles,” *Fuel*, vol. 67, no. 5, pp. 651–656, 1988.

[35] E. Boyapati and A. OatesiL, “A mathematical model for stockpile management,” in *Stored Product Protection, Proceedings of the 6th International Working Conference on Stored-Product Protection*. Cabi, 1994, pp. 684–688.

[36] C. Sensogut and A. Ozdeniz, “Statistical modelling of stockpile behaviour under different atmospheric conditions—western lignite corporation (wlc) case,” *Fuel*, vol. 84, no. 14, pp. 1858–1863, 2005.

[37] P. Newman, D. Cole, and K. Ho, “Outdoor slam using visual appearance and laser ranging,” in *Robotics and Automation, 2006. ICRA 2006. Proceedings 2006 IEEE International Conference on*. IEEE, 2006, pp. 1180–1187.

[38] S. Scheding, E. Nebot, M. Stevens, H. Durrant-Whyte, J. Roberts, P. Corke, J. Cunningham, and B. Cook, “Experiments in autonomous underground guidance,” *Ultrasonics*, vol. 10, p. 4, 1997.

[39] J. Ryde and N. Hillier, “Performance of laser and radar ranging devices in adverse environmental conditions,” *Journal of Field Robotics*, vol. 26, no. 9, pp. 712–727, 2009.

[40] M. Kam, X. Zhu, and P. Kalata, “Sensor fusion for mobile robot navigation,” *Proceedings of the IEEE*, vol. 85, no. 1, pp. 108–119, 1997.

[41] I. Ashokaraj, A. Tsourdos, P. Silson, and B. White, "Sensor based robot localisation and navigation: Using interval analysis and extended kalman filter," in *Control Conference, 2004. 5th Asian*, vol. 2. IEEE, 2004, pp. 1086–1093.

[42] R. Chen, H. Zhao, and B. Xiao, "Self-localization of mobile robot based on monocular and extended kalman filter," in *Electronic Measurement & Instruments, 2009. ICEMI'09. 9th International Conference on*. IEEE, 2009, pp. 2–450.

[43] H. J. Kushner, "Dynamical equations for optimal nonlinear filtering," *Journal of Differential Equations*, vol. 3, no. 2, pp. 179–190, 1967.

[44] S. Thrun, W. Burgard, and D. Fox, *Probabilistic robotics*. MIT press, 2005.

[45] P. Li and V. Kadirkamanathan, "Particle filtering based likelihood ratio approach to fault diagnosis in nonlinear stochastic systems," *IEEE transactions on systems, man and cybernetics. Part C, Applications and reviews*, vol. 31, no. 3, pp. 337–343, 2001.

[46] F. Gustafsson, F. Gunnarsson, N. Bergman, U. Forssell, J. Jansson, R. Karlsson, and P.-J. Nordlund, "Particle filters for positioning, navigation, and tracking," *Signal Processing, IEEE Transactions on*, vol. 50, no. 2, pp. 425–437, 2002.

[47] M. Baumann, D. Eck, L. Lemmer, and K. Schilling, "Ukf sensor data fusion for localisation of a mobile robot," in *Robotics (ISR), 2010 41st International Symposium on and 2010 6th German Conference on Robotics (ROBOTIK)*. VDE, 2010, pp. 1–8.

[48] E. Wan, R. Van Der Merwe *et al.*, "The unscented kalman filter for nonlinear estimation," in *Adaptive Systems for Signal Processing, Communications, and Control Symposium 2000. AS-SPCC. The IEEE 2000*. IEEE, 2000, pp. 153–158.

[49] T.-F. Lu, "Preparation for turning a bucket wheel reclaimer into a robotic arm," in *Robotics and Biomimetics, 2008. ROBIO 2008. IEEE International Conference on*. IEEE, 2009, pp. 1710–1715.

[50] T.-F. Lu, "Bucket wheel reclaimer modeling as a robotic arm," in *Robotics and Biomimetics (ROBIO), 2009 IEEE International Conference on*. IEEE, 2009, pp. 263–268.

[51] M. S. Grewal and A. P. Andrews, *Kalman filtering: Theory and Practice with MATLAB*. John Wiley & Sons, 2014.

[52] M. S. Grewal, L. R. Weill, and A. P. Andrews, *Global positioning systems, inertial navigation, and integration*. John Wiley & Sons, 2007.

[53] E. Kaplan and C. Hegarty, *Understanding GPS: principles and applications*. Artech house, 2005.

[54] L. S. Monteiro, T. Moore, and C. Hill, "What is the accuracy of dgps?" *Journal of Navigation*, vol. 58, no. 02, pp. 207–225, 2005.

[55] L. Liu and M. G. Amin, "Performance analysis of gps receivers in non-gaussian noise incorporating precorrelation filter and sampling rate," *Signal Processing, IEEE Transactions on*, vol. 56, no. 3, pp. 990–1004, 2008.

[56] K. Butcher, C. Cheesman, J. Hill, and A. Oermann, “Automatic ship loading.”

[57] M. D. Adams and P. J. Probert, “The interpretation of phase and intensity data from amcw light detection sensors for reliable ranging,” *The International journal of robotics research*, vol. 15, no. 5, pp. 441–458, 1996.

[58] C. Ye and J. Borenstein, “Characterization of a 2-d laser scanner for mobile robot obstacle negotiation,” in *ICRA*, 2002, pp. 2512–2518.

[59] T. F. Coleman and Y. Li, “An interior trust region approach for nonlinear minimization subject to bounds,” *SIAM Journal on optimization*, vol. 6, no. 2, pp. 418–445, 1996.

[60] S. Zhao, “Automatic underwater multiple objects detection and tracking using sonar imaging,” Master’s thesis, University of Adelaide, 2010.

[61] N. Otsu, “A threshold selection method from gray-level histograms,” *Automatica*, vol. 11, no. 285-296, pp. 23–27, 1975.

[62] W. E. Lorensen and H. E. Cline, “Marching cubes: A high resolution 3d surface construction algorithm,” in *ACM siggraph computer graphics*, vol. 21, no. 4. ACM, 1987, pp. 163–169.

[63] F. Bernardini, J. Mittleman, H. Rushmeier, C. Silva, and G. Taubin, “The ball-pivoting algorithm for surface reconstruction,” *Visualization and Computer Graphics, IEEE Transactions on*, vol. 5, no. 4, pp. 349–359, 1999.

[64] C. Runge, “Über empirische funktionen und die interpolation zwischen äquidistanten ordinaten,” *Zeitschrift für Mathematik und Physik*, vol. 46, no. 224-243, p. 20, 1901.

[65] C. De Boor, “A practical guide to splines, revised edition, vol. 27 of applied mathematical sciences,” 2001.

[66] L. Piegl and W. Tiller, *The NURBS book*. Springer Science & Business Media, 2012.

[67] E. T. Lee, “Choosing nodes in parametric curve interpolation,” *Computer-Aided Design*, vol. 21, no. 6, pp. 363–370, 1989.

[68] K.-H. Lee and R. Ehsani, “Comparison of two 2d laser scanners for sensing object distances, shapes, and surface patterns,” *Computers and electronics in agriculture*, vol. 60, no. 2, pp. 250–262, 2008.

[69] R. Watanabe, S. Sato, and S. Tomita, “Method and apparatus for use in separation and recovery of non-magnetic metal pieces,” Aug. 15 1978, uS Patent 4,106,627.

[70] D. Meagher, “Geometric modeling using octree encoding,” *Computer graphics and image processing*, vol. 19, no. 2, pp. 129–147, 1982.

[71] C. B. Barber, D. P. Dobkin, and H. Huhdanpaa, “The quickhull algorithm for convex hulls,” *ACM Transactions on Mathematical Software (TOMS)*, vol. 22, no. 4, pp. 469–483, 1996.

[72] T. Davies and R. Martin, “Low-discrepancy sequences for volume properties in solid modelling,” in *Proceedings of CSG*, vol. 98. Citeseer, 1998, p. 13.

[73] I. M. Sobol, "On the distribution of points in a cube and the approximate evaluation of integrals," *USSR Computational mathematics and mathematical physics*, no. 7, pp. 86–112, 1967.

[74] J. Kruger and R. Westermann, "Acceleration techniques for gpu-based volume rendering," in *Proceedings of the 14th IEEE Visualization 2003 (VIS'03)*. IEEE Computer Society, 2003, p. 38.

Appendix A

3DOF Laser Scanning System

The specification of the LMS200 laser measurement device and the kinematics of the scanning system are detailed here.

LMS200 Laser Measurement System

The LMS200 laser measurement system, manufactured by SICK Optic Electronic, is a non-contact measurement device using infrared laser beams. It is capable to produce a radial scan of 180° with an angular resolution of 0.25° to scan the surroundings two-dimensionally. Table A.1 shows the field of vision and the angular resolution of the LMS200. The measurement resolution, which is defined as the smallest possible distance different from zero between two consecutive individual measurement values, is 10 *mm*. A typical accuracy of the LMS200 is ± 15 *cm* at a scanning range of 1 to 8 *m* plus a systematic error of 5 *mm*. The measurement data are output in a binary format via the RS-232/RS-422 serial interface.

Table A.1 LMS200 scanning configurations

Configuration	1	2	3
Angular resolution	0.25°	0.5°	1°
Scanning range	100	180	180
No. of scans	401	361	181

Kinematics of the Scanning System

The 3DOF laser scanning system used for this study is designed to survey the ship loading process [56]. The Quickset QPT-50 pan and tilt platform provides pitch and yaw movement for the LMS200. The chain and sprocket system convert the rotary motion of the motor into a linear motion that allows the LMS200 move along the linear track. Fig. A.1 illustrates the coordination definitions of the entire system based on the modified Denavit-Hartenberg parameters. The fixed Frame 0 is located to the base as the world coordinate and the Frame 6 is located at the centre of the LMS200.

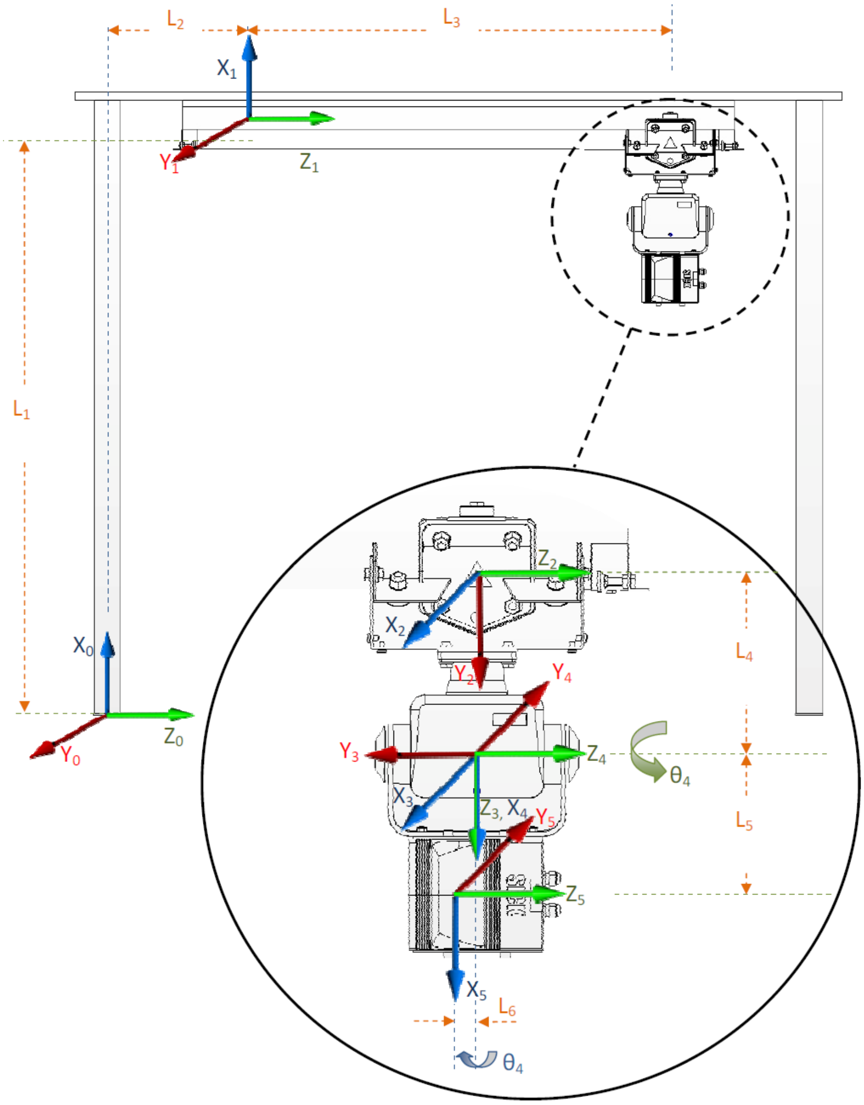

Fig. A.1 Coordinator defined for kinematic analysis.

The general transformation matrix of this system is:

$$
{}^{i-1}_{i}\mathrm{T} = \begin{vmatrix} \cos\theta_i & -\sin\theta_i & 0 & a_{i-1} \\ \sin\theta_i\cos\alpha_{i-1} & \cos\theta_i\cos\alpha_{i-1} & -\sin\alpha_{i-1} & -\sin\alpha_{i-1}d_i \\ \sin\theta_i\sin\alpha_{i-1} & \cos\theta_i\sin\alpha_{i-1} & \cos\alpha_{i-1} & \cos\alpha_{i-1}d_i \\ 0 & 0 & 0 & 1 \end{vmatrix} \tag{A.1}
$$

where α_i is the angle between Z_i and Z_{i+1} measured about X_i. a_i is the distance from Z_i and Z_{i+1} measured along X_i. d_i is the distance from X_{i-1} to X_i measured along Z_i. θ_i is the angle between X_{i-1} and X_i measured about Z_i.

Table A.2 shows the link analysis of the scanning system.

Table A.2 Link analysis of the 3DOF laser scanning system.

	α_{i-1}	a_{i-1}	θ_i	d_i
1	0	L_1	0	L_2
2	0	0	0	L_3
3	-90°	0	θ_3	L_4
4	90°	0	$90^\circ + \theta_4$	0
5	0	L_5	0	$-L_6$

Substituting these link parameters into Eq. A.1, the transforming matrix from the Frame 0 to the Frame 6 is:

$$
{}^{6}_{0}\mathrm{T}= \begin{vmatrix} -\cos\theta_3\sin\theta_4 & -\cos\theta_3\cos\theta_4 & \sin\theta_3 & L_1 + L_6\sin\theta_3 - L_5\cos\theta_3\sin\theta_4 \\ \cos\theta_4 & -\sin\theta_4 & 0 & L_4 + L_5\cos\theta_4 \\ \sin\theta_2\sin\theta_4 & \sin\theta_2\cos\theta_4 & \cos\theta_3 & L_2 + L_3 + L6\cos\theta_3 + L_5\sin\theta_3\sin\theta_4 \\ 0 & 0 & 0 & 1 \end{vmatrix} \tag{A.2}
$$